

# **Magneto-optical super-Nyquist Sampling of linear and non-linear Spin-Wave Phenomena**

## **Dissertation**

zur Erlangung des Doktorgrades der Naturwissenschaften  
(Dr. rer. nat.)

der Naturwissenschaftlichen Fakultät II  
Chemie, Physik und Mathematik

der Martin-Luther-Universität  
Halle-Wittenberg

vorgelegt von

Herrn Rouven Dreyer  
geboren am 02.07.1987 in Delmenhorst



*Supervisor:* Prof. Dr. Georg Woltersdorf

1. *Referee:* Prof. Dr. Georg Woltersdorf

2. *Referee:* Prof. Dr. Georg Schmidt

3. *Referee:* Prof. Dr. Dirk Grundler

*Date of submission:* 18.11.2021

*Date of public defense:* 23.06.2022

*Chair of the examination committee:* Prof. Dr. Thomas Thurn-Albrecht



---

# Abstract

---

This thesis presents a novel magneto-optical sampling technique for the simultaneous detection of linear and non-linear spin-dynamics in the frequency domain. By exploiting aliasing effects, our approach overcomes fundamental limitations in terms of frequency resolution. Without the restriction of a fixed frequency grid, we demonstrate direct mapping of the spin-wave dispersion in yttrium iron garnet (YIG) with remarkable precision. We present different approaches to obtain the Gilbert damping parameter locally. Moreover, we perform spatially-resolved imaging of spin-wave modes in extended layers and micron-sized structures to map the spatial distribution of these modes. Besides conventional rf-excitation, we demonstrate in the second part the unique features of super-Nyquist sampling magneto-optical Kerr microscopy (SNS-MOKE) in a magneto-elastic excitation scheme by employing surface acoustic waves (SAWs) as driving mechanism of the spin system. Here, we directly access the wave vectors of the elastically excited magnetization dynamics, and thus investigate the conversion efficiency as a function of sample size, rf-frequency, and external bias field. Finally, we use SNS-MOKE to obtain non-linear spin-wave phenomena in  $\text{Ni}_{80}\text{Fe}_{20}$  microstructures and extended layer samples in the low bias field regime. We demonstrate the existence of coherent non-linear spin waves (NLSWs) emerging at odd half-integer multiples of the driving frequency and propose a phase-locking concept for these non-linear magnons. At the same time, we obtain a large number of integer harmonics creating a six-octave spanning frequency comb. For all investigated concepts, our findings might pave the way towards novel magnonic applications.



---

# Kurzzusammenfassung

---

In dieser Dissertation wird eine neuartige magnetooptische Mikroskopietechnik zur simultanen Detektion von linearer und nichtlinearer Spindynamik im Frequenzbereich präsentiert. Durch die direkte Ausnutzung von Aliasfrequenzen überwindet diese Messtechnik grundlegende Limitierungen in Bezug auf die Frequenzauflösung. Ohne die Einschränkung eines festen Frequenzrasters lässt sich eine direkte Vermessung der Spinwellendispersion in Yttrium-Eisen-Granat mit bemerkenswerter Genauigkeit demonstrieren. Zusätzlich bietet die *Super-Nyquist Sampling MOKE* (SNS-MOKE) Technik verschiedene Möglichkeiten zur lokalen Bestimmung der Gilbert Dämpfung. Darüber hinaus ermöglichen orts aufgelöste Messungen der Spinwellendynamik, sowohl in ausgedehnten Schichten als auch in mikrometergroßen Strukturen, eine detaillierte Abbildung der räumlichen Verteilung dieser Moden. Im zweiten Teil dieser Arbeit werden die einzigartigen Eigenschaften der SNS-MOKE Methode in einem magnetoelastischen Anregungsschema angewendet, welches sich fundamental von der konventionellen Hochfrequenz (HF)-Anregung unterscheidet. Dabei werden akustische Oberflächenwellen zur Anregung des Spinsystems verwendet. Eine direkte Detektion des Wellenvektors der elastisch angeregten Magnetisierungsdynamik erlaubt eine Untersuchung der Konversionseffizienz in Abhängigkeit von der Probengröße, der HF-Frequenz und des externen Magnetfeldes. Abschließend wird SNS-MOKE zur frequenz aufgelösten Untersuchung von nichtlinearen Spinwellenphänomenen in  $\text{Ni}_{80}\text{Fe}_{20}$  Mikrostrukturen und ausgedehnten Schichten im Bereich niedriger Magnetfelder angewendet. Hier lässt sich die Existenz von kohärenten, nichtlinearen Spinwellen bei ungeraden, halbzahligen Vielfachen der HF-Frequenz experimentell beweisen. Unter Zuhilfenahme einer weiteren Frequenzkomponente wird ein Konzept zur Stabilisierung der Phasenlage der nichtlinearen Spinwellen vorgestellt, welches ebenfalls die Kontrolle der Phasenlage ermöglicht. Gleichzeitig lassen sich in solchen Messungen eine große Anzahl ganzzahliger Harmonischer beobachten, die einen sechs Oktaven überspannenden Frequenzkamm bilden. Die in dieser Arbeit untersuchten Konzepte und Phänomene könnten den Weg zu neuen Anwendungen im Bereich der Magnonik und Spintronik ebnen.



---

# Contents

---

<b>List of Figures</b>	<b>ix</b>
<b>List of Acronyms</b>	<b>xiii</b>
<b>1. Introduction</b>	<b>1</b>
<b>2. Theoretical Background</b>	<b>5</b>
2.1. Magnetization Dynamics . . . . .	5
2.1.1. Macroscopic Theory . . . . .	6
2.1.2. Contributions to the effective Field . . . . .	7
2.1.3. Ferromagnetic Resonance . . . . .	10
2.1.4. Kittel Equation . . . . .	11
2.1.5. The Landau-Lifshitz-Gilbert Equation . . . . .	12
2.1.6. Gilbert Damping . . . . .	13
2.2. Spin Waves in thin magnetic Films . . . . .	14
2.2.1. Dipole-exchange Spin Waves . . . . .	15
2.2.2. Dipolar Spin-Wave Approximation . . . . .	16
2.3. Spin-Wave Mode Repulsion . . . . .	18
2.4. Non-linear Magnetization Dynamics . . . . .	20
2.4.1. Suhl Instabilities . . . . .	20
2.4.2. Non-linear Spin-Wave Generation at low magnetic bias Fields . . . . .	22
2.5. The magneto-optical Kerr Effect . . . . .	23
<b>3. Super-Nyquist Sampling MOKE</b>	<b>27</b>
3.1. Magneto-optical Kerr Microscopy . . . . .	27
3.2. Super-Nyquist Sampling MOKE . . . . .	29
3.2.1. Sampling of Magnetization Dynamics at arbitrary Frequencies . . . . .	29
3.2.2. Microscopy Setup for SNS-MOKE Detection . . . . .	33
3.2.3. Measurement of Resonance Lineshapes . . . . .	37
<b>4. Local Magnetization Dynamics in YIG</b>	<b>41</b>
4.1. Measurement Geometry . . . . .	42
4.1.1. Sample Layout . . . . .	42
4.1.2. Field-swept Spectra . . . . .	42
4.2. Spin-Wave Dispersion in 200 nm YIG Layers . . . . .	44
4.2.1. Spatially-resolved Imaging of Spin Waves in YIG . . . . .	44

---

4.2.2.	Spatially-resolved Spin-Wave profiles near an avoided Crossing . . . . .	45
4.2.3.	Spin-Wave Dispersion . . . . .	46
4.2.4.	Dipole Gap . . . . .	48
4.3.	Local Gilbert Damping . . . . .	53
4.3.1.	Angular-resolved Measurement . . . . .	54
4.3.2.	Frequency-dependent Analysis of minimal Dispersion . . . . .	55
4.3.3.	Determination of the Gilbert Damping Parameter . . . . .	56
4.4.	Magnonic Band Structure Engineering . . . . .	58
4.4.1.	Manipulating the Dispersion Relation . . . . .	59
4.4.2.	Variations of the Magnonic Waveguide . . . . .	59
<b>5.</b>	<b>Spin Waves in confined YIG Structures</b>	<b>65</b>
5.1.	Local Investigation of Spin Waves in YIG Microstructures . . . . .	66
5.1.1.	Sample Preparation . . . . .	66
5.1.2.	Gilbert Damping of freestanding Monocrystalline YIG Bridges . . . . .	66
5.1.3.	Spatially-resolved Imaging of standing Spin-Wave Modes . . . . .	68
5.2.	Transfer of YIG Elements to arbitrary Substrates . . . . .	68
<b>6.</b>	<b>Surface acoustic Wave driven Spin Dynamics</b>	<b>71</b>
6.1.	Measurement Concept . . . . .	72
6.1.1.	Surface acoustic Wave Generation by interdigital Transducers . . . . .	73
6.1.2.	Strain-induced Birefringence . . . . .	75
6.2.	SAW-driven Dynamics in Nickel Structures . . . . .	77
6.2.1.	Angular-resolved Measurements . . . . .	77
6.2.2.	Spatially-resolved Imaging of SAW-driven Spin Dynamics . . . . .	80
6.3.	SAW-driven FMR in transferred YIG Structures . . . . .	84
6.3.1.	Sample Layout and IDT Characteristics . . . . .	85
6.3.2.	Spin-Wave Spectra for different IDT Harmonics . . . . .	85
6.3.3.	Angular-resolved Measurements . . . . .	86
6.3.4.	Imaging of SAW-driven FMR in YIG Structures . . . . .	88
<b>7.</b>	<b>Non-linear Spin-Wave Generation</b>	<b>91</b>
7.1.	Experimental Configuration . . . . .	92
7.1.1.	Sample Fabrication . . . . .	92
7.1.2.	Measurement Geometry . . . . .	92
7.1.3.	Detection of uniform and non-uniform Magnons . . . . .	93
7.2.	Magneto-optical Sampling of non-linear Spin Dynamics . . . . .	95
7.2.1.	Non-linear Spin-Wave Excitation in Ni <sub>80</sub> Fe <sub>20</sub> Elements . . . . .	95
7.2.2.	Threshold Determination of NLSW Generation . . . . .	99
7.3.	Spatially-resolved Imaging of NLSWs . . . . .	101
7.4.	Wave-Vector Analysis . . . . .	105
7.5.	Control of Propagation Direction . . . . .	108

7.6. Phase Locking of non-linear Spin Waves . . . . .	109
7.6.1. NLSW Generation with additional Seed Frequency . . . . .	110
7.6.2. Imaging of Phase-Locked non-linear Excitation . . . . .	112
7.6.3. Phase Locking to a Seed Frequency . . . . .	114
<b>8. Frequency Comb Generation in Ni<sub>80</sub>Fe<sub>20</sub></b>	<b>117</b>
8.1. Indication of an All-Magnonic Frequency Comb . . . . .	117
8.2. Field-resolved Detection of higher Harmonic Generation . . . . .	118
8.3. Spatially-resolved Analysis of the Frequency Comb . . . . .	121
8.3.1. Wave Vectors of the Frequency Comb . . . . .	123
8.3.2. Lifetime Calculation . . . . .	124
8.3.3. Origin of the Frequency Comb . . . . .	125
<b>9. Conclusion</b>	<b>127</b>
<b>A. Appendix</b>	<b>I</b>
A.1. Magnetic Characterization of Ni <sub>80</sub> Fe <sub>20</sub> Samples . . . . .	I
A.1.1. Extended Layer Sample . . . . .	I
A.1.2. Ni <sub>80</sub> Fe <sub>20</sub> Elements . . . . .	II
A.2. Magnetic Characterization of YIG . . . . .	II
A.3. Exchange Coupling in a YIG/Ni <sub>80</sub> Fe <sub>20</sub> Bilayer . . . . .	III
A.4. Spatially-resolved Imaging of SAW-induced Dynamics in Co . . . . .	IV
A.4.1. Spatially-resolved Imaging of SAW-driven FMR in a Co Patch . . . . .	V
A.4.2. Wave-vector Analysis of SAW-driven FMR in a Co Patch . . . . .	VI
A.5. Micromagnetic Simulation of NLSW Generation in Ni <sub>80</sub> Fe <sub>20</sub> Elements . . . . .	VII
A.5.1. Field-swept Spectra of NLSWs Generation . . . . .	VII
A.5.2. Micromagnetic Simulation of spatially-resolved NLSW Generation . . . . .	IX
<b>Bibliography</b>	<b>XI</b>
<b>Curriculum Vitae</b>	
<b>List of Publications</b>	
<b>Acknowledgments</b>	
<b>Eidesstattliche Erklärung</b>	



---

# List of Figures

---

2.1. Schematic of magnetization dynamics. . . . .	12
2.2. Illustration of a non-uniform spin wave. . . . .	14
2.3. Calculated spin-wave dispersion for 20 nm $\text{Ni}_{80}\text{Fe}_{20}$ . . . . .	17
2.4. Calculated mode repulsion for 200 nm YIG. . . . .	19
2.5. Schematic of different magnon-magnon scattering processes. . . . .	21
2.6. Spin-wave decay rate and non-linear dispersion. . . . .	23
2.7. Schematic of the magneto-optical Kerr effect. . . . .	25
3.1. Schematic of TR-MOKE and SNS-MOKE functional principle in frequency space. . . . .	30
3.2. Generation of alias frequencies due to under sampling. . . . .	32
3.3. Optical microscopy setup for SNS-MOKE detection. . . . .	34
3.4. Coplanar waveguide for rf-excitation. . . . .	35
3.5. Frequency-dependent detector noise. . . . .	36
3.6. Field-swept spectra for linewidth determination with SNS-MOKE. . . . .	37
4.1. Measurement geometry with different spin-wave excitations. . . . .	42
4.2. Field-swept spin-wave spectra. . . . .	43
4.3. Spatially-resolved imaging of spin waves in YIG. . . . .	44
4.4. Line scans of spin-wave modes close to an avoided crossing. . . . .	45
4.5. Spin-wave dispersion of YIG. . . . .	46
4.6. Avoided crossing in the spin-wave dispersion. . . . .	49
4.7. Dipole gap under field reversal. . . . .	51
4.8. The dipole gap's change under in-plane field rotation. . . . .	52
4.9. Angular-resolved spin-wave spectra at 4 GHz. . . . .	54
4.10. Frequency-dependent analysis of the point of minimal dispersion. . . . .	55
4.11. Gilbert damping and linewidth in points of flat dispersion. . . . .	57
4.12. Conceptual illustration of a soft magnonic waveguide. . . . .	60
4.13. Dispersion engineering with different gap sizes. . . . .	61
4.14. Modification of the spin-wave dispersion. . . . .	62
5.1. Schematic of monocrystalline YIG bridges. . . . .	66
5.2. Gilbert damping determination in a freestanding YIG bridge. . . . .	67
5.3. Spatially-resolved imaging of standing spin-wave modes in YIG bridges. . . . .	68
5.4. False-color image of a transferred YIG platelet on top of a CPW. . . . .	69

5.5. Spatially-resolved imaging of standing spin-wave modes in a transferred YIG platelet. . . . .	70
6.1. Illustrated sample geometry for magneto-elastic driving. . . . .	72
6.2. Schematic of an interdigital transducer structure for SAW excitation. . . . .	73
6.3. Characterization of the interdigital transducer. . . . .	74
6.4. Spatially-resolved imaging of SAW driven dynamics with additional field modulation. . . . .	76
6.5. Field-swept spectra of SAW-driven FMR in Ni elements. . . . .	77
6.6. Angular-resolved SAW-driven magnetization dynamics in different element geometries. . . . .	78
6.7. Angular-resolved SAW-driven magnetization dynamics as function of frequency. . . . .	79
6.8. Spatially-resolved imaging of SAW-driven dynamics in different element geometries. . . . .	81
6.9. Spatially-resolved imaging at different field amplitudes and IP orientations. . . . .	82
6.10. Wave-vector spectra of SAW-driven dynamics in the $20\ \mu\text{m} \times 10\ \mu\text{m}$ ellipse with a fixed bias field and varying angular orientations. . . . .	83
6.11. Wave-vector spectrum of the IDT structure at different frequencies. . . . .	85
6.12. SAW-driven magnetization dynamics in a YIG microstructure. . . . .	86
6.13. Angular-resolved measurements of SAW-driven dynamics in two different YIG elements. . . . .	87
6.14. Spatially-resolved imaging of different SAW-driven spin-wave modes in a YIG element. . . . .	88
6.15. Wave-vector spectra and spin-wave amplitude as a function of magnetic field. . . . .	89
7.1. Sample and measurement geometry for non-linear spin-wave generation. . . . .	93
7.2. Comparison of uniform and non-uniform magnons in three different element geometries. . . . .	94
7.3. Power-dependent analysis of FMR mode and NLSW response. . . . .	96
7.4. Magneto-optical sampling of non-linear spin waves at half-integer harmonics. . . . .	97
7.5. Threshold of non-linear spin-wave generation. . . . .	100
7.6. Spatially-resolved imaging at half-integer harmonics. . . . .	102
7.7. Phase switching of the NLSW excitation. . . . .	103
7.8. Phase stability of NLSW excitation. . . . .	104
7.9. Phase-resolved imaging of NLSW and 2D-FFT obtained from SNS-MOKE measurements and micromagnetic simulations. . . . .	106
7.10. Frequency-resolved investigation of the non-linear wave-vector components. . . . .	107
7.11. Angular-resolved field-swept measurements of NLSW generation. . . . .	108
7.12. Wave-vector spectra for different field orientations. . . . .	109
7.13. Injection locking of NLSW generation by using a seed frequency. . . . .	111
7.14. Spatially-resolved imaging of $5\ \mu\text{m} \times 4\ \mu\text{m}$ rectangular element with additional seed frequency. . . . .	112
7.15. Imaging of stabilized non-linear spin waves at different seed frequencies. . . . .	113

7.16. Phase locking of NLSW generation. . . . .	115
8.1. Field-swept measurements of multiple harmonics of 319 MHz . . . . .	119
8.2. Reconstructed time trace with 79 MHz fundamental frequency. . . . .	121
8.3. Spatially-resolved imaging of higher harmonics within an all-magnonic frequency comb. . . . .	122
8.4. Extracted in-plane wave-vector distribution of the frequency comb for different fundamental frequencies. . . . .	123
8.5. Spin-wave decay rate in k-space for 0.5 mT. . . . .	124
8.6. Model of the switching process under rf-excitation. . . . .	126
A.1. Frequency-resolved measurements to obtain the Kittel fit and determine the Gilbert damping. . . . .	I
A.2. Frequency-resolved measurements in $\text{Ni}_{80}\text{Fe}_{20}$ . . . . .	II
A.3. Frequency-resolved SNS-MOKE and inductive FMR measurements in YIG. . . . .	III
A.4. Exchange-coupled $\text{Ni}_{80}\text{Fe}_{20}$ element on top of YIG layer. . . . .	IV
A.5. Spatially-resolved imaging at different field amplitudes and orientations in Co. . . . .	V
A.6. Wave-vector spectra of SAW-driven dynamics for different field amplitudes and orientations. . . . .	VI
A.7. Micromagnetic simulations of the field-resolved spin-wave spectra analyzed at different frequencies with different spatial variations of the saturation magneti- zation. . . . .	VIII
A.8. Micromagnetic simulations of spatially-resolved NLSW excitations with different spatial variations of the saturation magnetization. . . . .	IX



---

# List of Acronyms

---

<b>2D-FFT</b>	two-dimensional fast Fourier transform
<b>AIO<sub>x</sub></b>	aluminium oxide
<b>Au</b>	gold
<b>BLS</b>	Brillouin light scattering
<b>BV</b>	backward volume
<b>BVSW</b>	backward volume spin wave
<b>CCD</b>	charge coupled device
<b>CMOS</b>	complementary metal-oxide semiconductor
<b>CPW</b>	coplanar waveguide
<b>DE</b>	Demon Eshbach
<b>DMI</b>	Dzyaloshinskii–Moriya interaction
<b>ESR</b>	electron spin resonance
<b>FFT</b>	fast Fourier transform
<b>FMR</b>	ferromagnetic resonance
<b>FVSW</b>	forward volume spin wave
<b>GaAs</b>	gallium arsenide
<b>GGG</b>	gadolinium gallium garnet
<b>HHG</b>	high-harmonic generation
<b>HWHM</b>	half-width at half maximum
<b>IDT</b>	interdigital transducer
<b>IP</b>	in-plane
<b>I-MOKE</b>	longitudinal magneto-optical Kerr effect
<b>LED</b>	light emitting diode
<b>LIA</b>	lock-in amplifier
<b>LLG</b>	Landau-Lifshitz-Gilbert
<b>MgO</b>	magnesium oxide
<b>MOKE</b>	magneto-optical Kerr effect
<b>MSSW</b>	magneto-static surface wave
<b>Ni</b>	nickel
<b>NLSW</b>	non-linear spin wave
<b>NV</b>	nitrogen vacancy
<b>OOP</b>	out-of-plane
<b>p-MOKE</b>	polar magneto-optical Kerr effect
<b>PID</b>	proportional-integral-derivative

---

<b>PLD</b>	pulsed laser deposition
<b>PLL</b>	phase-locked loop
<b>PMMA</b>	polymethyl methacrylate
<b>PSSW</b>	perpendicular standing spin wave
<b>RAM</b>	random access memory
<b>rf</b>	radio frequency
<b>SAW</b>	surface acoustic wave
<b>SHE</b>	spin-Hall effect
<b>SNR</b>	signal-to-noise ratio
<b>SNS</b>	super-Nyquist sampling
<b>SNS-MOKE</b>	super-Nyquist sampling magneto-optical Kerr microscopy
<b>SOC</b>	spin-orbit coupling
<b>SOT</b>	spin-orbit torque
<b>ST-FMR</b>	spin-torque ferromagnetic resonance
<b>STT</b>	spin-transfer torque
<b>t-MOKE</b>	transversal magneto-optical Kerr effect
<b>TR-MOKE</b>	time-resolved magneto-optical Kerr microscopy
<b>TR-STXM</b>	time-resolved scanning transmission x-ray microscopy
<b>VNA</b>	vector network analyzer
<b>VNA-FMR</b>	vector network analyzer ferromagnetic resonance
<b>XMCD</b>	x-ray magnetic circular dichroism
<b>YAG</b>	yttrium aluminium garnet
<b>YIG</b>	yttrium iron garnet

# Introduction

---

Over the last decades, Moore's law described the continuous progress in information and communication technology. However, the rapid increase of integrated devices' density per chip is close to its fundamental limits [1, 2]. The current architecture of processor units might be one of the last possible before a further size reduction leads to quantum effects preventing fundamental functions. Thus, novel concepts for different computational operations are highly demanded. While some of these concepts are already applied to a large variety of applications, e.g., machine learning [3] or spintronic operations [4, 5], others are just at the edge of becoming an alternative to state-of-the-art technology, such as magnonics [6] and quantum computing [7].

In information and communication technology, spin-based effects have shown to be a remarkable extension to conventional electronics [8, 9]. Here, the electron's spin is exploited as an additional degree of freedom enabling the control of spin-torque nano-oscillators by spin currents [10–15]. This concept made its way towards application in spin-transfer torque (STT) or spin-orbit torque (SOT) random access memory (RAM) devices [16]. Besides employing the electron's spin, the collective excitation of the spin system - also referred to as spin waves - appears to be a promising concept for energy-efficient technology [17–19]. In this approach, the spin wave - quantized by its quasi-particle, the magnon - is utilized to transport information between devices without the transport of the electron itself, and thus without the fundamental restriction of Joule heating [20]. This emerging field is known as magnonics [18, 21, 22], where devices do not solely transfer data but also manipulate the transferred information. In recent years, a large number of conventional electronic concepts was successfully transferred to the world of magnonics. Besides spin-wave guiding [23], functional devices such as magnonic directional couplers [24], magnonic diodes [25] and magnon transistors [22] have been demonstrated. Recent magnonic devices focus on antiferromagnetic materials due to their inherently large bandwidth and vanishingly small stray fields [26, 27].

However, the possibility of performing magnonic operations is strongly related to the magnetic quality factor of the material represented by the Gilbert damping constant [28]. While most proof-of-principle concepts employ the low-damping material yttrium iron garnet (YIG) [29] their integration into conventional electronics is restricted due to the utilized substrate [30]. So far, only gadolinium gallium garnet (GGG) substrates allow for the fabrication of high-quality thin-film YIG-based devices. Thus, experimental investigations aim for either optimizing YIG-

based devices fabricated on other substrates than GGG or searching for alternative classes of magnonic materials [19]. Recently, a novel fabrication and transfer process of monocrystalline YIG devices [31] expanded the range of possible applications with this promising material system to magneto-elastic excitations on surface acoustic wave (SAW) carrying substrates and low-temperature cavity magnonics. Both of these examples exploit fundamental effects of magnetism to form novel types of devices. Magneto-elastic excitations [32–34] can be implemented directly to conventional electronics since the excitation scheme utilized for these devices is present in modern computing technology as narrow frequency filters or microwave delay lines [35]. Additionally, an elastic excitation of the magnetic system might pave the way towards novel types of coupled magnetic systems where mechanical resonances interact with magnetic excitations. Similar coupling phenomena of magnons and photons are exploited in cavity magnonics [36, 37] which bridges the gap between magnonics and quantum computing since degenerated magnon states at crossing points of the magnetic and photonic dispersion branches might mimic a two-level system [38]. While most experimental approaches utilize macroscopic YIG spheres and three-dimensional cavities [39–41], the reduction of size as well as two-dimensional cavity approaches are highly demanded. In addition, the interaction of spin-wave modes within magnetic layers or heterostructures [42, 43] acts as an exciting playground for strong-coupling phenomena [44] and might find its way towards quantum computing [45].

In recent years, non-linear effects have revealed their potential for magnonic devices [46, 47]. Non-linear magnon-scattering processes can be utilized for frequency conversion, but in most cases, only a down-conversion of the excitation frequency is achieved [48–51]. The generation of higher harmonics is so far restricted to a few harmonics only [52, 53]. Fortunately, the discovery of a novel class of non-linear magnons [54] facilitates possibilities for all-magnonic frequency conversion in future devices.

The investigation of magnetization dynamics in novel spintronic and magnonic materials or devices primarily relies on electrical detection techniques such as ferromagnetic resonance (FMR) [32, 55, 56]. However, these techniques average across the entire device and are thus not sensitive to local properties. Therefore, a more elaborated detection approach for local dynamics in micron-sized structures exploits the device's interaction with light waves. In these experimental approaches, local properties such as the wavelength or the propagation direction of spin waves can be obtained in the time or frequency domain by either using time-resolved magneto-optical Kerr microscopy (TR-MOKE) [57–60], Brillouin light scattering (BLS) [61–65], nitrogen vacancy (NV) center magnetometry [66–69] or time-resolved scanning transmission x-ray microscopy (TR-STXM) [70–72]. Nevertheless, all these techniques suffer from certain limitations, which make experiments on magnonic materials challenging. In this thesis, we present a novel approach of Kerr microscopy that allows for the detection of linear and non-linear magnetization dynamics with arbitrarily high-frequency resolution [73]. As we will show, this technique enables precise mapping of the spin-wave dispersion and allows for a local determination of magnetic properties, such as the Gilbert damping parameter. In addition,

the detection is decoupled from the excitation frequency which allows for a coherent detection at arbitrary frequencies, such as the ones of non-linear spin-wave phenomena.

The second chapter of this thesis covers the investigated magnetic effects and provides the formalism used to describe the obtained phenomena. In chapter 3, the SNS-MOKE technique is introduced in detail, while its measurement capabilities are demonstrated in chapter 4 for an extended YIG layer and in chapter 5 for YIG microstructures. In the following chapter, the possibility of magneto-elastic coupling of SAWs to micron-sized magnetic elements is presented in a spatially-resolved fashion to link the excited spin waves' wave vector to external control parameters. In chapter 7, SNS-MOKE offers novel insight into non-linear spin-wave phenomena. Here, we demonstrate the first spatially-resolved observation of NLSWs at odd half-integer multiples of the driving frequency and propose a concept which grants direct control of these non-linearities. Finally, we reveal how non-linear processes in combination with spatially-varying properties of the magnetic material might be used for all-magnonic high-harmonic generation (HHG) in chapter 8.



# Theoretical Background

---

This chapter covers basic theoretical concepts of magnetization dynamics and describes more advanced phenomena investigated in this thesis. The first part of this chapter will introduce the equation of motion for magnetization dynamics and present solutions for the uniform precessional motion as well as for non-uniform cases. These collective excitations of the magnetic systems are referred to as spin waves or magnons. We will furthermore consider Gilbert damping as a relaxation mechanism and derive the Landau-Lifshitz-Gilbert (LLG) equation. In the next step, these concepts are applied to realistic sample geometries investigated in the experiments to obtain the spin-wave dispersion. In addition, we will discuss particular cases where different spin-wave modes interact with each other and thus modify the spin-wave dispersion by opening frequency gaps in the spectrum. These modifications will be taken into account to model experimental results properly. Afterwards, non-linear spin-wave phenomena are introduced to understand the experimentally obtained features shown in chapter 7. Finally, we introduce the interaction of magnetization dynamics with light waves as one of the basic detection mechanisms for spin-wave phenomena.

## 2.1. Magnetization Dynamics

In the experiments, ferromagnetic and ferrimagnetic materials were investigated, but also antiferromagnetic materials might be a topic in future experiments due to their lack of stray fields. In ferromagnetic materials, the magnetic moments are aligned parallel to an externally applied magnetic bias field. For small fields, domains of different magnetization direction emerge to minimize the energy caused by stray fields [74]. These domains expand as the field increases until the magnetic material is saturated and all magnetic moments are aligned in the same direction [75]. This order persists in a remanent state as the field is switched off. In the antiferromagnetic state, the magnetic moments align antiparallel to each other, and therefore, the net magnetization is zero. The intermediate ferrimagnetic order consists of two sub-lattices that are ordered antiparallel. Due to their different number of magnetic moments per unit cell, a non-vanishing net magnetization remains, which allows to treat ferrimagnets as a ferromagnet in most cases.

### 2.1.1. Macroscopic Theory

The description of a single magnetic moment  $\boldsymbol{\mu}$  in an applied magnetic field  $\mathbf{H}$  is given by a precessional motion [74].

$$\frac{\partial \boldsymbol{\mu}}{\partial t} = -\gamma \boldsymbol{\mu} \times \mathbf{H} \quad (2.1)$$

The shown expression is the so-called Larmor-precession with the gyromagnetic ratio  $\gamma = g\mu_B/\hbar$ , where  $g \approx 2$  is the Landé factor,  $\mu_B$  is the Bohr magneton and  $\hbar$  the reduced Planck's constant. An atomistic treatment of each individual spin in a solid (with roughly  $10^{22}$  electrons) strongly increases the computational demand of the problem. Therefore, it is mostly used in simulations, where net magnetization averaged over space, e.g., in a unit cell, is of interest. For an analytical treatment of solids, a macroscopic approach is elaborated. Here, the sum of the single magnetic moments in a defined volume  $V$  is expressed by the magnetization  $\mathbf{M} = \sum \boldsymbol{\mu}/V$ , the macrospin approximation [74]. While this approximation is suitable to describe most ferromagnetic phenomena, for others, such as exchange coupling, it is still required to have the microscopic description in mind. In this macroscopic approach, equation 2.1 changes to

$$\frac{\partial \mathbf{M}}{\partial t} = -\gamma \mathbf{M} \times \mathbf{H}_{\text{eff}}, \quad (2.2)$$

known as the Landau-Lifshitz-Equation [76] which derives the precessional motion of the magnetization  $\mathbf{M}$ . Here,  $\mathbf{H}_{\text{eff}}$  is the effective magnetic field, which contains all magnetic contributions, such as dipolar fields  $\mathbf{H}_d$ , additional anisotropies  $\mathbf{H}_{\text{ani}}$ , exchange fields  $\mathbf{H}_{\text{ex}}$ , magneto-elastic contributions  $\mathbf{H}_{\text{me}}$  and a Zeeman term due to the external magnetic field  $\mathbf{H}_0$  [57, 74]. It can be expressed with the aid of the Helmholtz free energy functional  $\mathcal{F}[\mathbf{M}] = \int_V (\varepsilon_0 + \varepsilon_{\text{ani}} + \varepsilon_d + \varepsilon_{\text{ex}} + \varepsilon_{\text{me}}) dV$ , which can be understood as the integral of all contributing energy densities [77]. The derivative of  $\mathcal{F}[\mathbf{M}]$  with respect to the magnetization results in the effective field  $\mathbf{H}_{\text{eff}}$  and reads as follows:

$$-\frac{\partial \mathcal{F}[\mathbf{M}]}{\partial \mathbf{M}} = \mathbf{H}_{\text{eff}} = \mathbf{H}_0 + \mathbf{H}_{\text{ani}} + \mathbf{H}_d + \mathbf{H}_{\text{ex}} + \mathbf{H}_{\text{me}}. \quad (2.3)$$

For an adequate description of many ferromagnetic phenomena, additional contributions to the free energy must be considered, such as interlayer coupling through Dzyaloshinskii–Moriya

interaction (DMI). In the following, we first introduce the contributions to the free energy which are of interest in the experiments and subsequently find solutions of equation 2.3 for specific cases of the effective field describing the most fundamental magnetization dynamics.

### 2.1.2. Contributions to the effective Field

Besides the exchange interaction, on which the ferromagnetic order is based, dipolar contributions due to shape anisotropy or magneto-crystalline anisotropy influence the magnetization, leading to a preferred orientation of the magnetization along a crystallographic axis. In the case of an uniaxial anisotropy, the energy is maximized along the so-called "hard" axis while it is minimized along the "easy" axis. In the absence of an external field, the magnetization tends to align along the easy axis of the system.

#### Shape Anisotropy and dipolar Fields

The dipole-dipole-interaction is a long-range effect, and its contribution to the magnetic order is rather small compared to the exchange interaction ( $E_d \approx 0.1 \text{ meV} \ll E_{\text{ex}} \approx 100 \text{ meV}$ ). However, this interaction is crucial for the existence of long-wavelength spin waves and their anisotropic behavior. In a confined magnetic material, such as a thin film, these dipolar fields have a non-vanishing contribution due to the broken symmetry at the interfaces of the thin film. Dipole moments at interfaces create stray fields outside and a demagnetization field within the ferromagnetic material. The energy density is written as  $\varepsilon_{\text{dipolar}} = \frac{1}{2} \mathbf{H}_d \cdot \mathbf{M}$ . Here,  $\mathbf{H}_d$  is the demagnetization field caused by the magnetization. It can be expressed as

$$\mathbf{H}_d = -\mathcal{N} \cdot \mathbf{M}, \quad (2.4)$$

via the demagnetization tensor  $\mathcal{N}$ , which couples the demagnetizing fields to the magnetization. The trace of this tensor is 1, and for the particular case of an ellipsoid  $\mathcal{N}$  becomes diagonal, which grants a free orientation of the magnetization [74]. For a thin magnetic film in the  $xy$ -plane, only the  $\mathcal{N}_{zz}$  component persists. Since the dipolar contribution strongly depends on the shape of the sample, its impact on the magnetization is called shape anisotropy, and different geometrical shapes can be considered via  $\mathcal{N}$  [78].

#### Exchange Interaction

In contrast to the dipole-dipole coupling, the exchange interaction has a very short interaction length and mostly acts on the neighboring spins while its coupling strength is comparably larger. Here, a microscopic treatment is mandatory, to understand the impact of the exchange

interaction. In itinerant ferromagnets, the main ingredients for the emergence of ferromagnetic order are the localized 3d electrons. The energy of these 3d states lies below the Fermi level for spin-up electrons. Due to the exchange splitting, the 3d band of spin-down electrons is found above the Fermi level. Thus, the exchange coupling is responsible for the magnetic order in solids, since it favors a occupation of the majority states [74]. The exchange interaction tries to align adjacent spins either parallel or antiparallel to each other which results in the minimization of the exchange energy [79]. Local impurities or other variations of this alignment, therefore, increase the exchange energy. The exchange energy  $f_{ij}$  can be derived quantum-mechanically via a Heisenberg Hamiltonian for two neighboring spins  $\mathbf{S}_{i,j}$  via  $f_{ij} = -\mathcal{J}_{ij}^{\text{ex}} \mathbf{S}_i \mathbf{S}_j$ , with the exchange constant  $\mathcal{J}_{ij}^{\text{ex}}$ . If  $\mathcal{J}_{ij}^{\text{ex}} > 0$ , the coupling of adjacent spins is of ferromagnetic order, while for  $\mathcal{J}_{ij}^{\text{ex}} < 0$  the magnetic moments couple antiferromagnetically [74, 79]. In the continuum approximation ( $\mathcal{J}_{ij}^{\text{ex}} = \mathcal{J}^{\text{ex}}$ ), an effective exchange field has the form

$$\mathbf{H}_{\text{ex}} = \frac{2Z\mathcal{J}^{\text{ex}}}{\mu_0\mu_B^2Ng^2} \mathbf{M}, \quad (2.5)$$

where  $\mu_0$  is the vacuum permeability,  $Z$  is the atomic number and  $N$  the number of atoms. The energy density of the exchange interaction  $\varepsilon_{\text{ex}} = A_{\text{ex}}|\nabla\mathbf{M}|^2$  [75, 77] allows a more general formulation of the exchange field  $\mathbf{H}_{\text{ex}} = A_{\text{ex}}\nabla^2\mathbf{M}$ , where  $A_{\text{ex}}$  is the exchange stiffness constant [57, 80].

### Magneto-crystalline Anisotropy

In crystalline structures, the response of the magnetic moments to an external field becomes orientation-dependent due to the coupling of the spin moment to the orbital magnetic moment. This coupling leads to different magnetic fields along different crystallographic axes [81]. A typical origin of such a magneto-crystalline anisotropy is the growth-induced stress which results in the modification of the spin-orbit coupling (SOC) in a magnetic layer, for example when the lattice constants of substrate and magnetic layer do not match perfectly or due to surface roughness.

The materials investigated in this work (yttrium iron garnet (YIG) grown on gadolinium gallium garnet (GGG) and  $\text{Ni}_{80}\text{Fe}_{20}$ ) have very small magneto-crystalline anisotropy compared to other energy contributions, and therefore, they are neglected in the further discussion [74].

### Magneto-elastic Coupling

As seen in the previous part, strain-induced anisotropy contributions may act on the magnetization. This could happen due to lattice mismatch but also on larger scales. Here, the inverse effect of the magnetostriction, known as magneto-elasticity, gives rise to an additional

anisotropy field, when the entire magnetic layer is stressed or local stress is applied. Two different regimes have to be considered here: On one hand, a static strain which acts similar as the magneto-crystalline anisotropy and on the other hand, a dynamic contribution responsible for the effects observed in experiments. Here we follow the theoretical description of Dreher *et al.* [32, 33]. In their approach, they express the effective magnetic field as the derivative of the Gibbs free energy with respect to the magnetization components  $M_i$  via

$$\begin{aligned}\mu_0 \mathbf{H}_{\text{eff}} &= -\nabla_M \mathcal{G}^{\text{tot}} \\ &= -\nabla_M \left( \mathcal{G} + \mathcal{G}^{\text{d}} + \frac{\mathcal{W}}{M_s} \right).\end{aligned}\quad (2.6)$$

In comparison to  $\mathcal{F}$  the Gibbs free energy  $\mathcal{G}$  allows to consider variations of pressure. Here,  $\mathcal{G}^{\text{tot}}$  composed of a static part  $\mathcal{G}$  and a dynamic contribution  $\mathcal{G}^{\text{d}}$  which represents the dynamics driven a time-varying magneto-elastic coupling. The static contribution of the effective field contains all the components introduced in the previous sections (cf. equation 2.3). Furthermore, the elastic energy density  $\mathcal{W}$  is required which can be expressed by means of Einstein summation convention as  $\mathcal{W} = \frac{1}{2} \mathcal{C}_{ijkl} \epsilon_{ij} \epsilon_{kl}$  where  $\mathcal{C}_{ijkl}$  are the components of the elastic constants tensor and  $\epsilon_{ij}$  with  $i, j \in \{x, y, z\}$  being the elements of the strain tensor. The essential part for the dynamic excitation is  $\mathcal{G}^{\text{d}}$  which can be expressed as follows:

$$\begin{aligned}\mathcal{G}^{\text{d}} &= b_1 \left[ \epsilon_{xx}(x, t) M_x^2 + \epsilon_{yy}(x, t) M_y^2 + \epsilon_{zz}(x, t) M_z^2 \right] \\ &\quad + 2b_2 \left[ \epsilon_{xy}(x, t) M_x M_y + \epsilon_{yz}(x, t) M_y M_z + \epsilon_{xz}(x, t) M_x M_z \right]\end{aligned}\quad (2.7)$$

The coefficients  $b_1$  and  $b_2$  are the magneto-elastic coupling constants [33]. For a strain-induced excitation of magnetization dynamics, Dreher *et al.* applied a propagating surface acoustic wave (SAW) to their magnetic sample. Following their formalism, from equation 2.7 the effective dynamic driving field  $\mu_0 \mathbf{H}_{\text{me}}$  due to a propagating SAW can be determined for an in-plane (IP) field configuration via

$$\mu_0 \mathbf{H}_{\text{me}} = \begin{pmatrix} 2b_2 \epsilon_{xz} \cos \phi_0 \\ 2b_1 \epsilon_{xx} \sin \phi_0 \cos \phi_0 - 2b_2 \epsilon_{xy} \cos 2\phi_0 \end{pmatrix}, \quad (2.8)$$

where  $\phi_0$  is the magnetization's IP angle with respect to the propagation direction of the SAW. This IP angle plays an important role in the coupling of the SAW to the spin system. It is, therefore, an essential parameter for the experimental investigation of SAW-driven spin

dynamics. In addition, the coupling should be independent of field's amplitude sign and orientation, resulting in a predicted fourfold symmetry [33]. Expression 2.8 is valid for both common types of SAWs - Rayleigh and Love waves [82]. Both types of waves and their influence on magneto-elastic driving will be further discussed in chapter 6. A modification of the model utilized to describe the magneto-elastic coupling in a better agreement with experimental observations was introduced by Küß *et al.* by implementing dipolar coupling and DMI into the formalism [34].

### 2.1.3. Ferromagnetic Resonance

In analogy to electron spin resonance (ESR) the spin system itself fulfills a resonance condition in the presence of an external magnetic bias field combined with a spatially uniform high-frequency excitation field [74]. For the case of an unbounded ferromagnet in a single domain state (anisotropies are neglected), the magnetization aligns parallel to the applied field  $\mathbf{H}_0$ . In the following, the effective field and the magnetization can be separated into static and time-dependent parts:

$$\mathbf{H}_{\text{eff}}(t) = H_0 \mathbf{e}_z + \mathbf{h}_0 e^{i\omega t} \quad (2.9)$$

$$\mathbf{M}(t) = M_s \mathbf{e}_z + \mathbf{m}_0 e^{i\omega t} \quad (2.10)$$

The amplitudes  $\mathbf{h}_0$  and  $\mathbf{m}_0$  oscillate as a function of time with  $e^{i\omega t}$  in the  $xy$ -plane and are assumed to be much smaller compared to the static contributions  $H_0 \mathbf{e}_z$  and  $M_s \mathbf{e}_z$  pointing in the  $z$ -direction, respectively. In this approximation, higher-order terms of the time-varying field and magnetization as well as coupling terms of  $\mathbf{h}_0$  and  $\mathbf{m}_0$  can be neglected, which results in a solution of equation 2.2. By solving the linearized equation of motion one finds the relation between the introduced time-dependent components mediated by the Polder susceptibility tensor  $\mathcal{P}$  via  $\mathbf{m}_0 = \mathcal{P} \cdot \mathbf{h}_0$ . This tensor can be written as follows,

$$\mathcal{P} = \begin{pmatrix} \chi & i\kappa & 0 \\ -i\kappa & \chi & 0 \\ 0 & 0 & 0 \end{pmatrix} \quad (2.11)$$

$$\chi = \frac{\omega_M \omega_H}{\omega_H^2 - \omega^2} \quad (2.12)$$

$$\kappa = \frac{\omega_M \omega}{\omega_H^2 - \omega^2}, \quad (2.13)$$

with  $\omega_H = \gamma\mu_0 H_0$  and  $\omega_M = \gamma\mu_0 M_s$ . Equations 2.11-2.13 describe the case of uniform precession and offer the resonance condition in presence of a transversal magnetic field at  $\omega = \omega_H$  - known as the ferromagnetic resonance (FMR) [75]. In this simplified treatment, one finds a singularity at the position of the FMR  $\mu_0\omega_H$ , which depicts the neglect of energy dissipation. However, by introducing damping, as present in a real system (see section 2.1.5), the model describes the physics more realistically by only slightly affecting the position of the FMR.

#### 2.1.4. Kittel Equation

To derive the resonance position obtained in the last section as a function of excitation frequency, which corresponds to the most common type of FMR experiments, we assume the simple case of internal dipolar contributions to the effective field and a diagonal demagnetization tensor  $\mathcal{N}$ . The demagnetizing field reads as follows:

$$\mathbf{H}_d = -\mu_0 (\mathcal{N}_{xx} m_x \mathbf{e}_x + \mathcal{N}_{yy} m_y \mathbf{e}_y + \mathcal{N}_{zz} (m_z + M_s) \mathbf{e}_z) \quad (2.14)$$

By assuming small dynamic excitation amplitudes [74] and following the procedure depicted in section 2.1.3, the magnetization can be written as  $\mathbf{M} \approx M_s \mathbf{e}_z + \mathbf{m}(t)$  where  $\mathbf{m}(t) = m_0 e^{i\omega t}$  is an oscillating field component in the  $xy$ -plane, while the static components is aligned along  $z$ -direction. Thus equation 2.2 can be used and results in the general Kittel equation from which the resonance frequency  $\omega_0$  of the system can be derived [83]:

$$\omega_0 = \mu_0 \gamma \sqrt{(H_0 + (\mathcal{N}_{xx} - \mathcal{N}_{zz} M_s)) \cdot (H_0 + (\mathcal{N}_{yy} - \mathcal{N}_{zz} M_s))} \quad (2.15)$$

For the particular case of an IP magnetized thin film the Kittel equation changes to the more common form:

$$\omega_0 = \mu_0 \gamma \sqrt{H_0 \cdot (H_0 + M_s)} \quad (2.16)$$

Here, the Kittel equation is derived for a simplified case of internal fields and it increases in complexity when additional field components are introduced, e.g., due to lateral confinement of the ferromagnetic layer or magneto-crystalline anisotropy [74]. Nevertheless, the solution for this

simplified case points out the importance of this relation for ferromagnetic resonance experiments since it determines the effective magnetization and the gyromagnetic ratio. However, only the uniform mode's prediction in an extended thin film is included in this particular case using the macrospin model. Moreover, to describe confined systems and non-uniform excitations of the magnetic system adequately, the geometry of the sample has to be considered, and exchange interaction needs to be involved.

### 2.1.5. The Landau-Lifshitz-Gilbert Equation

For a realistic description of the magnetic system, which avoids the anomaly at resonance condition described in section 2.1.3, energy dissipation needs to be added to the equation of motion 2.2. In real magnetic systems, an perturbation of the magnetization away from its equilibrium position along the direction of an effective field will always result in a relaxation back to its initial state aligned along the effective field after a given time.

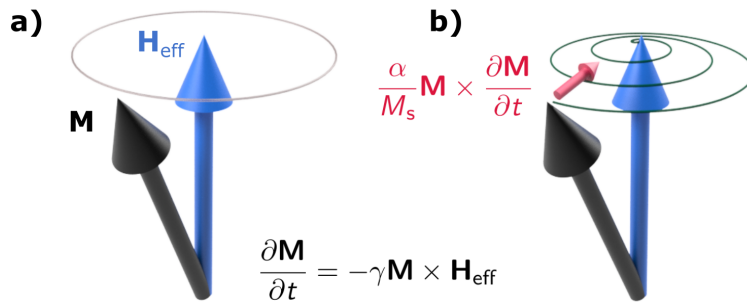


**Figure 2.1 | Schematic of magnetization dynamics.** Panel a) depicts the case of an undamped precessional motion of  $\mathbf{M}$  around the effective magnetic field  $\mathbf{H}_{\text{eff}}$ . In b) the more realistic case is drawn, where a torque-like damping term mediates the magnetization's relaxation back to its equilibrium position along  $\mathbf{H}_{\text{eff}}$ .

This process of energy dissipation is mediated by the spin-lattice-relaxations on the nanosecond time scale. Hence, the equation of motion (equation 2.2) has to be modified by adding a torque-like damping term.

$$\frac{\partial \mathbf{M}}{\partial t} = -\gamma \mathbf{M} \times \mathbf{H}_{\text{eff}} + \gamma \frac{\lambda}{M_s} \mathbf{M} \times (\mathbf{M} \times \mathbf{H}_{\text{eff}}) \quad (2.17)$$

$$= -\gamma \mathbf{M} \times \mathbf{H}_{\text{eff}} + \frac{\alpha}{M_s} \mathbf{M} \times \frac{\partial \mathbf{M}}{\partial t} \quad (2.18)$$

The initial version of the equation of motion (equation 2.17) contains a phenomenological

damping parameter  $\lambda$  added by Landau and Lifshitz [76], which describes the relaxation process adequately for very low damping values. If the damping becomes large, the correct description is still given by the LLG equation 2.18 with the appropriate expression for the damping introduced in 1955 by Gilbert [84].

### 2.1.6. Gilbert Damping

The Gilbert damping parameter  $\alpha$  defined in equation 2.18 is one of the key parameters in magnetic material characterization. In addition, it plays an important role in modern research for suitable magnonic materials since the Gilbert damping mainly defines the spectral quality factor of magnonic oscillators as well as the magnon's propagation length. One of the lowest damping values of  $\alpha \approx 1 \times 10^{-5}$  was reported for thin-film YIG [28, 55], while metallic  $\text{Ni}_{80}\text{Fe}_{20}$  has a value of  $\alpha = 8 \times 10^{-3}$  (cf. appendix A.1.1) [57, 80]. The effective Gilbert damping  $\alpha_{\text{eff}} = \alpha_{\text{Gilbert}} + \alpha_{\text{ext}}$  consists of different contributions with either intrinsic or extrinsic origin. Eddy currents generated in a metallic layer due to the precession of the magnetization may result in the dissipation of energy and thus increase the intrinsic damping. For metallic thin films, this contribution is proportional to the conductivity, but this effect is comparably small to the total Gilbert Damping [81]. For YIG this contribution vanishes since YIG is an insulator. Another intrinsic mechanism can be described via magnon-phonon-scattering, which mostly occurs in magnetostrictive materials such as nickel (Ni), for which it is much more pronounced compared to  $\text{Ni}_{80}\text{Fe}_{20}$  and YIG [81]. A strong contribution to the Gilbert damping in thin ferro- and ferrimagnetic layers originates in the relaxation mechanism due to electron-magnon scattering. Here, the itinerant electrons [85] interact with the localized electrons, which cause the magnetization in most ferromagnetic materials, via an exchange field. Besides the change of electron energy levels also the orbital momentum is influenced due to the SOC. Thus, the SOC is the main effect causing intrinsic Gilbert damping in the investigated materials.

Extrinsic contributions to effective damping can be distinguished into two classes of effects. First, sample inhomogeneities might lead to an increased Gilbert damping since most inductive measurements integrate the obtained FMR signal over the entire sample. This contribution can be seen as a constant zero-frequency offset, which adds to the intrinsic linewidth of the resonance independent of the excitation frequency. Therefore, this offset in linewidth is typically not contributing in most experiments where frequency-dependent changes of the linewidth are investigated to derive the Gilbert damping parameter. However, this effect can be minimized by reducing the sample's volume, which contributes to the obtained FMR signal by either using micro-patterned coils to probe the dynamics locally or by employing optical detection techniques where the laser's spot size defines the probed sample volume. In addition, magnon-magnon scattering effects might result in an increased damping [86, 87]. Here, most prominent is the two-magnon scattering in cases of degenerated magnon states in the spin-wave dispersion (see section 2.2). This effect mainly occurs for either flat branches in the dispersion or branches that include a sign change in the group velocity. This sign change is observable for

backward volume spin waves (BVSWs) due to the curvature in their magnon band structure. However, such a valley of degenerated states in the spin-wave dispersion might also be a result of geometrically tailored magnetic structures [51]. Moreover, higher-order magnon-magnon scattering processes broaden the resonance line and thus increase the damping when large radio frequency (rf)-driving amplitudes are used [88]. These effects are further discussed in section 2.4.2.

## 2.2. Spin Waves in thin magnetic Films

In the following, we will also consider a spatially non-uniform precessional motion of the spin system as a consequence of dipole-dipole and exchange coupling. By taking these additional field components into account, an accurate description of experimentally observed phenomena at different resonance conditions than FMR is given.

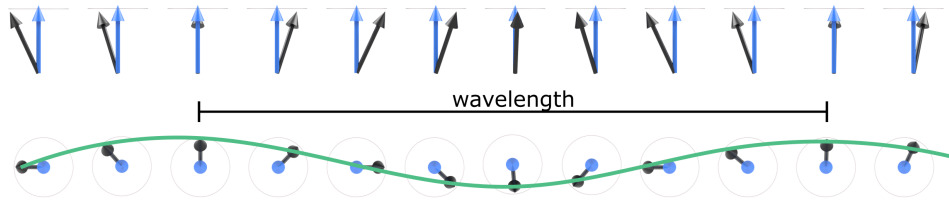


**Figure 2.2 | Illustration of a non-uniform spin wave.** The blue arrows depict the direction of the external field, while the black arrow shows the magnetization. Neighbouring spins have a slight phase shift leading to a non-uniform precessional mode of the spin system. The amplitude of the spin-wave is depicted in green indicating its wavelength.

These non-uniform excitations, such as shown in Fig. 2.2, which are of strong interest in realistic thin-film systems, are referred to as dipole-exchange spin waves. They can be approximated with either pure dipole spin waves for large wavelengths or exchange spin waves for large wave vectors. As one of the first, Herring and Kittel [83] derived the dispersion for exchange spin waves with a non-uniform magnetization in the magneto-static approximation. Therefore, they solved Maxwell's equations to obtain the dipolar field generated by the dynamic magnetization. Within this approximation, the dipolar field of a propagating spin-wave mode with wave vector  $\mathbf{k}$  and an amplitude  $\mathbf{m}_k$  reads as follows:  $\mathbf{h}_k \approx \frac{4\pi}{k^2} \mathbf{k}(\mathbf{k} \cdot \mathbf{m}_k)$  [89]. With this dipolar field component and additional exchange fields  $\propto A_{\text{ex}} \nabla^2 \mathbf{M}$ , the dispersion for propagating spin waves has the form

$$\omega_k = \sqrt{(\omega_H + A_{\text{ex}} \omega_M k^2) \cdot (\omega_H + A_{\text{ex}} \omega_M k^2 + \omega_M \sin^2 \Theta_k)}, \quad (2.19)$$

where  $\omega_H = \gamma\mu_0 H_0$ ,  $\omega_M = \gamma\mu_0 M_s$ , while  $\Theta_k$  defines the polar angle between  $\mathbf{M}$  and the film normal and  $A_{\text{ex}}$  denotes the exchange stiffness constant [90]. For IP geometries ( $\Theta_k = 90^\circ$ ), as investigated in this work, equation 2.19 simplifies for uniform magnetization ( $|\mathbf{k}| = 0$ ) to the Kittel equation 2.16. However, this approximation of the dipolar fields results in a frequency shift of the uniform mode for different out-of-plane (OOP) field orientations, which is in contrast to experimental findings for very small wave vectors [57]. Nevertheless, for  $|\mathbf{k}| \gg 0$  the dispersion develops proportional to  $k^2$  for all angular orientations in agreement with experiments. These type of propagating spin waves is typically referred to as exchange spin waves.

### 2.2.1. Dipole-exchange Spin Waves

The problem of angular dependent changes in FMR condition (cf. equation 2.19) was investigated by Damon and Eschbach [91]. They predicted the spin-wave dispersion in the dipole-exchange regime correctly by solving Maxwell's equations within the magneto-static approximation with the aid of a high-frequency susceptibility. The novel finding from this approach was the existence of magneto-static surface wave (MSSW) also known as Damon Eschbach (DE) spin-wave modes. A different approach utilized by Kalinikos and Slavin [92] extended the known dispersion to the regime of small wave vectors, enabling a detailed prediction of dipolar and exchange spin-waves modes. Employing perturbation theory, they presented an analytical expression, which is still used as the most common expression to derive dipole-exchange spin-wave modes in modern physics. The dispersion relation reads as follows:

$$\omega_n = \sqrt{(\omega_H + A_{\text{ex}}\omega_M k_n^2) \cdot (\omega_H + A_{\text{ex}}\omega_M k_n^2 + \omega_M F_{nn})}, \quad (2.20)$$

with the expression  $F_{nn}$  for IP magnetized films ( $\Theta_k = 90^\circ$ ):

$$F_{nn} = 1 - P_{nn} \cos^2 \phi_k + \omega_M \frac{P_{nn}(1 - P_{nn}) \sin^2 \phi_k}{\omega_H + A_{\text{ex}}\omega_M k_n^2} \quad (2.21)$$

In the thin film approximation ( $k_n \cdot L \ll 1$ ), the total wavenumber  $k_n$  can be accessed via  $\sqrt{k_{\parallel}^2 + (n\pi/L)^2}$  where  $L$  is the layer thickness and  $n$  is the mode number of the perpendicular standing spin wave (PSSW) along the film thickness. The IP angle  $\phi_k$  changes the nature of the spin-wave mode from surface mode ( $\phi_k = 90^\circ$ ) to volume type modes ( $\phi_k = 0^\circ$ ), as shown in Fig. 2.3. For  $n \neq 0$ , expression 2.20 allows to describe PSSW modes, which appear

as quantized modes in thin magnetic layers and show an exchange dominated behavior [62]. The dipolar kernel  $P_{nn}$  of the  $n^{\text{th}}$  mode can be expressed as shown in reference [93] for the relatively simple cases of totally pinned or unpinned surface spins, as well as for more complex intermediate states [92]. This dipolar kernel plays an essential role in the observation of mode repulsion in the vicinity of an avoided mode crossing as discussed in section 4.2.4. This rather special phenomenon will be further discussed in section 2.2.2.

### 2.2.2. Dipolar Spin-Wave Approximation

For the proper description of some experimental findings, it is useful to neglect the exchange interaction ( $A_{\text{ex}} = 0$ ) and only consider the dipolar coupling of the magnetic moments to understand the dipolar properties of spin-wave modes mostly observed in this thesis. Optical detection techniques are diffraction-limited, and thus the largest observable wave vector is given by the spatial resolution. Therefore, these techniques are primarily sensitive to spin waves of dipolar nature. By neglecting the exchange interaction, the dispersion relation simplifies for two prominent cases where  $\mathbf{M}$  is aligned in the film plane.

#### Magneto-static Surface Spin-Wave Modes

The MSSWs or DE modes [91] propagate along the surface of the film for  $\mathbf{k} \perp \mathbf{M}$  and can be either located at the bottom or at the top interface of the ferromagnetic layer depending on propagation direction and orientation of the external magnetic field. In the DE geometry, the spin-wave dispersion is positive; hence the group velocity and phase velocity of the spin waves are both positive. The approximate dispersion relation is given by

$$\omega^2 = \omega (\omega_H + \omega_M) + \frac{\omega_M^2}{4} [1 - e^{-2k_{\parallel}L}] , \quad (2.22)$$

where  $k_{\parallel}$  is the IP wavenumber. The qualitative description of DE waves in the dipolar regime is presented in Fig. 2.3a) for a 20 nm thick  $\text{Ni}_{80}\text{Fe}_{20}$  layer as a blue dashed line, while the solid blue line shows the DE mode for dipole-exchange spin waves derived with equation 2.20.

#### Backward Volume Spin-Wave Modes

The second well studied case describes the BVSW modes, which propagate in the direction of  $\mathbf{M}$  ( $\mathbf{k} \parallel \mathbf{M}$ ). The maximum intensity is located between the two interfaces and thus the wave is referred to as a volume wave. In contrast to the DE modes, waves in the backward volume (BV) geometry have a negative dispersion in the dipolar regime. Here, group and phase velocity

have different signs and the dipolar approximation of the dispersion is derived by

$$\omega^2 = \omega_H \left[ \omega_H + \omega_M \left( \frac{1 - e^{-k_{\parallel} D}}{k_{\parallel} D} \right) \right]. \quad (2.23)$$

The negative group velocity in this particular geometry shows the anisotropic behavior of dipolar spin waves while this anisotropy vanishes in the exchange regime. Due to their band curvature, BV modes host frequency degenerated states in the magnonic band structure. Thus, these modes are most suitable for two-magnon scattering induced linewidth broadening [81] (cf. section 2.1.6). The BV branch is shown in Fig. 2.3a) as a dashed green line, while the dipole-exchange case is depicted as a solid line (green). Equally to the DE case, the dipole-exchange branch starts to follow its  $\propto k^2$  behavior for large wavenumbers as depicted in Fig. 2.3b).

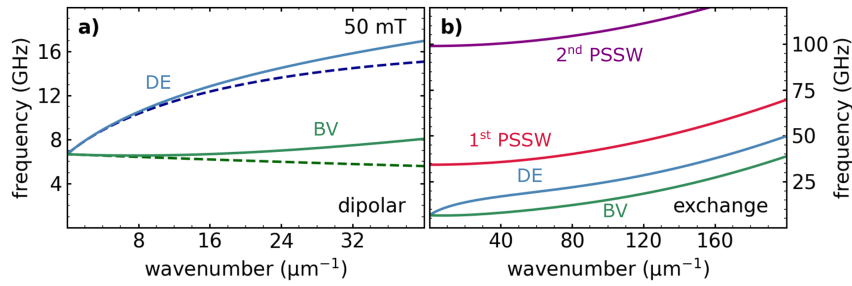


**Figure 2.3 | Calculated spin-wave dispersion for 20 nm  $\text{Ni}_{80}\text{Fe}_{20}$ .** a) The spin-wave dispersion is calculated for the dipole-dominated regime. The dashed lines depict the purely dipolar contribution from equation 2.22 and 2.23 while the solid lines derived from 2.20 show a slight deviation for larger wavenumbers including the exchange interaction. b) The DE and BV modes follow a  $k^2$  behavior in the exchange dominated regime. PSSW modes propagate at higher frequencies.

The solid lines in Fig. 2.3 depict the dipole-exchange branches for DE and BV geometry in blue and green, respectively. Depending on the film thickness and material parameters, additional PSSW modes emerge at higher frequencies for different mode numbers  $n$ , as shown in b). The PSSW modes are exchange dominated, as visible by their  $k^2$  behavior. Another well-studied example of dipole-exchange spin waves is the so-called forward volume spin wave (FVSW) mode appearing in OOP magnetized film samples [92]. However, since only IP magnetized samples are investigated in this work, the FVSW will not be further discussed.

### 2.3. Spin-Wave Mode Repulsion

After introducing the basic concept of magnetization dynamics, the following sections will cover more advanced features which need to be considered to understand the presented experimental results. A well-known phenomenon of two coupled oscillators is the degeneracy of states which might result in the formation of an avoided crossing in the dispersion depending on the coupling strength [44]. Such an energy degeneracy also exists for spin-wave mode branches in the dispersion, and depending on the type of the interacting spin waves, the coupling of these modes becomes strong. The formalism shown in the last section can be seen as a simplified way to calculate the dispersion since the coupling of different modes is not implemented. However, the approach introduced by Kalinikos and Slavin [92, 93] also addresses this problem by using perturbation theory to derive a simple approximate expression, which describes the interaction of two spin-wave modes correctly. In the following, we demonstrate how this formalism is applied. For further details, please follow the references [92, 93]. At first, we define the exchange part of the interacting modes as

$$\Omega_n = \omega_H + \omega_M A_{\text{ex}} (\kappa_n^2 + k_{\parallel}^2), \quad (2.24)$$

where  $\Omega_n$  describes the  $n^{\text{th}}$  mode of the spectrum. With this, the dispersion relation (equation 2.20) may be rewritten as

$$\omega_n^2 = (\Omega_n + \omega_M - \omega_M P_{nn}) \cdot (\Omega_n + \omega_M P_{nn} \sin^2 \phi_k), \quad (2.25)$$

which is valid for the case of IP magnetized films [93]. Note that the initial expression from reference [92] for spin-wave mode repulsion addresses crossings in perpendicular magnetized films (OOP); however, by utilizing Kalinikos' approach from 1981 the formalism becomes applicable to tangentially magnetized films (IP). This is an important fact since the IP geometry is mainly used in publications where mode crossings appear [61, 64, 94, 95]. In this geometry, the only possible crossing within a single extended ferromagnetic layer might appear for DE modes and PSSW modes in the dipolar dominated regime. In contrast, OOP magnetized samples host a variety of FVSWs which have a large number of crossing points with PSSWs [92]. In both cases, the mode crossing in the dispersion results in a frequency degeneracy, similar to effects obtained for magnons and phonons in cavity magnonics [36]. In the following, the hybridization of two interacting spin-wave modes with mode number  $n$  and  $m$  is taken into account by a first-order approximation of perturbation theory [92]. This results in the following secular equation describing the behavior of the hybridized modes in the near the crossing:

$$(\omega_n^2 - \omega_{nm}^2)(\omega_m^2 - \omega_{nm}^2) = \omega_M^2 \Omega_n \Omega_m P_{nm}^2 \quad (2.26)$$

Here, the strength of the mode repulsion is mediated by the mixed dipolar kernel  $P_{nm}$  of the two interacting modes. Equation 2.26 yields two solutions of  $\omega_{nm}$  for positive frequencies depicting the two hybridized modes near the crossing. These hybridized modes around the avoided crossing (dipole gap) are referred to as  $\omega_{nm}$  and  $\omega_{mn}$ . A typical avoided crossing of DE and 1<sup>st</sup>-order PSSW mode is shown in Fig. 2.4, where the red and green lines depict hybridized modes.

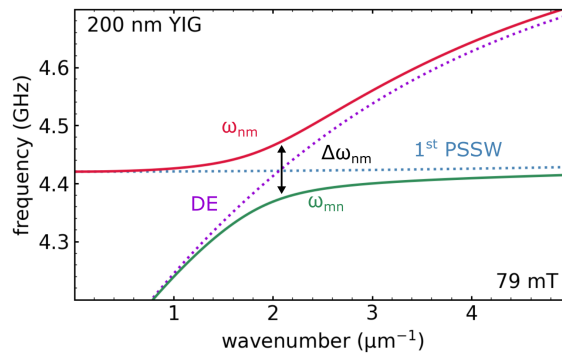


**Figure 2.4 | Calculated mode repulsion for 200 nm YIG.** The dotted lines depict the DE (violet) and PSSW (blue) dispersion branches obtained by equation 2.25. The solid lines show the two hybridized mode branches obtained by equation 2.26. The applied pinning parameters for this calculation are  $d_1 = 1 \times 10^6 \text{ m}^{-1}$  and  $d_2 = 6 \times 10^6 \text{ m}^{-1}$ .

By assuming  $n = 0$  for the DE mode, this results in an OOP wavenumber of zero. However, the spatial profile across the film thickness of the DE mode has to be considered to obtain an avoided crossing of DE and PSSW mode. Otherwise, no modal overlap between the two modes can be obtained, and thus no dipole gap will appear. For this purpose,  $\kappa_{\text{DE}}$  is modeled by the following relation

$$[\kappa_{\text{DE}}^2 - d_1 d_2] \tan(\kappa_{\text{DE}} L) = \kappa_{\text{DE}} (d_1 + d_2), \quad (2.27)$$

where  $d_{1,2}$  are the pinning parameters of the two interfaces and  $L$  is the film thickness. The wavenumber along the film thickness for the 1<sup>st</sup>-order PSSW mode is given by  $\kappa_{\text{PSSW}} = \pi/L$ . As a next step, the expressions for the dipolar kernels  $P_{nn}$ ,  $P_{mm}$  and the mixing term  $P_{nm}$  must be used for the general case as shown in reference [92] and not for totally pinned or totally unpinned spins. In both of these extreme cases, the solution of 2.26 will not represent the

experimentally obtained results. The coupling results in the formation of an upper and a lower branch in the vicinity of the magnonic bandgap. The magnitude of the frequency splitting is determined by the coupled dipolar contribution  $P_{nm}$  including the in-plane and normal wave vector components of both modes as well as the pinning parameters on the interfaces [92]. The strength of the mode repulsion  $\Delta\omega_{nm}$  can be expressed by

$$\Delta\omega_{nm} = \frac{\omega_M \sqrt{\Omega_n \Omega_m}}{\omega_0} P_{nm}, \quad (2.28)$$

where  $\omega_0$  is the frequency of the crossing [92]. From this expression, it is clearly shown that the repulsion strongly scales with the mixed dipolar kernel  $P_{nm}$ , and therefore this term has to be considered carefully. Equations 2.26 and 2.28 will be utilized and discussed in detail in chapter 4.2. The utilized equation 2.26 can be further extended for the case of rather thick films with transversal oriented interacting spin-wave modes [96] or for non-vanishing anisotropy terms [97].

## 2.4. Non-linear Magnetization Dynamics

As discussed in the last section, spin-wave phenomena occur in various orientations and geometries, which result in an inherent non-linearity due to the curvature of the magnonic band structure. So far, only small driving amplitudes are considered where the dynamic rf-driving field is much smaller compared to the externally applied bias field ( $\mathbf{h}_{rf} \ll \mathbf{H}_0$ ). As in every field of physics, the response of a system, here given by the precessional motion of the spin system, becomes non-linear as the amplitude of an inertia passes a well-defined threshold value. In the non-linear response regime, parametric excitations due to oscillatory variations might result in the generation of spin waves with different frequencies [79]. A common type of these parametric excitations is found in the so-called parallel-pumping geometry where the external bias field is applied parallel with respect to the rf-driving field [51, 79, 98–100]. However, the non-linear effects discussed in this work were obtained in perpendicular pumping geometry, and thus parametric excitations due to parallel pumping are only briefly discussed.

### 2.4.1. Suhl Instabilities

Typically, in the linear driving regime, the equation of motion is solved to derive the condition of linear ferromagnetic resonance. However, in the non-linear regime, a more common approach is based on a Hamiltonian formalism - known as S-Theory - introduced by L'vov [101], Zakharov [102], Krivosik and Patton [103] to describe the so-called 1<sup>st</sup> and 2<sup>nd</sup>-order Suhl

instabilities and higher-order processes far above the non-linear threshold [104]. Experimentally, in conventional inductive FMR experiments, the 1<sup>st</sup>-order Suhl instability, which can be described as a three-magnon scattering process, results in an emerging second resonance peak on the lower field side of the FMR condition [75, 105]. This phenomenon, also referred to as subsidiary absorption, results in the decay of a uniformly pumped magnon into two magnons with opposing wave vectors considering energy conservation. The parallel-pumping geometry depicts this scattering process in the case when the obtained magnons are visible at half of the driving frequency  $f_{ff}$ . Whenever the 1<sup>st</sup>-order Suhl process is forbidden, e.g., when the spin-wave manifold does not provide accessible states at low frequencies [106], the 2<sup>nd</sup>-order Suhl instability is the leading non-linear process. In this four-magnon scattering process, the uniform mode saturates, and two magnons might spontaneously scatter into two frequency degenerated ones with opposing wave vectors to achieve momentum conservation [79]. In addition, the phases of the pair of generated magnons is correlated due to a uniform pumping field [101, 102]. A more general description of magnon scattering processes is given by Fig. 2.5. Here, the three most common scattering processes are depicted. In panel a) the scattering of a magnon at a sample inhomogeneity might result in a different wave vector while the frequency stays constant. Panel b) and c) show energy and momentum conservation for three and four magnon scattering processes [107, 108].

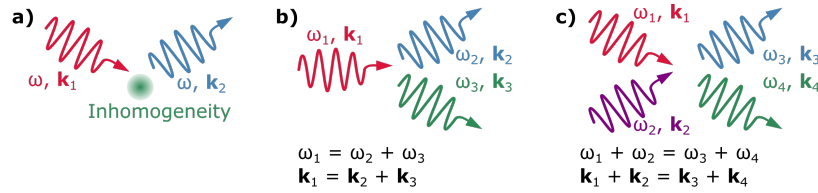


**Figure 2.5 | Schematic of different magnon-magnon scattering processes.** a) Two-magnon scattering at sample inhomogeneities is depicted. b) and c) show the generalized three and four-magnon scattering processes and their energy and momentum conservation, respectively.

Typically, a threshold amplitude can be derived from S-Theory for the 2<sup>nd</sup>-order Suhl instability, which allows to predict the onset of non-linear dynamics:

$$|c_0|_{\text{crit.}} = \min_{\omega_k = \omega_0} \left( \sqrt{\frac{\eta_k}{|\tilde{W}_{00,k(-k)}|}} \right) \quad (2.29)$$

Here,  $|c_0|_{\text{crit.}}$  is the critical mode amplitude, which scales with the  $h_{\text{rf}}$ ,  $|\tilde{W}_{00,k(-k)}|$  is a complex coefficient depicting the decay of two uniform magnons into two magnons with opposing wave vectors  $k$  and  $-k$ , while  $\eta_k$  is the relaxation rate of the corresponding mode [103].

### 2.4.2. Non-linear Spin-Wave Generation at low magnetic bias Fields

So far, all introduced non-linear phenomena are adequately described by S-Theory [101, 103] assuming energy conservation for these processes, which is given for systems invariant under translations in time. Within this formalism, also higher-order contributions might result in multi-magnon scattering processes leading to odd half-integer harmonics, but are predicted to only appear for very large driving power levels [104]. However, in the case of periodic driving, this time-translation symmetry is broken, resulting in a situation where energy conservation is not mandatory [80]. Such an additional periodic driving can be achieved in the low bias field regime, where the stiffness of the magnetization is reduced. Here, the external driving field is on the same order of magnitude as the bias field ( $\mathbf{h}(t) \approx \mathbf{H}_0$ ). Therefore, Bauer *et al.* [54] introduced a model capable of describing amplitude-phase oscillations occurring within the magnetization's precessional period in the low bias field regime. In this regime and above a certain rf-threshold field, they reported the existence of non-linear magnons at odd half-integer multiples of the driving frequency. Moreover, the calculated threshold of these non-linear spin waves (NLSWs) is significantly lower compared to the Suhl instabilities in this regime (obtained with equation 2.29), which means that these novel types of NLSWs are predicted to dominate. Additionally, they claim that the observed amplitude-phase oscillations emerge coherently [80]. In the following, we will briefly describe the basics of the model and show an exemplary calculation. For further details, please refer to references [54, 80]. In their approach, Bauer *et al.* solve the equation of motion (eq. 2.18) in reciprocal space to obtain the spin-wave lifetime as well as the non-linear dispersion for each particular point in k-space within the strong modulation regime. Therefore, the LLG equation is transformed into the Mathieu equation by substituting the magnetization component with  $f(x)$  where  $x$  is a dimensionless parameter  $x = \omega_p t/2$ , as described in reference [54]. This results in

$$f''(x) + (a - 2q \cos(2x))f(x) = 0, \quad (2.30)$$

where  $a = (\omega_k/\omega_{\text{mod}})^2$  includes the spin-wave frequency  $\omega_k$  as well as the modulation frequency  $\omega_{\text{mod}}$ , while  $q$  depicts the modulation strength. The modulation emerges from the inherent change of the spin-wave's frequency during the precessional motion due to the large driving field amplitude. The Mathieu equation can be solved by the ansatz

$$F(a, q, x) = e^{i\nu(a,q)x} P(a, q, x), \quad (2.31)$$

where  $\nu(a, q)$  is the complex Mathieu exponent and  $P$  denotes a periodic function. The real part of  $\nu(a, q)$  results in the (non-linear) spin-wave dispersion as a function of  $k_x$  and  $k_y$ . By integrating the equation of motion with a Runge-Kutta integrator [80], the imaginary part yields the spin-wave lifetime and allows to determine threshold values above which NLSWs become critical by increasing the rf-driving field for fixed frequency and bias field. An exemplary calculation for a 20 nm thick  $\text{Ni}_{80}\text{Fe}_{20}$  layer is depicted in Fig. 2.6. Here, an rf-field amplitude

of 0.27 mT and an external bias field of 6.6 mT are used. For the applied frequency of 2.3 GHz this setting gives rise to  $3/2 f_{\text{rf}}$  NLSW at threshold condition since the decay rate approaches zero.

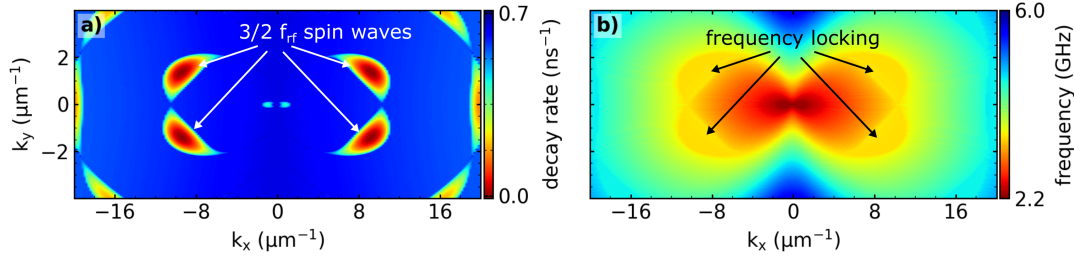


**Figure 2.6 | Spin-wave decay rate and non-linear dispersion.** a) Calculated spin-wave decay rate for 20 nm  $\text{Ni}_{80}\text{Fe}_{20}$  in the strong modulation regime. The color code indicates four magnon peaks in  $k$ -space becoming critical under rf-excitation with a field amplitude of 0.27 mT<sub>p</sub>. Panel b) shows the corresponding non-linear dispersion, where frequency locking at  $k$ -points of critical NLSWs is observed.

The  $k$ -space image in Fig. 2.6a) depicts the decay rate as function of  $k_{x,y}$ . Here, four dominant peaks reach the critical value. From the obtained non-linear dispersion in b), one can link these peaks to a frequency of  $3/2 f_{\text{rf}}$ . By obtaining the non-linear spin-wave dispersion, a frequency shift towards larger frequencies compared to the linear dispersion can be found. Moreover, the  $k$ -space areas hosting the NLSWs show a pronounced frequency-locking effect [54]. Here, the dispersion does not develop linearly, but different wave vectors condense at the same frequency, which is an odd half-integer of the driving frequency [80]. Additional features appear at the outer edges of a) which belong to higher-order processes such as high-harmonic generation (HHG). From their calculations, Bauer *et al.* predicted the threshold of odd half-integer NLSWs to be lower compared to Suhl instabilities for  $\text{Ni}_{80}\text{Fe}_{20}$  in the frequency range below 5 GHz, which means that NLSWs generation tend to be the dominant process in this regime. This model is utilized in chapter 7 by performing simulations as a function of frequency, rf-amplitude and external bias field to compare these results to experimental findings.

## 2.5. The magneto-optical Kerr Effect

A fundamental approach of detecting static and dynamics magnetization is given by its coupling to light waves via the SOC. The first evidence for a connection of the magnetization of a solid and an interacting light wave was given by Faraday in 1845 as he proposed the change of the polarization state of a light wave passing through a glass plate with an externally applied magnetic field [74]. The so-called Faraday effect allows to directly link the induced magnetization to a rotation of the polarization state. However, it is restricted to either very thin or transparent samples for the given wavelength of the passing light. For ferromagnetic

samples, which are mostly not transparent for visible light, Kerr discovered a change in the polarization state for a reflected light wave on a polished iron surface in 1877 [74]. In addition to the polarization state's rotation, a shift from a linearly to an elliptically polarized state can also be observed. In general, the magneto-optical Kerr effect (MOKE) can be described in the presence of SOC via the magneto-optic permittivity tensor  $\mathcal{E}_{ij}$ . With an externally applied magnetic field along z-direction, the tensor changes from a diagonal one to a Skew-symmetric matrix with off-diagonal elements  $\mathcal{E}_{xy} \neq 0$ :

$$\mathcal{E} = \varepsilon_r \varepsilon_0 \begin{pmatrix} 1 & iQ & 0 \\ -iQ & 1 & 0 \\ 0 & 0 & 1 \end{pmatrix} \quad (2.32)$$

Here,  $\varepsilon_r$  is the relative permittivity of the material and  $\varepsilon_0$  corresponds to the vacuum permittivity. The refractive index  $n^2 = \varepsilon_r$  and the magneto-optical constant  $Q$  are both complex quantities, and thus the magneto-optical properties of the material are complex as well [109]. On the macroscopic scale, the Kerr rotation can be understood as a consequence of the Lorentz force. Linearly polarized light can be separated into the superposition of a left hand and a right hand circularly polarized state. Both of these states act on a bound electron and lead to either clockwise or counter-clockwise electron's movement. In the absence of a magnetic field, both movements are equal in magnitude. However, for magnetized samples, these two directions are not equal anymore since the acting Lorentz force enhances one orientation while it attenuates the other one [110]. Thus, the Lorentz-force can be seen as the source of the permittivity tensor's off-diagonal elements since it mixes the  $x$  and  $y$  component of the electron's movement [74]. Here, the SOC is crucial to distinguish between clockwise and counter-clockwise movement and results in  $\mathcal{E}_{xy} \neq 0$ . Consequently, the two polarization states experience a different refractive index, which results in slightly different phase velocities that correspond to a phase shift. This effect is also referred to as circular birefringence [74]. The experienced phase shift results in a polarization state's rotation as the reflected light is recomposed into a linear state. Moreover, the absorption coefficients for both circularly polarized waves might also be influenced by the magnetization, which leads to a change in amplitude and transforms the linear polarization state into an elliptical one. In the experiments, the complex Kerr angle  $\Phi_k = \theta_k + i\eta_k$  consists of both contributions and is typically decomposed by using additional quarter-wave plates [110, 111]. Nowadays, the basis for most optical detection techniques of magnetization dynamics is the MOKE. Here, one has to distinguish between three distinct geometries: The polar magneto-optical Kerr effect (p-MOKE), longitudinal magneto-optical Kerr effect (l-MOKE) and transversal magneto-optical Kerr effect (t-MOKE), as depicted in Fig. 2.7.

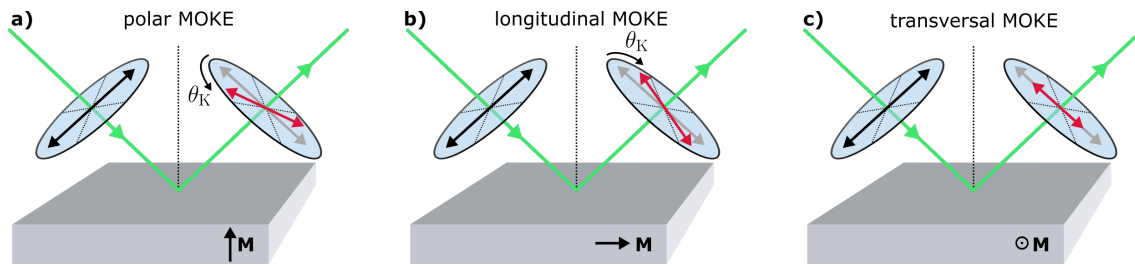


**Figure 2.7 | Schematic of the magneto-optical Kerr effect.** The three different geometries of the MOKE are shown in a)-c) for different IP and OOP field orientations resulting in Kerr rotation and ellipticity.

The typical configuration of data storage is the p-MOKE, where the magnetization points OOP. While the film needs to be magnetized OOP for static MOKE loops in p-MOKE geometry, this is not mandatory for dynamic measurements aiming for the precessional motion of the magnetization. In this thesis, the external bias field and thus the magnetization is oriented in the film plane. Nevertheless, the precessional motion generates a tiny OOP component, which can be detected by means of p-MOKE. Note that the amount of Kerr rotation and ellipticity strongly depends on the utilized wave length [112, 113]. For the investigated materials ( $\text{Ni}_{80}\text{Fe}_{20}$  and YIG), a laser with a wavelength of approximately 520 nm is a good compromise between amplitude of the Kerr rotation and the microscope's spatial resolution.



---

# Super-Nyquist Sampling MOKE

---

Different technical approaches are typically used in experiments to observe the introduced magnetization dynamics in the linear and non-linear regime. The most common way of investigating FMR phenomena is the absorption of inductively provided rf-power while sweeping the external magnetic field. This technique is applicable for most sample geometries and dimensions by proper scaling of the rf-antennas and offers, in most cases, good estimates for the Gilbert damping and other magnetic properties. However, local properties are not addressed since the inductive technique averages the obtained properties across the entire layer or structure. Purely local measurements of magnetization dynamics become possible by exploiting magneto-optical effects. Different fundamental processes, such as the magnetic circular dichroism, the magneto-optical Faraday, or the magneto-optical Kerr effect (MOKE) convert local properties of the sample (e.g., the magnetization) into a measurable change in the properties of the interacting light used as probe [74]. Static magnetic properties can be easily obtained to characterize a magnetic material [111]. In addition, these effects are also used to image the dynamics in the time or frequency domain by using x-ray magnetic circular dichroism (XMCD) [114], Brillouin light scattering (BLS) [61, 63] or time-resolved magneto-optical Kerr microscopy (TR-MOKE) [57, 58]. In the first experimental part of this thesis, we introduce a novel type of frequency-resolved Kerr microscope for the local detection of magnetization dynamics in frequency space. Therefore, we first describe the functional principle of the state-of-the-art techniques and reveal their limitation. In the next step, we depict the electrical concept on which our technique is based. In the end, proof-of-principle measurements of a ferromagnetic  $\text{Ni}_{80}\text{Fe}_{20}$  element were demonstrated.

## 3.1. Magneto-optical Kerr Microscopy

In recent years, the magneto-optical Kerr effect has become an essential tool for investigations of magnetic material systems. In static experimental geometries, the Kerr effect can be utilized to record magnetic hysteresis loops to evaluate intrinsic properties of the material system, such as the saturation magnetization, anisotropies, and coercive fields. While for these measurements, mainly a focused laser spot is utilized to detect changes in the magnetic properties via MOKE, a different approach exploits the introduced effects in wide-field microscopy to image the domain structure of a ferromagnetic sample. With the accessibility of ultra-short pulsed laser

sources, time-resolved investigations of magnetic properties accelerated the development of novel storage technologies, including magnetic materials [58]. With pulse lengths on the order of femtoseconds, pump-probe experiments have revealed novel dynamics, e.g., ultrafast demagnetization [115–117]. In wide-field Kerr microscopy, pump-probe experiments allow for an investigation of all-optical switching phenomena as a function of time [118].

### Time-resolved MOKE

One of the most important properties for developing novel magnonic and spintronic applications is the Gilbert damping parameter  $\alpha$  of the magnetic system. Typically, the damping parameter is investigated by inductively carried out FMR experiments. Such experiments reveal the resonance linewidth and allow to obtain the damping by frequency-dependent analysis of the linewidth. However, inductive detection suffers from the lack of spatial resolution and does not distinguish between different materials within one layer stack. TR-MOKE experiments have proven to be a reliable alternative to overcome these limitations [58]. Here, a short pump pulse is utilized for the excitation of the magnetic system, and subsequently, the magnetization is detected with a much weaker probe pulse. Thus, the magnetization's relaxation can be recorded stroboscopically by varying the time delay between pump and probe pulses. Careful analysis of Kerr rotation and ellipticity allows for material sensitive detections [119, 120]. However, these experiments require high-intensity pump pulses typically provided by amplified laser systems operated in the kHz regime. These repetition rates are required to ensure that the magnetic system is relaxed to its initial state and the implemented heat due to the strong pulse is completely dissipated. A slightly different approach of time-resolved investigation is the continuous or pulsed excitation of the magnetic system by exploiting the Oersted field of a coplanar waveguide (CPW) (as in conventional FMR experiments) and detecting the resonance lineshape locally by means of MOKE. A significant advantage of this technique is the absence of the strong pump pulse, which provides the possibility of using high numerical aperture objective lenses without the thermal destruction of the magnetic device. Thus, the spatial resolution is diffraction-limited, and spatially-resolved images of micron-sized magnetic devices are feasible. Furthermore, less intense laser-pulse sources with repetition rates of 80 MHz can be used to enhance the signal-to-noise ratio (SNR) significantly. Typically, Lock-In detection is achieved by either modulating the external bias field or the microwave's amplitude. In this technique, either the external bias field is fixed while the frequency is swept to map the FMR or vice versa. Additionally, a phase shifter is required to switch the obtained signal component from the real to the imaginary part of the dynamic susceptibility.

### Limitations of heterodyne TR-MOKE

The introduced variant of TR-MOKE, which is, in fact, a heterodyne MOKE technique, has two important limitations. First, the real and imaginary parts of the dynamic susceptibility are not detected simultaneously; therefore, at least two measurements with careful phase analysis

are necessary to restore the full amplitude and phase information. Second, the excitation frequency in this geometry is limited to multiples of the laser's repetition rate. This restriction is imposed by the heterodyne detection scheme as explained in following: The ultrashort laser pulses represent a comb in frequency space, as depicted in Fig. 3.1a). These comb lines mix with the applied rf-excitation frequency, and by this process, a DC component is generated whenever  $f_{\text{rf}} = n \cdot f_{\text{rep}}$ , where  $n$  is an integer harmonic number. The imprinted sidebands due to the applied modulation scheme appear in this case exactly at the modulation frequency (as shown in Fig. 3.1a)) which allows for Lock-in detection. However, this detection scheme does not produce stable and reliable results as soon as the rf-frequency does not match one of the laser's frequency comb lines perfectly. In frequency-resolved measurements, this might be no problem for broad resonance lineshapes as in  $\text{Ni}_{80}\text{Fe}_{20}$ , where resonances appear on the order of several 100 MHz [121]. However, it might fail to obtain narrow frequency linewidths typically occurring in oxides such as YIG [122]. Therefore, one aim of this thesis is to establish a further development of this TR-MOKE technique which allows for overcoming the introduced limitations. Besides these limitations, the coupling of the uniform rf-field to the non-uniform spin-wave modes is not very efficient, and thus, a modulation and detection scheme is required, which provides large signal amplitudes and low noise levels.

## 3.2. Super-Nyquist Sampling MOKE

In the following sections, the utilized variant of TR-MOKE will be introduced in detail. First, the synchronization scheme is depicted, which allows overcoming the limitations of conventional heterodyne TR-MOKE setups. Afterwards, the optical setup is introduced, followed by different characterization steps.

### 3.2.1. Sampling of Magnetization Dynamics at arbitrary Frequencies

If we consider the same excitation geometry as introduced in section 3.1, a small variation  $\varepsilon$  of  $f_{\text{rf}}$  away from one of the comb lines will result in a different mixing frequency. Thus no signal component is detectable at DC but at an intermediate frequency  $\varepsilon$  (and higher harmonics), which corresponds to the difference of  $f_{\text{rf}}$  with the nearest comb line. In conventional experiments, this frequency component and its sidebands are not accessible in a phase-stable fashion. Typically, the microwave source uses a reference frequency generated by the laser's repetition rate as a time standard to guarantee a stable difference frequency generation at DC. However, the lock-in amplifier (LIA) is running on its internal time standard and is only synchronized to the modulation source to enable demodulation at the modulation frequency. The basic idea of the novel-developed super-Nyquist sampling magneto-optical Kerr microscopy (SNS-MOKE) technique [73] is to stabilize the fs-laser, the rf-source as well as the LIA to an external time

standard to access the introduced offset frequency  $\varepsilon$  as demodulation frequency for Lock-in detection. Therefore, a 10 MHz Rubidium time standard (Efratom LPRO 101) is utilized as reference input of LIA and rf-source. For this purpose, a laser system with variable resonator length is required to stabilize the laser's repetition rate. This is provided in both used laser systems by additionally purchased options, in which a free space resonator mirror is controlled via a piezo stage operated in the range of 0V to 150V. The required signal of the laser's repetition rate is obtained by a photodiode output of the laser system, which is divided by a factor of 8 to provide a 10 MHz signal. Subsequently, this frequency is compared with the Rubidium standard by using a phase-locked loop (PLL) which compares the two frequencies and generates an error voltage corresponding to the difference of both frequencies. The error signal is amplified to a suitable range and applied to the piezo actuator, which changes the resonator length intending to minimize the frequency offset. Note that it is crucial to bring the repetition rate as close as possible to the external reference frequency; otherwise, the piezo range will not be sufficient to stabilize the laser by using the PLL. This is facilitated by using an additional stepper motor to change the mirrors' position in coarse steps close to the estimated stabilization point. The voltage range of the piezo corresponds to a frequency range of  $\approx 100$  Hz.

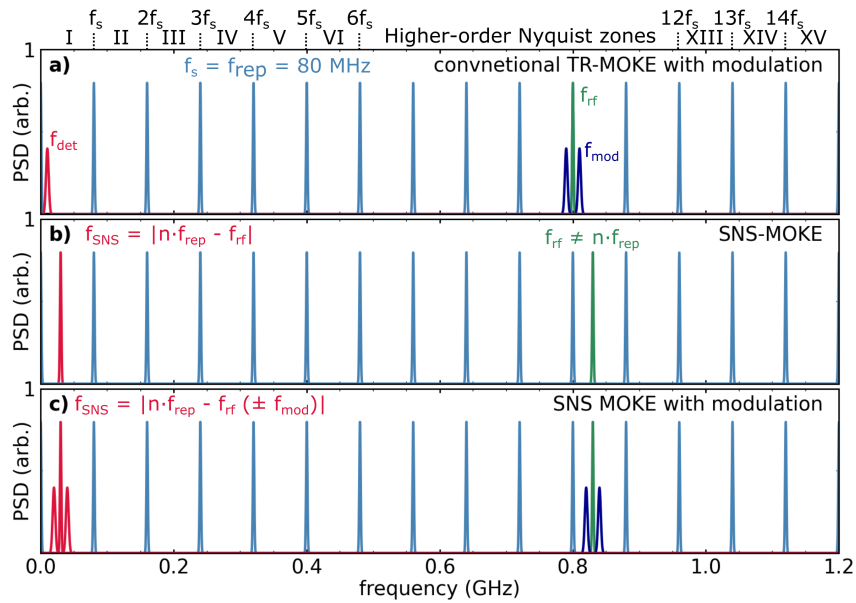


**Figure 3.1 | Schematic of TR-MOKE and SNS-MOKE functional principle in frequency space.**

The short laser pulse, represented by a frequency comb with 80 MHz spacing, is depicted in light blue while the rf-excitation frequency is shown in green. Panel a) shows the case of conventional TR-MOKE measurements, where the rf-frequency matches one of the comb lines to convert the additional modulation sidebands (dark blue) down to the accessible regime close to DC (detection frequency in red). b) and c) demonstrate the SNS-MOKE configuration where the rf-excitation has an offset to its nearest neighbor in the frequency comb. Aliasing effects result in the downconversion of the high-frequency precessional motion down to the regime accessible by the Lock-In amplifier in the lowest-order Nyquist zone (red). In c) additional sidebands due to field modulation appear also as sidebands of the lowest alias frequency and thus detection at  $f_{SNS}$  and/or  $f_{SNS} \pm f_{mod}$  is possible.

If the laser is locked to the same time standard as LIA and rf-source by using a PLL, the sampling of magnetization dynamics at arbitrary frequencies becomes possible. This is enabled because the LIA exactly knows in this configuration how large the chosen offset frequency  $\varepsilon$  between laser comb line and rf-frequency is. Therefore, direct and phase-stable demodulation at  $\varepsilon$  becomes possible, as depicted in Fig. 3.1b). This detection scheme is the typically used method in the experiments presented in this thesis. In addition, this technique can be easily combined with modulation techniques as used in conventional TR-MOKE setups. This would result in Lock-In demodulation at  $\varepsilon \pm f_{\text{mod}}$  and provided the expected signals at arbitrary rf-frequencies as depicted Fig. 3.1c). Such an approach might be helpful to decompose different signal components in the obtained dynamic signal.

### Influence of the Temperature on Laser Stability

From initial measurements, we found that it is highly required to stabilize the entire laser system in temperature to keep the laser (Toptica FFPro-TVIS) within the piezo's control range. This is further important since most laser parameters, such as wavelength, output power, and repetition rate, strongly depend on the temperature. This means, by stabilizing the repetition rate, additional changes in the temperature of the system will lead to a reduced intensity or changes in the phase relative to the master clock. The Toptica FFPro-TVIS system requires (without an external heater) a warm-up time of approximately 20 h to work in a stable regime, where thermal equilibrium is reached within the system, and the properties stay constant. With the aid of an external heater for temperature stabilization, this warm-up behavior is strongly improved, and the system can be used after a warm-up time of 2 h while only tiny readjustments are required. Within this stabilized regime, a timing jitter of less than 5 ps can be obtained between the rf-excitation at 6 GHz and the 80 MHz repetition of the laser over a measurement time of 12 h.

### Exploiting Aliasing Effects in the Case of Under-Sampling

Until now, the implemented stabilization results only in the possibility of using the modulation technique at arbitrary driving frequencies. As we will show in the following, this scheme grants even more advantages for direct demodulation at the frequency offset  $\varepsilon$ . In doing so, it is recommended to look at this excitation scheme in the time domain. Here, the short laser pulse samples the magnetization's precessional motion as a function of time. To fully reconstruct the dynamics of an oscillatory motion, one has to consider the Shannon-Nyquist sampling theorem, which states that the sampling frequency  $f_s$  needs to be at least twice as large as the highest frequency component of the signal to avoid aliasing effects [123]. If we now assume an rf-excitation of approximately 1 GHz, this would require a sampling frequency of at least 2 GHz (if non-linear higher harmonic processes are neglected). However, the laser repetition frequency  $f_{\text{rep}}$  is fixed at 80 MHz, and therefore, the Shannon-Nyquist criterion is not fulfilled. In such a case of extreme under-sampling, a large number of so-called alias frequencies are

generated in higher-order Nyquist zones. These appear in frequency space as the difference of the rf-driving frequency and the  $n^{\text{th}}$  harmonic of  $f_{\text{rep}}$  beginning with the nearest harmonic that obeys  $|f_{\text{rf}} - n \cdot f_{\text{rep}}| \leq f_{\text{rep}}/2$ . Typically, these alias frequencies are avoided by using suitable filters. However, in SNS-MOKE we explicitly exploit these aliasing phenomena to convert the GHz magnetization dynamics down to the MHz or kHz regime, which allows for detection by employing low-noise balanced detectors and LIAs. An example for this conversion is depicted in Fig. 3.2, where the magnetization is driven by an rf-frequency of 839 MHz. The under-sampling of the dynamics by means of the 80 MHz laser pulses results in alias frequencies, which can be understood as frequency components in higher-order Nyquist-zones, which fold over to the lowest-order Nyquist-zone close to DC. This component can also be obtained in the frequency domain, as the 10<sup>th</sup> harmonic of the frequency comb mixes with the 839 MHz rf-excitation. Again, the lowest-order alias frequency at 39 MHz can be used for direct demodulation.

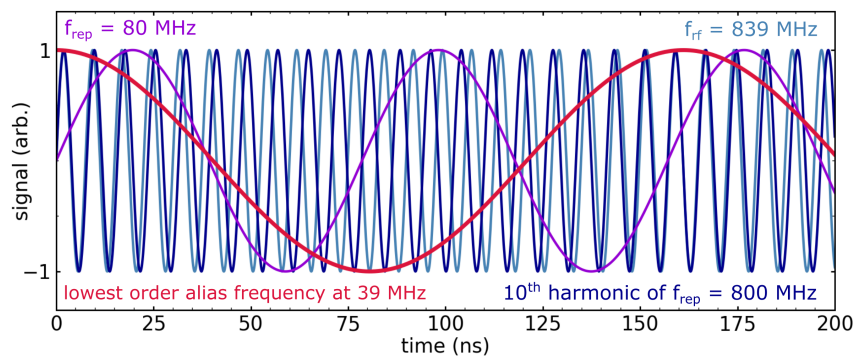


**Figure 3.2 | Generation of alias frequencies due to under sampling.** The aliasing process can be understood in the time domain as under sampling of a fast oscillating signal with a sampling frequency which does not fulfill the Nyquist criterion. The red line emerges in this case of under sampling from higher-order Nyquist zones of the sampling frequency, which is in this particular case the 10<sup>th</sup> harmonic.

This direct demodulation is possible because amplitude and phase information of the magnetization's precessional motion are conserved within each alias component. By sweeping the frequency (or the field) across a magnetic resonance, each alias component will experience the same change in amplitude and phase while passing the resonance. Since this effect appears for all alias frequencies, the system's spectral response appears broad, and the resulting signals might be misleading. However, selecting only the lowest-order alias frequency as the Lock-In demodulator one directly accesses a signal component that is either proportional to the real or imaginary part of the dynamic susceptibility. Moreover, by using a dual-channel LIA, both signal components are detected simultaneously, since the phase shift of 90° between the two demodulation frequencies corresponds to the phase shift between real and imaginary parts in the complex plane. In comparison to section 3.1, the perfect setting of the phase is not required anymore since a mixture of real and imaginary parts always allows to reconstruct the pure real or imaginary component. The exploited aliasing process can be seen as an inherent modulation, which renders an external modulation unnecessary, and thus enhances the SNR in comparison

to microwave amplitude modulation. A few requirements need to be considered to facilitate arbitrary frequency settings in SNS-MOKE. In the particular case of a 80 MHz short-pulsed laser system, the repetition rate gives the spacing between the comb lines, meaning that the largest offset to the nearest comb line is 40 MHz (above this frequency the nearest line is not the  $n^{\text{th}}$  but the  $(n+1)^{\text{th}}$ ). Thus, the detector electronics, as well as the LIA, must provide a bandwidth of at least 40 MHz. In all experiments, this is governed by a home-build balanced low-noise detectors with a bandwidth of 40 MHz and by using a dual-channel Zurich Instruments lock-in amplifier (LIA) (HF2LI) with 50 MHz input bandwidth.

### 3.2.2. Microscopy Setup for SNS-MOKE Detection

The electrical scheme explained in the last section overcomes the major restrictions of conventional TR-MOKE systems. A more detailed view on the optical setup is mandatory to fully understand how the obtained signals in this thesis are generated and detected. Both SNS-MOKE setups used in this thesis work in the same way and mostly use the same components; therefore, only one of them is described in detail here.

#### The optical Setup

The utilized fs-laser (Toptica FFPro TVIS) allows for varying the output wavelength in the visible range rendering it as a suitable tool for the wavelength-dependent MOKE investigations in different materials. However, in this thesis, it is set to a stable wavelength of 520 nm, which can be taken as a good compromise between minimal spot size on the sample and magnitude of the MOKE response for the investigated materials. Before entering the microscope, the laser beam is expanded to ensure a diffraction-limited spot size at the sample, which results in a beam diameter of  $\approx 5$  mm in the beam path. Subsequently, a pair of optical elements (cf. Fig. 3.3) consisting of a half-wave plate and a Glan-Thompson polarizer guarantees for perfectly s-polarized light at the sample. The half-wave plate is used to rotate the laser's polarization, and thus it allows to change the intensity of the s-polarized laser light after passing the polarizer. A 45:55 pellicle beam splitter is used to reflect the light towards the polarization-maintaining microscopy objective ( $NA = 0.9$ ), as depicted in Fig. 3.3. On the sample, the focal spot size is on the order of 300 nm. Here, the light interacts with the magnetization via MOKE. The reflected light is passing the objective and is transmitted through the pellicle beam splitter. Subsequently, a combination of half-wave plate and Wollaston prism allows for balanced detection. The Wollaston prism splits the incoming beam into two beams with orthogonal polarization states. In the absence of magneto-optic response, the half-wave plate is oriented such that both photodiodes of the balanced detector acquire the same laser intensity resulting in a difference signal of approximately zero. When the reflected laser light experiences a tiny rotation of its polarization state due to the MOKE, the Wollaston prism converts the change of polarization into a disbalance of intensities of the two out-coming beams. Thus, the

balanced photodetector will detect a non-vanishing difference signal proportional to the Kerr rotation (and/or ellipticity), which can be analyzed by means of Lock-in demodulation.

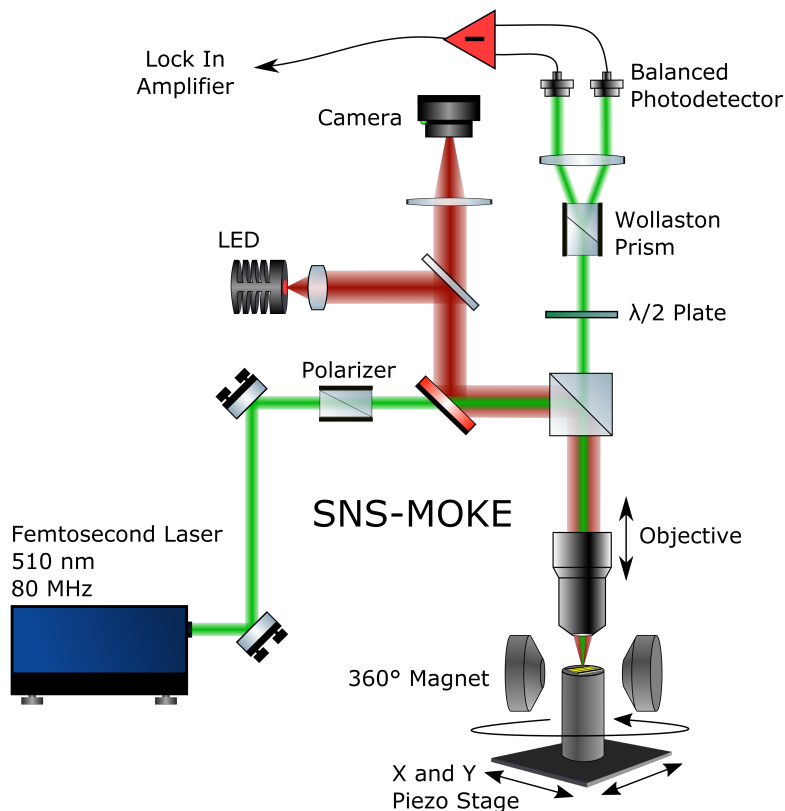


**Figure 3.3 | Optical microscopy setup for SNS-MOKE detection<sup>1</sup>.** The optical paths of laser sampling (green) and wide-field imaging (red) are depicted. The sample is positioned within the poles of a electro-magnet and can be controlled via a piezo stage. Due to the MOKE, the reflected laser light experiences a rotation of its polarization state which is detected by means of a balanced detector and a LIA.

### Excitation Scheme

To saturate the magnetic moments and to identify the position of the FMR, an electromagnet provides an IP bias field with a magnitude of about  $\pm 300$  mT, which can be set to any IP angular orientation in the range of  $0^\circ$  and  $360^\circ$ . The dynamics within the magnetic sample are typically excited by an Oersted field generated by an rf current-carrying CPW or strip-line. The magnetic sample is either placed on top of the signal line of the CPW to experience a homogeneous IP rf-field or next to the waveguide where an OOP field forces the magnetization to precess around its equilibrium position, as indicated in Fig. 3.4. Due to the shape anisotropy in thin magnetic layers, the magnetization precesses on an elliptical trajectory, as indicated in the Fig. 3.4. In sample geometries where birefringence contributes to the change of polarization,

<sup>1</sup>Figure reprinted from [73] with the permission of American Physical Society.

the SNS-MOKE scheme will detect this component in addition to dynamic changes of magnetic origin. In such a case, an additional modulation technique is required. Therefore, modulation coils are mounted close to the sample holder to provide an AC-magnetic field of several 100 Hz and amplitude of up to 3 mT.

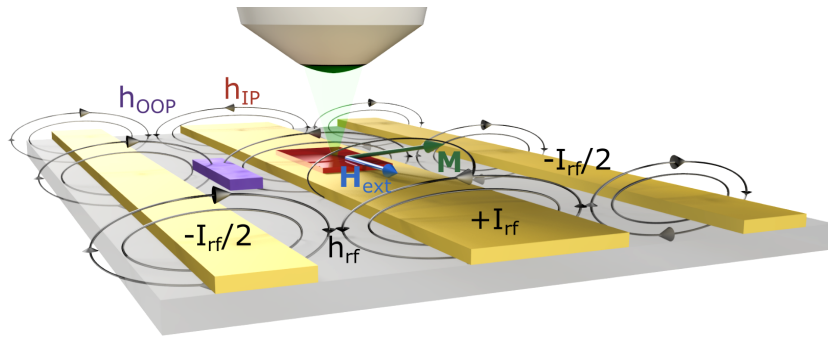


**Figure 3.4 | Coplanar waveguide for rf-excitation.** The rf-field induced magnetization dynamics are sampled in the focus of the laser. Magnetic elements can either experience an out-of-plane (OOP) or an in-plane (IP) rf-field generated by the signal and/or ground lines of the CPW.

### Sample Alignment and Image Stabilization

In order to perform spatially-resolved imaging of extended magnetic layers or microstructured devices, the sample holder is attached to a 3D piezo stage, which provides lateral scanning area of  $80\ \mu\text{m} \times 80\ \mu\text{m}$  and also allows to set the focal distance between objective and sample. Many experiments performed in this setup contain micron-sized structures and require stability of the lateral laser spot's position over days. Hence, an imaging system consisting of a light emitting diode (LED) and a charge coupled device (CCD) camera is implemented, which allows for wide-field imaging of the sample (see Fig. 3.3). This possibility initially enables a good alignment of the sample and the microscope objective by obtaining the sharpness of the CCD image. Moreover, an image stabilization algorithm can be used to keep the sample in position for long-term measurements. For this purpose, a reference image is stored and compared to the actual image of the sample. A proportional-integral-derivative (PID) control routine accesses the three-axis piezo stage to stabilize the laser spot in lateral position and maintains the focal distance of the objective with respect to the sample constant. With this stabilization routine, long-term measurements in microstructured devices are feasible and easily reproducible.

### Balanced Detector

The home-build balanced detector is designed for super-Nyquist sampling (SNS) purposes with a low noise behavior and a bandwidth of 40 MHz. The photocurrents of the two matched diodes are subtracted directly to generate the difference signal. The bandwidth of this stage is set to 40 MHz by using a suitable broadband operational amplifier. In addition, both diode

signals are added to provide a sum signal representing the sample's reflectivity since it stays constant under changes of the polarization state. The amplification factor here is much weaker, and the bandwidth is on the order of kHz. Nevertheless, the sum signal allows to map the topography of the sample and helps to track changes in reflectivity due to laser-induced defects during the measurement. In all measurements, the sum signal and the demodulated difference signal are recorded simultaneously to match the obtained dynamics with the lateral structure of the sample. The difference output of the detector is designed such that the noise level over the frequency range of 40 MHz is less than  $1 \mu\text{V}$ , and thus it is much lower compared to the expected signals of several  $\mu\text{V}$  or mV. We experimentally analyzed the detector behavior as a function of alias frequency. First, we obtained the average signal at the difference output without laser illumination to characterize the pure electrical response as a function of frequency and possible electro-magnetic crosstalk from other devices. The averaging time per frequency step was 10 s. For different integration times, the dark traces in Fig. 3.5a)-c) depict a flat response over the entire frequency range. The average noise level is shown in panel d) for the three different time constants without laser.

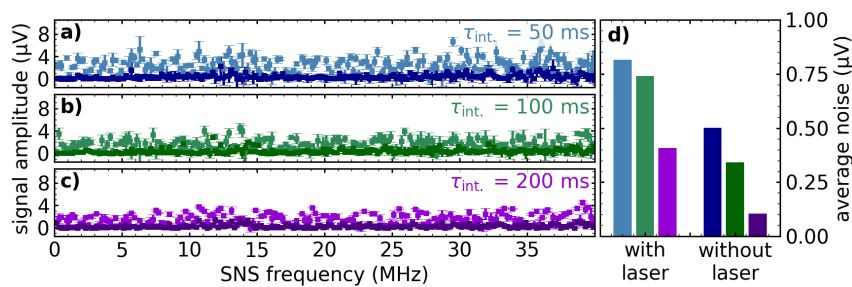


**Figure 3.5 | Frequency-dependent detector noise.** In panel a)-c) the average signal amplitude with errorbars is shown as a function of the chosen SNS alias frequency for three different integration times of the LIA. Light colors depict the case of a realistic measurement while dark colors show the pure electrical noise level of the detector. Panel d) represents the averaged detector noise level for the pure electrical path on the right hand side and with laser illumination and the corresponding frequency mixing process on the left hand side.

As a next step, the averaged signal was recorded under realistic measurement conditions for an rf-excitation frequency of 4 GHz plus SNS frequency  $\varepsilon$ . Here, a magnetic  $\text{Ni}_{80}\text{Fe}_{20}$  layer was used with an applied bias field of 0 mT. Due to the off-resonant precessional motion of the magnetic moments, a non-zero average signal is expected and can be seen in panels a)-c). The noise level for this analysis is shown in d) on the left-hand side and indicates that even for 50 ms integration time, a noise level of  $1 \mu\text{V}$  is feasible. These measurements give a more realistic frequency-dependent noise behavior of the entire setup since fluctuations of the laser intensity, timing jitter between rf-source and laser repetition frequency, and the magnetization dynamics itself are taken into account.

### 3.2.3. Measurement of Resonance Lineshapes

To demonstrate one of the most basic measurement techniques of SNS-MOKE, we performed a field-swept experiment, also referred to as optical FMR, on a 20 nm thick  $\text{Ni}_{80}\text{Fe}_{20}$  layer on top of a CPW. The rf-frequency is set to 3.201 GHz with a fixed driving amplitude of 0 dBm at the sample. Therefore, the alias frequency used for the demodulation is 1 MHz. The external field is aligned along with the CPW in DE geometry.

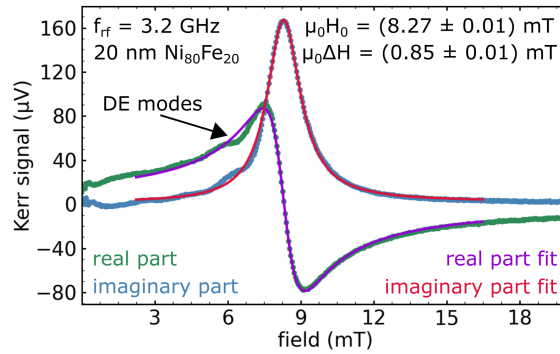


**Figure 3.6 | Field-swept spectra for linewidth determination with SNS-MOKE.** By sweeping the external bias field a Lorentzian lineshape is observed in both signal channels (green and blue). One corresponds to the real and the other one to the imaginary part of the dynamic susceptibility. Slight deviations appear in the case of additional spin-wave modes. Fitting results are depicted in violet and red for both channels resulting in the shown resonance field and linewidth.

Here, the real and imaginary parts of the dynamic susceptibility  $\chi$  are the measured signal components of the SNS-MOKE setup with a corresponding phase angle  $\varphi$ . Clearly, the FMR is detected by sweeping the magnetic field. Both signal components are obtained simultaneously, as described in section 3.2, and can be fitted with the following expression [81]:

$$\Im(\chi) \cos \varphi + \Re(\chi) \sin \varphi = y_0 + I \cdot \frac{\Delta H \cos \varphi + (H - H_0) \sin \varphi}{\Delta H^2 + (H - H_0)^2} \quad (3.1)$$

The main fit parameters of this equation are the half-width at half maximum (HWHM)  $\Delta H$ , the resonance field  $H_0$ , the amplitude of the signal  $I$  and the phase angle  $\varphi$ . Additionally, an offset parameter  $y_0$  can be used to fit the data in cases of non-magnetic background signals. As described in section 3.2.2, one Lock-In channel represents the real part of the dynamic susceptibility  $\chi$ , while the other corresponds to the imaginary part. Therefore, the phase angle  $\varphi$  should be  $0^\circ$  for real and  $90^\circ$  for the imaginary part. In this detection scheme, intermediate phase angles could occur due to an imperfect phase setting or temperature-dependent drifts of the setups phase. However, since both Lock-In components are measured and recorded

simultaneously, no loss of information due to such an intermediate phase happens. By fitting the data, one can easily reconstruct the real and imaginary parts by readjusting the phase angle. As soon as propagating or standing spin waves emerge in the spectrum, the fit does not match perfectly anymore, as indicated on the lower field side of Fig. 3.6. One solution for one or two additional spin-wave peaks is simply adding another Lorentzian peak to the fit routine. However, this increases the uncertainty since the number of fitting parameters is increased, but in most cases, this helps to obtain the real linewidth of the fundamental resonance. Note, for a large number of spin-wave modes close to the FMR with large amplitudes, this routine fails, and other approaches need to be found, as demonstrated in chapter 4. The obtained linewidth is typically analyzed as a function of frequency to determine the Gilbert damping  $\alpha$  as depicted for  $\text{Ni}_{80}\text{Fe}_{20}$  elements and an extended layer in the appendix A.1.

### Measurement Options

Two basic measurements types were typically carried out with varying parameters of the rf-driving field and orientation of the external bias field. First, field-swept measurements allow to obtain the resonance position and can directly be compared with inductively carried out experiments. Frequency-dependent analysis of the resonance linewidth results in the Gilbert damping parameter, known as a useful figure of merit for magnonic materials. Power-dependent measurements allow detecting non-linear threshold values, a saturation of modes, or temperature-dependent shifts of the resonances. In addition, simple frequency or rf-power-dependent measurements can be performed at a fixed bias field. Second, spatially-resolved measurements facilitate the phase-resolved observation of coherent propagating and standing spin-wave modes and provide direct access to the wave vector to map out the spin-wave dispersion for a given set of external parameters. The SNS-MOKE further allows analyzing more complex effects, such as voltage-induced changes in perpendicular magnetic anisotropy in ultra-thin iron layers [111], voltage-induced domain wall motion [124] or current-induced linewidth changes due to the spin-Hall effect (SHE). In addition, the determination of the coercive field of ferromagnetic layers and microstructures is possible by exploiting the phase flip in field-swept measurements. This procedure allows obtaining p-MOKE loops in a dynamic fashion [31, 125]. Such experiments additionally render SNS-MOKE a valuable tool for the investigation of antiferromagnetic layers coupled to a ferromagnet. Furthermore, by slightly changing the setup, quasi-static MOKE loops in longitudinal configuration can be obtained with similar spatial resolution.

### Comparison to other optical Detection Techniques

The advantages of SNS-MOKE in contrast to inductive FMR and optical TR-MOKE have been shown in detail in section 3.2 and reference [73]. In addition to that, the following chapters will demonstrate that our novel type of magneto-optical sampling microscopy is a competitive alternative to other purely optical detection methods. The following techniques were typically

used to investigate spin-wave phenomena in a spatially-resolved manner: (1) BLS [61–65], (2) time-resolved scanning transmission x-ray microscopy (TR-STXM) [70–72] and (3) nitrogen vacancy (NV) center magnetometry [66–69]. The latter one is explained in more detail in chapter 8.

(1) In BLS, a light wave scatters inelastically with magnetic excitations and either creates or annihilates a magnon resulting in the possibility to measure coherent and incoherent thermal magnons. Typically, an rf-excitation is used to drive specific magnon modes in the magnetic systems, and the response spectrum is detected over a broad frequency range. However, this technique is phase insensitive and thus does not distinguish in its basic version between coherent and incoherent magnons. The frequency resolution of BLS appears to be very high at first glance but is limited to a few 10 MHz depending on the free spectral range of the setup [126]. In addition, spatially-resolved imaging suffers from the lack of phase sensitivity since spin-wave wavelengths obtained in the magnitude are a factor of two smaller. Moreover, BLS measurements need seconds to minutes to acquire enough photon counts for a reasonable SNR, and thus require remarkable long-term stability for spatially-resolved measurements over days. Nevertheless, BLS is an impressive technique due to the possibility of measuring incoherent and coherent magnons and additionally choosing a specific wave vector for the detection.

(2) The spatial resolution of TR-STXM is impossible to reach for SNS-MOKE due to the use of short-wavelength x-ray radiation in large facility synchrotron sources. The accessibility of such sources is one of the limiting factors for their usage. In addition, this technique suffers from frequency-resolution issues similar to TR-MOKE techniques. However, for exchange spin-wave phenomena and for spatially-resolved detection in nanometer-sized magnetic structures TR-STXM is the perfect measurement instrument.

Both techniques offer outstanding measurement possibilities as long as high-frequency resolution is not demanded. If this is the case, SNS-MOKE will be a valuable alternative or extension to conventionally carried out experiments in the future.



# Local Magnetization Dynamics in YIG

---

In the second experimental chapter of this thesis, the SNS-MOKE technique is exploited to study spin waves in yttrium iron garnet (YIG) - a promising material candidate for future magnonic and spintronic devices [29]. Due to its low Gilbert damping parameter [28, 55], spin waves in YIG layers can propagate over large distances and are therefore a suitable carrier of information for wave-based computing [127]. In recent years, many electronic concepts have been successfully transferred to the field of magnonics using YIG in devices such as spin-wave guides [128], magnon-directional couplers [24], logic gates [129] and all-magnon transistors [22]. However, there are still open questions and challenges regarding the growth of the layers and their subsequent treatment (e.g., etching or additional layer deposition) of the material to form functional devices. As well as how these processes affect the local properties of the final YIG-based device. One way to address these effects is to locally detect intrinsic material parameters, such as the Gilbert damping, to assure it is conserved under the manipulation of the layer. The extremely low Gilbert damping parameter is directly linked to a very narrow frequency linewidth [130], which is a highly desired quantity for strong coupling phenomena in the field of quantum computing. The SNS-MOKE technique allows investigating YIG layers with an arbitrary high-frequency resolution, which is required to capture narrow resonance linewidths and to obtain a detailed picture of the spin-wave band structure. We present this technique as a novel approach to obtain the damping parameter locally by identifying regimes with nearly vanishing spin-wave group velocity in the magnonic band structure, as shown in section 4.3.3. In addition, the local character of this approach is emphasized by experimental and numerical analysis of the spin-wave dispersion in section 4.2. In doing so, we found strongly localized magnons in the vicinity of an avoided mode crossing in the dispersion. In section 4.2 the size of such an avoided crossing is obtained in a frequency-resolved manner and compared with theoretical predictions. Experiment and calculation revealed a strong coupling of interacting spin-wave modes. Finally, these considerations allow to locally manipulate the properties of the YIG layer such that a "soft" magnonic waveguide confines their propagation. This waveguide does not require additional etching of the YIG layer and therefore offers new possibilities for magnonic devices.

## 4.1. Measurement Geometry

### 4.1.1. Sample Layout

YIG is an insulating ferrimagnet with excellent properties for magnonic and spintronic applications [28, 29, 55]. The commercially purchased epitaxial YIG samples were grown by liquid phase epitaxy on a GGG(111) substrate, which has the smallest lattice mismatch with YIG and thus allows for near-perfect crystalline growth [131]. The nominal layer thickness of the YIG is 200 nm. The surface of the YIG film was polished before performing the next steps of material deposition to define the CPW structures. For an effective excitation of magnetization dynamics in YIG a 100 nm thick gold (Au) CPW is defined by means of electron beam lithography, lift-off and evaporation on top of the 200 nm thick YIG layer. The studies shown in this chapter were performed with two different waveguide geometries to access slightly different wave-vector regimes. Sample 1 has a 40  $\mu\text{m}$  gap, the signal line is 50  $\mu\text{m}$  wide and the ground lines have a width of 25  $\mu\text{m}$ . Sample 2 has a 12  $\mu\text{m}$  wide gap, while the waveguide's dimensions are 20  $\mu\text{m}$  and 10  $\mu\text{m}$  for signal line and ground lines. Both CPW structures are impedance matched for 50  $\Omega$ .

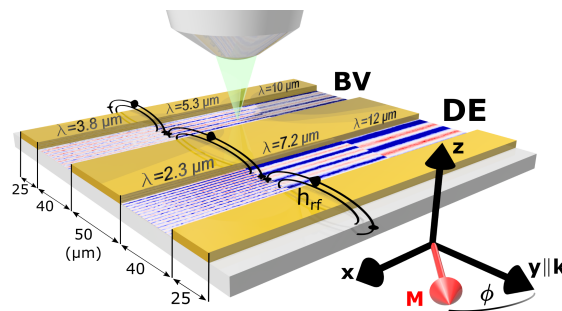


**Figure 4.1 | Measurement geometry with different spin-wave excitations.** The experimental geometry consists of a 200 nm thick YIG layer with a CPW deposited on top to provide an rf-field to drive the dynamics. Examples for such spin-wave excitations measured by means of SNS-MOKE are presented in the gap of the waveguide for DE and BV geometry. The corresponding wavelength is indicated next to the measurement.

### 4.1.2. Field-swept Spectra

In broadband electrical FMR as well as in time-resolved optical FMR experiments, field-swept measurements have been proven to be a helpful tool to reveal the resonance condition and indicate the presence of non-uniform spin-wave excitations as well as non-linear features. Figure 4.2 presents four of such field-swept SNS-MOKE measurements for different orientations of the external magnetic field at excitation frequencies of 4 GHz and 6 GHz. Due to the low Gilbert damping value of YIG, spin waves of several different wave vectors are likely excited

depending on the excitation profile of the waveguide. Thus they can propagate within the film plane over large distances. In the BV geometry, spin-wave modes are excited at slightly higher fields than the FMR, while in the DE geometry, several spin-wave modes appear on the lower field side of the FMR condition. Each of these peaks obtained in Fig. 4.2 corresponds to one specific wave vector [132], while the periodicity of the oscillatory features corresponds to the group velocity. Interestingly, the spin-wave intensity of DE modes in Fig. 4.2a) and b) is strongly suppressed around 65 mT and 130 mT, while in the vicinity of this suppression the periodicity (and therefore the group velocity) of the spin waves varies from the expected path. This behavior we link to an avoided crossing in the spin-wave dispersion between the DE and the 1<sup>st</sup>-order PSSW mode, as introduced in section 2.2.2. The avoided crossing, and the corresponding effects are further addressed in sections 4.2 and 4.2.4.

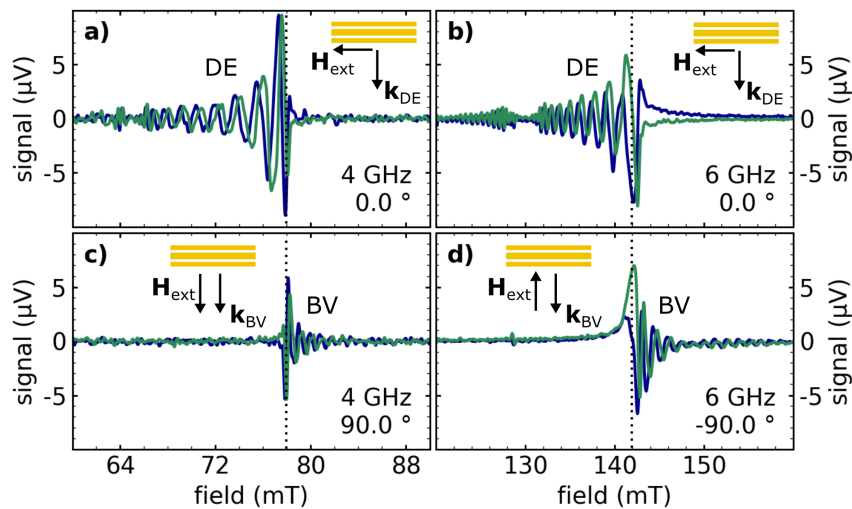


**Figure 4.2 | Field-swept spin-wave spectra.** The blue and green solid lines show the real and imaginary part of the dynamic susceptibility obtained locally by means of SNS-MOKE. The upper row shows the field swept measurements in DE geometry where spin waves propagate at lower field values than the FMR condition. The bottom row shows the same measurements, but in the BV geometry. Here, the spin waves appear on the higher field side of the FMR. Panel a) and c) are measured at 4 GHz and b) and d) at 6 GHz. The dotted black lines in all panels indicate the resonance field of the uniform mode. For the DE condition, we observe a suppression of the DE modes in Panel a) and b) in the range of 65 mT and 130 mT, respectively.

The presented spectra imply that classical analysis in terms of the linewidth of the FMR is nearly impossible without taking effects such as the wave-vector spectrum of the excitation field, spin-wave dispersion, and spin-wave propagation effects properly into account [58]. Therefore, an alternative approach of accessing the Gilbert damping parameter will be the main objective in section 4.3.

## 4.2. Spin-Wave Dispersion in 200 nm YIG Layers

In magnonics, propagating spin waves transfer information through devices, which either manipulate or direct the data to the next device [127]. Besides a small spin-wave damping parameter in such devices, it is crucial to understand the underlying mechanisms. Contributing spin-wave transport properties, such as group velocity or wave vector, strongly depend on the excitation frequency and the applied magnetic field, which defines the spin-wave dispersion. The dispersion introduced in chapter 2.2 is easily accessed by SNS-MOKE, which allows performing measurements with high-frequency resolution hardly obtainable by other optical techniques. In this section, the focus is set to spin-wave dispersion, also referred to as magnonic band structure. Here, in part 4.2.4 we demonstrate the appearance of an avoided crossing in the spin-wave dispersion and its reaction to a variety of external control parameters. Furthermore, we present a concept for a "soft" magnonic waveguide in 4.4.1, which utilizes this avoided crossing in the dispersion to engineer a defined track for spin-wave propagation locally.

### 4.2.1. Spatially-resolved Imaging of Spin Waves in YIG

Field-swept spectra such as those shown in Fig. 4.2 can be used to obtain the approximate FMR position in YIG, while each peak in the vicinity of the FMR conditions corresponds to a non-uniform wave vector excited by the rf-magnetic field of the CPW. The lateral scanning stage of the SNS-MOKE setup allows for phase-sensitive spatially-resolved imaging of these wave vectors in a point-by-point fashion.

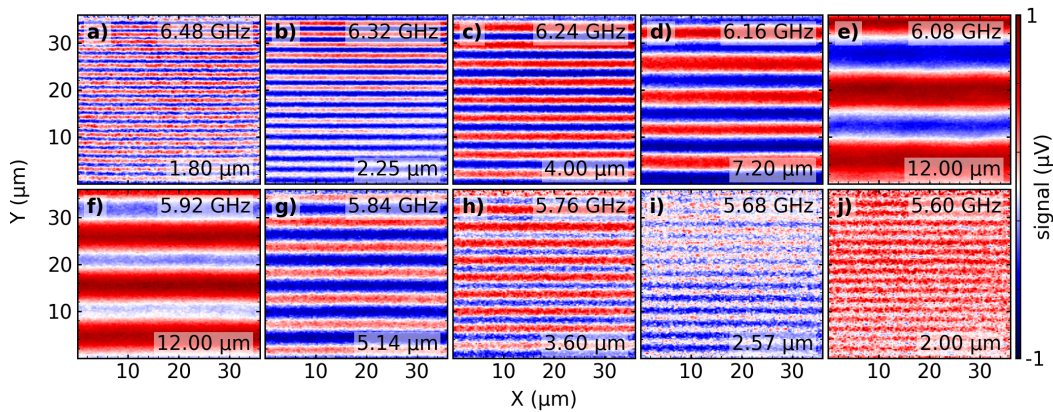


**Figure 4.3 | Spatially-resolved imaging of spin waves in YIG<sup>1</sup>.** The images in the first row were obtained in DE geometry at a fixed magnetic bias field of 142 mT. By increasing the frequency in steps of 80 MHz the wavelength of the spin waves decreases. In the second row, the BV geometry is shown. Here, the frequency is decreased from the FMR condition resulting in a decreased wavelength of the obtained modes. The numbers indicate the applied rf-frequency and the corresponding wavelength of the spin waves extracted by means of two-dimensional fast Fourier transform (2D-FFT). All images show the normalized real part of the measured signal as a function of lateral distance.

In Fig. 4.3 the spatial distributions of the excited spin waves are mapped within the gap of the CPW (as illustrated in Fig. 4.1) for both DE and BV geometries with varying frequency at a constant applied field of 141 mT. These images correspond to different spin-wave modes obtained in Fig. 4.2b) and d). As expected from equation 2.22, the wavelength of DE modes is decreasing by elevated frequency, while in BV geometry, a lowered frequency is required to access shorter wavelengths (cf. Fig. 2.3a)). The wavelengths in this measurement range from 1  $\mu\text{m}$  to 12  $\mu\text{m}$  and are therefore within the setup's spatial resolution limit. The vanishing contrast at small wavelengths is due to the less effective excitation of these wave vectors provided by the CPW. In this set of measurements, a frequency resolution of 80 MHz was used, which reproduces the basic trend of the two dispersion branches. However, the features obtained in Fig. 4.2 are nowhere to be found in this set of spatially-resolved images. The mode crossing is not accessible with the chosen frequency resolution of 80 MHz.

#### 4.2.2. Spatially-resolved Spin-Wave profiles near an avoided Crossing

Performing spatially-resolved imaging as shown in Fig. 4.3 requires a lot of measurement time (in this particular case 3 h per image). Therefore we reduce the measurement scheme to single-line scans in the direction of spin-wave propagation, which provides phase and amplitude information in the same manner as the entire mapping, but now on the time-scale of minutes. This procedure allows to map out the dispersion in a more detailed fashion by decreasing the frequency step size down to a few MHz. In comparison to the measurement shown in Fig. 4.3 line scans were performed at 79 mT using a frequency resolution of 2 MHz. This approach gives more insight into how wave vectors change as a function of applied rf-frequency.

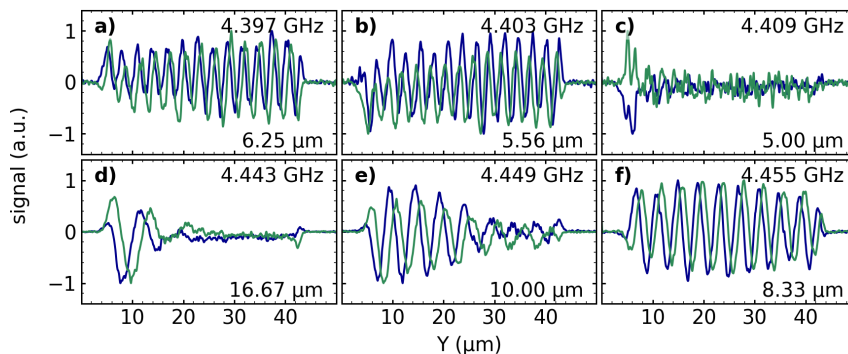


**Figure 4.4 | Line scans of spin-wave modes close to an avoided crossing.** The profile of the excited MSSW mode changes from an unperturbed oscillation within the gap to a strongly damped mode at the edge of the CPW as the frequency is increased. The measurement was performed at 79 mT in the DE geometry. By increasing the frequency in steps of 2 MHz the wavelength of the spin waves decreases, as shown in a)-b). In the upper row, three measurements below the avoided crossing are shown where c) is close to the avoided crossing. The second row depicts the development at frequencies higher than the crossing. d)-e) Localized modes with long-wavelength start to build up and finally reach the expected DE-like behavior in f).

Surprisingly, the excited DE spin waves strongly differ from the purely dipolar prediction in a frequency band of approximately 100 MHz. For the given values of the excitation frequency, the amplitude of the spin waves decays strongly with increasing distance from the antenna, as observed in Fig. 4.4c). For slightly larger frequencies, propagation of spin waves is no longer possible. At even higher frequencies, long-wavelength spin waves are localized at the edge of the CPW, as obtained in d). In Fig. 4.4f) the obtained wave vector is now again in agreement with the prediction for the DE modes. Taking the field-resolved measurements from Fig. 4.2 into account, this allows connecting the field range of reduced spin-wave intensity to the frequency range where spin-wave propagation appears to be forbidden.

### 4.2.3. Spin-Wave Dispersion

The obtained line scans are sufficient to extract wavelength and wave vector with the aid of a fast Fourier transform (FFT). By plotting the frequency as a function of the IP wavenumber, the dispersion relation is reconstructed for a fixed field amplitude. The resonance condition, where  $\mathbf{k}$  equals zero, is set by the external magnetic field. For 79 mT the resonance frequency can be found at 4 GHz in a 200 nm thick YIG layer. Frequencies higher than FMR will result in DE spin waves for  $\mathbf{M} \perp \mathbf{k}$  and lower frequencies lead to BV modes for parallel alignment of  $\mathbf{M}$  and  $\mathbf{k}$ , as depicted in Fig. 2.3. The following measurements were taken with a frequency resolution of 10 MHz (and 2 MHz in a range of  $\pm 50$  MHz around observed mode crossing).

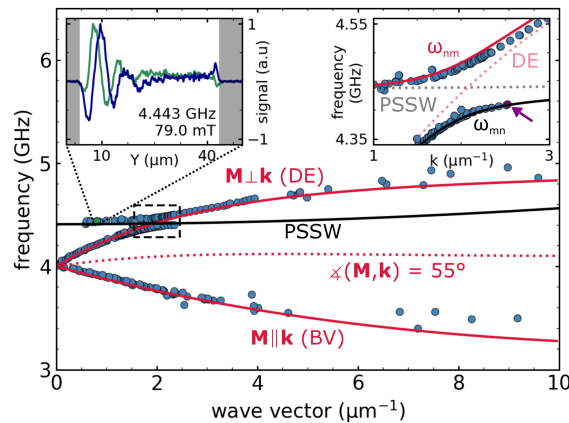


**Figure 4.5 | Spin-wave dispersion of YIG<sup>1</sup>.** The blue data points were obtained from line scans at varying frequencies by using FFT. The external bias field was fixed to 79 mT during all measurements. The different spin-wave dispersion branches for BV and DE (red) as well as for the 1<sup>st</sup>-order PSSW mode (black) are depicted as solid lines. The intermediate orientation of nearly flat dispersion is shown as dotted red line. The upper left inset shows a localized spin-wave mode in the vicinity of the avoided crossing within the gap of the CPW. The upper right inset magnifies the area of the avoided crossing in the dispersion. Here, the dotted lines represent the classical DE and PSSW dispersion branches, while the solid lines depict the calculated dispersion with mode repulsion following the formalism of Kalinikos and Slavin (cf. section 2.2.2).

Interestingly, we detect an avoided crossing in the spin-wave dispersion at frequencies where DE mode and 1<sup>st</sup>-order PSSW mode branches cross (upper right inset in Fig. 4.5). Here, the exchange interaction of interacting modes needs to be taken into account and leads to an opening of a so-called dipole gap due to the repulsion of these two modes [92]. By using the formalism of Kalinikos and Slavin [92, 93, 97] introduced in section 2.2.2, the dipole gap can be modeled. The expressions  $\omega_{nm}$  and  $\omega_{mn}$  describe the behavior of the hybridized modes in the vicinity of the crossing. The frequency splitting of the dipole gap at 79 mT is on the order of 90 MHz. Note that for larger wave vectors, the obtained values differ slightly from the predicted ones. The spin-wave intensity for these wave vectors appears to be very low due to the lowered excitation efficiency of the CPW for these wave vectors resulting in additional uncertainties. However, these modes are still within the resolution limit of the SNS-MOKE setup, and thus a different waveguide structure might be used to make this regime accessible. The spin-wave dispersion with its corresponding mode hybridization has been investigated for decades. First observations started with BLS experiments in the 1980s [61, 94]; however, such a detailed view on the magnonic band structure in IP magnetized YIG films has not been reported so far. The hybridized modes of 1<sup>st</sup>-order PSSW and DE mode were also calculated by Jorzick *et al.* [64], but in their microstructured sample geometry, the BLS data yields no indication of the dipole gap. Förster *et al.* [70] investigated the dispersion by means of TR-STXM and observed hybridization effects in their spectra for YIG layers of similar thickness. However, the region of the crossing was not mapped properly due to the limited frequency resolution. Such bandgaps were also the subject of investigations in other material systems. For Fe-N in a similar sample geometry Tacchi *et al.* [95] performed BLS measurements and calculated the spin-wave dispersion but were not able to obtain a crossing of DE and 1<sup>st</sup>-order PSSW mode experimentally. In addition, the calculated dipole gap did not fit the experimental mode frequency splitting of several GHz. Thus, additional experiments need to be considered to get further insight into the applicability of such mode-repulsion effects for magnonics.

### Strong Coupling Regime

The coupling strength  $g$  of the two interacting modes can be directly related to the frequency splitting of the dipole gap and the frequency linewidths of the interacting modes, as seen in equation 4.1. The splitting can be derived from measurements such as shown in Fig. 4.5 while the frequency linewidth of the obtained modes can be seen as the inverse of the spin-wave lifetime, introduced in equation 4.2. The dipole gap obtained in Fig. 4.5 allows extracting the frequency splitting, which can be analyzed as coupling strength  $g$ . From the experimental data, a frequency linewidth value of  $\Delta f = 200$  kHz can be extracted. The coupling constant is given by

$$g = \frac{f_{\text{Splitting}}}{\Delta f_{nm} + \Delta f_{mn}}, \quad (4.1)$$

where  $f_{\text{splitting}}$  is the size of the dipole gap and  $\Delta f_{i,j}$  is the frequency linewidth of the two interacting modes with mode number  $i, j$ . Here, a coupling constant of  $\approx 200$  can be derived. Typically,  $g > 1$  indicates strong coupling between two modes [44] and would allow for coherent information processing. Thus the regime of dipole gaps could be a playground for quantum computing and might allow hosting Rabi oscillations, as reported for magnon-phonon coupling [40, 133]. In cavity magnonics, coupling constants of 1 to 10 have been reported recently [37, 38, 41]. Our reported value appears to be much larger due to the extremely narrow linewidths of the interacting modes. In consequence of this finding, we investigated the dipole gap in the magnonic band structure in detail and aimed for possible control mechanisms of the splitting size in the following sections.

#### 4.2.4. Dipole Gap

The dipole gap and its surrounding yields several interesting features, e.g., a flat dispersion, localized spin-waves, a strong coupling regime, and spin-wave soliton formation [134]. We investigate the dipole gap for different experimental conditions to gain a more detailed understanding of this regime and identify control mechanisms allowing the utilization of the bandgap for magnonic devices. Therefore, we obtain the magnonic band structure as a function of rf-excitation frequency, field amplitude, field orientation, and different positions on the 200 nm YIG layer.

#### Frequency-dependent Change of the Dipole Gap

Theoretical considerations of the spin-wave dispersion suggest that the applied rf-frequency and therefore the applied bias-field change the nature of the dipole gap. In the following, we consider the basic dispersion branches for dipolar-exchange spin waves in the DE geometry (cf. equation 2.22) and for the 1<sup>st</sup>-order PSSW mode (cf. eq. 2.20) mode in a frequency-dependent manner. In that case, one can phenomenologically predict the behavior of the crossing point of these two modes. For a low resonance field of 5 mT (FMR condition at 1 GHz), the DE mode shows a strong change of frequency with IP wavenumber in the dipolar regime. Furthermore, the 1<sup>st</sup>-order PSSW appears at a frequency of about 600 MHz above FMR condition in the dispersion. For the case of a larger FMR frequency of 8 GHz with resonance condition at 209 mT, the excited PSSW mode occurs only 400 MHz above FMR. Since the dispersion of the first PSSW mode is nearly flat, we expect the crossing to appear in a similar frequency range above FMR, resulting in a relative shift of the splitting towards the FMR condition with increasing resonance frequency. On the other hand, for the large frequency case, the dispersion of the DE mode appears flattened compared to the low-frequency case due to a larger stiffness of the magnetization. Since the dispersion branch of the DE mode is approaching the 1<sup>st</sup>-order PSSW with a different slope for the two cases, their overlap strongly increases with frequency while the difference in group velocity decreases. This results in a

larger mode splitting since the range of forbidden wave vectors is increased. We experimentally determined the dispersion relation at different frequencies (and bias fields) and paid special attention to the avoided crossing to verify these theoretical assumptions.

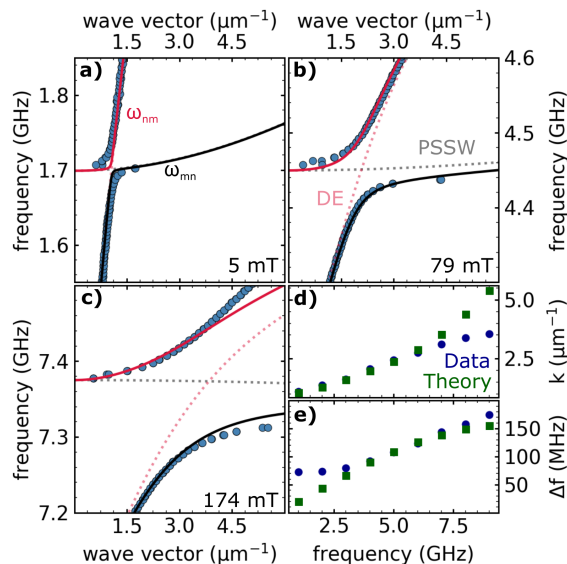


**Figure 4.6 | Avoided crossing in the spin-wave dispersion<sup>1</sup>.** a)-c) The blue data points were obtained from line scans at varying frequencies. For the three different resonance conditions shown, the external bias field of the measurement was fixed at 5 mT, 79 mT and 174 mT, respectively. The different spin-wave dispersion branches for DE (dotted red line) and PSSW mode (dotted grey line) are depicted. The solid red and black lines depict the calculated dispersion for the hybridized modes in the vicinity of the avoided crossing following the formalism from Kalinikos and Slavin introduced in section 2.2.2. Panel d) and e) show experimental results and theoretical predictions of the frequency dependent change of the wave vector at the splitting and varying size of the frequency splitting, respectively.

The theoretical predictions from equation 2.26 fit the experimental data obtained in Fig. 4.6a)-c) very well. As one can see in Fig. 4.6d) and e) the theory correctly predicts the field where the splitting occurs and the width of the frequency splitting above 3 GHz. Note, for higher frequencies, where the group velocities of the degenerate modes are nearly the same in the crossing regime, the model starts to diverge from experimental observations. The frequency-dependent change of the splitting allows controlling the bandwidth in which wave vectors are allowed to propagate and defines which are completely blocked.

### Simulation of the Magnon Dispersion

For the calculations of the expected dipole gaps in the presented figures, we utilized the formalism introduced by Kalinikos and Slavin [92, 93] for the case of an IP magnetized sample, as presented in section 2.2.2. Here it is mandatory to take intermediate pinning conditions as well as a more realistic wave-vector distribution of the DE mode across the film thickness. A Python-based fitting routine is utilized to determine the parameters to calculate the avoided

crossing, which allows for simultaneous fitting of several data sets, including avoided crossings obtained at different bias fields with the introduced formalism for one set of fitting parameters. In doing so, we obtained the following values for the exchange constant  $A_{\text{ex}} = 3.6 \text{ pJ m}^{-1}$ , saturation magnetization  $M_s = 138 \text{ kA m}^{-1}$  and thickness  $L = 192 \text{ nm}$  for the YIG film for the different avoided crossings shown in Fig. 4.6. These values are in good agreement with the literature and the nominal thickness of the YIG film of 200 nm. In addition, all values are close to experimentally observed values by means of inductive FMR, as shown in appendix A.2. From the same fitting routine, we extracted the pinning parameters  $d_1 = 1 \times 10^6 \text{ m}^{-1}$  and  $d_2 = 6 \times 10^6 \text{ m}^{-1}$ .

### Field Reversal

Magneto-static surface wave modes are known to be surface modes and therefore strongly localized either to the top or bottom interface of the YIG layer, as explained in section 2.2. The localization depends on the direction of the applied magnetic field and the wave vector of the propagating spin wave. The experimental geometry consisting of the CPW allows for three different distinguishable excitation regimes. First, the case where the measured position is in between signal and ground lines. Here, the CPW excitation of DE modes is reciprocal with bias field direction because the pronounced DE spin waves (localized on the top interface) are either launched at the signal line or originate from the Oersted field of the ground line. Due to this symmetric excitation, no difference in the dispersion relation for positive and negative field direction is obtained. However, near the edges of the ground lines outside of the CPW, this symmetry is broken. Here the DE modes are localized to the top interface for one field direction but appear much weaker for the other direction due to their localization at the bottom interface. This observation reverses for a detection close to the other ground line where the wave vector switches sign to the opposite of the bias field. This non-reciprocity [135] of spin waves is an intensively studied topic in magnonics since reversing the external magnetic field switches the propagation characteristics, thus providing a method to control spin-wave propagation in magnonic devices, such as in a magnonic diode [25]. The low Gilbert damping parameter in YIG layers and YIG-based heterostructures allows for long-range studies of this effect because source and detector in spin-wave spectroscopy experiments can be separated by millimeters [136]. However, for a 200 nm thick YIG sample, the signal from the bottom interface is still sufficient for studying DE spin waves with different handedness at the same point of the sample experimentally by means of optical detection. Therefore, we investigated the dipole gap for different bias-field directions near one of the ground lines, as shown in Fig. 4.7.

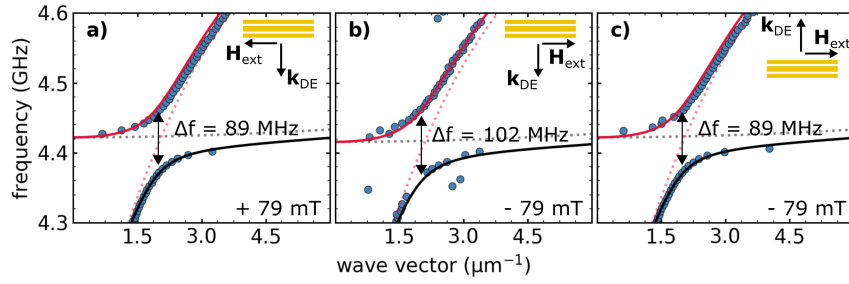


**Figure 4.7 | Dipole gap under field reversal.** Measurement of the dipole gap close to the bottom groundline in a) and b) and at the upper one in c). The magnetic field was set to 79 mT and  $-79$  mT, respectively. The detected spin-wave amplitude is strongly decreased in b) due to the localization of the excited mode on the opposite side of the sample. The size of the splitting varies under reversal of the magnetic field.

Here, we observe a change of the frequency splitting by 13 MHz for the 200 nm thick YIG layer as a consequence of the field reversal. This change of the frequency splitting appears to be very small compared to values reported by Kalinikos and Slavin [92] for pinned and unpinned layers. However, their investigated film thickness is on the order of  $5.6 \mu\text{m}$  resulting in very different pinning parameters, and they investigated FVSWs being more localized in the volume. Here, the observed change in the frequency splitting results from the different handedness of the excited spin waves for positive and negative field direction, which leads to slightly different pinning conditions. A straightforward way to verify the observation of a change in the frequency splitting under reversal of external bias field is to flip the wave vector as described before. In our geometry, presented in Fig. 4.1 we switch the sign of the wave vector by first completing one measurement at the bottom ground line and then performing the subsequent measurement at the top ground line. Here, the obtained dispersion (and frequency splitting) for the negative field direction is the same as on the upper ground line for the positive field direction and vice versa. This clearly indicates that the obtained change in frequency splitting corresponds to the different handedness of the surface spin-waves modes.

### Influence of the Field Orientation

Not only does reversing the applied field influence the magnonic bandgap, but so does IP rotation while the amplitude is kept constant. Due to the waveguide geometry, only spin waves with wave vectors perpendicular to the waveguide are effectively excited. These correspond to DE modes as the field is applied parallel to the CPW. When the applied field is rotated from DE towards BV geometry, the nature of the excited spin-wave mode changes from surface type to volume type modes. That means their group velocity changes, but also their localization shifts from the interfaces into the volume. To demonstrate the plausibility of the chosen model to explain the behavior of such intermediate state spin waves, we experimentally analyzed the dipole gap for different orientations of the external bias field at a fixed frequency and modeled the bandgap with the earlier introduced formalism.

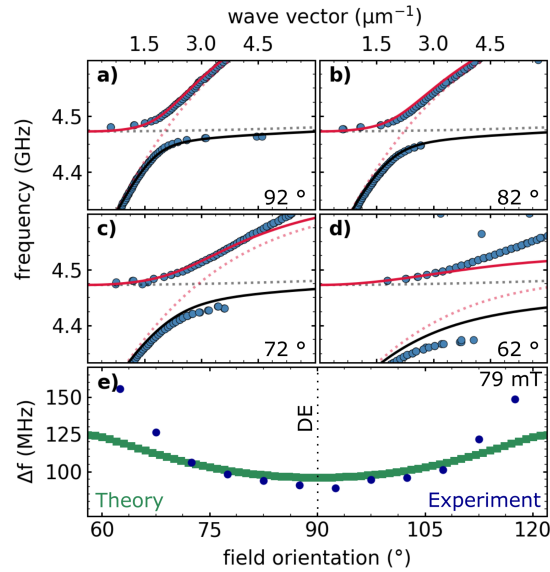


**Figure 4.8 | The dipole gap's change under in-plane field rotation.** The depicted dispersion measurements were taken at an external field amplitude of 79 mT while the orientation of the field was varied. Panels a)-d) show the obtained dispersion spectra for angular orientations of 92°, 82°, 72° and 65°. The splitting is smallest for pure DE spin waves and increases for intermediate angular orientations. In e) the green data points represent the theoretical predictions in the angle range between 60° and 120° while 90° represents the DE geometry. The blue data show the experimentally obtained frequency splittings. Within the range of  $\pm 20^\circ$  with respect to DE geometry, the SNS-MOKE data fits the prediction.

Figure 4.8a) and b) show the match between experimentally obtained data and calculation. For a slightly larger IP rotation of the magnetic field, the spin-wave dispersion starts to flatten, which results in a different group velocity in the vicinity of the mode crossing. Thus, the coupling of the modes increases, resulting in a broadened dipole gap, as seen in c) and d). The comparison of experimental data and theoretical prediction shown in Fig. 4.8e) supports the conclusion taken from the frequency-dependent analysis, where the DE dispersion flattens and reaches values close to the PSSW dispersion branch. In such cases, modeling the splitting with the introduced formalism becomes difficult, and the predictions diverge from the experimental results. Similarly, the findings of Fig. 4.6 show that the predicted position of the crossing in reciprocal space differs strongly from experimentally obtained data for cases of dispersion branches developing nearly parallel over a larger range of wave vectors. For these particular cases, it is still possible to either predict the frequency splitting or the gaps' position in k-space even though it fails to give a good estimate for both properties simultaneously. However, within a range of  $\pm 20^\circ$  relative to the DE geometry, the calculated frequency splittings and its change with IP field rotation matches the obtained magnonic bandgaps from SNS-MOKE measurements. The intensively-studied dipole gap allows for precise prediction of the spin waves' reciprocal space position and the size of frequency splittings within a wide range of parameters, such as rf-frequency, field amplitude, external bias field orientation as well as propagation direction of the contributing spin waves. Consequently, the next step is to identify different

concepts that exploit the magnon bandgap properties and allow to locally tune them.

### Determination of a local Gilbert Damping Parameter

By mapping out the dispersion with a high-frequency resolution, the localization of spin-wave modes at the edge of the antenna becomes visible in the vicinity of the dipole gap (cf. Fig. 4.4). In this regime, it is possible to determine a local Gilbert damping parameter by obtaining the decay length  $\lambda_{\text{prop}} = v_g \cdot \tau$  of the spin wave, by modeling the data with a damped oscillation. Here,  $\tau$  is the spin-wave lifetime, and  $v_g$  describes the group velocity of the excited spin wave. For the same frequency regime, the group velocity can be derived by taking the derivative of the fitted dispersion branch via  $v_g = \frac{\partial \omega}{\partial k}$  into account. The localization and strong suppression of magnon intensity near the avoided crossing corresponds to a group velocity that approaches zero and thus prohibits spin waves from propagating. In particular, the group velocity is reduced from values of  $200 \text{ m s}^{-1}$  down to less than  $10 \text{ m s}^{-1}$  (as indicated by the purple arrow in Fig. 4.5). The spin-wave lifetime obtained experimentally is directly linked to the intrinsic Gilbert damping parameter  $\alpha$ , and therefore a damping parameter can be obtained for the localized spin-waves in the vicinity of the dipole gap via

$$\tau = \frac{2}{\alpha} \cdot \frac{1}{\gamma \mu_0 (M_s + H_0)}, \quad (4.2)$$

where  $H_0$  is the applied magnetic field and  $M_s$  is the saturation magnetization of YIG. Careful analysis of avoided crossings in the magnonic band structure offers one possibility to determine the Gilbert damping parameter locally in 200 nm thick YIG layers since the modes are not allowed to propagate in this regime. However, this is only one alternative approach, which will be discussed and compared with other methods in section 4.3.3.

## 4.3. Local Gilbert Damping

The standard procedure to estimate the Gilbert damping constant  $\alpha$  in inductive and optical FMR type experiments is to sweep the external magnetic field and analyze the linewidth of the ferromagnetic resonance as a function of rf-frequency. To overcome limitations presented in section 4.1, we offer a slightly different approach to obtain a damping parameter locally, which can be applied to materials with narrow linewidths and low Gilbert damping.

### 4.3.1. Angular-resolved Measurement

The different spin-wave spectra shown in Fig. 4.2 are challenging to interpret in terms of their linewidth since the uniform mode is widely broadened due to an overlap with neighboring DE or BV modes. One possibility to reduce the broadening is to decrease the rf-power down to a regime where spin-wave modes are no longer effectively excited, and only a weak uniform mode remains detectable. However, the approach utilized in this work aims to suppress the spin-wave modes due to the measurement geometry, such that only the uniform excitation persists. For this purpose, the orientation of the external magnetic field is changed to control the spin-wave dispersion. As discussed in chapter 2.2, the DE and BV geometries are two limiting cases of the spin-wave manifold for  $\mathbf{M}$  oriented either parallel or perpendicular to  $\mathbf{k}$  within the film plane. However, the spin-wave dispersion also covers all intermediate field orientations between  $\mathbf{M}$  and  $\mathbf{k}$ . In the following, we investigated field-swept spectra, such as those shown in Fig. 4.2, as a function of IP field orientation to gain insight into the influence of the field direction on spin-wave propagation. In Fig. 4.9 field-swept measurements at different field angles were performed and plotted as a two-dimensional color-coded map, where the color represents the signal of the excited spin waves obtained by using Lock-In detection.

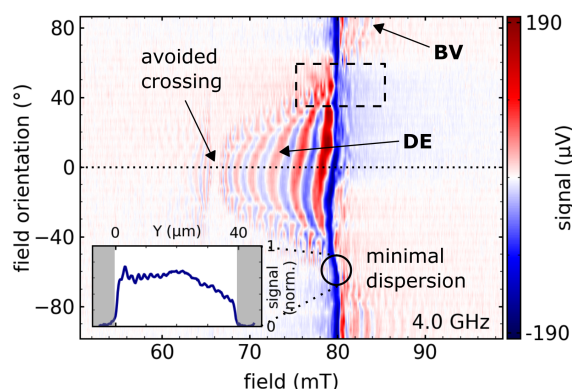


**Figure 4.9 | Angular-resolved spin-wave spectra at 4 GHz.** Imaginary part of the SNS-MOKE signal as a function of field and IP angular orientation of the magnetic field. The spin waves were excited with an rf-frequency of 4 GHz at a power level of 10 dBm. The different excitation regimes are depicted with black arrows, and the dashed box highlights the measurement area of fig. 4.10. The inset shows the spatial profile of the signal in the gap of the  $\zeta$  at  $-50^\circ$  in the case of a nearly flat dispersion. Here, the signal amplitude has a uniform character within the gap and changes only slightly close to the edges. Furthermore, small oscillatory features are visible which indicates an overlap of different spin-wave modes.

For  $0^\circ$  orientation (DE geometry) the magnetic field is aligned along the waveguide, and spin waves are excited perpendicularly to the applied field direction; thus, DE modes are propagating perpendicular to the applied field. Again DE modes appear to be suppressed due to the mode repulsion nearby the dipole gap. For IP angles of  $\pm 90^\circ$ , the launched spin

waves propagate parallel to the magnetization of the sample, which corresponds to the BV geometry. By rotating the external field from DE to BV geometry, the excited spin-wave spectrum narrows, and for one of these intermediate IP orientations, the dispersion becomes nearly flat (cf. Fig. 4.5), which prohibits spin-wave propagation. Furthermore, the flat dispersion leads to simultaneous excitations of different wave vectors at field values close to the FMR. Under such conditions, the spin-wave spectrum appears as a single Lorentzian peak, enabling straightforward field-dependent linewidth analysis. Compared to the pure DE or BV condition, the extracted linewidth is reduced, but still, some broadening mechanisms such as two-magnon scattering exist.

### 4.3.2. Frequency-dependent Analysis of minimal Dispersion

Measurements, such as shown in Fig. 4.9, were adapted to a wide frequency range to utilize the concept of minimal dispersion linewidth analysis for Gilbert damping determination. With a further reduced rf-power level of  $-25$  dBm, angular-resolved measurements at a variety of excitation frequencies were carried out, such as those shown in Fig. 4.10.

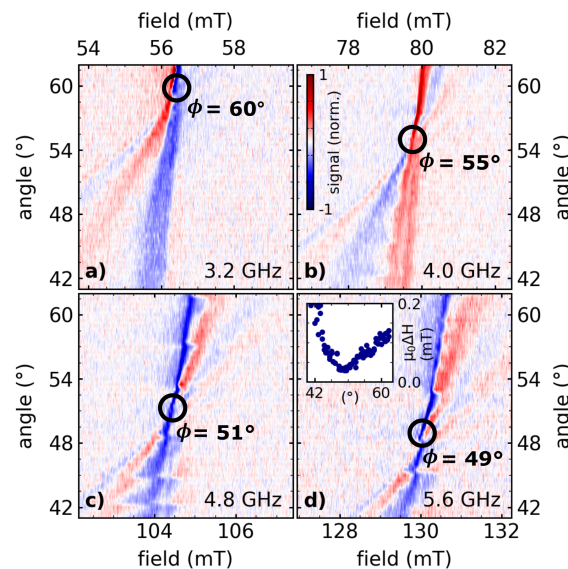


**Figure 4.10 | Frequency-dependent analysis of the point of minimal dispersion.** Imaginary part of the obtained signal plotted as a function of field and angular orientation of the magnetic field. In a)-d) the angular-resolved measurements of the point of minimal dispersion are plotted for frequencies ranging from 3.2 GHz to 5.6 GHz. The inset in panel d) shows the angular-resolved change of linewidth. Here, a minimal linewidth is found in the point of minimal dispersion with a value of  $30 \mu\text{T}$ . In the vicinity of the minimal dispersion, the linewidth starts to broaden slightly due to different spin-wave modes emerging close to the uniform mode.

Determination of the frequency-dependent linewidth requires previous analysis of the point of minimal dispersion for each of these frequencies, since this point changes nearly linearly

with frequency, as one can see in Fig. 4.10 by following the black circles. This behavior can be understood by taking the angular components of the dispersion relation 2.20 in the dipolar-dominated regime into account. The expression for  $\omega_n$  contains one part which connects the dipolar kernel  $P_{nn}$  with the field term  $\omega_H$  and another one which interacts with its IP orientation  $\cos^2 \phi_k$ . Thus, the overall angular-dependent dipolar contribution decreases for increasing external bias fields. The group velocity of DE modes for larger bias fields decreases as well. Therefore, the angular-resolved dispersion for 1 GHz appears significantly different from the one at 8 GHz. As discussed in section 4.2.3, the group velocity of DE modes is largest for low external bias field. Simultaneously, the group velocity for BV mode in the dipolar regime is small for low bias fields and gets more pronounced for increasing field values. Thus it is expected that the point of minimal dispersion shifts with increasing bias field from BV towards DE geometry in the observed frequency range. Since the entire spin-wave band shifts in the same way. By taking equation 2.20 into account, it is possible to directly derive the point of minimal dispersion in a frequency-dependent manner. For such an IP orientation, the group velocity in the range between  $0 \mu\text{m}^{-1}$  to  $10 \mu\text{m}^{-1}$  is changing by less than  $25 \text{ m s}^{-1}$ , which means the dispersion for these angles becomes nearly flat. Note that the minimum in dispersion is not fixed to exactly one angle but persists over a range of approximately  $\pm 5^\circ$  relative to the experimentally obtained value. In this regime, the minimum in group velocity remains stable while the dispersion gradually changes from the BV to the DE regime.

### 4.3.3. Determination of the Gilbert Damping Parameter

As pointed out in the last section, the obtained lineshape in the point of minimal dispersion reduces to a single Lorentzian peak which can be fitted using equation 3.1. The analysis introduced in section 3.2.2 can be applied to the obtained spectra at the point of minimal dispersion (cf. inset in Fig. 4.10). Here, the real and imaginary parts of the dynamic susceptibility  $\chi$  are the measured components of the SNS-MOKE setup with a corresponding phase angle  $\varphi$ .

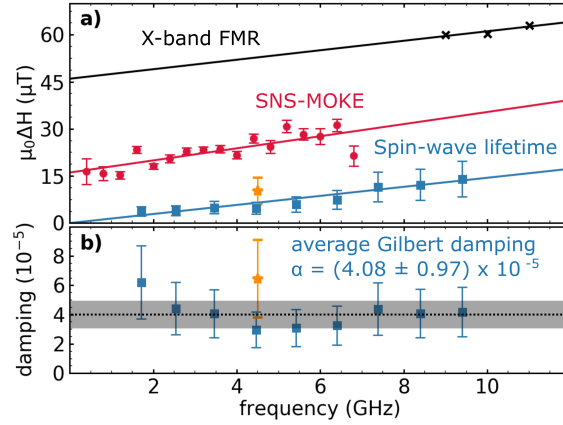


**Figure 4.11 | Gilbert damping and linewidth in points of flat dispersion<sup>1</sup>.** a) The SNS-MOKE linewidth data are shown as red circles with error bars as a function of frequency, where the solid red line indicates the fit of the data to obtain the Gilbert damping. Inductive FMR data and a corresponding fit measured in the same sample are depicted in black. The calculated linewidths from localized spin waves in the vicinity of an avoided crossing are shown as blue squares with their corresponding error bars. The solid blue line depicts the average damping value of these spin-wave lifetime data points. The damping values with errors for each of the localized modes are shown in b) with an averaged value indicated as a black dashed line with its standard deviation shown as a grey area. In both panels, a yellow star indicates a localized spin-wave mode within a magnonic waveguide, as discussed in section 4.4.

The obtained linewidth in the point of minimal dispersion is analyzed as function of frequency and fitted linearly to determine the Gilbert damping factor  $\alpha$  and the intrinsic linewidth broadening  $\Delta H_0$ :

$$\Delta H = \Delta H_0 + \frac{\alpha}{\gamma} f_0 \quad (4.3)$$

Here,  $f_0$  is the resonance frequency and the gyromagnetic ratio  $\gamma$  is given in  $\text{Hz T}^{-1}$ . The intrinsic zero-frequency linewidth is mainly dominated by sample inhomogeneities but also contains other processes such as two-magnon scattering [81]. The red data points presented in Fig. 4.11a) were obtained in the point of minimal dispersion from data sets such as presented in section 4.3.2. The frequency-dependent change in linewidth appears linear and can be interpreted as Gilbert damping with an additional zero-frequency offset. The Gilbert damping constant  $\alpha$  obtained from this set of data is  $(5.41 \pm 1.07) \times 10^{-5}$ , while the intrinsic linewidth of  $(16 \pm 1) \mu\text{T}$  is considerably small. Compared to conventional inductive FMR measurements in the range of 10 GHz (so-called x-band FMR) measured on the same sample, the zero-frequency offset is reduced by 70% due to the local character of the SNS-MOKE technique. The increased offset obtained by inductive x-band FMR can be explained by sample inhomogeneities whose effects add consecutively throughout the entire sample. Typical values obtained in the literature are on the order of 100  $\mu\text{T}$  to 300  $\mu\text{T}$  [55, 137, 138]. Nevertheless, for a perfectly

local measurement without broadening effects, the desired zero-frequency offset should be zero. Since the optical detection only collects the signal from an area defined by the laser's focal spot size, the remaining zero-frequency linewidth is not solely explained due to inhomogeneities of the sample but more likely due to two-magnon scattering in the case of a flat dispersion. To avoid this type of line broadening, we analyzed localized spin-wave modes observed in the vicinity of an avoided crossing in the spin-wave dispersion, as presented in section 4.2.4. Here, we exploit the significantly decreased group velocity due to the curvature of the magnonic band structure close to the crossing point. Again, the dispersion is flat, but spin-wave propagation and two-magnon scattering are only allowed within a narrow range of wavenumbers in the vicinity of the crossing. As presented in section 4.2.3, these localized modes can be expressed via an exponentially damped oscillation, which allows extracting the propagation length. By employing equation 4.2, we calculated the corresponding Gilbert damping parameter of such spin-wave modes (shown in Fig. 4.11b)) which leads to an averaged Gilbert damping constant of  $(4.08 \pm 0.97) \times 10^{-5}$  for frequencies ranging from 1 GHz to 8 GHz. From this data, the linewidth can be calculated over the entire frequency range as indicated by blue squares in Fig. 4.11a). Following this procedure, we find a similar damping value as obtained with SNS-MOKE in the point of minimal dispersion. The experimentally observed Gilbert damping constants agree with results presented by other groups for extended YIG layers [55, 122, 139]. However, the intrinsic linewidth obtained in these publications is on the order of a few 100  $\mu\text{T}$ . In contrast, both of our presented techniques provide low Gilbert damping constants and simultaneously a very narrow intrinsic linewidth of less than 20  $\mu\text{T}$ . This emphasizes the local character of the damping measurement by means of SNS-MOKE. Results of similar quality were only presented for macroscopic YIG spheres inside a microwave cavity [39, 140, 141], but not for thin-films YIG so far.

#### 4.4. Magnonic Band Structure Engineering

In this section, we now combine the possibility of controlling the magnonic band structure and the technique of damping determination for localized spin waves to apply this concept for spin-wave guiding. The presented results from section 4.2 described the main control parameters which allow for manipulating the spin-wave dispersion, namely the rf-frequency and the external magnetic field (its amplitude, sign, and IP direction). However, these variations affect the entire sample. Thus, the presented concept aims for more localized control of the band structure.

#### 4.4.1. Manipulating the Dispersion Relation

Engineering of the magnon band structure can be achieved by a variety of possible treatments of the sample, e.g., by using a microstructured coil that generates an OOP magnetic field, changing the thickness of the magnetic material by etching grooves in the magnonic material or placing ferromagnetic elements next to each other, where the stray fields enhance the external bias field in the direction of the applied field. Typically it is desirable to avoid direct treatment, such as etching of the YIG layer due to defects and local modifications induced by the process, which might result in an enhanced damping parameter [131]. Therefore, the approach used in this experiment uses ferromagnetic elements on top of the YIG layer to locally modify the effective field. This concept of a "soft" magnonic waveguide may give rise to new magnonic devices since the YIG layer itself needs no further treatment, and spin-wave propagation is provided in confined areas. The basic idea of this experiment is to initialize the spin-wave excitation within the dipole gap, which prohibits the propagation of spin waves for the entire layer. In a confined area, defined by the ferromagnetic elements, a modification of the magnon band structure shifts the dispersion branches up or downwards in frequency and makes it possible to excite spin waves in this particular area of the sample. Mapping the dispersion relation at different values of the applied bias field provides an accurate estimate for the magnetic field required to shift the dispersion such that spin-wave propagation is only allowed within the magnonic waveguide. For a 200 nm thick YIG layer, a change of 1 mT shifts the dispersion up by approximately 50 MHz.

#### 4.4.2. Variations of the Magnonic Waveguide

The approach utilized in these experiments uses additional  $\text{Ni}_{80}\text{Fe}_{20}$  stripes on top of the YIG layer, which are aligned perpendicular to the CPW and thus point in the same direction as the wave vectors of propagating DE modes, as presented in Fig. 4.12. The  $\text{Ni}_{80}\text{Fe}_{20}$  stripes were defined employing electron-beam lithography and deposited directly next to one of the ground lines of the CPW by evaporation and lift-off technique. The thickness of the  $\text{Ni}_{80}\text{Fe}_{20}$  stripes is 10 nm, their width is 10  $\mu\text{m}$  while they expand in the direction of spin-wave propagation on a scale of 100  $\mu\text{m}$ .

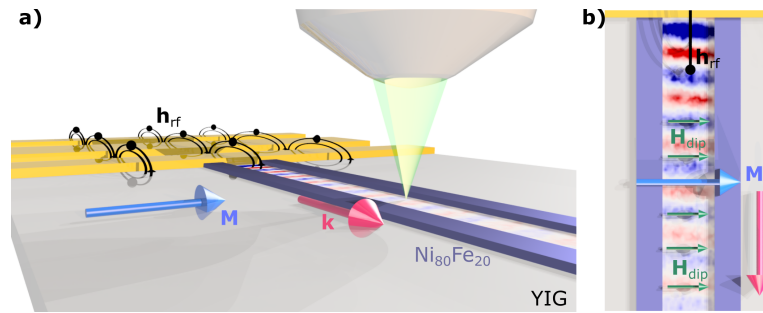


**Figure 4.12 | Conceptual illustration of a soft magnonic waveguide.** a) The magnonic waveguide is oriented in the direction of spin-wave propagation, while the magnetization is aligned parallel to the CPW (DE geometry). b) The dipolar stray fields  $\mathbf{H}_{\text{dip}}$  within the magnonic waveguide allow for spin-wave propagation launched by the rf-field of the CPW for suitable points in the dispersion.

### Damping Parameter for Magnonic Waveguide Modes

For the magnonic waveguide scheme presented in Fig. 4.12 we investigated the Gilbert damping of localized spin waves, as demonstrated in section 4.3.3. The separation of the two  $\text{Ni}_{80}\text{Fe}_{20}$  stripes which form the waveguide is  $5\ \mu\text{m}$  in this measurement. In comparison to the Gilbert damping constant presented in Fig. 4.11b) (blue squares), the analysis of the waveguide mode (shown as a yellow star in Fig. 4.11b)) was performed at the lower branch of the hybridized mode near the avoided crossing, while all other values were obtained at the upper branch. This is caused by the chosen geometry, since a localized waveguide mode is only accessible at the lower branch, while propagation next to the waveguide is prohibited. On this lower branch, the signal amplitude is reduced due to the excitation of larger wave vectors with a reduced excitation efficiency of the CPW. Hence, the propagation length and group velocity analysis becomes less precise, expressed by the enhanced error bars. Here, one finds a Gilbert damping parameter of  $(6.4 \pm 1.3) \times 10^{-5}$ , which is slightly enhanced compared to previous measurements but still in good agreement. Thus it indicates, that the deposition of additional ferromagnetic elements conserves the excellent magnetic properties.

### Variations of the Magnonic Waveguide

The local modification of the dispersion relation is mediated by the dipolar stray field generated in the gap of this soft magnonic waveguide due to surface charges at the edges of the  $\text{Ni}_{80}\text{Fe}_{20}$  stripes. The strength of the modification strongly depends on the lateral separation of the two  $\text{Ni}_{80}\text{Fe}_{20}$  stripes as well as their thickness. Waveguides with different gap sizes of  $2.5\ \mu\text{m}$ ,  $5\ \mu\text{m}$  and  $10\ \mu\text{m}$  were utilized to apply different amounts of local field variation. The dispersion relation for each waveguide is mapped and compared to the reference measurement on bare YIG to point out the amount of frequency shift provided by these waveguides. The obtained shift in Fig. 4.13 clearly depends on the gap size as expected.

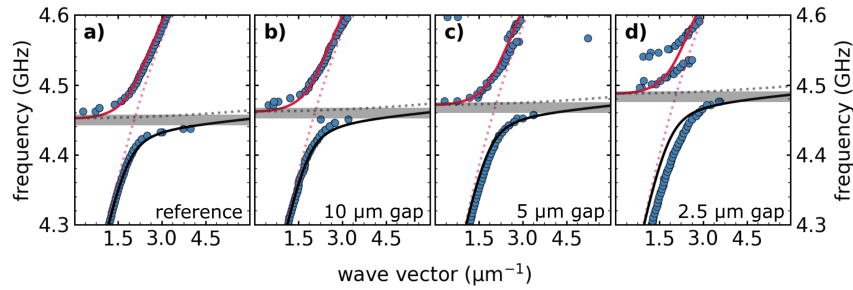


**Figure 4.13 | Dispersion engineering with different gap sizes.** In panel a) the reference measurement without a magnonic waveguide is shown. In b)-d) the dispersion relation was obtained for magnonic waveguides with different gap sizes on the same sample. The solid red and black lines depict the calculated spin-wave dispersion in the vicinity of the crossing, while the dotted lines represent the pure DE and PSSW dispersion branches. The grey area indicates the dipole gap and its shift towards higher frequencies with decreasing gap size of the magnonic waveguide. The gap sizes in b), c) and d) are  $10\ \mu\text{m}$ ,  $5\ \mu\text{m}$  and  $2.5\ \mu\text{m}$ , respectively. For smaller magnonic waveguide structures, other features above the dipole gap appear. For example, for the  $5\ \mu\text{m}$  soft magnonic waveguide a small gap opens, for  $2.5\ \mu\text{m}$  this additional gap approaches the size of the dipole gap's splitting.

Surprisingly, besides the dipole gap, an additional bandgap appeared in the dispersion for small gap widths (upper part of Fig. 4.13c) and d)). This additional bandgap is a typical feature of a magnonic crystal [56, 136, 142] formed by the ferromagnetic stripes. For a gap size of  $2.5\ \mu\text{m}$  (cf. Fig. 4.13d)) the additional bandgap appears in the vicinity of the dipole gap, while for  $5\ \mu\text{m}$  this additional splitting shifts towards larger frequencies away from the dipole gap and for  $10\ \mu\text{m}$  this additional splitting itself nearly vanishes. At the same time, the dipole gap shifts towards higher frequencies while the gap size of the magnonic waveguide is reduced. The grey area in Fig. 4.13 indicates the shift of the dipole gap. For the smallest waveguide separation, a frequency shift of 40 MHz is achieved, which corresponds to a dipolar field of approximately 1 mT within the gap of the magnonic waveguide. The best results for this type of magnonic waveguides we find for a gap size of  $5\ \mu\text{m}$ . Here, the waveguide mode propagates on a scale of several  $10\ \mu\text{m}$ , and the dispersion shift is sufficient to block spin-wave propagation in the rest of the YIG layer. In addition to bandgaps opening in the dispersion of a single magnetic layer or due to magnonic crystals, one also finds avoided crossings in exchange coupled heterostructures. In such YIG/ $\text{Ni}_{80}\text{Fe}_{20}$  bilayers, the uniform mode of the  $\text{Ni}_{80}\text{Fe}_{20}$  layer offers a variety of bandgaps at crossing points with PSSWs within the YIG layer [42, 43, 143, 144]. This effect is further investigated in appendix A.3.

### Magnonic Waveguide with $5\ \mu\text{m}$ Gap Width

We subsequently performed spatially-resolved imaging for two different positions in the magnonic band structure to support the findings from the dispersion analysis. These frequency positions in the dispersion are termed as "states" in the following.

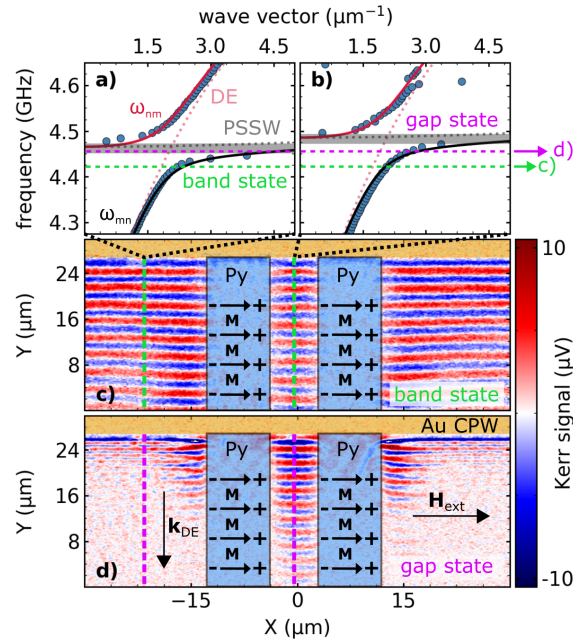


**Figure 4.14 | Modification of spin-wave dispersion<sup>1</sup>.** In a) and b) the spin-wave dispersion is plotted for two different regions on the sample. The dispersion shown in a) is mapped on the unmodified YIG with a lateral distance of  $15\ \mu\text{m}$  to the magnonic waveguide, while the data for b) was taken within the magnonic waveguide's gap. The grey area indicates the dipole gap, which slightly shifts towards higher frequencies within the magnonic waveguide in b). The colored dashed lines depict the "band" and "gap" states. In both cases, the external field was fixed at  $79\ \text{mT}$ . Panel c) shows a spatially-resolved measurement at  $4.427\ \text{GHz}$  (in the "band" state). At this frequency, spin-wave propagation in both parts is allowed with slightly different wave vectors. This changes in d) where the excitation is set to  $4.452\ \text{GHz}$  ("gap" state), a region where the spin waves are not allowed to propagate in the unmodified YIG, but within the magnonic waveguide. The black arrows indicate the magnetization within the  $\text{Ni}_{80}\text{Fe}_{20}$  stripes, resulting in magnetic surface charges and a corresponding dipole field within the waveguide's gap.

In Fig. 4.14 the result for a magnonic waveguide with a gap size of  $5\ \mu\text{m}$  is presented. The dispersion within the magnonic waveguide shifts towards larger frequencies by the amount of  $25\ \text{MHz}$  (Fig. 4.14b)), which corresponds to a change in the effective field by roughly  $0.5\ \text{mT}$ . The field shift can be estimated directly by applying the formalism of Kalinikos and Slavin to model the obtained data. The direct comparison of the band structures measured on the reference position and within the magnonic waveguide allows identifying two different possible states. First is the "band" state, where spin-wave propagation is allowed in the entire layer, while the wave vector is only slightly different within the waveguide. The second case is called the "gap" state, in which propagation is only possible in the confined area of the magnonic waveguide, while it is prohibited in the rest of the layer due to stray fields of the  $\text{Ni}_{80}\text{Fe}_{20}$  stripe. Here, a dipolar field within the gap is generated by magnetic surface charges on the edges of the  $\text{Ni}_{80}\text{Fe}_{20}$  stripes, as depicted in Fig. 4.14c) and d). While in the "band" state, shown in c), both areas host spin waves, the "gap" state in Fig. 4.14d) consists mainly of a spin-wave beam localized within the magnonic waveguide's gap. Here, the excited spin wave propagates over several  $10\ \mu\text{m}$ . A slight enhancement of propagation length is found outside the waveguide due to the local stray fields provided on the edges of the  $\text{Ni}_{80}\text{Fe}_{20}$  stripes. Nevertheless, inside of

the waveguide, the stray field is defined between the two stripes and can be controlled by their distance, as shown in Fig. 4.13. Note that a third "inverse gap" state can be found in the upper regime of the bandgap, resulting in long-wavelength propagation outside the waveguide and strong suppression of spin waves within. The dipole field has to be increased by either reducing the gap width or changing the thickness of the ferromagnetic material to make this waveguide work for larger propagation lengths. A more detailed material, thickness, and shape-dependent analysis for such waveguide structures have to be carried out to utilize this effect for magnonic devices further. Furthermore, the interplay of the additional magnonic crystal bandgaps with the strongly frequency-dependent dipole gap must be investigated to improve this concept. Moreover, current-carrying wires could provide controllable dipole fields within the waveguide and allow for dynamic switching of the "gap" state, which allows adapting this concept in a more dynamic fashion.



# Spin Waves in confined YIG Structures

---

In this chapter, we will continue the investigation of yttrium iron garnet, but instead of extended layers; here, micron-sized freestanding structures are of interest. Such devices might play an essential role for future magnonic devices since they allow to locally utilize the excellent magnetic properties of YIG in a three-dimensional fashion, which is highly envisioned in the emerging field of cavity magnonics [36, 40, 41, 145, 146]. For this purpose, a novel fabrication process for YIG structures was introduced by Heyroth *et al.* [31], which allows fabricating freestanding YIG structures of arbitrary shape with dimensions ranging from a few 100 nm up to several tens of  $\mu\text{m}$ . This fabrication process might give rise to studies on spin-based effects on the nano-scale while antennas or read-out devices can be structured below the freestanding elements. One of the limitations of YIG is the fact that perfect crystalline growth is only achieved on GGG substrates. Unfortunately, this substrate shows a paramagnetic phase in the low-temperature regime [147], where most experiments in the field of cavity-magnonics are carried out. Most experiments utilize macroscopic YIG spheres instead of thin-film samples to avoid these paramagnetic signal contributions. Thus it is highly demanded to identify processes that allow for crystalline growth of YIG microstructures on arbitrary substrates or to find transfer mechanisms. Both problems are addressed in detail in the Ph.D. thesis from Philip Trempler [131]. Here, we demonstrate the experimental investigation of freestanding YIG bridges by means of SNS-MOKE. Spatially-resolved experiments allow determining the Gilbert damping parameter of individual structures [31]. In addition, standing spin-wave modes in transferred YIG platelets [30] are characterized. The possibility of fabricating micron-sized YIG devices with low Gilbert damping parameters and the subsequent transfer of these structures onto another device opens a completely novel playground for magnonic experiments. One of these particular experiments is the magneto-elastic excitation of transferred YIG microstructures, as demonstrated in chapter 6.3.

## 5.1. Local Investigation of Spin Waves in YIG Microstructures

### 5.1.1. Sample Preparation

This part will give a brief overview of the processing of monocrystalline freestanding YIG bridges on a GGG substrate. For further details, please refer to Heyroth *et al.* [31] and the thesis of Philip Trempler [131]. Here, a two resist approach is used and combined with different acceleration voltages by means of electron-beam lithography to define the structure of the YIG element [131]. Room temperature pulsed laser deposition (PLD) is used for a well-defined growth of YIG layers, and only the defined structure persists after performing lift-off technique [31]. A subsequent annealing process in an oxygen atmosphere results in a crystallization of the deposited YIG structure [55]. In this particular case, an array of 3000 bridges was defined in the gap of a CPW providing an OOP rf-field to excite the magnetization dynamics within each structure, as depicted in Fig. 5.1.

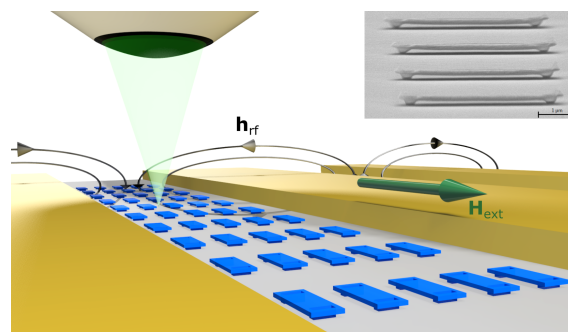


**Figure 5.1 | Schematic of monocrystalline YIG bridges.** An array of 3000 bridges is fabricated in the gap of a CPW to provide OOP excitation. The laser allows to sample the dynamics in each of the individual bridges. The inset in the upper right shows a transmission electron microscopy image of these bridges (inset taken from [131]).

### 5.1.2. Gilbert Damping of freestanding Monocrystalline YIG Bridges

Conventional inductive investigation of the magnetization dynamics offers reasonable estimates for linewidth and damping properties for extended films but makes the analysis of micron-sized elements extremely difficult. In the case of this sample, such inductive FMR experiments result in a broad resonance linewidth since the local properties of the individual bridges vary slightly. Thus an inductive measurement averages over all of these different structures [131]. Detecting local properties by inductive means is possible by specially tailored antenna structures fitting the investigated element. However, SNS-MOKE allows for a direct local investigation of individual bridges in arbitrary waveguide geometries. In contrast to the measurements shown in section 4.3, spin-wave propagation is limited to discrete standing spin-wave modes within

the element. Due to the reduced possibilities of spin-wave excitation, the field-swept spectrum presented in Fig. 5.2a) obtained in BV geometry shows only a discrete number of spin-wave modes. Furthermore, spin-wave modes along the short axis of the bridge are strongly suppressed since the lateral size in this direction is only  $1\ \mu\text{m}$ . Two pronounced resonance peaks close to each other can be distinguished. The careful analysis allows addressing these two peaks to the two different sides of the bridges, which start crystallization from the pedestal and end it in the center. However, a tiny point defect is found in the center [131]. The two sides of the span crystallize with a tiny tilt, and thus the external field can only be perfectly aligned with one side of the bridge, which results in a small shift of the main resonance position of the other side. Such a growth-induced shift in resonance position can be identified as a small anisotropy field [31].

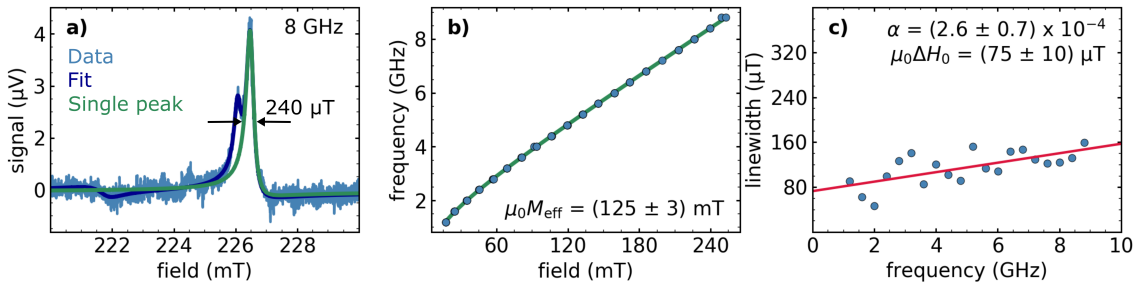


**Figure 5.2 | Gilbert damping determination in a freestanding YIG bridge.** a) Field-swept measurements in  $90^\circ$  geometry at 8 GHz. The data set can be fitted with three Lorentzian peaks allowing to access the linewidth of the main resonance peak. Panel b) shows the frequency as a function of the resonance field and the corresponding Kittel fit. In c) the extracted linewidth data is plotted as a function of frequency. The red line depicts the zero frequency linewidth and allows to obtain the Gilbert damping parameter.

The identification of the main resonance and the fact that no additional broadening due to BVSWs occurs allows performing optical FMR measurements as a function of frequency. Figure 5.2b) presents the frequency as a function of obtained resonance field. By fitting the data with the Kittel equation 2.16, the effective magnetization can be derived. The corresponding resonance linewidth is shown as a function of frequency in panel c). Here, the slope can be identified with a Gilbert Damping parameter of  $\alpha = (2.6 \pm 0.7) \times 10^{-4}$  while the zero-frequency linewidth offset is  $75\ \mu\text{T}$ . In comparison to extended YIG layers, as investigated in chapter 4, perfectly grown on a GGG substrate, the presented values for micron-sized freestanding bridges are slightly enhanced [28, 55, 122]. However, the obtained values are still surprisingly small since additional anisotropies due to strain might decrease the magnetic quality as well as the appearance of a second resonance peak close to the main resonance leading to an effective broadening.

### 5.1.3. Spatially-resolved Imaging of standing Spin-Wave Modes

Next, we performed spatially-resolved imaging of different pronounced spin-wave modes in the DE geometry to identify the mode structure in one individual bridge. Figure 5.3 reveals spatially-resolved SNS-MOKE measurements for parameters as indicated in a)-e). Besides a mostly uniform mode in b) a DE mode in a) and different BV modes in c)-e) are obtained for different external fields and excitation frequencies.

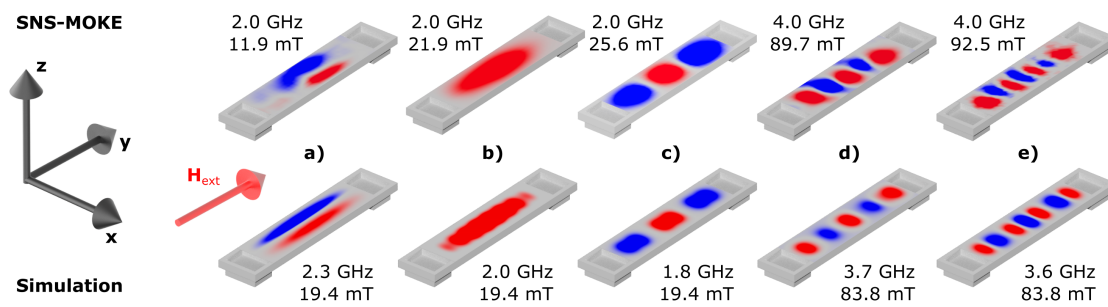


**Figure 5.3 | Spatially-resolved imaging of standing spin-wave modes in YIG bridges.** Top row: SNS-MOKE measurements of standing spin-wave modes in a freestanding monocrystalline YIG bridge obtained under different experimental conditions. Bottom row: micromagnetic simulations under comparable conditions. (modified version of image taken from reference [131])

Micromagnetic simulations were carried out for similar structures, as described in the references [31, 131], to compare the experimental findings to theoretical predictions. In the simulation, the bridge dimensions were  $2.7 \mu\text{m} \times 0.6 \mu\text{m}$  while the thickness was estimated to be 110 nm, which corresponds to the experimental geometry. The distance between span and substrate is on the order of 100 nm [131]. For a slightly larger saturation magnetization of 132 mT, compared to the effective magnetization of  $(125 \pm 3)$  mT obtained from the measurements in Fig. 5.2b), the micromagnetic simulation matches the spatially-resolved SNS-MOKE data for similar experimental conditions as demonstrated in Fig. 5.3. In addition to YIG bridges, even larger and more complex freestanding structures are thinkable. First experimental investigations of such structures are presented in reference [31].

## 5.2. Transfer of YIG Elements to arbitrary Substrates

The growth of high-quality YIG elements, as demonstrated in the last section, encouraged the idea of using the same process on other substrates. However, SNS-MOKE experiments performed on bridges grown on yttrium aluminium garnet (YAG) and magnesium oxide (MgO) (as well as  $\text{LiNbO}_3$ ) revealed much broader resonance lines [131] compared to the findings of Fig. 5.2a) or did show no clear FMR lineshape at all. Fortunately, another promising process

was successfully demonstrated by Trempler *et al.* [30]. Here, an array of freestanding YIG bridges grown on GGG was separated from the substrate by covering the span of the bridge with an aluminium oxide (AlO<sub>x</sub>) mask and removing the connection to the substrate by subsequent dry-etching. By using ammonia solution, the remaining AlO<sub>x</sub> can be dissolved, and the YIG platelets remain in liquid solution [131]. This process allows transferring the monocrystalline span of previously investigated bridges to arbitrary substrates and their integration into complex experimental structures [30].

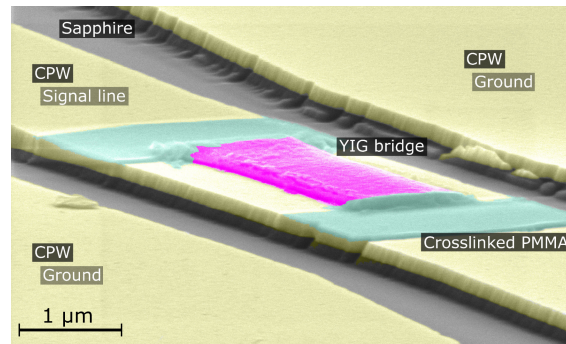


**Figure 5.4 | False-color image of a transferred YIG platelet on top of a CPW<sup>2</sup>.** On top of the signal line of the tailored CPW two cross-linked polymethyl methacrylate (PMMA) patches were used to attach the YIG platelet.

In this study, a previously detached YIG platelet is contacted to an Au layer by using cross-linked PMMA. The Au layer is subsequently patterned by dry etching using a hard mask to form a CPW. This process allows matching the waveguide's dimensions perfectly to the size of the transferred element. In this way, the rf-excitation is most effectively used to excite the dynamics within one single element, which additionally allows for inductive measurements of the same device [30]. However, these inductive investigations do not give any information about the spatial distribution of different spin-wave modes.

### Standing Spin Waves in YIG Bridges

To obtain the mode profile in this particular transferred devices, as demonstrated for freestanding bridges on GGG, we performed spatially-resolved imaging of the transferred YIG element on top of the Au CPW (depicted in Fig. 5.4). This experimental geometry provides a local IP excitation field - a geometry hardly thinkable for optical experiments in YIG devices fixed on GGG substrate.

<sup>2</sup>Figure reprinted from [30] with the permission of AIP Publishing.

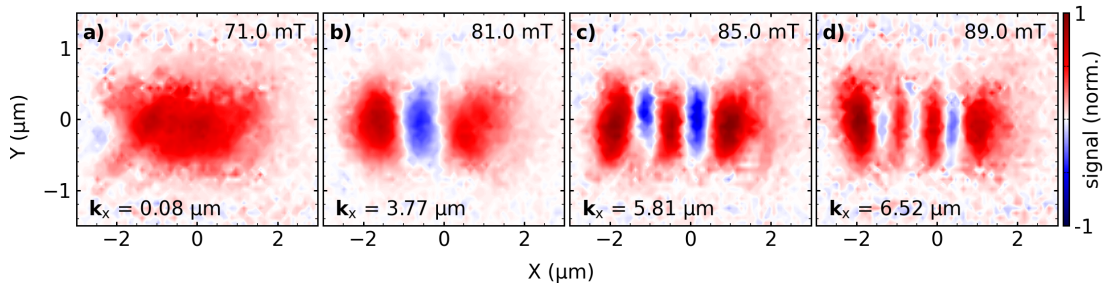


**Figure 5.5 | Spatially-resolved imaging of standing spin-wave modes in a transferred YIG platelet.** By using an IP rf-field at a frequency of 4 GHz different spin-wave modes can be identified. While panel a) shows a mostly uniform mode, corresponding to the main resonance, b)-d) present standing spin-wave modes in BV geometry.

The IP excitation field allows to excite different spin-wave modes at low rf-power levels of  $-25$  dBm at 4 GHz excitation frequency. The experimental findings obtained with SNS-MOKE are in agreement with micromagnetic simulations [30, 131]. As reported in reference [30] for similar transferred elements, a linewidth of  $195 \mu\text{T}$  was determined by means of SNS-MOKE, which means that the transfer process does not change the magnetic properties drastically. In addition, transferred YIG devices were investigated inductively at low temperatures [30]. Such experiments were not conceivable with YIG on top of its GGG substrate due to the large paramagnetic background in the low-temperature regime, which results in an enhanced damping [148, 149]. Indeed, these findings pave the way towards novel YIG-based magnonic experiments, e.g., in the field of hybrid quantum magnonics [36, 37, 150] or magneto-elastic driving of the magnetization dynamics [32, 33] (as demonstrated in chapter 6.3). Additionally, transferred YIG structures might be a suitable candidate for hosting non-linear phenomena since large precession angles can be easily achieved by strong IP rf-fields. In particular, odd half-integer NLSW in YIG were predicted [80].

---

# Surface acoustic Wave driven Spin Dynamics

---

After demonstrating the local measurement capabilities of the SNS-MOKE detection scheme in extended YIG layers and YIG microstructures excited by coplanar waveguide generated rf-fields, the following chapter covers a completely different excitation mechanism for magnonic applications. While the rf-current flowing across a CPW generates a magnetic field at radio frequencies which directly couples to the spin system via a Zeeman torque, the approach presented in this chapter exploits surface acoustic waves (SAWs) in combination with micron-sized ferromagnetic structures. SAW-based devices are known for decades and can be found in a variety of electrical applications as frequency filters or delay lines [82, 151]. Typically, devices using SAWs are grown on piezoelectric substrates and contain a pair of interdigital transducers (IDTs) [152]. These finger-like structures allow to launch and detect a SAW with defined frequency and wavelength traveling across millimeter distances between a pair of identical IDTs. This concept has been successfully transferred by Weiler *et al.* [32], and Dreher *et al.* [33] to the field of magnetism by performing vector network analyzer ferromagnetic resonance (VNA-FMR) experiments and developing a theoretical description of strain-induced magnetization dynamics caused by magneto-elastic coupling. The excitation scheme exploits the magneto-elasticity (inverse effect of magnetostriction [74]) of a magnetic material deposited on top of a SAW carrying substrate. The strain induced by the SAW can be considered as a dynamic anisotropy field [153] within the magnetic material leading to a dynamic driving at the rf-frequency determined by the SAW, as discussed in section 2.1. Over the years, this research field expanded and includes a variety of material systems [32, 34, 65, 154–157], excitation geometries [154, 158–160] and IDT designs [161–163]. Moreover, SAW-driven magnetization dynamics exhibit novel ways of investigating magnetic skyrmions [164] and magnon-phonon coupling in nanomagnets [165, 166]. However, most of the published results use low and rather uncommon frequencies for magnonic applications [163, 167–169] since the fabrication of high-frequency IDT structures requires high-resolution electron-beam lithography. For this purpose, higher harmonics of the fundamental IDT frequency are utilized in recent publications [34, 170, 171] to access spin dynamics above 4 GHz. Nevertheless, local properties of the SAW excited magnetization dynamics were only addressed in very few studies for low-frequency excitations [167, 172, 173]. Most of the experiments were performed with an inductive detection scheme by investigating the absorbed rf-power with the aid of a vector network analyzer (VNA) and a pair of identical IDTs [174, 175]. The experiments presented in

this chapter demonstrate the possibilities of coherent optical detection of SAW driven FMR in different material systems and offer a novel view on the magneto-elastic excitation scheme in a local fashion. Here, different higher harmonics of the IDT frequency are used to investigate SAW-driven magnetization dynamics allowing for a frequency-dependent analysis. First, in section 6.2 the characterization of a IDT structure is demonstrated, which is subsequently used to investigate Ni elements with different lateral dimensions. Spatially-resolved experiments are carried out to obtain further insight into the spin-wave spectrum excited due to magneto-elastic coupling. Finally, the SAW excitation concept is combined with the transfer process of YIG microstructures demonstrated in section 5.2. This combination of concepts allows for on-chip magneto-elastic excitations of low damping YIG structures giving rise to novel applications in future magnonics.

## 6.1. Measurement Concept

The first publications [32, 33] using the magneto-elastic coupling as the driving mechanism for magnetization dynamics utilized extended Ni layers on top of  $\text{LiNbO}_3$ . In these experiments, the absorbed rf-power transmitted via a delay line consisting of two identical IDTs is detected as a function of external bias field and field orientation. Here, we will verify the usability of optical measurements on such samples with the SNS-MOKE setup by exploiting the MOKE as probe technique, as depicted in Fig. 6.1.

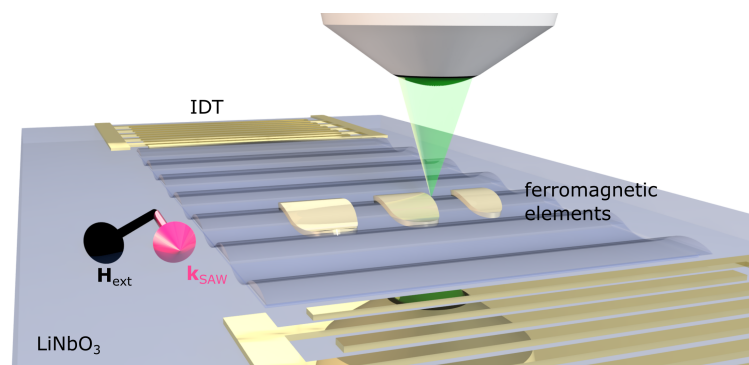


**Figure 6.1 | Illustrated sample geometry for magneto-elastic driving.** The IDT structure launches SAWs which propagate along the surface of the  $\text{LiNbO}_3$  substrate. The strain applied to the magnetic elements couples magneto-elastically to the magnetization and allows to excite spin dynamics. The IP magnetic field needs to be oriented in the most favorable fashion with respect to the wave vector of the SAW.

In all presented measurements in this section the thickness of the Ni elements is 35 nm. The Ni elements and the IDTs were defined by using individual electron-beam lithography steps.

### 6.1.1. Surface acoustic Wave Generation by interdigital Transducers

As introduced, SAW-based devices are an intensively studied topic due to their applicability in microelectronics and telecommunication technology [82, 151]. Hence, the design rules for IDTs with a given base frequency are well known [35]. Different design approaches are possible, either resulting in a very efficient conversion between the applied electrical signal and the SAW at the fundamental frequency or leading to different transmissions bands at higher harmonics of the design frequency. The dimensions of the IDT structures in combination with the piezoelectric properties of the used material define the fundamental wave vector of the propagating SAW and thus the frequency of the IDT.

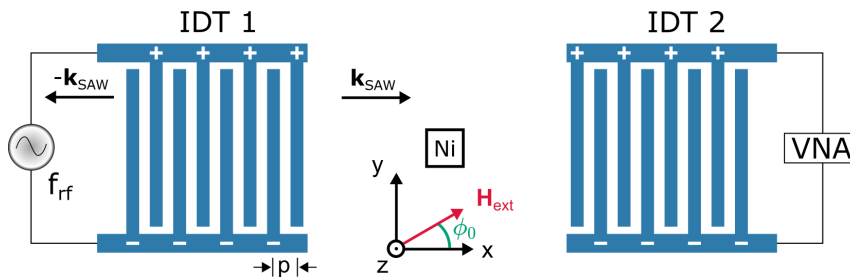


**Figure 6.2 | Schematic of an interdigital transducer structure for SAW excitation.** A pair of identical bidirectional single-electrode IDTs is used to launch and detect the SAW. While the SAW travels across the piezoelectric substrate it can magneto-elastically couple to the magnetization of a ferromagnetic element. The angle  $\phi_0$  denotes the angle between  $\mathbf{M}$  and  $\mathbf{k}_{\text{SAW}}$ .

The most common IDT layout is a bidirectional single-electrode IDT [152], which means that the SAW is launched in both directions symmetrically. Such a design of a IDT structure is depicted in Fig. 6.2a), where the metalization ratio is chosen to be 50:50. Here, the wavelength of the SAW (at its fundamental frequency) is defined by two times the pitch distance  $p$ :  $v/f_{\text{SAW}} = \lambda_{\text{SAW}} = 2p$ , where  $f_{\text{SAW}}$  is the IDT frequency and  $v$  the sound velocity of a given type of SAW for the utilized piezoelectric substrate. In this geometry, higher odd harmonics due to the rectangular excitation profile are not explicitly suppressed, and thus accessible in the experiments. However, depending on the piezoelectric substrate, the nature of the traveling SAW can be different [171]. The two prominent types of SAWs are Rayleigh waves [176] and Love waves [82], which differ in their strain components and velocities. Rayleigh waves contain longitudinal (in  $x$ -direction) and transversal (in  $z$ -direction) strain components which result in non-vanishing strain tensor components  $\epsilon_{xx}$ ,  $\epsilon_{xz}$  and  $\epsilon_{zz}$  (introduced in section 2.1.2). Pure Rayleigh waves have no shear components in  $y$ -direction. In contrast to that, Love waves have dominant transversal shear components with  $\epsilon_{xy} \neq 0$ . Due to the involved strain components in the magneto-elastic excitation, both surface waves access different parts of the spin-wave manifold. Typically,  $yz$ -cut  $\text{LiNbO}_3$  is used in experiments to launch Rayleigh waves. As presented by Weiler *et al.* [32], Rayleigh waves typically lead to enhanced coupling of the SAW to the magnetization dynamics as the orientation between  $\mathbf{M}$  and  $\mathbf{k}_{\text{SAW}}$  is on the order of

$\phi_0 = 45^\circ$ . In contrast to that, Love waves couple most effectively for  $\phi_0 = 0^\circ$  and  $90^\circ$ , as demonstrated by Küss *et al.* [171].

### Characterization of the interdigital Transducers

The transmission characteristics of a pair of IDTs can be obtained in different ways: Whereas the most common approach is a transmission measurement with a VNA, which allows determining the fundamental frequency of the IDT and its higher harmonics. Such a measurement is shown in Fig. 6.3a). Here, the time-gating functionality of the VNA [177] is utilized, which allows distinguishing the electromagnetic crosstalk between the IDTs as well as transient signals and slower signals by the SAW due to their different propagation speeds. The propagation speed of a Rayleigh wave on the used  $\text{LiNbO}_3$  is  $3488 \text{ m s}^{-1}$  [178]. This approach requires a pair of identical IDTs to launch and detect the SAW, and due to non-perfect fabrication or damages in one of the IDTs this method is not in any case applicable. A different way is to exploit the strain-induced birefringence detected by SNS-MOKE without field modulation. In this case, the amplitude of the strain-induced background signal depends on the frequency applied to the IDT and thus, the frequency of the rf-source can be tuned while the amplitude of the SNS-MOKE signal is recorded. This detection scheme allows obtaining the fundamental frequencies of the IDT as well as higher odd harmonics, as demonstrated in Fig. 6.3b).

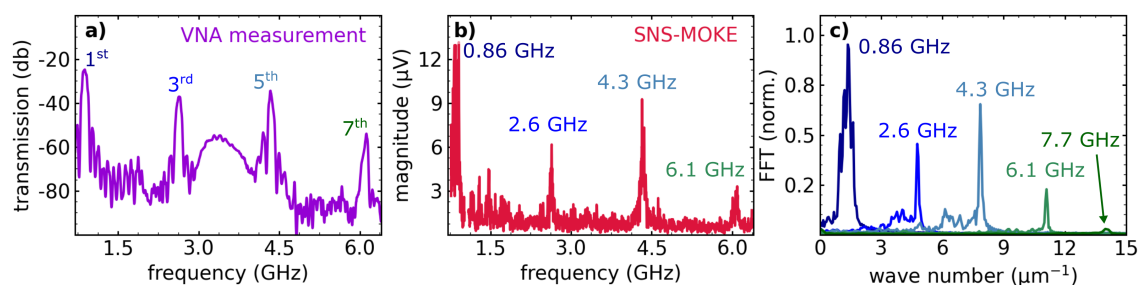


**Figure 6.3 | Characterization of the interdigital transducer.** VNA transmission through a pair of IDTs as a function of frequency is shown in a). To avoid electromagnetic crosstalk a time-gating window was utilized. Panel b) shows frequency-resolved SNS-MOKE measurements of the strain-induced birefringence on the substrate in between the two IDTs. In both techniques the fundamental frequency and three higher odd harmonics are visible. In c) the FFT spectra of spatially-resolved measurements of the strain-induced birefringence for five different frequency components is presented.

To further utilize the SNS-MOKE technique for characterizing the IDT structures, spatially-resolved imaging of the strain-induced birefringence reveals the wave vector of the propagating SAW. The extracted Fourier spectra of these images are shown in panel c). Surprisingly, in contrast to VNA and frequency-resolved SNS-MOKE measurements, here, an additional frequency component at 7.8 GHz is revealed. The magnitude of this birefringent component is on the order of the noise floor but appears clearly in a spatially resolved map. This characterization shows that SAW driven magnetization dynamic is feasible in five different frequency bands

with the used IDT structures, while each frequency band hosts a different wave vector of the propagating SAW. Therefore, depending on the applied frequency, a wave-vector dependent analysis of the SAW-driven magnetization dynamics becomes possible.

### 6.1.2. Strain-induced Birefringence

In the experiments discussed so far, a dynamic Kerr rotation only occurs in the case of magnetic excitations. However, in the magneto-elastic excitation geometry, an additional rotation of the reflected light can be detected on the entire substrate where the SAW propagates. The magnitude of this rotation component strongly depends on the lateral position and the conversion efficiency of rf-power to the propagating SAW. This additional effect arises from the piezoelectric properties of the LiNbO<sub>3</sub> substrate in combination with the birefringence caused by the propagating SAW [179]. Here, the SAW launched by the IDT via the piezoelectric effect has a wavelength of a few micrometers, defined by the IDT pitch distance. On this length-scale the birefringence of the substrate is modulated by the varying strain caused by the SAW leading to a tiny modulation of the detected signal at the excitation's alias frequency. As depicted in section 3.2.2, one of the major advantages of the SNS-MOKE technique is the fact that no additional modulation is required to obtain a signal detected at a matching alias frequency. However, for some experimental configurations, it is helpful to extend the scheme in a way that SNS-MOKE and field-modulated measurements (cf. Fig. 3.1c)) become possible at the same time. In the particular case of SAW-driven FMR experiments, an additional field modulation is strongly required since the SNS-MOKE detection scheme is sensitive to dynamic changes in the polarization state of the reflected light [179]. Thus a superposition of magnetic and non-magnetic signal contribution is expected in the SNS-MOKE detection channel. Both signal components can be disentangled by using a modification of the SNS-MOKE scheme with an additional field modulation in the frequency regime of 1 kHz. This modulation results in the formation of sidebands next to the rf-excitation (as depicted in Fig. 3.1c)). The purely field-dependent signal components in the sidebands mix with the frequency comb of the short laser pulse. Thus, additional alias frequencies can be obtained as sidebands of the lowest-order alias frequency, as shown in Fig. 3.1c). The demodulation frequency  $\varepsilon$  of the purely field-dependent signal components can be derived via

$$\varepsilon = |f_{\text{rf}} - n \cdot f_{\text{rep}}| \pm f_{\text{mod}} = f_{\text{SNS}} \pm f_{\text{mod}}, \quad (6.1)$$

where  $f_{\text{mod}}$  is the additional modulation frequency. By utilizing a multi-frequency LIA simultaneous demodulation at different frequencies is achieved, e.g., at  $f_{\text{SNS}}$  and  $f_{\text{SNS}} + f_{\text{mod}}$ . Thus the separation of magnetic signal and strain-induced background is feasible which we demonstrate by performing a spatially-resolved measurement on one of the Ni elements.

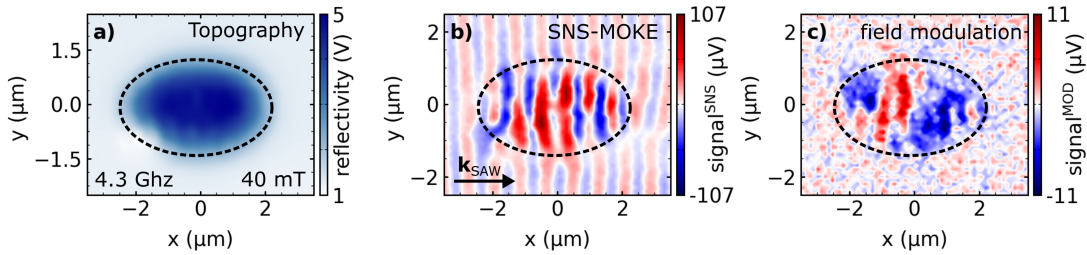


**Figure 6.4 | Spatially-resolved imaging of SAW driven dynamics with additional field modulation**

In panel a) the topography of the element is shown. In b) SNS-MOKE measurements offer a large strain-induced background due to the propagation of the SAW superimposing the magnetic signal within the ferromagnetic element. The additional field modulation is applied in c) to decompose the signal components and obtain only the magnetic part of the signal.

The topography of the element is depicted in Fig. 6.4a) and thus magnetic signals under resonance condition are solely expected within the element's lateral dimensions. However, one can see in Fig. 6.4b) that the strain-induced birefringence covers the entire substrate as the SAW propagates. In this particular case, the ferromagnetic element shows an enhanced dynamic signal at this frequency, but it is superimposed with a birefringent background. Indeed, an additional field modulation strongly suppresses the background signal, as can be seen in Fig. 6.4c), while a field-dependent signal in the Ni element persists. The remaining signal obtained in Fig. 6.4c), albeit of purely magnetic nature, mimics the wave vector of the SAW. Two possible explanations for the existence of this wave-vector component are thinkable: The first is due to the back-action of the excited magnetization dynamics on the SAW [33], which might result in a field-dependent phase shift or change in magnitude. Another explanation might be that the dynamics are directly driven at this wave vector and other wave-vector components result from internal magnon-scattering processes. This question can not be answered entirely but will be further addressed in section 6.2.2 and 6.3.4.

### SNS-MOKE Detection of SAW-driven FMR

The concept of SAW-driven FMR is depicted in Fig. 6.1 containing a pair of IDTs structured on a piezoelectric substrate and ferromagnetic elements in between. The external magnetic field can be rotated in the plane of the sample. For a Ni element on top of a  $\text{LiNbO}_3$  a field-dependent spectrum contains a background signal of several  $\mu\text{V}$  as shown in Fig. 6.5a) which appears to be mostly independent of the applied field. This strain-induced background can be suppressed by simultaneous detection on one of the field-modulated sidebands, as shown in panel b). Note that the modulation strength of the field can be used to enhance the magnetic signal components but might also broaden the SAW-driven FMR linewidth when the modulation strength is chosen too large.

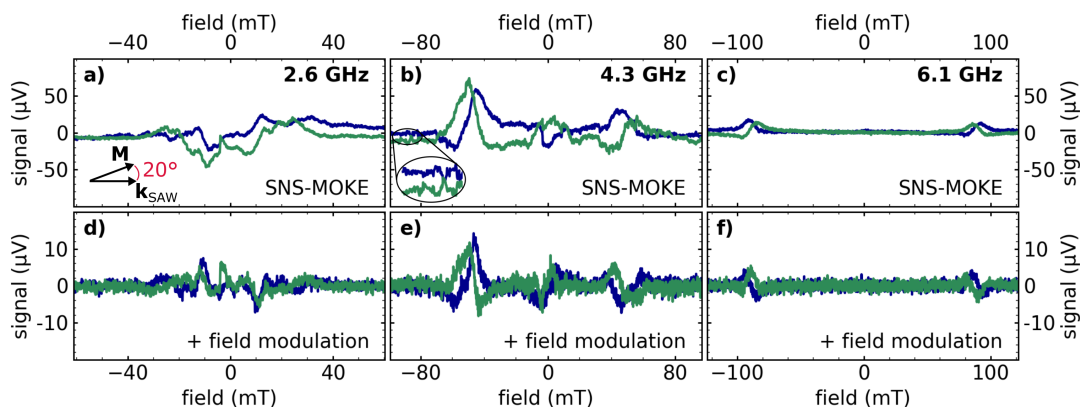


**Figure 6.5 | Field-swept spectra of SAW-driven FMR in Ni elements.** a)-c) SNS-MOKE measurements in a  $10\ \mu\text{m} \times 5\ \mu\text{m}$  elliptical Ni element at three different IDT harmonics. The field is oriented  $20^\circ$  with respect to the SAW propagation direction. Besides strong resonant features a mostly field independent background signal is obtained, as indicated by the magnified region in b). By utilizing an additional field modulation only magnetic components persists in the spectra as shown in d)-e).

Here, the additional field modulation allows further insight into the signals' origin and facilitates spatially-resolved imaging without a strain-induced background in the following experiments. The next section will first focus on an element size-dependent investigation and compare the obtained results to theoretical predictions from Dreher *et al.* [33].

## 6.2. SAW-driven Dynamics in Nickel Structures

In the following, we utilize SNS-MOKE to investigate SAW-driven magnetization dynamics in a similar fashion as demonstrated in previous publications by Weiler *et al.* [32]. Therefore, measurements such as shown in Fig. 6.5 were carried out in an angular-resolved manner to identify the angular orientation  $\phi_0$  of the most effective coupling of the SAW to the magnetization dynamics within the element. These findings give the possibility to go beyond the conventional electrical detection methods since the optical setup allows for spatially-resolved detection of the excited dynamics within individual micron-sized elements.

### 6.2.1. Angular-resolved Measurements

The depicted IP field orientation of  $20^\circ$  in Fig. 6.5 implies that the field orientation plays an essential role for the SAW-driven excitation, as depicted in equation 2.8. By varying the IP orientation of the magnetic field, different branches in the spin-wave manifold become accessible, which results in essential changes of the dipolar spin waves' nature. The field amplitude and IP orientation-dependent SAW-driven FMR was experimentally and theoretically investigated by

Dreher *et al.* [33] for the case of an extended Ni layer. In their experimental work, a VNA was utilized to obtain changes in transmitted power through a pair of identical IDT antennas. They observe an increased absorption of rf-power for field orientations nearly parallel to the SAW's propagation wave vector. However, they obtained a slight deviation between experimental results and theoretical prediction for IP oriented fields. In their experiments, the obtained SAW-driven resonances shift towards larger bias fields for higher frequencies - as expected - but broaden significantly and persist at angular field orientations close to the propagation direction of the SAW (on the order of  $10^\circ$ - $20^\circ$ ). In contrast to that, their model predicts less broadened resonances and an enhanced signal located at  $45^\circ$  orientation, where the coupling of the Rayleigh wave to the spin system is maximum [34]. This phenomenon is most pronounced for frequencies around 2.5 GHz and requires further experimental investigation. One possibility for this mismatch might emerge from long-range dipolar fields in extended layer structures, which give rise to changes of the spin-wave manifold.

### Influence of the Element's Size

To validate the assumption that dipolar fields in extended layers are causing the mentioned features, the experiments presented in this thesis will evaluate the angular-resolved field-dependent spectra for varying lateral element sizes as well as for different SAW frequencies. By imaging the obtained data sets as a function of field orientation and amplitude in a two-dimensional map, a comparison to previously published results is possible.

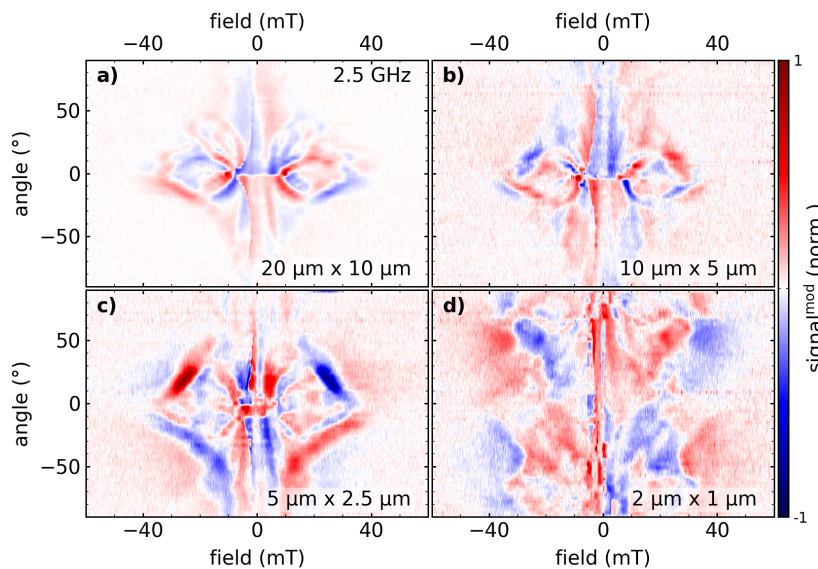


**Figure 6.6 | Angular-resolved SAW-driven magnetization dynamics in different element geometries.** Field-swept measurements analyzed at the modulation frequency are shown for different orientations of the external magnetic field. The size of the investigated elliptical elements is reduced from  $20\ \mu\text{m} \times 10\ \mu\text{m}$  in a) down to  $2\ \mu\text{m} \times 1\ \mu\text{m}$  in d), which results in a different shape of the obtained fourfold symmetry.

Figure 6.6 presents the angular-resolved field-swept spectra of four investigated element dimensions at a fixed excitation frequency of 2.5 GHz. In the case of a  $20\ \mu\text{m} \times 10\ \mu\text{m}$  elliptical-shaped element, the resonances are located close to the  $0^\circ$  axis and fade out for larger angles, as shown in Fig. 6.6a). This observation corresponds to the findings from Dreher *et al.* [33] for an extended Ni layer excited at a similar SAW frequency which points out that these are not measurement artifacts due to the integrating nature of the measurements technique they used but also persists in truly local measurements. Interestingly, the obtained resonance positions shift towards larger angular orientations for smaller element sizes at the same driving frequency, as seen in b) and c). The  $2\ \mu\text{m} \times 1\ \mu\text{m}$  element shown in Fig. 6.6d) provides resonant features over a broad range of field orientations with a maximum around  $\pm 50^\circ$ . Surprisingly, this obtained fourfold symmetry for small elements matches the prediction made by Dreher *et al.* for similar frequencies where the dipole interaction is not taken into account [33]. Thus, the assumption of long-range dipolar fields forcing the resonance position towards the  $0^\circ$  axis is emphasized because their impact is reduced by shrinking element geometry, even at low frequencies.

### Angular-resolved Experiments with different IDT Harmonics

Another approach to overcome the contributions caused by dipolar fields is to increase the frequency of the SAW which also changes the wave vector of the excitation. As shown in recent publications [34, 170, 171], a frequency above 4 GHz results in an angular-resolved pattern matching the predicted  $45^\circ$  fourfold symmetry for pure Rayleigh wave excitations very precisely. Therefore, angular-resolved measurements for different harmonic frequencies of the IDT (cf. Fig. 6.3) were carried out and compared.

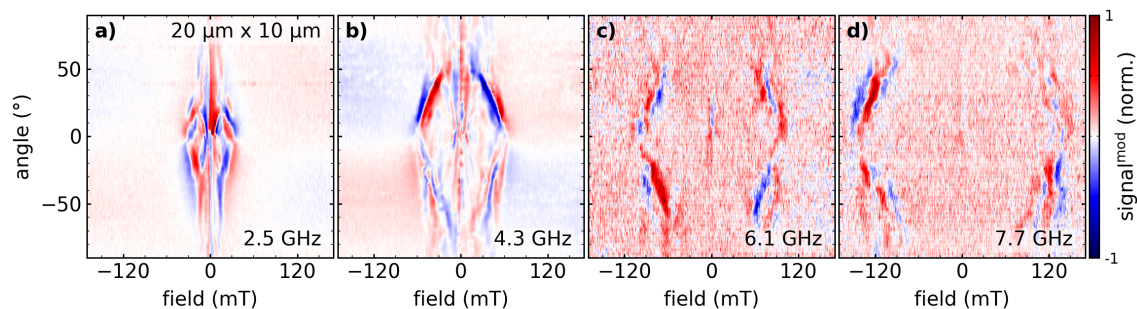


**Figure 6.7 | Angular-resolved SAW-driven magnetization dynamics as function of frequency.** Field-swept measurements at different angular orientations are shown for four harmonics of the IDT fundamental frequency, corresponding to different wavelengths of the SAW.

As shown in Fig. 6.7a), the 2.5 GHz excitation within a  $20\ \mu\text{m} \times 10\ \mu\text{m}$  element is in agreement with extended film data in this frequency regime for Ni [32, 156] as well as other materials for similar frequencies [168]. However, for an increased frequency, as shown in panel b), the

resonances shift towards larger field amplitudes as well as to slightly larger angular orientations. This observed effect is further enhanced for 6.2 GHz and 7.8 GHz shown in c) and d), respectively. In this case, signal components close to 0 mT completely vanish while the resonances at larger field values persist. The increased noise level in c) and d) is due to the weaker excitation of the SAW, as demonstrated in Fig. 6.3. Moreover, it seems that the amplitude in the four quadrants for higher frequencies is not perfectly symmetric anymore. Such behavior might be caused by phase shifts between the contributing strain components [33]. From this angular-resolved investigation of different sample geometries, we confirmed previous publications and revealed that dipolar fields might cause the mismatch of experimental data and theoretical prediction for low SAW frequencies and large element geometries. Only recently, angular-resolved experiments in extended Ni films by Gowtham *et al.* [170] and Küß *et al.* [34] reveal that for excitation frequency above 4 GHz the described deviation vanishes and the theoretical model fits the observations, which is in agreement with our results for large rf-frequencies. In addition, Küß *et al.* [171] implemented dipolar fields into the model introduced by Dreher *et al.* [33] to ensure valid predictions for lower frequency excitations. In the following, our findings allow for a detailed spatially-resolved analysis of the different element geometries and the excited wave-vector components within the Ni elements.

### 6.2.2. Spatially-resolved Imaging of SAW-driven Spin Dynamics

The demonstrated possibility of performing measurements at the SNS frequency as well as at field-modulated sidebands emphasizes the advantage of SNS-MOKE for the spatially-resolved imaging of spin waves driven by SAWs. In the following, spatially-resolved measurements with both simultaneously detected signal contributions were performed to identify the efficiency of the field-modulation technique in order to suppress the strain-induced birefringent background.

#### Imaging of different Element Geometries under equivalent Conditions

Before proceeding with the wave-vector analysis, a more detailed view on the influence of the element size is required. From angular-resolved imaging (cf. Fig. 6.6) we know, that the signals are distributed at different angular orientations depending on the element's size. We assume that the obtained intensity in the images will be different, but it is unclear if this affects the obtained wave-vector spectrum. Therefore, we first compare spatially-resolved images in four element geometries under the same experimental conditions, as shown in Fig. 6.8.

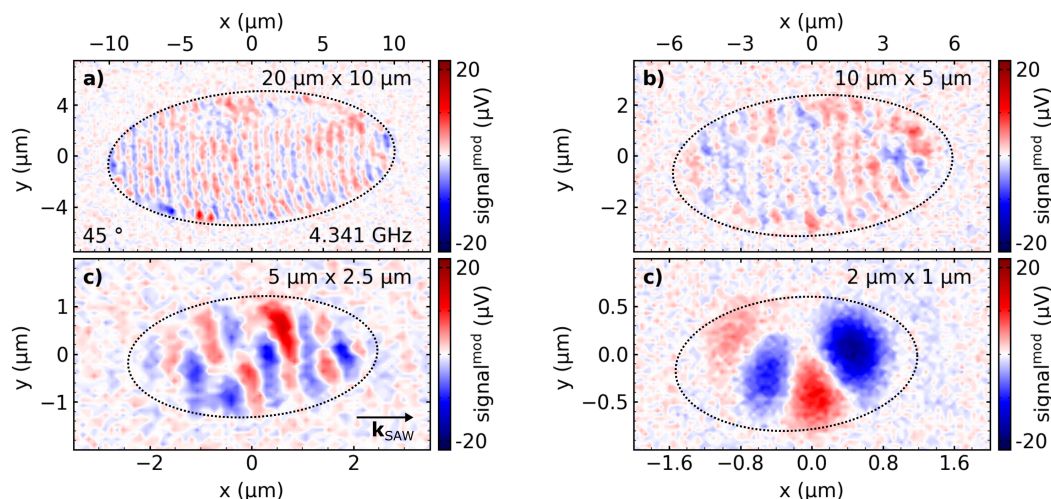


**Figure 6.8 | Spatially-resolved imaging of SAW-driven dynamics in different element geometries.** The signal components of magnetic origin are recorded in a point-wise fashion. All images were taken at 4.3 GHz and a fixed bias field of 55 mT. The external magnetic field is aligned in  $45^\circ$  orientation. The  $20\ \mu\text{m} \times 10\ \mu\text{m}$  elliptical element in a) has a smaller signal amplitude, compared to the small  $2\ \mu\text{m} \times 1\ \mu\text{m}$  element in d).

The images of the magnetic signal components were obtained with a field orientation of  $45^\circ$  with respect to the propagating SAW. As expected from Fig. 6.6, the coupling efficiency in this geometry results in a larger signal component in the smallest element in d), compared to the  $20\ \mu\text{m} \times 10\ \mu\text{m}$  elliptical element in a). In particular, the chosen field orientation does not match the resonance condition of the largest element, as shown in Fig. 6.6a). Surprisingly, in all geometries, the obtained spin-wave image contains a wave-vector component which appears as the one of the SAW. In contrast to the pure SNS-MOKE signal, this wave-vector pattern only exists within the element dimensions, meaning that its origin is magnetic. Besides this, it appears that additional wave-vector components appear, but they seem to vary stronger between the elements, as discussed in the following by utilizing 2D-FFT.

### Imaging at different Field Orientations

Therefore, the appearance of the different wave-vector components is investigated for the  $5\ \mu\text{m} \times 2.5\ \mu\text{m}$  ellipse in more detail by performing spatially-resolved imaging at different field amplitudes and field orientation angles. Two clear statements arise from this experiment shown in Fig. 6.9. First, the obtained signal intensities of wave-vector components clearly corresponding to the SAW depend on the external field amplitude and its IP orientation. For example, at  $-55^\circ$  and 35 mT shown in Fig. 6.9a) a strong signal which contains the wave vector of the SAW is obtained, but for an increased field of 65 mT as presented in d) the amplitude of the excited dynamics is strongly reduced. For the same field amplitudes but an IP field angle of  $-15^\circ$  the signal is further reduced, as shown in q) and t). In pure SNS-MOKE detection, these tiny changes are superimposed by the birefringent background.

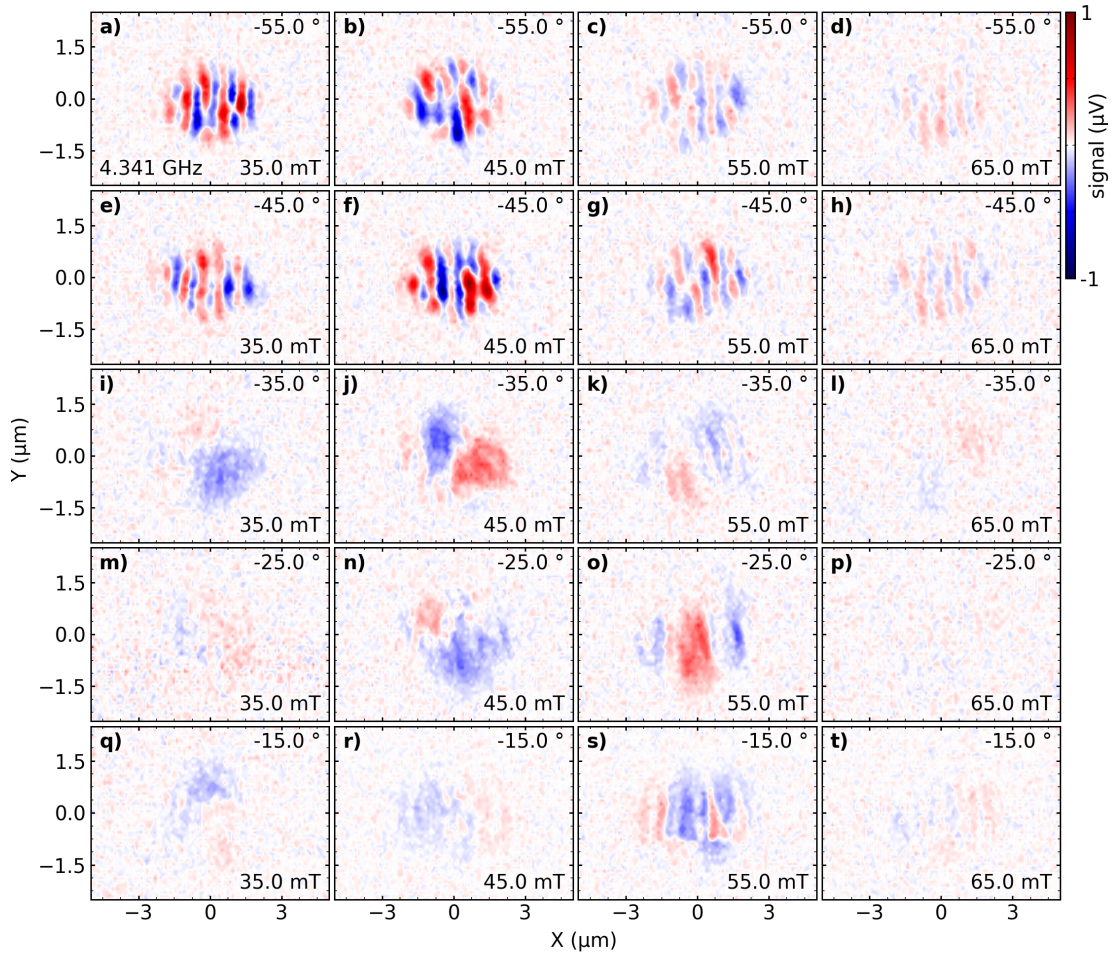


**Figure 6.9 | Spatially-resolved imaging at different field amplitudes and IP orientations.** For different field amplitudes (rows) and angular orientations (columns) the spatially-resolved response in the field-modulation channel is shown for a  $5\ \mu\text{m} \times 2.5\ \mu\text{m}$  elliptical element. The excitation frequency is 4.3 GHz.

The second observation besides the very pronounced wave vector of the SAW in some measurements (i.e. a), b), e) and f)) for large field angles, is that other components dominate the excitation in the lower angle regime, as obtained in j), k), n) and o). One has to mention that at least for large element geometries, the separation of magnetic and SAW based signal is not achievable as easy as expected. As reported by Dreher *et al.* [33], the equations of motion for strain waves and magnetization dynamics are coupled, which results in a back-action of the magnetization on the propagating SAW. In this particular case, the excited magnetization will dynamically influence the properties of the SAW, and thus the SAW contains a field-dependent component. By utilizing the field modulation as described, only signal components are detected, which change with the magnetic field. Therefore the field-independent SAW outside the ferromagnetic element is suppressed, but these signal components persist within the element as the magnetization acts back on the propagating strain wave.

Besides the wave-vector component corresponding to the one of the SAW, different wave vectors due to strain-induced magnetic excitations can be identified in Fig. 6.9. In the configuration of  $-45^\circ$  or  $-55^\circ$  relative to the SAW's propagation, additional magnetic contributions with larger wavelength are obtained. These excitations become dominant at  $-35^\circ$  and  $-25^\circ$  in the investigated  $5\ \mu\text{m} \times 2.5\ \mu\text{m}$  elliptical-shaped element at 4.3 GHz and reduce in intensity for even smaller IP angles over the entire field range. In addition to the change in intensity, the wave-vector distribution itself changes with the IP field rotation. Furthermore, it appears as if the long-wavelength component are aligned with the external magnetic field. This we further analyzed in appendix A.4 for an extended Co patch. Similar behavior is also observed for larger sample geometries, as shown as a 2D-FFT in Fig. 6.10 for a  $20\ \mu\text{m} \times 10\ \mu\text{m}$  elliptical element. Here, the described features experience the strongest excitation at smaller angular orientations, while a rotation of the large-wavelength dipolar components with field orientation is revealed.

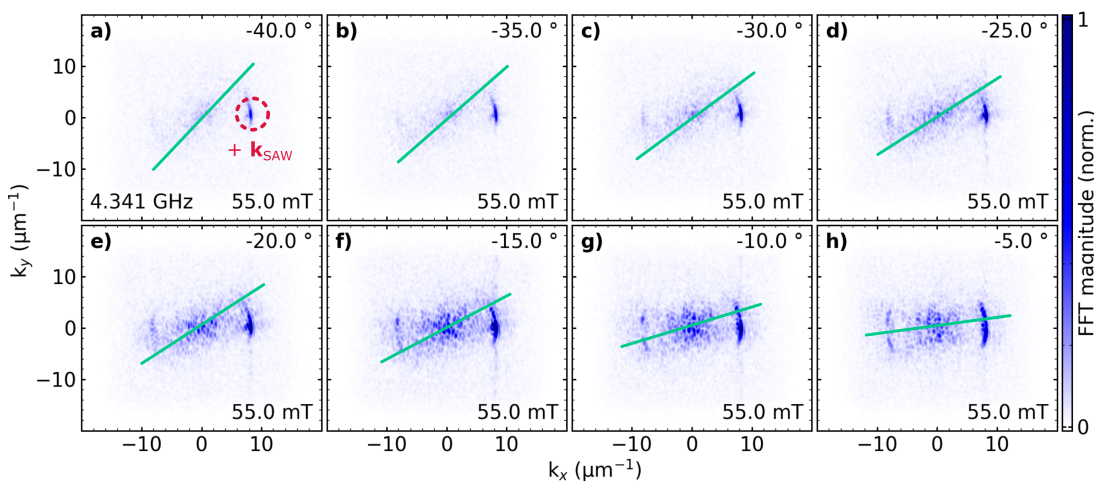


**Figure 6.10 | Wave-vector spectra of SAW-driven dynamics in the  $20\ \mu\text{m} \times 10\ \mu\text{m}$  ellipse with a fixed bias field and varying angular orientations.** 2D-FFT of the spatially-resolved measurements obtained in a  $20\ \mu\text{m} \times 10\ \mu\text{m}$  elliptical element at fixed bias field of 55 mT are shown for varying angular orientations of the IP bias field. The red circles indicate the wave-vector component belonging to the SAW. As a guide for the eye, a green solid line indicates a magnetization component which aligns with the external field direction.

While it is hard to judge if either the SAW drives the magnetization with the same wave vector or the excited magnetization influences the propagation properties of the SAW, the conversion of the SAW's wave vector to different components in  $k$ -space can be clearly identified. This conversion might be mediated by either a broken lateral translational invariance in micron-sized structures or magnon-magnon scattering effects.

The experimental findings from the first part of this chapter are reproducing previous findings from literature for SAW-driven magnetization dynamics in nickel films. Moreover, it is remarkable that the literature's predictions mostly fit the results for tiny sample geometries. For larger element dimensions, strain-induced magnetization dynamics occur only for angular orientations of the magnetic field close to the propagation direction of the SAW. Here, the different sample geometries allow linking the effect to long-range dipolar fields. Furthermore, obtained resonances in large sample geometries broaden in the small frequency range [163, 174] and thus, analysis in terms of damping becomes challenging. Unfortunately, most publications present SAW-driven FMR experiments only for frequencies below 2.5 GHz in extended films. These experiments are mostly limited to the dipolar-field dominated regime and suffer from line broadening. Only a few recent publications [170, 171] contain excitation frequencies far above 4 GHz indicating that higher excitation frequencies help to overcome limitations of the dipolar regime, as presented for small element sizes as well as for large rf-frequencies in this work. In addition to these results, the spatially-resolved investigations by SNS-MOKE allows us to analyze the wave-vector spectrum within the ferromagnetic elements up to frequencies of 8 GHz and thus offers an entirely novel approach of studying spin waves driven by magneto-elastic excitations in contrast to conventional VNA-FMR experiments. The SNS-MOKE further yields the possibility of distinguishing between effects appearing at the excitation wavelength of the SAW and additional wave-vector components which tend to align with the external magnetic bias field and have an imprint of DE or BV-like spin waves. In the future, these findings require theoretical support to be understood in detail, while further experiments in small sample geometries and high excitation frequencies are desirable to highlight the applicability of SAW driven magnetization dynamics for future spintronic and magnonic devices.

### 6.3. SAW-driven FMR in transferred YIG Structures

As pointed out in the previous chapters, due to its exceptional low Gilbert damping parameter yttrium iron garnet is one of the most suitable material systems for magnonic and spintronic applications. The possibility of performing local investigations of SAW-driven dynamics, such as shown in section 6.2, in high-quality micron-sized YIG structures, would extend the scope of this excitation scheme towards novel applications for future technologies. Unfortunately, successful direct growth of high-quality YIG on a suitable piezoelectric substrate such as  $\text{LiNbO}_3$  has not been reported so far [131]. The lattice mismatch impairs the desired quality of YIG structures grown on other substrates than GGG. Even the room-temperature PLD growth process introduced by Heyroth *et al.* [31] did not provide sufficient quality for direct growth of YIG devices on top of a piezoelectric substrate used for SAW excitation. One reason is due to the different thermal expansion coefficients of the substrate in contrast to YIG, and thus additional stress is applied during crystallization which might cause defects [131]. In addition, due to the lattice mismatch of the substrate and YIG additional small-angle grain boundaries

appear in the span [131]. SAW-driven FMR experiments in YIG were so far only performed below 10 MHz by Uchida *et al.* [154] or in hybrid devices, where a YIG layer grown on GGG is attached face-down on the SAW carrying substrate by Kryshnal *et al.* [159, 160, 180]. However, as a consequence of the successfully demonstrated transfer of low damping YIG microstructures [30] (cf. section 5.2), the utilization of mechanical excitations in such micron-sized YIG elements will emerge in a variety of new experiments which were not conceivable before.

### 6.3.1. Sample Layout and IDT Characteristics

To allow for a novel excitation type of magnetization dynamics in YIG, we utilized the transfer process explained in section 5.2 and attached a single YIG element to a *yz*-cut LiNbO<sub>3</sub> substrate, which allows hosting SAWs with the same properties as used in section 6.2. Further details about the growth and transfer processes of the YIG platelet can be found in the thesis of Philip Trempler [131]. The transfer was performed for two different orientations of the YIG platelet relative to the wave vector of the propagating SAW, namely 0° and 60°. In both cases, the lateral dimension of the transferred structure is 3.6 μm × 1.5 μm while the thickness of the platelet is 160 nm. The platelet was fixed with AlO<sub>x</sub> to provide a good mechanical coupling of the SAW to the YIG. The IDT characterization was performed by using SNS-MOKE and reveals the following frequencies and corresponding wave vectors. Since only one IDT is usable in this sample, no additional VNA characterization was carried out.

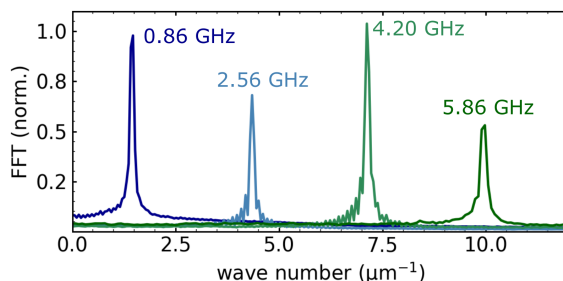


**Figure 6.11 | Wave-vector spectrum of the IDT structure at different frequencies.** By performing spatially-resolved imaging of the strain-induced birefringence the wave-vector spectrum of the IDT structure is extracted. Four discrete frequencies with different wave vectors allow for magneto-elastic excitation of the YIG device. The wavelength of the SAW ranges from 4.3 μm at the IDT fundamental frequency down to 0.63 μm at 5.86 GHz.

### 6.3.2. Spin-Wave Spectra for different IDT Harmonics

In the following, magneto-elastically driving of the magnetization dynamics (cf. section 6.2) is investigated in one of the transferred high-quality YIG elements introduced in chapter 5 by means of SNS-MOKE. The investigated structure is aligned parallel with respect to the

SAW's propagation direction. Here, the excitation frequency was set to odd harmonics of the IDT fundamental frequency (as obtained in Fig. 6.11), and field-swept measurements were carried out. For this purpose, the laser spot is centered on the investigated YIG structure and stabilized in its lateral position. In this measurement, the field is applied in the direction of SAW's propagation.

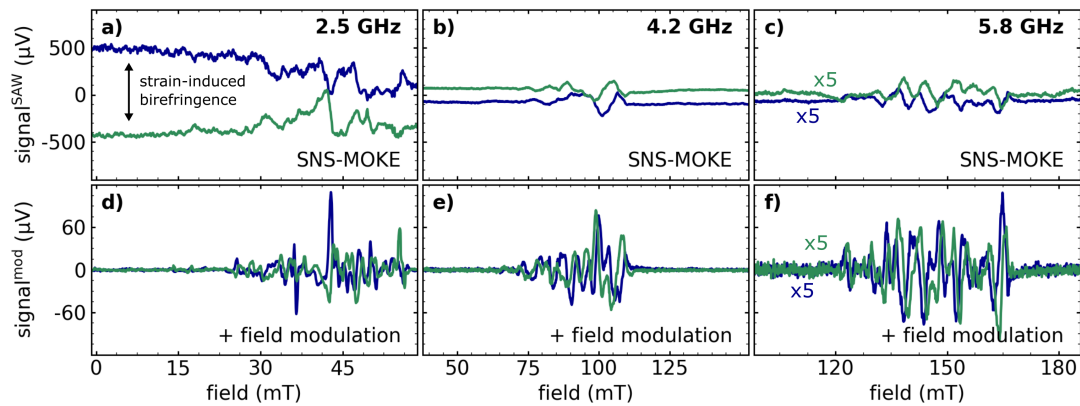


**Figure 6.12 | SAW-driven magnetization dynamics in a YIG microstructure.** Detection of SAW-driven dynamics at different harmonics of the IDT obtained in  $0^\circ$  magnetic field orientation. Panel a)-c) depict the SNS-MOKE detection including a strong strain-induced birefringence component. By applying field modulation only magnetic components persist as shown in d)-f).

The micron-sized YIG element shows strong signal components at different odd harmonics of the IDT fundamental frequency obtained in  $0^\circ$  orientation of the external bias field. In addition, a mostly field independent strain-induced background becomes visible in Fig. 6.12a)-c) with similar signal intensity as the magnetic components, as expected from section 6.1.2. By applying the field modulation, only the magnetic contributions persist, and the signal reveals a variety of different magnetic modes precessing within the YIG element. At first glance, it seems surprising that even in  $0^\circ$  orientation, large signal components appear, since the coupling of Rayleigh waves is most efficient at  $45^\circ$  orientation of the external field [33]. In contrast, Love waves couple to the magnetization aligned along  $0^\circ$  and  $90^\circ$  [171]. Thus, one explanation would be that the Rayleigh wave converts its strain components to shear components within the pedestals or the bridge. Moreover, the experimental findings for small Ni elements indicated that the driven dynamics in the most minor structures cover a broad range of angular orientations, which might further contribute to the broad spectrum obtained in transferred YIG elements.

### 6.3.3. Angular-resolved Measurements

From initial experiments in section 6.2 for small element dimensions and the theoretical description [32, 33] of magneto-elastic coupling, one would expect a fourfold symmetry of the

obtained resonances for SAW driven FMR experiments in small YIG elements. This assumption might be valid for ferromagnetic layers directly grown on the SAW carrying substrate. In such a case, a pure Rayleigh wave results in the described fourfold symmetry [33]. In the particular case of a transferred YIG platelet attached to two separated AlOx pedestals, the mechanical coupling of the Rayleigh wave might be different and results in additional shear and torsion components [131]. These components could give rise to different strain components leading to a more complex excitation configuration. Therefore, a more detailed view on the angular-resolved spectrum is essential for further experiments.

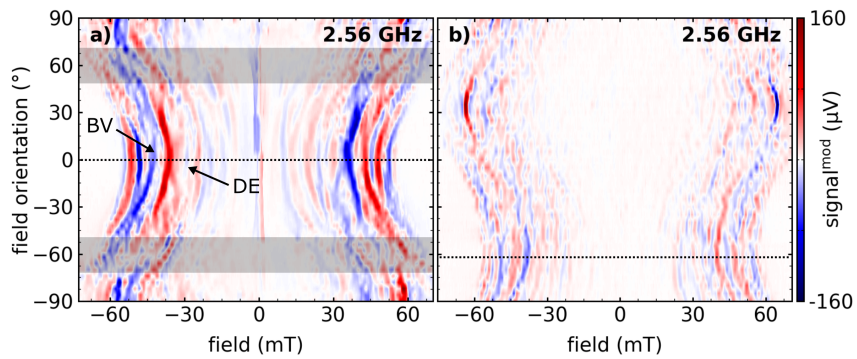


**Figure 6.13 | Angular-resolved measurements of SAW-driven dynamics in two different YIG elements.** The field-modulated SNS-MOKE signal of field-swept measurements performed at different angular orientations is shown for two different orientations of the YIG platelet relative to the wave vector of the SAW. In a) the easy axis of the bridge is aligned parallel to the propagation direction of the SAW, while in b) the bridge is rotated by  $60^\circ$ . The gray areas in a) indicate the regions of suppressed spin-wave excitation within the element. On the lower field side, DE spin waves are expected, while the strong signal components at larger bias fields belong to BV-like modes.

By performing angular-resolved field-swept measurements, in all orientations, signal components are obtained in the field-modulated SNS-MOKE signal, as demonstrated in Fig. 6.13 for both transferred bridge samples. Interestingly, the signals intensity distribution appears to be very different in comparison to the results obtained in Ni elements (cf. section 6.2.1). For the transferred bridge aligned parallel to the propagation of the SAW, the signal amplitude appears to be largest for an IP field orientation of  $0^\circ$  ( $\mathbf{M} \parallel \mathbf{k}_{\text{SAW}}$ ) and additional maxima are obtained at  $\pm 90^\circ$  ( $\mathbf{M} \perp \mathbf{k}_{\text{SAW}}$ ). In the  $\pm 45^\circ$  IP orientation the amplitude is reduced in comparison to  $0^\circ$  orientation. In addition, the peak positions as a function of IP field rotation reveal an anisotropic behavior, which coincides with the shape anisotropy for this structure [131]. Interestingly, the BVS modes at larger bias fields show an enhanced amplitude compared to the DE-like modes at lower fields. By comparing the results from a) with the second sample geometry where the YIG platelet is rotated by roughly  $-60^\circ$  with respect to the propagation direction of the SAW, the influence of shape anisotropy becomes more obvious. Here, the easy axis can be found at a field orientation of  $-60^\circ$ , while the hard axis appears at  $30^\circ$ . Surprisingly, for at least one spin-wave mode, the signal amplitude is largest along the hard axis, as indicated in Fig. 6.13b). This might be caused by a more efficient coupling of the SAW to this part of

the spin-wave spectrum. Due to a better match of pronounced device axis and wave vector of the excitation, the horizontally oriented YIG bridge acts as a good model system to study SAW-driven dynamics in YIG. Therefore, the following experiments focus on this particular sample geometry.

### 6.3.4. Imaging of SAW-driven FMR in YIG Structures

In the horizontally aligned YIG element BVS modes are expected to appear in  $0^\circ$  orientation for field values above the main resonance of the system. Hence, spatially-resolved imaging of field-dependent signal components within the YIG platelet for different amplitudes of the external magnetic field was performed, as shown in Fig. 6.14.

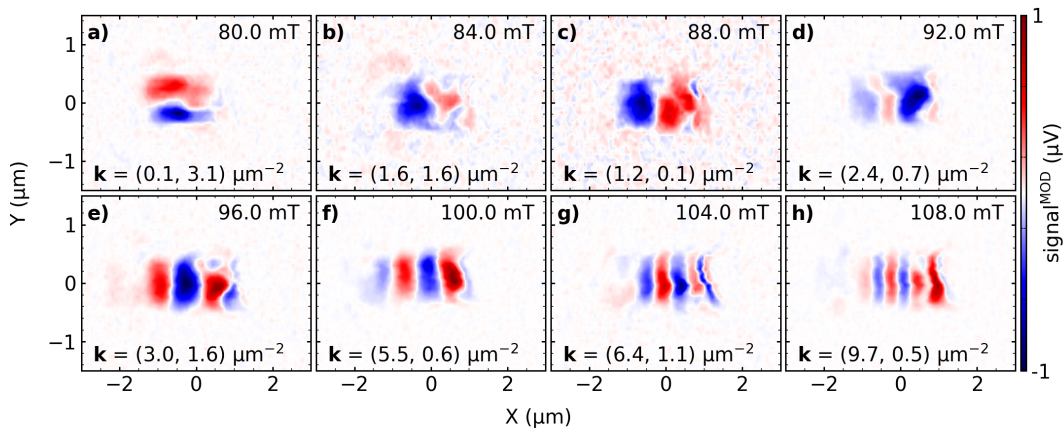


**Figure 6.14 | Spatially-resolved imaging of different SAW-driven spin-wave modes in a YIG element.** Field-dependent normalized signal amplitude of SAW-driven spin-wave excitations obtained by SNS-MOKE with additional field modulation. The extracted wave-vector components indicate a DE-like spin-wave mode in a) and BV-like modes in d)-h). Panel b) and c) show a decreased SNR compared to the BV-like modes.

Here, different standing spin-wave modes can be clearly distinguished at their corresponding field values, which are indicated by each panel's extracted in-plane wave-vector components. For Fig. 6.14a) a DE-like mode is shown, while in d)-h) BV-like modes are obtained. An intermediate regime is depicted in b) and c) where a mostly uniform excitation is expected. While such uniform modes show large signal intensities in YIG elements excited by rf-magnetic fields (cf. Fig. 5.3), they show comparably low signal amplitudes in the case of SAW-driven dynamics. This behavior is a direct consequence of used the excitation geometry. Typically, a uniform excitation in such devices will result in a dominant uniform precessional motion. However, in the case of a propagating SAW, this is not the case anymore since the time-dependent propagating excitation field couples very ineffectively to the uniform mode.

### Wave-Vector Conversion

As a next step, we investigate the wave-vector conversion in a stripe-like YIG structure in more detail. The device can host a large number of standing spin-wave modes along its easy axis (cf. Fig. 6.14), which correspond to BVS modes when the field is applied along the long axis of the element. In the following, the wave-vector components and the intensity of the excited modes are investigated. In doing so, a qualitative statement about the wave-vector conversion and the coupling efficiency is possible.

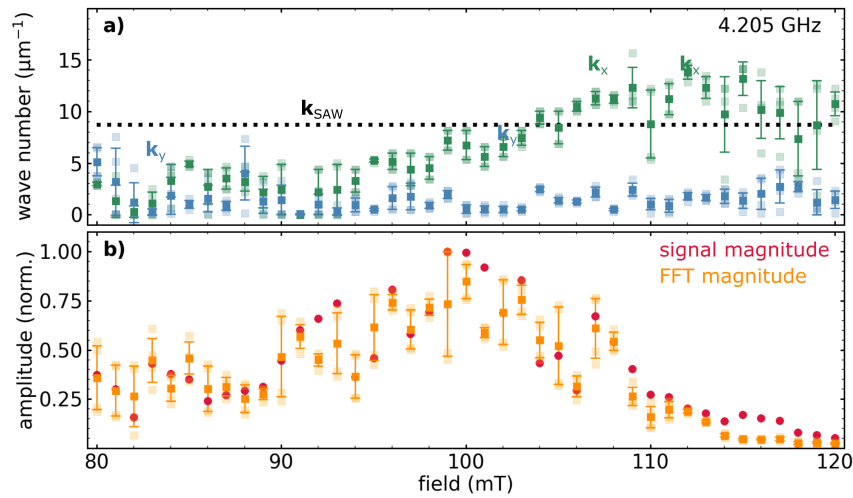


**Figure 6.15 | Wave-vector spectra and spin-wave amplitude as a function of magnetic field.** Panel a) depicts the wave-vector components  $k_{x,y}$  obtained from spatially-resolved imaging at 4.205 GHz. The corresponding spin-wave amplitude extracted from 2D-FFT data (orange) for the pronounced wave vector and the magnitude of the raw images (red) are depicted in b).

For this, the wave-vector spectrum as a function of the applied bias field for one SAW frequency is examined and analyzed in terms of measured intensity. Figure 6.15a) shows the extracted wave-vector components for a 4.205 GHz SAW excitation. The wavenumber of the SAW is depicted with a dotted black line. Panel b) shows the signal intensity extracted at the dominant wave vector from the 2D-FFT (orange) and the signal's magnitude obtained from the raw spatially-resolved image (red). These two normalized amplitudes are in good agreement for most field values, indicating only one dominant wave-vector component. In the case of a large difference between these two values, multiple wave-vector components might contribute to the magnitude obtained from the raw data, and thus superimpose to a larger value shown as red data points. However, the obtained 4.205 GHz data set in a) and b) indicates that for pronounced  $k_y$  components (on the lower field side), the signal amplitude appears very low, which means that the SAW couples very ineffectively to DE modes in this geometry. For increasing  $k_x$  wavenumbers also the amplitude increases (for larger field values). Here, the signal amplitude of BV spin-wave modes scales up with field while different standing spin-wave modes with increasing  $k_x$  components are excited. A maximum in detected intensity is approached for

wave vectors close to the one of the SAW, which also appears as the maximum wave vector for an efficient excitation. For further increased bias fields, the intensity drops drastically while wave-vector components of the SAW can still be extracted, which mostly emerge at the edges of the YIG platelet. In the intermediate regime, where a uniform mode at FMR condition is expected, no increase in the intensity is observed, which implies that the largest intensities are found for wave vectors close to the one of the SAW excitation. Remarkably, the lower-order standing spin-wave modes are very similar in intensity to the wave vector with the largest coupling efficiency.

In comparison to the presented results in micron-sized nickel elements (cf. section 6.2) the transferred YIG structure hosts a variety of discrete and distinguishable standing spin-wave modes. These can be identified in terms of their wavelength and distinguished from the SAW excitation. Therefore, YIG devices with different element geometries which might host different modes are very interesting for future studies. In addition, the wave-vector analysis reveals that short-wavelength excitations are converted into different wavelengths of magnetic excitations without significant loss of coupling efficiency, while lower frequency SAWs do not up-convert to smaller spin-wave wavelengths. This result helps to explain the obtained effects in micron-sized Ni elements, where primarily the wave vector of the SAW was obtained. Since the YIG bridge is not interacting with the propagating SAW in the underlying substrate, it is obvious that the signal components at the SAW's wave vector are magnetic excitations and not due to back-action effects. Thus, we believe that this is also the case for Ni elements, since the effect was observable independent of the element's size. For future experiments, high-frequency SAW excitations are most promising in either Ni or YIG microstructures since they allow for short-wavelength excitations which can easily convert to different wavelengths by setting the external bias field to a suitable value.

---

# Non-linear Spin-Wave Generation

---

The fourth experimental part of this thesis will further exploit one of the major advantages of the SNS-MOKE technique in terms of spin-wave detection, which is the possibility of measuring coherent excitations at arbitrary frequencies. So far, only the particular alias frequency was obtained, which directly belongs to the excitation (or to a modulated sideband of the excitation). The fact that the SNS-MOKE scheme allows for arbitrary frequency settings directly results in a genuinely frequency-resolved measurement technique. By using a multi-frequency LIA, simultaneous detection of the phase-resolved signals is achievable, as long as the expected signals appear coherently. This novel technique will be utilized to study strongly non-linear phenomena which play an essential role in the roadmap of magnonics. They grant the possibility of switching a magnetic state by passing a threshold power level or generating higher harmonics of the excitation within a magnonic device.

Typically, non-linear effects in magnetism occur when the driving force (e.g., the rf-field) is getting large; hence the system (e.g., the magnetization) is not able to follow this excitation linearly [181, 182]. As known from other fields in physics, non-linear processes in magnonics may result in the excitation of higher harmonics [52] due to multi-magnon scattering events [107]. One of the most pronounced effects is the three-magnon scattering, which dominantly occurs in the so-called parallel-pumping geometry [51, 183, 184], where the rf-excitation points in the same direction as the external magnetic bias field. In this geometry, the excited magnon decays into two magnons at half of the driving frequency with non-uniform opposite wave vectors. However, the phase in this pair of magnons is correlated [102]. Another non-linear process is depicted by four-magnon scattering. Here, two uniform magnons scatter into two non-uniform magnons at degenerated frequencies, as depicted in Fig. 2.5. These prominent effects are described by the Suhl [105, 185] and in the framework of S-Theory by L'vov [101] and Zakharov [102] (cf. section 2.4). In this framework, also higher-order processes might occur as soon as other processes with lower thresholds are forbidden [104]. However, recently Bauer *et al.* [54] modified the theory by taking amplitude-phase-oscillations occurring for larger precession angles into account, which might be present in the case of low external bias fields. By using this modified theoretical approach, they predicted a variety of different non-linear spin waves in the low bias field regime appearing at half-integer multiples of the excitation, such as  $1/2 f_{\text{rf}}$ ,  $3/2 f_{\text{rf}}$  or  $5/2 f_{\text{rf}}$ . The strongly elliptical precessional motion explains the existence of this type of spin waves with excursion angles of about  $30^\circ$  resulting in an inherent frequency modulation during one period of the spins' precession. However, direct experimental

verification of the predicted non-linearities is missing since Bauer *et al.* only detected these magnons indirectly by observing their influence on the uniform mode. Solely the work by Schultheiss *et al.* [186] demonstrates detection of odd half-integer harmonics in spin-valve nanocontacts utilizing BLS. In addition to a direct validation of Bauer's model, it is unclear under which experimental conditions these non-linear magnons emerge coherently and how they can be manipulated in magnonic devices.

This chapter presents a detailed experimental investigation of Bauer's prediction for  $\text{Ni}_{80}\text{Fe}_{20}$  microstructures and compares them to theoretical predictions obtained by micromagnetic simulations and the analytic model [54]. At first, we perform SNS-MOKE measurements to identify suitable conditions for non-linear spin wave (NLSW) generation and to obtain the threshold of the  $3/2 f_{\text{ff}}$  spin waves in these samples, as shown in section 7.2.2. As a next step, in section 7.3, we exploit the SNS-MOKE technique to perform spatially-resolved imaging of NLSW to address the phase stability of these modes and extract the generated non-linear wave vectors as a function of frequency. In the last part, we identify concepts to control the different properties of these non-linearities. The possibility of controlling the phase of the excited NLSWs is highly envisioned for applicability in future magnonic devices.

## 7.1. Experimental Configuration

### 7.1.1. Sample Fabrication

The samples investigated in this chapter consist of a gallium arsenide (GaAs) substrate equipped with a 100 nm thick gold CPW defined by means of electron beam lithography and lift-off technique. The  $50 \Omega$  impedance matched waveguide has a gap width of  $25 \mu\text{m}$  while the signal line is  $50 \mu\text{m}$  wide. On top of the signal line 20 nm thick  $\text{Ni}_{80}\text{Fe}_{20}$  elements are fabricated by electron beam lithography and lift-off technique. The sample geometry provides nearly uniform IP excitation in the center of the waveguide, onto which the elements are placed (as indicated in Fig. 7.1). Different element geometries can be found on this sample: Elliptical and rectangular elements with lateral dimensions of  $40 \mu\text{m} \times 20 \mu\text{m}$ ,  $30 \mu\text{m} \times 15 \mu\text{m}$ ,  $20 \mu\text{m} \times 10 \mu\text{m}$ , and  $5 \mu\text{m} \times 4 \mu\text{m}$  respectively. A second sample with a waveguide entirely covered with 20 nm thick  $\text{Ni}_{80}\text{Fe}_{20}$  was produced with the same treatment.

### 7.1.2. Measurement Geometry

The experimental results presented in this chapter were obtained in the DE geometry if not differently mentioned. Thus, the external magnetic field points along the waveguide. To access the non-linear excitation regime, a broadband rf-amplifier (MiniCircuits: ZVA-183X-S+) with a

gain of 20 dB is used. The maximum power level at the sample is on the order of 25 dBm. At these large power levels, reflections may damage connected devices; therefore, a circulator is implemented to protect the rf-source. The rf-excitation was monitored directly at the sample's CPW output, which allows for calibrating the set power level at the rf-source to the real transmitted power. Thus the rf-field at the sample can be reconstructed.

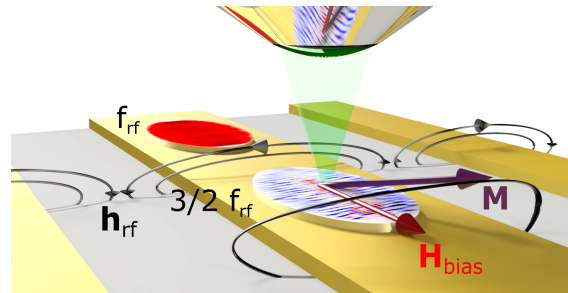


**Figure 7.1 | Sample and measurement geometry for non-linear spin-wave generation.** On top of the Au waveguide different  $\text{Ni}_{80}\text{Fe}_{20}$  elements were deposited. The external magnetic bias field is applied in the direction of the waveguide. Due to the large rf-driving field the magnetization (violet) precesses strongly elliptical with excursion angles of up to  $30^\circ$  leading to an inherent frequency modulation which results in a variety of different non-linear signal components. One of the elements shows a spatially-resolved pattern of a uniform precessional mode at the driving frequency  $f_{\text{rf}}$  while the other one shows a non-linear precession at  $3/2 f_{\text{rf}}$ .

### 7.1.3. Detection of uniform and non-uniform Magnons

By using a large-facility synchrotron source, Bauer *et al.* [54] demonstrated that in the low bias field regime, the number of uniform magnons saturates, as expected for 2<sup>nd</sup>-order Suhl instability [185]. In contrast, the number of non-uniform magnons is further increased. The calculated spin-wave lifetime for these non-uniform magnons turned out to be surprisingly larger than expected for Suhl instabilities. Thus, they linked these types of non-linearities to a different regime of non-linear driving processes, the so-called strong modulation regime.

We first aim to reproduce these findings by employing SNS-MOKE measurements. While the SNS-MOKE can easily access the uniform magnons by detecting at the corresponding alias frequency, the setup needs a slight modification to obtain the incoherent response of all excited (uniform and non-uniform) magnons. Here, half of the incoming laser beam is blocked by a black metal sheet to change the measurement geometry from p-MOKE to I-MOKE. In doing so, one accesses the  $M_x$  component, which is obtained along the direction of the applied magnetic field. By increasing the rf-power, the precession cone gets large, and thus an rf-dependent shortening of  $M_x$  can be observed. In contrast to a stroboscopic measurement; here, the rf-source is slightly detuned from the 10 MHz clock signal to detect the incoherent part of this precessional motion in a time-averaged manner. For this purpose, the rf-power is modulated in its amplitude allowing for Lock-In demodulation at this frequency. This scheme is similar to the conventional TR-MOKE detection, as introduced in Fig. 3.1a). For a comparison of these

time-averaged I-MOKE data with the ones obtained by SNS-MOKE in p-MOKE geometry, the  $M_z$  component of the detected signal must be transformed to  $M_x$  and normalized to  $M_s$ . First, the peak amplitude of the imaginary part of the dynamic susceptibility at a given combination of driving frequency and static bias field is extracted as a function of rf-field amplitude. The obtained data sets presented in blue in Fig. 7.2 represent the reconstructed  $M_x$  component of the measured SNS-MOKE signal. With increasing rf-field, the uniform response of the signal at  $f_{rf}$  (detected at the corresponding alias frequency) increases linearly with rf-power (and quadratic with rf-field) until a certain threshold value is reached. At this point the uniform magnons start to saturate [187]. Interestingly, the time-averaged I-MOKE signal (shown in green) detected in the same devices follow the uniform response up to the threshold rf-field but increases further after passing this power level. The time-averaged I-MOKE signal does not contain the uniform magnons only but also all other dynamic contributions, which effectively reduce the magnetization in the direction of  $M_x$ . This additional shortening of  $M$  is due to non-linear excitations, which might also occur incoherently at different frequencies, such as higher harmonics.

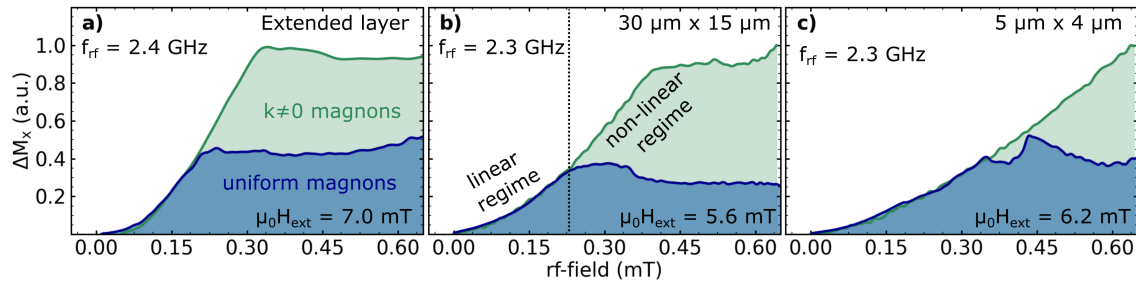


**Figure 7.2 | Comparison of uniform and non-uniform magnons in three different element geometries.** Two measurements of SNS-MOKE and time-averaged I-MOKE are plotted showing the saturation of the number of uniform magnons at the threshold level while the non-uniform magnons are further populated. These magnons above the threshold value occur due to non-linear magnon-magnon scattering processes at  $f_{rf}$  and different frequencies than the driving rf-frequency.

The effect of saturation is observed in all sample geometries at similar threshold fields, as shown in Fig. 7.2a) for an extended layer sample, in b) for a  $30 \mu\text{m} \times 15 \mu\text{m}$  rectangular element and in c) for a  $5 \mu\text{m} \times 4 \mu\text{m}$  rectangle. But one should mention that the increase of non-uniform excitations strongly differs, as seen in Fig. 7.2c) for the smallest element. The origin of non-linear magnetization dynamics is linked to the large elliptical excursion cones of the magnetization in the film plane [88, 187] which result in the saturation of the uniform mode. In this case, the energy dissipation from the spin system to the lattice will be mediated not only by the Gilbert damping of the uniform mode; moreover, non-linear processes will redistribute the uniform magnon's energy to non-uniform magnons and thus open additional channels for non-linear damping [188]. With this comparison of linear and non-linear magnetization dynamics in all investigated  $\text{Ni}_{80}\text{Fe}_{20}$  elements, we reproduced one of the results from Bauer *et al.* [54] by employing a table-top magneto-optical microscopy setup. With these measurements, we further

point out that all of these element geometries host non-linear phenomena. Therefore, the next step is to identify these types of non-linear magnetization dynamics. To further support our results, we perform micromagnetic simulations (see appendix A.5) and employ the k-space model (cf. section 2.4.2).

## 7.2. Magneto-optical Sampling of non-linear Spin Dynamics

In the following, we will utilize the SNS-MOKE technique (in p-MOKE configuration) to record the dynamically driven magnetization at different frequency components simultaneously. For this purpose, the laser spot is centered on the device under investigation, and different linear and non-linear frequency components of the dynamic response are detected with the aid of a multi-frequency LIA as a function of the applied bias field. Here, we detect up to five frequencies connected to the expected non-linear features in the magnetization dynamics, if not noted differently. In most measurements, the response of the system is recorded at alias frequencies corresponding to the rf-excitation at  $f_{\text{rf}}$ , the second harmonic at  $2 f_{\text{rf}}$  and half-integer harmonics at  $1/2 f_{\text{rf}}$ ,  $3/2 f_{\text{rf}}$  and  $5/2 f_{\text{rf}}$ . The corresponding alias frequencies are calculated via

$$\varepsilon = \begin{cases} |f_{\text{rf}} - i f_{\text{rep}}| & \text{uniform mode at } f_{\text{rf}} \\ |n f_{\text{rf}} - j f_{\text{rep}}| & n^{\text{th}} \text{ integer harmonic of } f_{\text{rf}} \\ |m/2 f_{\text{rf}} - k f_{\text{rep}}| & m^{\text{th}} \text{ half-integer harmonic of } f_{\text{rf}} \end{cases} \quad (7.1)$$

where  $i, j, k$  are integer harmonic numbers of the sampling frequency given by the laser's frequency comb and  $n, m$  are integer numbers depicting the non-linear harmonics of the excited magnetization dynamics. Thus, the demodulation frequency  $\varepsilon$  can be set to different values allowing for a simultaneous measurement of multiple non-linear frequency components. For the particular case of a 4.005 GHz rf-excitation the nearest comb line is the 50<sup>th</sup> harmonic of the sampling frequency and the alias frequency is 5 MHz. If we now assume a non-linear signal component at the second harmonic of the excitation (8.010 GHz in this case) the nearest sampling component would be the 100<sup>th</sup> harmonic and the resulting alias frequency is 10 MHz. Therefore, the linear and non-linear response are clearly decoupled in the detection via SNS-MOKE. This multi-frequency approach makes SNS-MOKE a competitive alternative to BLS for the detection of discrete coherent frequency components.

### 7.2.1. Non-linear Spin-Wave Excitation in $\text{Ni}_{80}\text{Fe}_{20}$ Elements

As depicted in Fig. 7.2, at a certain power level, the non-linear regime is accessed, which hosts a variety of different non-linear magnons. So far, it has not been shown that these non-linear

processes occur coherently. Hence, the initial experiments aim to find the predicted non-linear excitations and point out whether they appear coherently or are not detectable at all by means of SNS-MOKE. In the following, SNS-MOKE measurements of the three introduced element geometries (cf. section 7.1.3) are analyzed at  $f_{rf}$  and  $3/2 f_{rf}$  as a function of the applied rf-power.

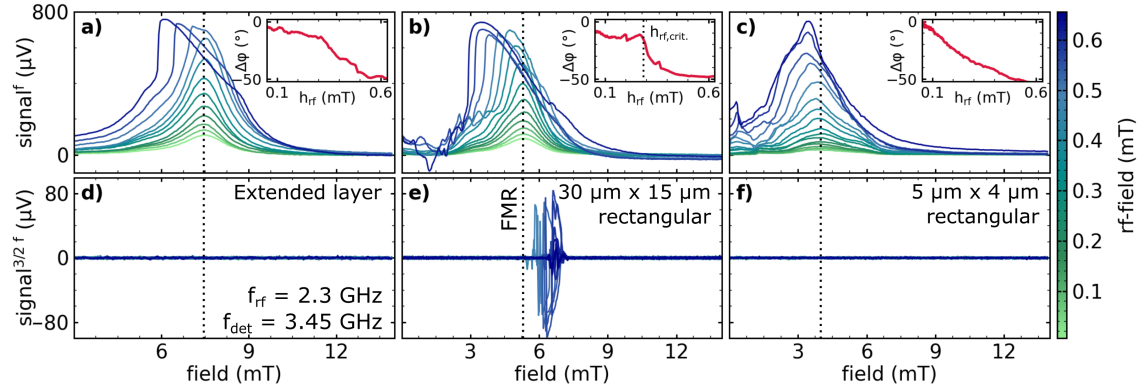


**Figure 7.3 | Power-dependent analysis of FMR mode and NLSW response.** a)-c) The imaginary part of the uniform response at  $f_{rf}$  is analyzed as a function of applied rf-power for three different element geometries. The uniform mode saturates for increasing power levels and shifts towards lower fields. In addition, a phase shift due to the onset of non-linear phenomena is obtained, as shown in the insets. d)-f) Simultaneously detected signals at  $3/2 f_{rf}$  are presented. In panel f), non-linear signal components appear above threshold condition. The threshold rf-field for a  $30 \mu\text{m} \times 15 \mu\text{m}$  elliptical element at 2.3 GHz is on the order of  $0.3 \text{ mT}_{\text{rms}}$  and coincides with the rapid phase shift observed for this sample. The signal components appear slightly above the resonance field. The rapidly occurring changes of the signal's sign indicates a lack of phase stability over time. For the other two geometries, no NLSW signals are visible.

The experimental results shown in Fig 7.3 allow us to identify sample geometries and rf-field amplitudes at which NLSW generation occurs coherently. In Fig. 7.3a)-c) the imaginary part of the optically detected FMR component obtained at  $f_{rf}$  is shown as a function of rf-power, as indicated by the color code. Here, we distinguish between the case of a) an extended layer, b) a  $30 \mu\text{m} \times 15 \mu\text{m}$  elliptical element and c) a  $5 \mu\text{m} \times 4 \mu\text{m}$  rectangular element. All three elements show similar behavior in the  $f_{rf}$  channel. The lineshape appears as a Lorentzian peak for lower excitation levels, while variations of this shape become visible as the power increases. Within the linear excitation regime, the amplitude scales up with increasing rf-power. At the threshold level, the main resonance saturates, and the peak position of the signal starts to shift towards lower fields. Here, the phase of the detected signal changes, as depicted in the insets of Fig. 7.3. In this excitation regime, the excursion angle of the precessional motion gets large. That shortens the magnetization in the direction of the applied bias field and shifts the FMR condition towards lower fields [187, 189]. In addition, a phase shift is clearly linked to the onset of NLSW generation [54] and the corresponding saturation of the uniform mode. While the population of uniform magnons saturates, additional channels for the transfer of energy become accessible. These additional damping mechanisms couple back to the uniform mode

and introduce the observed phase shift [54]. Panel d)-f) show the simultaneously measured response at  $3/2 f_{rf}$  for the three elements. For the extended layer, as well as for the smallest element, no coherent signal components become visible. But surprisingly, after exceeding the threshold value, coherent signal components emerge in the intermediate geometry, as shown in Fig. 7.3e). Here, NLSWs at  $3/2 f_{rf}$  appear at field values slightly above the FMR condition and shift with increasing power towards higher field values. In the vicinity of the threshold, the lineshape of this non-linear signal component appears very unstable in phase since its sign flips for minor changes of the field. Interestingly, by accessing larger driving amplitudes, the signal stabilizes over a broader field range (as shown in Fig. 7.4). The phase stability will be discussed in section 7.3.

Within a phase-stable regime, simultaneous detection at half-integer multiples of the driving frequency allows to directly investigate the non-linearities predicted by Bauer *et al.* [54] in the low bias field regime. In addition, by detecting the response at  $f_{rf}$ , the excited NLSW modes' influence on the uniform mode is revealed. Besides the excitation of  $3/2 f_{rf}$  modes, a variety of other frequency components become visible obtained by a series of field-swept measurements at integer and half-integer harmonics at fixed rf-amplitude, as presented in Fig. 7.4.

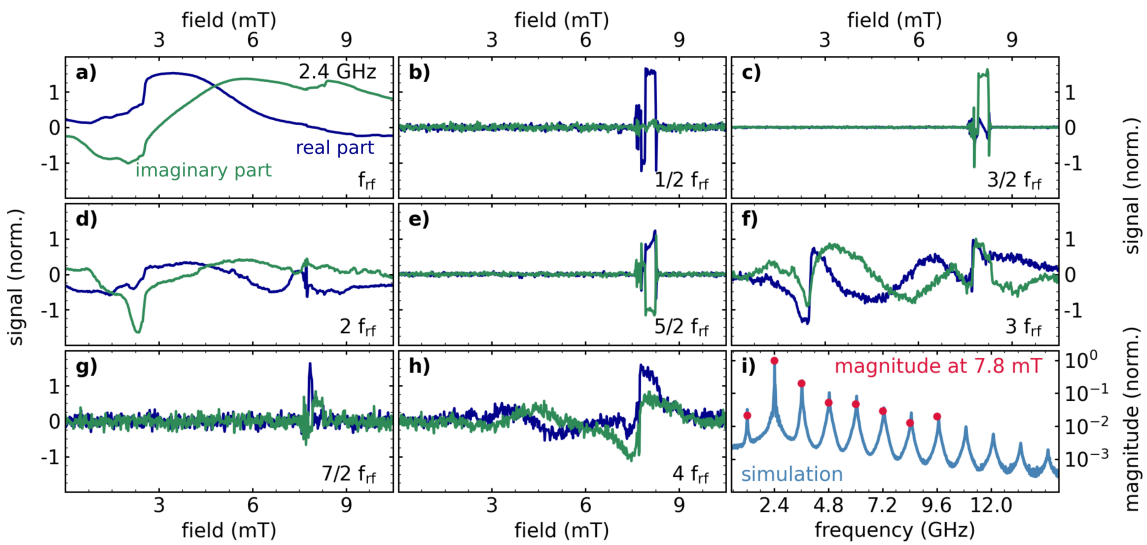


**Figure 7.4 | Magneto-optical sampling of non-linear spin waves at half-integer harmonics.** The  $30 \mu\text{m} \times 15 \mu\text{m}$  elliptical element is driven with a large rf-amplitude while linear and non-linear magnetization dynamics are analyzed at different harmonics of the driving frequency, as presented in a)-g). The FMR mode is presented in a) while integer harmonics at  $2 f_{rf}$ ,  $3 f_{rf}$  and  $4 f_{rf}$  are shown in d), f) and g), respectively. For large driving amplitudes, half-integer multiples at  $1/2 f_{rf}$ ,  $3/2 f_{rf}$ ,  $5/2 f_{rf}$  and  $7/2 f_{rf}$  become visible in a narrow field range around 7.8 mT as presented in b), c), e) and g), respectively. Panel i) depicts the magnitude analyzed at a fixed field value of 7.8 mT for all detected harmonics (red), whereas the blue spectrum is obtained by micromagnetic simulations under equivalent conditions.

In all shown components, non-linear effects are taking place for a fixed rf-frequency of 2.4 GHz. The field regime where signal components of the well-known higher harmonics in d), f), and h)

can be found as broad as the uniform mode presented in a), while the field range in which the half-integer non-linearities emerge appears very narrow. Hence, these two types of non-linearities must be distinguished in the following to understand the underlying non-linear mechanisms.

### Higher-Harmonic Generation

In comparison to half-integer harmonics, signal components with oscillatory features appear at integer multiples of the excitation [52]. This is a well-known non-linear process for  $\text{Ni}_{80}\text{Fe}_{20}$  and appears much stronger for smaller field values compared to the 7.8 mT used in this investigation. Koerner *et al.* [190] demonstrated that frequency comb generation takes place in polycrystalline  $\text{Ni}_{80}\text{Fe}_{20}$  samples as a result of the highly anharmonic precession of the magnetization in combination with the imperfection of the  $\text{Ni}_{80}\text{Fe}_{20}$  layer in the field regime around 1 mT. The LLG equation itself offers a non-linear behavior which results in the formation of at least a few harmonics but is not sufficient to establish a frequency comb, as reported by Demidov *et al.* [52]. Thus, the magnetic material's grain structure has to be considered, giving rise to slightly different magnetic properties, e.g., saturation magnetization or anisotropy in neighboring grains, which become relevant for low external bias fields. By this mechanism, frequency comb generation for low magnetic bias fields can be shown. This effect strongly decays as the bias field increases, which explains the comparable low intensity of the integer harmonics relative to the uniform mode at 7.8 mT in our experiments. In addition, sample geometry, thickness, and quality of the film play an important role in explaining the further deviation from the frequency comb generation. The generation of higher harmonics is further discussed in chapter 8.

### NLSW at Half-Integer Harmonics

The second set of strongly non-linear features found in Fig. 7.4 show that for large excitation amplitudes, non-vanishing signal components appear at the corresponding alias frequencies of the first few half-integer multiples of the driving frequency. This chapter will cover detailed investigations of these non-linear half-integer harmonics. Their appearance is rather surprising since no clear indication of a coherent excitation has been presented so far. The signal components do not only appear at  $3/2 f_{\text{ff}}$  but also at other odd half-integer multiples as measured by Schultheiss *et al.* [186] in spin-valve nanocontacts. Interestingly, the ratio of amplitudes at this frequency components is given by  $I_{3/2} > I_{5/2} > I_{1/2}$ . At the same time, higher harmonics show mostly a very low amplitude at the investigated power levels by means of SNS-MOKE. To corroborate our findings, we performed micromagnetic simulations of NLSW excitation for a similar sample geometry. A typical spectrum for a 2.4 GHz excitation is depicted as blue line in Fig. 7.4i). The ratio of peak amplitudes in the different harmonics matches the experimental observations, where the  $3/2 f_{\text{ff}}$  NLSW is the dominant feature. The field regime around 7.8 mT where the NLSW appear also contains interesting features in the integer harmonic channels. In particular, a pronounced dip in the ferromagnetic resonance at  $f_{\text{ff}}$  can be detected in this field range while the higher harmonics show a resonance-like feature that

appears as a phase jump. The feedback of NLSW generation on the phase of the FMR mode was observed by Gerrits *et al.* [187] and explained by Bauer *et al.* [54] within their theoretical model.

### Micromagnetic Simulation

One should note that the obtained NLSW signals are appearing in a narrow field range and seem to shift towards larger fields as the uniform response broadens. We believe that a phase-stable formation of a standing spin-wave pattern only emerges in this field regime, while the field range in which odd half-integer harmonics exist without a stable phase is much broader. From measurements, such as shown in Fig. 7.2, we know that non-linear features appear on a similar field range as the uniform excitation itself. To further emphasize this assumption, micromagnetic simulations were carried out to determine the ideal NLSW response at odd half-integer harmonics. As presented in appendix A.5, the obtained signals cover a field range indeed as broad as the FMR linewidth and appear symmetrically around the FMR condition. However, in the experiments at least a narrow part of the spectrum becomes stable in phase and offers a field range where the phase-resolved detection of NLSW generation is possible in a reproducible fashion.

### Analytical k-Space Model

To further corroborate our experimental findings, we utilize the model presented by Bauer *et al.* to analytically obtain the threshold conditions and the wave vectors of  $3/2 f_{\text{rf}}$  spin waves in a frequency-resolved manner (as shown in section 2.4.2). For the calculation, we used a  $\text{Ni}_{80}\text{Fe}_{20}$  thickness of 20 nm, the saturation magnetization  $M_s = 800 \text{ kA m}^{-1}$ , the exchange constant  $A_{\text{ex}} = 13 \text{ pJ m}^{-1}$  and a damping constant of  $\alpha = 0.008$ . By applying this model, the spin-wave decay rate, as well as the frequency in the  $k_{x,y}$ -space, is calculated. This allows addressing the threshold of the  $3/2 f_{\text{rf}}$  spin waves by systematically increasing the rf-driving field for fixed frequency and bias field until the threshold is exceeded and the non-linear components become critical. For this threshold condition, the wave-vector components of the  $3/2 f_{\text{rf}}$  spin waves can be accessed [54].

#### 7.2.2. Threshold Determination of NLSW Generation

The obtained threshold value from the measurement shown in Fig. 7.3 is on the order of 0.3 mT for an applied frequency of 2.3 GHz and thus within the range of theoretical prediction from Bauer *et al.* [54]. To further compare our obtained results to the prediction from the analytical model, we performed measurements such as shown in Fig. 7.3 for different frequencies and on different element geometries. Here, the threshold is identified by the first appearance of signal components within the half-integer response channels. In doing so, we obtain a set of

threshold values shown in Fig. 7.5, where the different green and blue color shades represent the lateral dimensions of elliptical and rectangular elements, respectively.

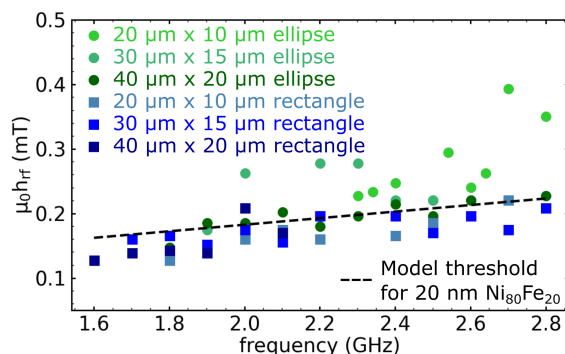


**Figure 7.5 | Threshold of non-linear spin-wave generation.** The threshold values for the different elliptically shaped elements are presented in green, while the blue data points represent the rectangular shaped  $\text{Ni}_{80}\text{Fe}_{20}$  elements. The black dotted line depicts the theoretical prediction from the analytical model. For small elliptical elements the threshold value appears to be increased compared to the prediction.

The different elements have slight variations in their threshold behavior but show an overall trend of increasing threshold value with applied microwave frequency. To validate our experimental findings, we aim for comparison with the theoretical prediction. Therefore, we utilized the model from Bauer *et al.* (introduced in section 2.4.2) and calculated the spin-wave relaxation rate for the  $3/2 f_{\text{rf}}$  component as a function of frequency. The threshold values in this model are given by an rf-field amplitude at which the relaxation rate is approaching zero and NLSWs become critical. The obtained result from the analytical calculation is shown as a black dashed line in Fig. 7.5. The experimental results match the prediction over a broad frequency range for most investigated geometries, whereas the prediction is only made for an extended film.

### Explanation of enhanced Threshold Values

Note that for the smallest elliptical element NLSW generation was not verifiable below 2.3 GHz, and above this frequency barrier, the threshold is enhanced compared to other sample geometries. For an even smaller rectangular-shaped element with lateral dimensions of  $5 \mu\text{m} \times 4 \mu\text{m}$ , no observation of the  $3/2 f_{\text{rf}}$  NLSWs was possible at all (as depicted in Fig. 7.3). The same observation was made on a sample with an entirely  $\text{Ni}_{80}\text{Fe}_{20}$  covered waveguide, which acts as an extended film sample compared to the other investigated geometries. However, we are convinced that the half-integer non-linearities exist in the mentioned geometries since we obtain a saturation of the uniform mode in the SNS-MOKE measurements, as well as a dynamic shortening of the magnetization with time-averaged I-MOKE in all of the investigated element geometries. In addition, all of these devices show a phase shift at the transition to the non-linear regime. Furthermore, micromagnetic simulations reveal that those odd half-integer

multiples indeed appear in all geometries over a broad field range. Therefore, we link the possible observation of these non-linear features to their coherence over time. The formation of a phase-stable response might not be guaranteed close to the real threshold of these non-linear features. Hence, we will focus on the stabilization mechanism of these NLSW in section 7.6. This stability of a standing spin-wave pattern strongly depends on the sample geometry. For medium-sized elements, pinning conditions at the edges of the element favor the formation of standing waves from the scattered magnon pairs, while inhomogeneous fields at the boundary of the element might prohibit this formation for the smallest structures. Moreover, an increased threshold is expected for smaller elements due to the enhanced effective damping we examined by micromagnetic simulations. In particular, for a  $30\ \mu\text{m} \times 15\ \mu\text{m}$  element we obtain a threshold rf-field of 0.3 mT at 2.3 GHz, while this value is strongly increased for the same frequency in a small element to a value of 0.6 mT. These values become even more enhanced if a granular structure is assumed.

### Limitations of SNS-MOKE

The direct comparison of experimental results (Fig. 7.4) and micromagnetic simulations (appendix A.5) reveals the limitation of the utilized technique. The SNS-MOKE spectrum of NLSW is restricted to a narrow field range slightly above FMR condition (mainly located at the rising edge of the peak), in which a stable phase pattern seems to emerge. While the  $3/2\ f_{\text{ff}}$  signal from simulations covers a broader response with its maximum at FMR condition. As pointed out earlier, we are convinced that in the experiments, these NLSW are generated in the same broad field range as obtained by theory. This hypothesis needs to be confirmed in future experiments by investigating NLSW excitation with techniques also capable of detecting incoherent magnons, such as BLS. Such BLS measurements within the low bias field regime will also allow determining threshold conditions more precisely.

## 7.3. Spatially-resolved Imaging of NLSWs

Throughout the last section, we observed non-linear signal components at half-integer multiples of the driving frequency and identified their threshold behavior. Within the stable regime for reproducible measurements, the following section aims for spatially-resolved imaging of this NLSW. Imaging in this regime allows for the validation of the theoretically predicted wave vectors of the NLSW at  $3/2$  of the driving frequency. In the analytical model [54], these emerge at intermediate propagation orientations between DE and BV geometry in the spin-wave dispersion.

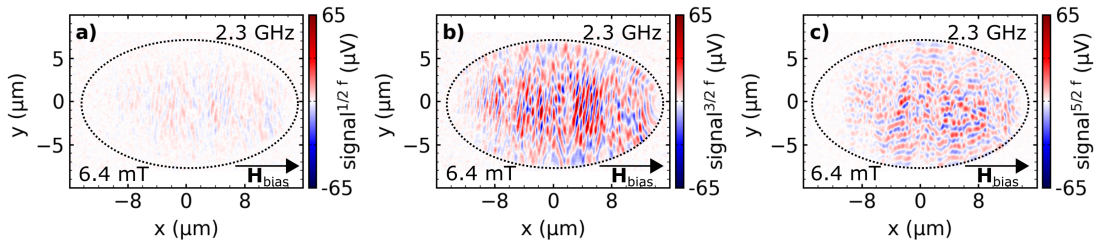


**Figure 7.6 | Spatially-resolved imaging at half-integer harmonics.** For an external bias field of 6.4 mT and an rf-frequency of 2.3 GHz the dynamic response at  $1/2 f_{rf}$ ,  $3/2 f_{rf}$  and  $5/2 f_{rf}$  is shown in a), b) and c), respectively. The  $3/2 f_{rf}$  component shows the largest signal amplitude. The wave-vector pattern for  $5/2 f_{rf}$  NLSW differs from the others, indicating that higher-order non-linear processes might be involved.

The measurements presented in Fig. 7.6 were carried out for an rf-frequency of 2.3 GHz and a bias field of 6.4 mT. Here, the dynamic response at different frequency components is mapped in a point-wise fashion. The parameter space was set to a stable regime in phase above the threshold, which offers an intense standing spin-wave pattern at  $3/2 f_{rf}$  within the lateral dimensions of the ferromagnetic element, as shown in Fig. 7.6b). In addition, NLSW signal components are obtained at  $1/2 f_{rf}$  and  $5/2 f_{rf}$  (see Fig. 7.6a) and c)) while the response at  $f_{rf}$  remains uniform. The ratio of the average signal amplitudes is in agreement with the findings from Fig. 7.4. Interestingly, the patterns obtained in a) and b) appear similar, while the excited wave-vector pattern for the largest frequency component contains additional wave vectors. This observation might be an indicator for higher-order non-linear processes.

### Stability of NLSW Generation

As mentioned in section 7.2.2, excitation amplitudes close to the threshold value result in randomly occurring phase flips of the detected signal at half-integer harmonics. A comparison with micromagnetic simulations reveals that SNS-MOKE detection of NLSW is only possible within a narrow field range above the resonance field, where the phase stability is given. In the following, we will investigate the phase stability of the obtained NLSW signal. In contrast to techniques where phase-instabilities do not influence the obtained signal; here, the phase sensitivity of the SNS-MOKE allows identifying these specific regimes of different stability. The coherence of NLSW generation depends on several experimental parameters, and thus it strongly depends on their stability over time. These parameters are the rf-frequency and the rf-power as well as the external magnetic field.

### Microwave Frequency

We assume that the frequency in the measurement scheme is the most stable observable because all components are locked to the same master clock, which provides a very stable

frequency standard. If a tiny frequency jitter is assumed, this would directly lead to visible phase variations in all signal channels. Since this is not the case, we can neglect this scenario and focus on the two other possibilities.

### Microwave Power

A more crucial component is the applied rf-power whose influence on the stability we analyzed in two different ways. First, we set all parameters to a stable condition. By switching the rf-source off and on again, the phase of the obtained NLSW signal is recorded continuously. After each switching event, the phase either stays at its initial level or flips by  $180^\circ$ , indicating two possible phase states. This experiment is depicted in Fig. 7.7, where panel a) shows the status of the rf-source while the recorded phase is presented in b). The randomly occurring switching events are depicted by red and green markers in c).

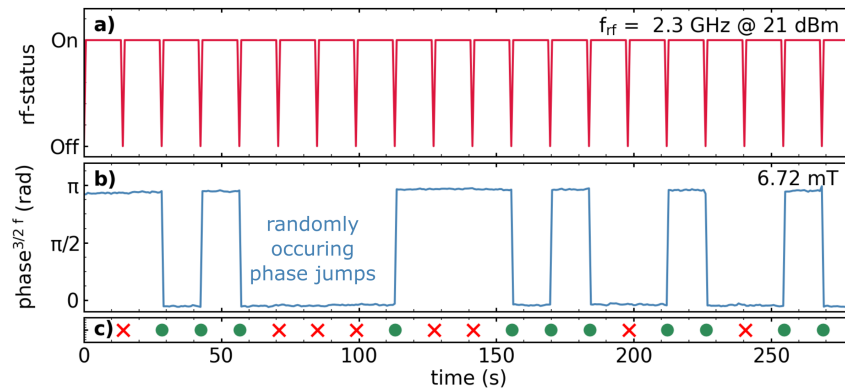


**Figure 7.7 | Phase switching of the NLSW excitation.** We mimic the phase-switching behavior by systematically switching the rf-power off for a short time, as indicated in a). In b) the resulting NLSW's signal phase is plotted as a function of time. In c) the randomly appearing switching of the phase after resetting the power level is shown.

To model this case more realistically, we investigated the stability of the rf-source over time. Here, only tiny changes on the order of  $0.01 \text{ dBm}$  appeared directly at the source. However, larger changes in transmitted power at the sample might be mediated by the rf-amplifier or temperature-dependent effects. Thus we prepare the magnonic system in a stable non-linear state, and after a short time, the rf-power is reduced in small steps of  $0.1 \text{ dBm}$ , to obtain how such small changes in power are affecting the stability. Observing the stability after each step allows us to identify a value below which the phase relation becomes unstable. Increasing the rf-power by a small step results in stability again, while the phase sets randomly to either the initial value or the flipped state. A stable regime of about  $2 \text{ dBm}$  can be identified, while bias field and rf-frequency stay constant. However, this regime of stability appears much larger than fluctuations of the rf-driving source and can only explain the obtained behavior close to the threshold.

### Magnetic bias Field

Similar behavior can be observed by varying the magnetic field from the stable regime to slightly larger or smaller field values, and again phase flips are observed on both sides of the stable regime. To further point out the stability mechanism, we performed a field-dependent measurement of the  $3/2 f_{ff}$  signal, where the signal is recorded over a measurement period of 100 s for each field step.

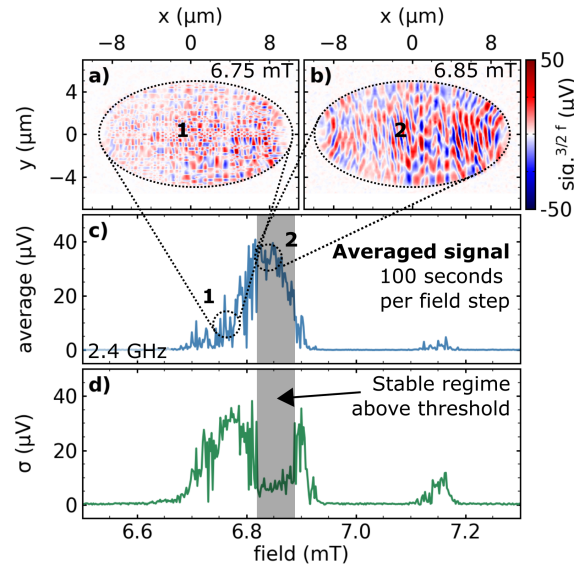


**Figure 7.8 | Phase stability of NLSW excitation.** Panel a) and b) show spatially-resolved images of the  $3/2 f_{ff}$  signal in a  $20 \mu\text{m} \times 10 \mu\text{m}$  elliptical element for slightly different bias fields. In a) the phase jumps randomly between different points, while b) shows a stable spin-wave pattern over the entire structure. For c) and d) a field-swept measurement was carried out and the signal was recorded for each measurement step over a time period of 100 s. The time-averaged magnitude of the signal is presented in c) and the corresponding standard deviation  $\sigma$  is shown in d). A regime with large average signal and low standard deviation can be identified as the stable regime in which spatially-resolved imaging of the NLSWs is possible.

For this experiment, demonstrated in Fig. 7.8c) and d), the time-averaged magnitude of the NLSW response at  $3/2 f_{ff}$  and its standard deviation  $\sigma$  is obtained for a  $20 \mu\text{m} \times 10 \mu\text{m}$  elliptical element. These two graphs allow distinguishing three different regimes accessible with SNS-MOKE: (1) No non-linear signals, a vanishing average signal, and low standard deviation  $\sigma$  (2) the unstable regime, which can be identified by a moderate average signal but mostly by the huge variations over time in terms of phase flips visible in the large standard deviation and (3) the stable regime with a small standard deviation and a large average value. Interestingly, the regime of phase flips appears on the lower and upper field side of the non-linear signal, which gives rise to possible explanations. Either the power or the bias field contains a tiny jitter component which is sufficient to change the state in the non-stable regime from below to above threshold resulting in a continuous resetting of the phase in one of the two possible

states. In addition, a) and b) show spatially-resolved images taken in the unstable phase-flip and the stable regime, respectively.

Since the phase stability in SNS-MOKE measurements is only given in a narrow field regime, variations of the external bias field strongly influence the stability of NLSW. We assume the field jitter itself to be on the order of 0.01 mT, while the jitter of the detection electronic is larger. Thus, an average value is determined in the experiment to take this detector noise into account. However, the described behavior is only sufficient to change the stability in the direct surrounding of the signal but leaves a stable part of the spectrum in between. Thus we are convinced that a coherent standing spin-wave pattern in the experimental geometry can only be established in the narrow field regime above FMR condition, while incoherent magnons cover a much broader field range, as expected from simulations. In addition, it is known from theoretical investigations [102] that the phase relation of parametrically excited magnon pairs (in parallel pumping geometry) is correlated to the excitation; however, the phase of the individual magnons might be distributed stochastically [102]. For such a case it has been shown, that parametrically pumped magnons (at  $1/2 f_{rf}$ ) favor two different phase states [191]. The phase of the individual waves needs to be stable during measurement time in order to form a phase-stable standing spin-wave pattern within the investigated elements. Fluctuations of the phase will directly result in a different distribution within the pattern and thus change the signal's phase at the measurement point. This might explain some of the observations in our experiments. Here, the stable regime would correspond to a stable phase of the individual magnons, while the unstable regime with its randomly occurring phase flips is linked to slow changes in the spin-wave pattern which is still observable within the measurement time. Thus, the incoherent part of the spectrum might be connected to rapid changes in the phase of the magnon pair and thus results in a vanishing average signal. Therefore, to obtain a phase-resolved spin-wave pattern and to access the wave vectors of NLSW by utilizing SNS-MOKE, phase stability over time is strongly required. Thus the identification of this regime is essential for the following experimental analysis.

## 7.4. Wave-Vector Analysis

The identification of a coherent NLSW generation at odd half-integer harmonics enables the possibility of performing spatially resolved measurements, as shown in Fig. 7.6. These measurements provide direct access to the wave vectors of the NLSWs. The patterns observed in the X- and Y-Channel of the LIA can be investigated with the aid of a complex 2D-FFT to reveal the wave vector components of the standing waves in the  $k_{x,y}$ -plane.

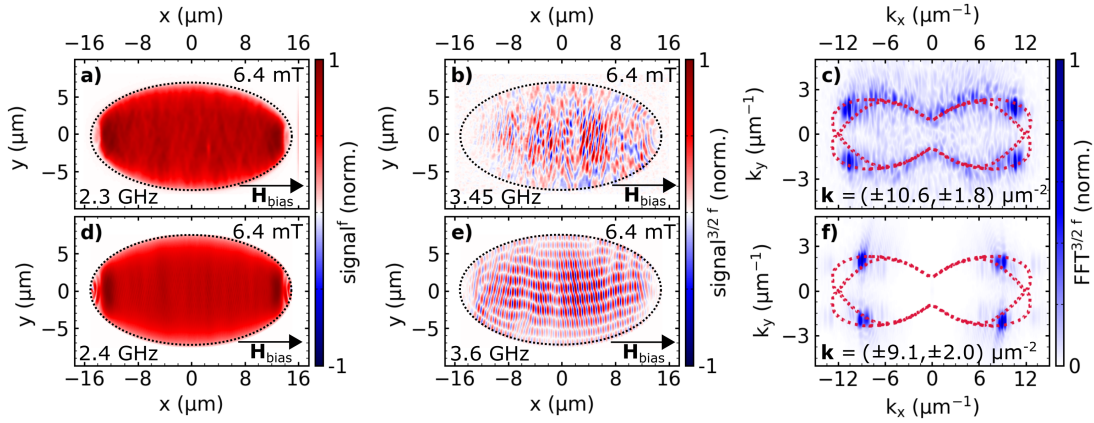


**Figure 7.9 | Phase-resolved imaging of NLSW and 2D-FFT obtained from SNS-MOKE measurements and micromagnetic simulations.** Comparison of SNS-MOKE results (upper row) and micromagnetic simulations (bottom row) for a  $30 \mu\text{m} \times 15 \mu\text{m}$  elliptical element with an applied external bias field of 6.4 mT. In a) and b) the experimentally obtained uniform response at  $f_{rf}$  and the NLSW signal at  $3/2 f_{rf}$  is shown, respectively. Panel c) presents the 2D-FFT of the NLSW signal and reveals the dominant wave-vector components. The spatially-resolved images obtained from the simulation are depicted in d) and e). The spin-wave pattern of the  $3/2 f_{rf}$  response is shown in f). The red lines in c) and f) are iso-frequency lines obtained by the analytical model with similar parameters as used in the simulation (cf. 2.4.2).

The upper row in Fig. 7.9 presents the experimentally obtained phase-resolved data of a) the uniform response at  $f_{rf}$  and b) the  $3/2 f_{rf}$  signal above threshold. Panel c) shows the 2D-FFT pattern extracted from b) where four dominant peaks become visible at propagation directions close to the BV geometry, but with non-zero  $k_y$  component. Comparing these results to the pattern observed by micromagnetic simulations in e) and its 2D-FFT shown in f) reveals that these features appear in the simulations as well but at slightly shifted values. In the experiments, additional features are visible in the observed 2D-FFT pattern. These features follow the iso-frequency line in the non-linear spin-wave dispersion obtained with the analytical model (red). We link these additional signal components to magnon-magnon scattering events, which result in the population of possible magnon modes at the same frequency (cf. Fig. 2.5). For a perfect film, the simulations do not contain these features. Therefore, simulations for a more realistic layer were carried out, where the polycrystalline structure of the  $\text{Ni}_{80}\text{Fe}_{20}$  is modeled by a small spatial variation of the magnetic properties (see appendix A.5).

### Frequency-dependent Change of the Wave Vector

To further understand the nature of the observed wave vectors and how they can be utilized in the future, we extend the presented wave-vector analysis to the next dimension - the rf-frequency. Hence, a series of measurements at different external parameters was executed. For each excitation frequency, the threshold value from measurements, such as shown in section 7.2.2,

and the corresponding bias field values were estimated. Subsequently, spatially-resolved imaging was performed for this set of parameters within the stable regime.

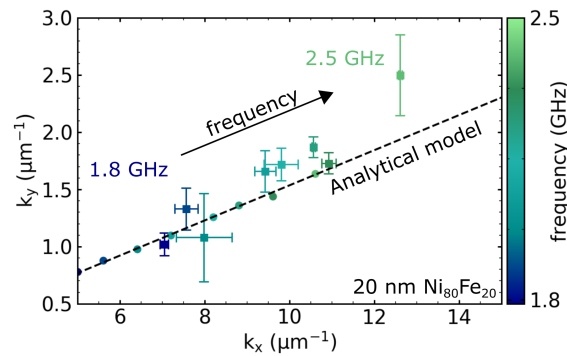


**Figure 7.10 | Frequency-resolved investigation of the non-linear wave-vector components.** The wave-vector components of  $3/2 f_{rf}$  NLSWs for different excitation frequencies were determined by utilizing 2D-FFT. The color code represents the excitation frequency of the measurement (squares with error bars). The color-coded points were calculated by using the analytical model. The dashed line demonstrates the linear development of the theoretical prediction with frequency for a 20 nm thick  $\text{Ni}_{80}\text{Fe}_{20}$  film.

The color-coded data points with corresponding error bars in Fig. 7.10 represent the wave vectors of NLSWs above threshold condition as a function of frequency. Here, an increase of the wave-vector components with frequency is shown in the range from 1.8 GHz to 2.6 GHz. In their publication, Bauer *et al.* predicted a wave vector for 2.5 GHz for a slightly different sample thickness of 40 nm, which allows no direct comparison to our results. Because of that, we exploited their analytical model to find the wave vectors of  $3/2 f_{rf}$  spin waves at threshold condition for a sample thickness of 20 nm. The data points from these calculations are presented with the same color code, and a dashed line indicates the trend of increasing wave-vector components with frequency. The obtained values from the analytical model provide slightly smaller wave vector components, similar to the micromagnetic simulations obtained in Fig. 7.9. However, the model calculation is valid for an extended film and therefore matches the results obtained experimentally in a  $30 \mu\text{m} \times 15 \mu\text{m}$  elliptical element in an excellent fashion.

The presented experimental results confirm most of the predictions made by Bauer *et al.* [54] for  $\text{Ni}_{80}\text{Fe}_{20}$  devices. Thus, the precise generation of large wave vector NLSWs is feasible and can be reproduced easily, since threshold rf-field, magnetic bias field, and rf-frequency dependency are investigated in detail. The next inevitable step is to discover possible control and stabilization mechanisms of NLSW generation in the low bias field regime since all results rely on the stable inherent NLSW excitation which settles at a random phase value. However, for wave-based applications, such as amplifiers or directional couplers, a precise setting of the phase is essential.

## 7.5. Control of Propagation Direction

In magnonics, spin-wave guiding has become an important aspect, and for this purpose, it is highly desired to control the propagation direction of the NLSW. As discussed in the introduction of this chapter, all measurements were carried out in the  $0^\circ$  geometry so far, which means that the external bias field is applied parallel to the waveguide. This IP orientation corresponds to the one used in the literature [54]. However, to identify possible control mechanisms of NLSW generation, we first investigate the non-linear response in an angular-resolved manner by performing field-swept measurements at different IP field orientations.

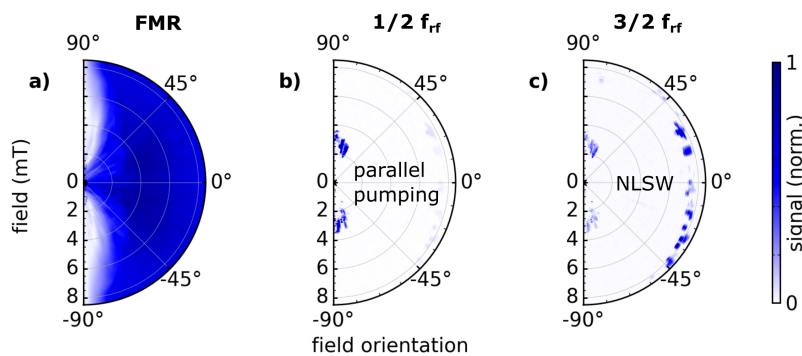


**Figure 7.11 | Angular-resolved field-swept measurements of NLSW generation.** Field-swept measurements were performed in the center of a  $\text{Ni}_{80}\text{Fe}_{20}$  element at different orientations of the magnetic bias field. In a) the uniform signal is shown, with a broad resonance where the magnetic field points along the waveguide at  $0^\circ$  (DE geometry). While  $90^\circ$  represents the parallel-pumping geometry. Here, no excitation is observed. In b) the  $1/2 f_{\text{rf}}$  response is shown, where non-linear signal components are dominant in parallel-pumping geometry. Panel c) contains the  $3/2 f_{\text{rf}}$  NLSWs which cover a wide range of field orientations between  $\pm 45^\circ$ , where they show largest signal amplitude.

The resulting polar signal distributions obtained at  $f_{\text{rf}}$ ,  $1/2 f_{\text{rf}}$  and  $3/2 f_{\text{rf}}$  are shown in Fig. 7.11. The magnetization dynamics are driven at 2.4 GHz far above threshold. The uniform response in panel a) shows the typical broad resonance along the  $0^\circ$  orientation (DE geometry) and a vanishing signal in the  $\pm 90^\circ$  geometry where the external bias field is aligned parallel with the rf-field generated by the CPW. This orientation results in a dynamic change of the magnetization in the applied field's direction leading to a change of the  $M_z$  component at half of the driving frequency. In this so-called parallel-pumping geometry [47, 48, 51, 99] a uniform magnon decays into two magnons at  $1/2 f_{\text{rf}}$  with  $\mathbf{k} \neq 0$  mimicking the easiest example for a three-magnon scattering process. This parametric excitation of  $1/2 f_{\text{rf}}$  magnons is directly observed as a strong signal component in Fig. 7.11b), only appearing in the  $\pm 90^\circ$  geometry at very low bias fields. In contrast to these signal components, the  $3/2 f_{\text{rf}}$  NLSWs, which are the dominant features in panel c), are present in the range of  $\pm 45^\circ$  and appear at comparably larger bias fields. Interestingly, the field range in which NLSWs are excited varies only slightly with the orientation of the bias field. Note that both dominant features from b) and c) appear as weaker signals in

the other detection channel as a result of non-linear frequency mixing processes. From this observation, subsequently, the question arises, how the generated wave-vector spectrum behaves under rotation of the external bias field. Therefore, two exemplary orientations were picked, and phase-resolved imaging at the corresponding bias fields was performed. The resulting 2D-FFT patterns are presented in Fig. 7.12, where a) depicts a field direction of  $32^\circ$  at a bias field of 7.58 mT, while in b) the field was set to a orientation of  $-34^\circ$  with a magnitude of 7.9 mT.

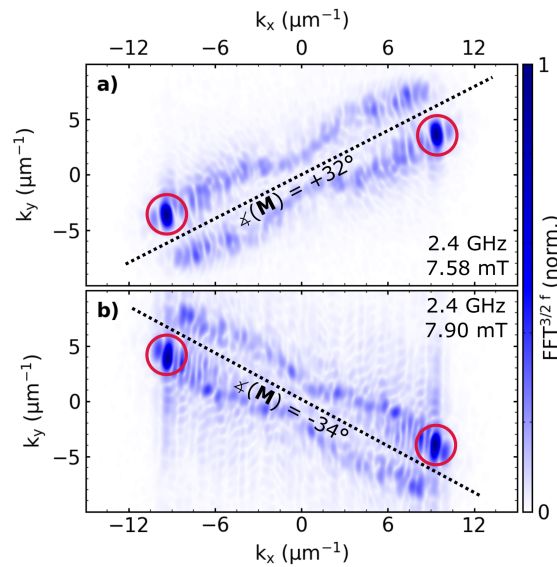


**Figure 7.12 | Wave-vector spectra for different field orientations.** For two orientations of the external bias field spatially-resolved imaging was performed and analyzed by means of 2D-FFT. The spin-wave manifold rotates with the external field, as indicated by the black dotted lines in a) and b). For both direction the intensity distribution changes with respect to the  $0^\circ$  geometry where the four peaks were equally populated. Under rotation the smaller  $k_y$  components show a larger intensity.

The obtained patterns, known from Fig. 7.9, obviously align with the applied external bias field indicated by the dotted line. Surprisingly, the pronounced direction of excited NLSW (red circles) changes, as in both cases, the direction with lower  $k_y$  components is preferred. In comparison to the  $0^\circ$  orientation, one direction seems to be favored leading to a distinguishable propagation of NLSW controlled by the external magnetic field orientation and might be used to couple one distinct wave vector out of a NLSW emitter.

## 7.6. Phase Locking of non-linear Spin Waves

The findings from previous sections allow us to precisely set the magnonic system to a state in which the strongly anharmonic precession results in the formation of coherent magnons at half-integer multiples of the excitation. While this process worked for most of the presented

geometries, it was not possible to directly observe NLSWs in the smallest elements. However, down-scaling of the element size is crucial for the integration of magnonic devices in complementary metal-oxide semiconductor (CMOS) technology. The lack of phase stability indeed motivates the further investigation of the NLSW in these small devices. By micromagnetic simulations, we found that the threshold value for NLSW generation increases with shrinking the lateral sample dimensions below a critical value. The experimental results from section 7.2.2 confirm that for the  $20\ \mu\text{m} \times 10\ \mu\text{m}$  elliptical element, the threshold is increased, while it is not accessible anymore for  $5\ \mu\text{m} \times 4\ \mu\text{m}$  rectangular elements. However, the experimentally obtained threshold only describes the phase-stable NLSWs, while the incoherent components of the spectrum might emerge at lower power levels. Therefore, stabilization of NLSW in arbitrary sample geometries to an external reference signal is highly demanded.

### 7.6.1. NLSW Generation with additional Seed Frequency

The approach utilized in this work is inspired by a concept from semiconductor laser physics, where a semiconductor laser with anti-reflection coating is pumped hardly but not able to start laser emission yet, since the external resonator is missing [192]. By seeding an external laser beam with narrow linewidth into the crystal, a coherent amplification of the seed light takes place. The tiny amount of injected coherent laser radiation forces the broad emission spectrum of the crystal to emit light with the same frequency and phase as the seed light [193]. In magnonics, injection or phase-locking became an intensively studied topic with the emergence of spin-Hall [88, 194–198] and spin-torque nano-oscillators [10–15]. Especially due to the possibility of synchronizing these devices for applications in neuromorphic computing [199, 200]. Recently, the influence of a second frequency source was demonstrated on non-linear spin-wave processes [201].

Transferred to our NLSW excitation, this scheme appears as follows: The magnonic system is prepared by driving at  $f_{\text{rf}}$  and a power level which would be sufficient to excite NLSWs in larger geometries. However, in the case of a small element, the threshold to establish a coherent response of the system at  $3/2 f_{\text{rf}}$  is not exceeded, although the observation of a saturating uniform magnon mode indicates the presence of intrinsically generated non-linear frequency components. At this point, a seed frequency component is introduced to the excitation scheme, as depicted in Fig. 7.13a). In analogy to a seed laser in optics, the utilized 'seed' frequency will slightly force the precessional motion to become anharmonic in a coherent way. Thus, a suitable seed frequency would be  $3/2 f_{\text{rf}}$ . Consequently, the additional rf-source must be stabilized to the master clock of the setup. In the following, a large rf-signal at  $f_{\text{rf}}$  (also referred to as 'pump') with an amplitude on the order of 20 dBm is applied to the  $5\ \mu\text{m} \times 4\ \mu\text{m}$  element while an additional seed frequency component with a power level of approximately 0 dBm is added at  $3/2 f_{\text{rf}}$  to the same path by using an rf-power combiner. The  $f_{\text{rf}}$  pump power level is large enough to generate NLSWs in the larger element geometries and has a value above the

observed saturation of the uniform mode (cf. Fig. 7.2). To estimate the combination of seed and pump power levels at which the expected process starts, we performed measurements in a two-dimensional way as a function of both power levels within the  $5\ \mu\text{m} \times 4\ \mu\text{m}$  element.

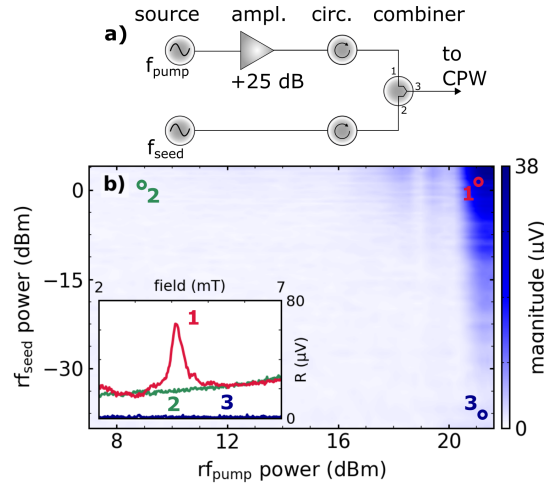


**Figure 7.13 | Injection locking of NLSW generation by using a seed frequency.** a) Modified excitation scheme for phase-locking experiments with additional seed frequency. b) NLSW response as a function of pump and seed frequency power levels for a  $5\ \mu\text{m} \times 4\ \mu\text{m}$  rectangular  $\text{Ni}_{80}\text{Fe}_{20}$  element. The inset shows field-resolved measurements for three different power combinations of pump and seed. The off-resonant background (1) for larger seed power levels is subtracted to obtain the regime of stabilized NLSW generation (2). In (3) no NLSW is possible even at large pump-power levels due to the small seed power.

In doing so, one clearly observes a power regime in which a large pump amplitude at  $f_{\text{rf}}$  with an additional  $3/2 f_{\text{rf}}$  seed component leads to a substantial enhancement of the non-linear signal response in the  $3/2 f_{\text{rf}}$  detection channel, as demonstrated in Fig. 7.13b). After passing a certain power level, tiny seed power levels are sufficient to stabilize the NLSW response. The inset in Fig. 7.13b) shows three exemplary situations with different combinations of pump and seed power levels. For both power levels being large, a clear maximum is obtained in the field-swept measurement. Note, the additional seed frequency component will simultaneously result in the excitation of the system at  $3/2 f_{\text{rf}}$ , which causes a uniform precession at the corresponding resonance condition. Additionally, DE spin-wave modes at slightly lower fields are expected to share the same field range with the generated NLSWs. Fortunately, these two excitations are easy to distinguish. The most straightforward proof of the non-linear nature of the signal components is the observation of other non-linear signals in the  $1/2 f_{\text{rf}}$  and  $5/2 f_{\text{rf}}$  channels since a coherent anharmonicity of the precession would directly generate signal components at all of these odd half-integer multiples. In contrast, the DE mode only appears at its fundamental frequency.

### 7.6.2. Imaging of Phase-Locked non-linear Excitation

To further verify that the observed excitation from Fig. 7.13 has a truly non-linear origin, spatially-resolved imaging was performed to analyze the wave vectors of the NLSW and identify the typical pattern in the reciprocal space. Such spin-wave patterns, as observed in section 7.4, clearly indicate the presence of NLSW and thus allow to distinguish DE-like spin waves from  $3/2 f_{rf}$  NLSW.

#### NLSW Stabilization in small Elements

By performing spatially-resolved measurements on one of the small  $5 \mu\text{m} \times 4 \mu\text{m}$  elements, as shown in Fig. 7.14, with additional seed frequency, one can obtain a phase-stable pattern in the  $3/2 f_{rf}$  detection channel. As discussed in section 7.2.2, it was not possible to obtain any coherent NLSW excitation in this sample geometry without additional seed frequency. Surprisingly, a pronounced NLSW pattern appears on top of a DE-like background, as shown in Fig. 7.14b). In addition, also  $1/2 f_{rf}$  and  $5/2 f_{rf}$  components can be observed in the same measurement. The corresponding 2D-FFT in panel c) provides a pattern that appears similar to the one presented before for spatially-resolved imaging of NLSW generation. Note that the DE-like background was filtered out to provide a more detailed picture of the NLSW excitation in k-space.

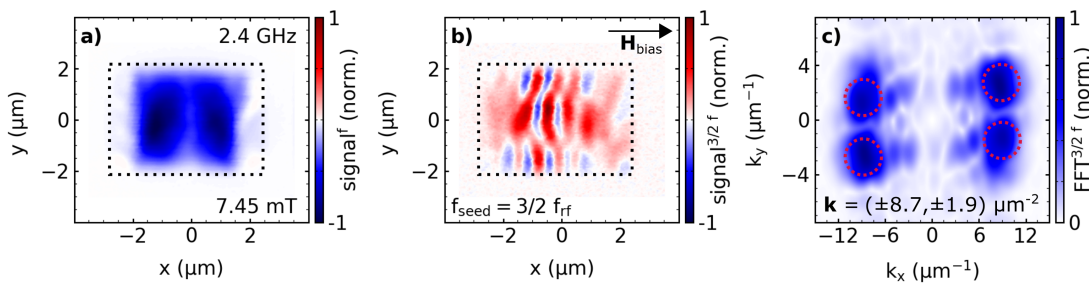


**Figure 7.14 | Spatially-resolved imaging of  $5 \mu\text{m} \times 4 \mu\text{m}$  rectangular element with additional seed frequency.** Panel a) and b) show spatially-resolved measurements of the  $5 \mu\text{m} \times 4 \mu\text{m}$  rectangular element at  $f_{rf}$  and  $3/2 f_{rf}$ , respectively. The 2D-FFT pattern in c) clearly shows the typical symmetry in k-space observed for NLSWs.

The NLSW wave-vector components obtained in this experiment are in agreement with observations for other geometries in section 7.4. Note that the element geometry is much smaller compared to previous measurements, which leads to a reduced resolution in k-space since the spatial resolution is still 300 nm. Therefore, the subsequent measurement will demonstrate the effect in a larger sample geometry, which provides a clear NLSW pattern.

### Variation of the Seed Frequency

The strong anharmonicity of the precessional motion originates in the large excursion angle and the strongly elliptic trajectory of the magnetization due to the geometry of the sample. As soon as NLSWs become visible at their corresponding alias frequency, automatically signal components at other half-integer multiples of the driving frequency emerge, as discussed in section 7.2.1. These half-integer NLSWs are a direct consequence of the strong modulation regime, and therefore they do not exist solely at one frequency. For this assumption, one would expect a stabilization of all NLSW signal components as soon as one of them overcomes the threshold to establish a coherent phase and gets stable over time. From this, the concept of varying the seed frequency to other half-integer multiples arises, which might decouple the  $3/2 f_{rf}$  NLSWs from DE spin-wave modes.

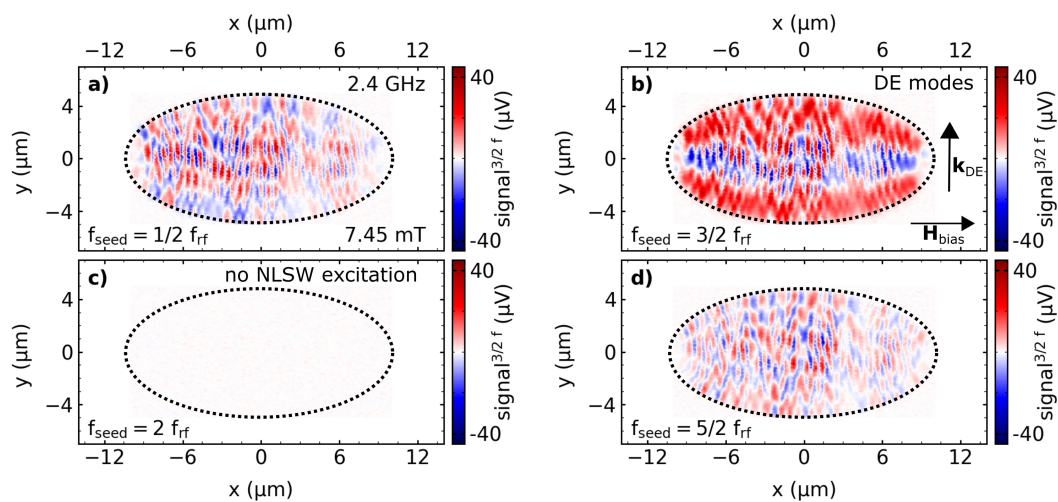


**Figure 7.15 | Imaging of stabilized non-linear spin waves at different seed frequencies.** The  $3/2 f_{rf}$  component in a  $20 \mu\text{m} \times 10 \mu\text{m}$  elliptical element at a driving frequency of 2.4 GHz is shown for different seed frequencies. Panel a) and d) demonstrate the NLSW generation at  $3/2 f_{rf}$  for seed frequencies of  $1/2$  and  $5/2$  of the driving frequency. In b) the NLSW is superimposed with the directly excited DE spin-wave mode at the corresponding field value of 7.45 mT. In addition, panel c) depicts the case of a  $2 f_{rf}$  seed frequency, which does not stabilize the NLSW generation and thus no coherent response is recorded.

As demonstrated in Fig. 7.15, the injection-locking process worked indeed for various cases. Here, different seed frequencies were used while the detection channel remained at the alias of  $3/2 f_{rf}$ . For odd half-integer multiples  $n/2 f_{rf}$  as seed frequency, the typical NLSW characteristics are observed in a phase-stable fashion within the lateral dimensions of the  $20 \mu\text{m} \times 10 \mu\text{m}$  elliptical element. Moreover, the observation of  $3/2 f_{rf}$  spin waves gets easier since the change of seed frequency allows to eliminate the DE-like background in the detection channel, which only occurs in Fig. 7.15b). To further validate this assumption, an integer multiple was used to seed the system. In particular, a seed frequency at  $2 f_{rf}$  does not stabilize the anharmonic precession.

Therefore, it does not result in any visible NLSW excitation at half-integer multiples of the driving frequency, as shown in c). The same behavior can be observed for additional  $f_{\text{rf}}$  or  $3 f_{\text{rf}}$  seed components. One has to mention, that the stable regime for NLSW with seed frequency occurs at a field value of 7.45 mT while the inherent process was stable at 6.85 mT for same experimental conditions (cf. Fig. 7.8b)).

### NLSW Stabilization in arbitrary Geometries

As shown in the last part for a  $20 \mu\text{m} \times 10 \mu\text{m}$  elliptical element, NLSW generation with additional seed is stabilized at slightly larger bias fields compared to the inherent excitation process in this element. However, it makes the non-linear features more robust against randomly appearing phase fluctuations, as discussed in section 7.3. Therefore, the presented driving scheme with an additional tiny seed frequency component allows controlling the properties of the generated NLSW more reliably. Fortunately, the stabilization process also works in cases where no inherent NLSW excitation was observable before, e.g., in the  $5 \mu\text{m} \times 4 \mu\text{m}$  element. Surprisingly, the non-linearities can also be stabilized in an entirely  $\text{Ni}_{80}\text{Fe}_{20}$  covered waveguide structure but are observed at comparably low signal intensity. We strongly suggest adapting this excitation scheme with seed frequency to overcome the limitation of the element's lateral dimensions or phase fluctuations for future experiments where coherent NLSW might be used.

#### 7.6.3. Phase Locking to a Seed Frequency

The concept of phase locking is well known in magnonics [51] in terms of synchronizing spin-torque [10–12, 14] and spin-Hall nano-oscillators [195, 196] to an external reference frequency. In such situations, the external frequency is utilized to stabilize the broad emission spectrum of the oscillator to the narrow linewidth of the seed frequency, as this frequency allows tuning the excited auto-oscillation over a broad frequency range. In addition, Brächer *et al.* [202] presented phase locking for parametric amplification of propagating spin waves, which allows to amplify or suppress the intensity of a magnon mode by controlling the phase shift between the spin wave and the rf-field of the magnon amplifier [47].

The concept presented by Brächer *et al.* is indeed a promising candidate for the control of NLSW excitation since they utilize the strongly non-linear three-magnon scattering process for the amplification. Thus we are convinced that such a concept is applicable to the presented stabilization process of NLSW generation. Adapted to the situation of  $3/2 f_{\text{rf}}$  spin-waves generation, a phase variation  $\Delta\theta$  of the seed frequency relative to the intrinsically excited and stabilized non-linear magnons at  $3/2 f_{\text{rf}}$  should allow to enhance or suppress the non-linear magnon mode and therefore provide an external control mechanism.

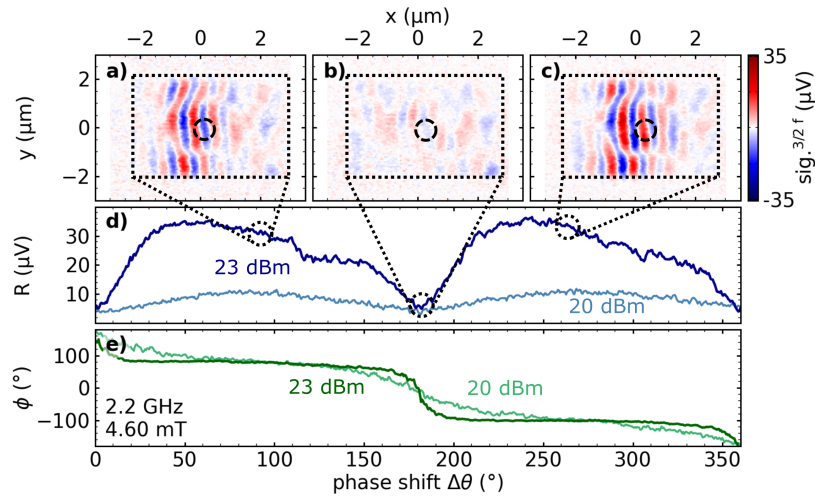


**Figure 7.16 | Phase locking of NLSW generation.** The  $5\ \mu\text{m} \times 4\ \mu\text{m}$  rectangular element is driven at 2.2 GHz and an additional seed frequency at  $3/2 f_{\text{rf}}$  is applied. The phase  $\Delta\theta$  of the weak seed component relative to the driving field is varied. In a)-c) we present spatially-resolved imaging of three different phase shifts. In b), the signal amplitude is suppressed, while the sign of the signal changes from a) to c). In d) and e), measurements of the magnitude and signal's phase  $\phi$  in the center of the element are presented, indicated by the black marker in a)-c). For a large pump-power level, the magnitude shows a clear minimum for a phase shift of  $0^\circ$ ,  $180^\circ$  and  $360^\circ$ , while in between two maxima can be obtained. The phase obtained in e) follows a plateau-like behavior for large power levels and a distinct phase jump in the minimum of the magnitude. For a reduced power level, the magnitude in d) shows a more sinusoidal development as the phase changes less rapidly. For an even lower value, no NLSW signal can be observed at all.

The phase shift variation  $\Delta\theta$  of the seed frequency allows indeed to control the signal amplitude of the NLSW signal obtained at  $3/2 f_{\text{rf}}$ , as demonstrated by spatially-resolved imaging in Fig. 7.16a)-c). The sign of the obtained signal in the center changes from a) to c), while a minimum in amplitude is observed in panel b). By performing a phase-resolved measurement in the center of the sample, as shown in d) and e), we identify a regime where the magnitude nearly vanishes as a function of phase shift  $\Delta\theta$  while in between these dips, the magnitude shows a broad maximum. A closer view on this behavior is governed by obtaining the signal's phase  $\phi$  as a function of seed phase shift  $\Delta\theta$ . Here, the phase of the NLSW switches sign while passing a minimum in magnitude, which results in the change of the signal's sign in the measurement area indicated by black circles in a)-c). For a large pump power level, the change of  $\Delta\theta$  does not affect the signal's phase over a broad plateau and only causes a rapid phase shift of  $180^\circ$  in the point of minimal magnitude. However, this behavior can be varied to a more smooth shift of the signal's phase and a sinusoidal change of the signal's amplitude by slightly reducing the pump or seed power level. Further reduction of the power level leads to a collapse of the stabilized NLSW generation, and only the DE-like background remains with a phase-independent magnitude and a linear change of the signal's phase.

The results presented in this section provide easily adaptable solutions for previously introduced problems. While the inherent NLSW generation was not possible in all types of geometries and

suffered from phase instabilities over time, the implementation of an additional seed frequency allows stabilizing these types of NLSWs. As discussed, this stabilization process works for all investigated sample geometries. Furthermore, by controlling the phase of the applied seed component, a possible control mechanism for the amplitude and phase of the NLSW is revealed. This concept might also be applicable for other material systems such as YIG, which did not show  $3/2 f_{\text{rf}}$  spin waves so far, even if predicted by Bauer *et al.* [54]. In combination with previously mentioned control possibilities, NLSW excitation with large wave vectors might be a promising candidate for future magnonic applications, such as NLSW emitters or magnon amplifiers.

---

# Frequency Comb Generation in $\text{Ni}_{80}\text{Fe}_{20}$

---

In the previous chapter, the process of high-harmonic generation (HHG) for a few harmonics at integer multiples of the excitation frequency was demonstrated. However, above the 5<sup>th</sup> harmonic of this process, no coherent signal was obtained by means of SNS-MOKE at the corresponding resonance field. Nevertheless, the generation of higher harmonics is of general interest for a broad field in physics and might pave the way towards novel types of applications. Non-perturbative frequency-multiplication processes over several octaves were observed at optical frequencies in response to highly intense laser pulses [203, 204]. In contrast to that, HHG in the field of magnonics has been studied with moderate success in recent years, since most experimental observations of HHG were restricted to a few harmonics only [52, 53], which is in agreement with the findings from chapter 7. However, it is highly desired to apply HHG for future magnonic and spintronic applications, where standard electrical signals might be up-converted to the GHz regime, feasible of driving magnetization dynamics within devices.

## 8.1. Indication of an All-Magnonic Frequency Comb

In the course of the last chapter, the possibility of NLSW excitations due to the strongly anharmonic precessional motion of the magnetization was discussed. As shown in section 7.2.1, this anharmonic motion does not only create spin waves at odd half-integer multiples of the driving frequency but also generates components that are integer multiples of the fundamental frequency. The latter harmonics show signal components distributed over a broad field range, also detectable at surprisingly low bias fields with large signal amplitudes. Therefore, a more detailed analysis of these low-field resonances at higher harmonics of the fundamental frequency is required. In doing so, we investigated HHG in polycrystalline  $\text{Ni}_{80}\text{Fe}_{20}$  layers in the low bias field regime by using nano-diamond magnetometry [67, 68, 205] and SNS-MOKE. The nano-diamonds contain NV centers, which feature a well-known ESR transition at 2.87 GHz. By applying a static magnetic field, the Zeeman splitting of the ESR broadens the accessible frequency range. Whenever a dynamic magnetic stray field oscillates at a frequency components matching the ESR cone at a given bias field, the NV-centers are sensitive to these dynamic field components. Thus, NV-centers have been proven to be a valuable local mapping technique

for magnetization dynamics over the last years since they are sensitive to dynamic stray fields on the nanometer scale [66, 69, 206]. In our NV-center magnetometry measurements [190], magnetic features became visible which were not matching the ESR condition at first glance. We detect a continuous imprint of the FMR which contributes to the signal by magnon-scattering processes. These processes result in a frequency component matching the ESR condition via  $f_{rf} + f_{\text{thermal}} = f_{\text{ESR}} + f_{\text{arb}}$ . [69]. Here, the excited magnon at  $f_{rf}$  might scatter with a thermal magnon  $f_{\text{thermal}}$  resulting in one frequency component matching the ESR condition and one magnon with different frequency. Even NLSW generation at  $3/2 f_{rf}$  is detectable with this technique [190]. Surprisingly, we additionally observed a large number of sharp replicas of the ESR line, which were not appearing in the absence of a ferromagnetic layer. These features were found in the field range below 3 mT and covered the range 50 MHz up to 2.87 GHz in NV-center magnetometry [190]. From these initial findings, it appears that the spacing between the replicas follows a  $1/n$  behavior, where  $n$  is the harmonic mode number, clearly indicating a frequency comb generated in the magnetic material itself [190]. To further understand the origin of this HHG, we investigate the same sample by means of SNS-MOKE with a multi-frequency LIA.

### Sample Geometry

The investigated sample contains a CPW which is entirely covered with a 20 nm thick Ni<sub>80</sub>Fe<sub>20</sub> film. The Au/Ni<sub>80</sub>Fe<sub>20</sub> waveguide structure was defined through electron beam lithography and lift-off technique. The CPW was partially covered by nano-diamonds containing NV centers. This geometry provides IP excitation of the dynamic magnetization as well as the NV-centers for a bias field applied parallel to the CPW. To obtain clear SNS-MOKE images, we detected on positions without nano-diamonds.

## 8.2. Field-resolved Detection of higher Harmonic Generation

At this point, it unclear if the scattering process via thermal magnons results in either coherent or incoherent excitations. Hence, a comparison of the two techniques is mandatory for the interpretation of obtained signals. NV-center magnetometry and SNS-MOKE are both sensitive to local magnetization dynamics but vary in some important details. The spatial resolution of SNS-MOKE is limited by the laser's focal spot size, while NV-centers are sensitive to dynamic stray fields on the nano-scale [206]. The obtained signal in SNS-MOKE is phase-sensitive, which only allows for the detection of coherent magnons in this geometry. In addition, it only accesses the dynamic  $M_z$  component, while the NV centers might respond to various components depending on their relative orientation. Furthermore, NV-center magnetometry is accessing all types of magnons matching the ESR condition, since it only detects the magnitude of the magnetization dynamics. However, due to the ESR of the NV-center, this technique is

only sensitive in a frequency range around 2.87 GHz defined by the Zeeman splitting at a given bias field. Thus, the NV-centers only detect signal components that are either directly excited at a suitable frequency or due to conversion effects mediated by scattering processes creating the required frequency component. SNS-MOKE does not suffer from this restriction and allows to distinguish between different frequency components as discussed in chapter 7.

The first indication of coherent HHG is given by field-swept measurements, as presented in Fig. 7.4. Signal components at the FMR condition are visible up to the 4<sup>th</sup> harmonic corresponding to a frequency of 9.2 GHz. The resonance condition for the employed excitation frequency is on the order of 5 mT. In comparison to the experiments performed by Koerner *et al.*, the resonance field of 3 mT defines the upper edge of observable features in NV-center magnetometry. Therefore, the excitation frequency (and so the resonance field) needs to be further reduced to get access to the HHG regime by means of SNS-MOKE, as obtained in NV center experiments. For this purpose, we performed SNS-MOKE detection at an rf-frequency of 319 MHz with the corresponding alias frequency of 1 MHz. For the 5<sup>th</sup> harmonic (1.595 GHz) the resulting alias frequency is 5 MHz.

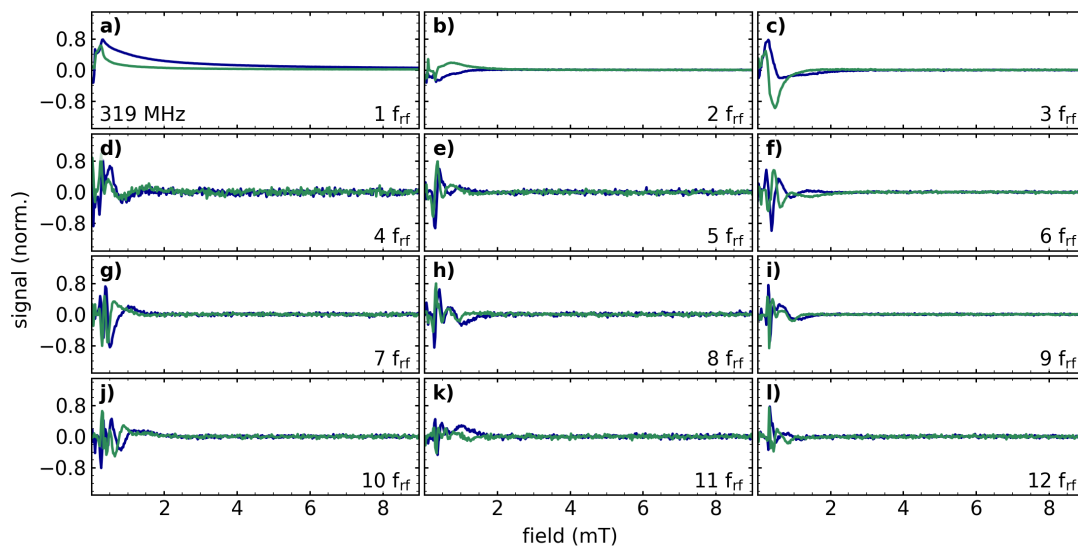


**Figure 8.1 | Field-swept measurements of multiple harmonics of 319 MHz.** The real and imaginary part of the dynamic susceptibility is detected in a field-swept measurements for an rf-excitation frequency of 319 MHz. Panel a) shows the response at the fundamental frequency, while the other panels depict the response in higher-harmonic detection channels.

By using this low rf-frequency, we obtain signal components in a large number of higher harmonics at low bias fields. Note that the results of the field-swept measurements exclude the rf-source and the amplifier as possible origin of the obtained higher harmonics in Fig. 8.1. Additional higher harmonics emitted from the rf-source or as a result of the amplification process would give rise to uniform signal contributions at different resonance fields (as discussed

in 7.6.3). In this particular case, the 5<sup>th</sup> harmonic of the 319 MHz fundamental frequency has its resonance field at 4 mT and thus would be visible in the investigated field range in Fig. 8.1e). However, the higher harmonic components shown in Fig. 8.1 appear all at the same resonance field as pretended by the fundamental frequency and are surprisingly restricted to this field range for all twelve harmonics shown here. Only the amplitude of the harmonics decreases as a function of harmonic number. This decrease of amplitudes scales up as the bias field increases, emphasizing the importance of very low resonance fields for the observation of this process. In Fig. 7.4 the highest harmonic component was the 4<sup>th</sup> at 9.2 GHz, here a detection of up to 12 harmonics was performed corresponding to a frequency of 3.8 GHz. In the present case, detection of other higher harmonics is possible, but yields no additional insight in field-resolved measurements. Note that due to the large power levels, impurities in the rf-excitation indeed exist. However, compared to the fundamental frequency, they appear at power levels of  $-40$  dBc for the first few harmonics and at even lower levels for higher harmonics. Still, it might be possible that these very tiny frequency components stabilize the frequency comb for coherent SNS-MOKE detection in analogy to the phase-locking effects obtained in section 7.6. Nevertheless, we are convinced that the detected harmonic signal components at low bias fields are not a result of spectral impurities and truly originate from non-linear frequency multiplication processes.

### Time-Trace Reconstruction

To access excitation conditions even more similar to the results shown by Koerner *et al.* [190], the rf-excitation needs to be on the order of 100 MHz or less. For example, a frequency of 57.4 MHz would match the ESR condition in NV-center magnetometry with its 50<sup>th</sup> harmonic. In SNS-MOKE, such low excitation frequencies will result in an off-resonant excitation of the spin system. Thus, field-swept measurements at lower frequencies are not offering any lineshape information (as indicated for 319 MHz in Fig. 8.1). In the following experiment, only magnitude and phase information at a fixed bias field for different harmonics of the excitation are recorded. To guarantee stable phase relations of the different harmonics relative to the fundamental frequency, the oscillator frequency of the LIA is fixed to the alias of the fundamental frequency, and only the harmonic number is varied. This technique is easily applicable for the chosen 1 MHz alias since higher harmonics of the alias ( $\varepsilon = n \cdot 1$  MHz) correspond to higher harmonics of the excitaton ( $n \cdot 79$  MHz). In contrast to a direct setting of the oscillator frequency to the corresponding alias of the harmonic, this method does not randomly reset the phase. In this scheme, the detection of magnitude and phase information allows reconstructing the time trace of the strongly anharmonic precessional motion via

$$A(t) = \sum_n R_n \sin(\omega_n t + \phi_n), \quad (8.1)$$

where  $R_n$  and  $\phi_n$  are the magnitude and phase values at harmonic number  $n$  and  $\omega_n$  is the frequency of the  $n^{\text{th}}$  harmonic.

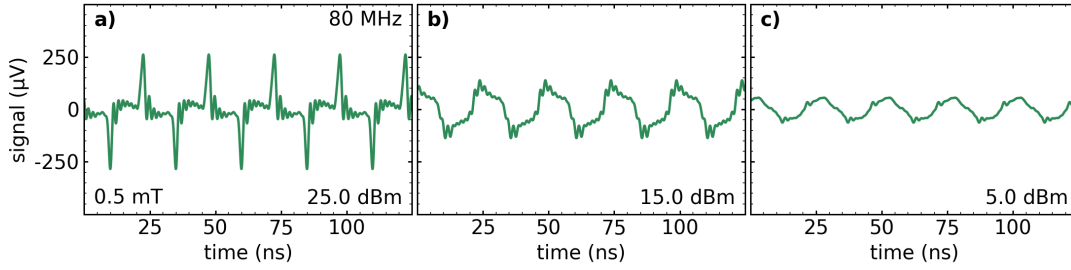


**Figure 8.2 | Reconstructed time trace with 79 MHz fundamental frequency.** Magnitude and phase values up to the 15<sup>th</sup> harmonic were recorded for a bias field of 0.5 mT and an rf-excitation frequency of 79 MHz. The reconstructed time trace is plotted for three different power levels showing the transition from a mostly linear response regime in c) to a highly non-linear regime in a).

The reconstructed time traces for measurements at 79 MHz and 0.5 mT bias field are shown in Fig. 8.2 for three different power levels. Each trace contains the signal components of 15 harmonics. In panel a) the precessional motion is strongly anharmonic due to large coherent signal components in higher harmonic channels. In c), the time trace for a low power excitation appears mostly harmonic, while b) represents the transition regime. The existence of up to 15 harmonics obtained in these measurements indicates the presence of a frequency comb spanning over a wide frequency range. Remarkably, the reconstructed time trace in a) shows the signature of solitonic behavior [134], which requires further investigation in future experiments.

### 8.3. Spatially-resolved Analysis of the Frequency Comb

To further understand the excitation mechanism of the higher harmonics which form the frequency comb, we investigated the HHG in a spatially-resolved manner. Therefore, we map the real and imaginary part of 20 different frequency components within an area of  $5 \mu\text{m} \times 5 \mu\text{m}$  in the center of the waveguide.

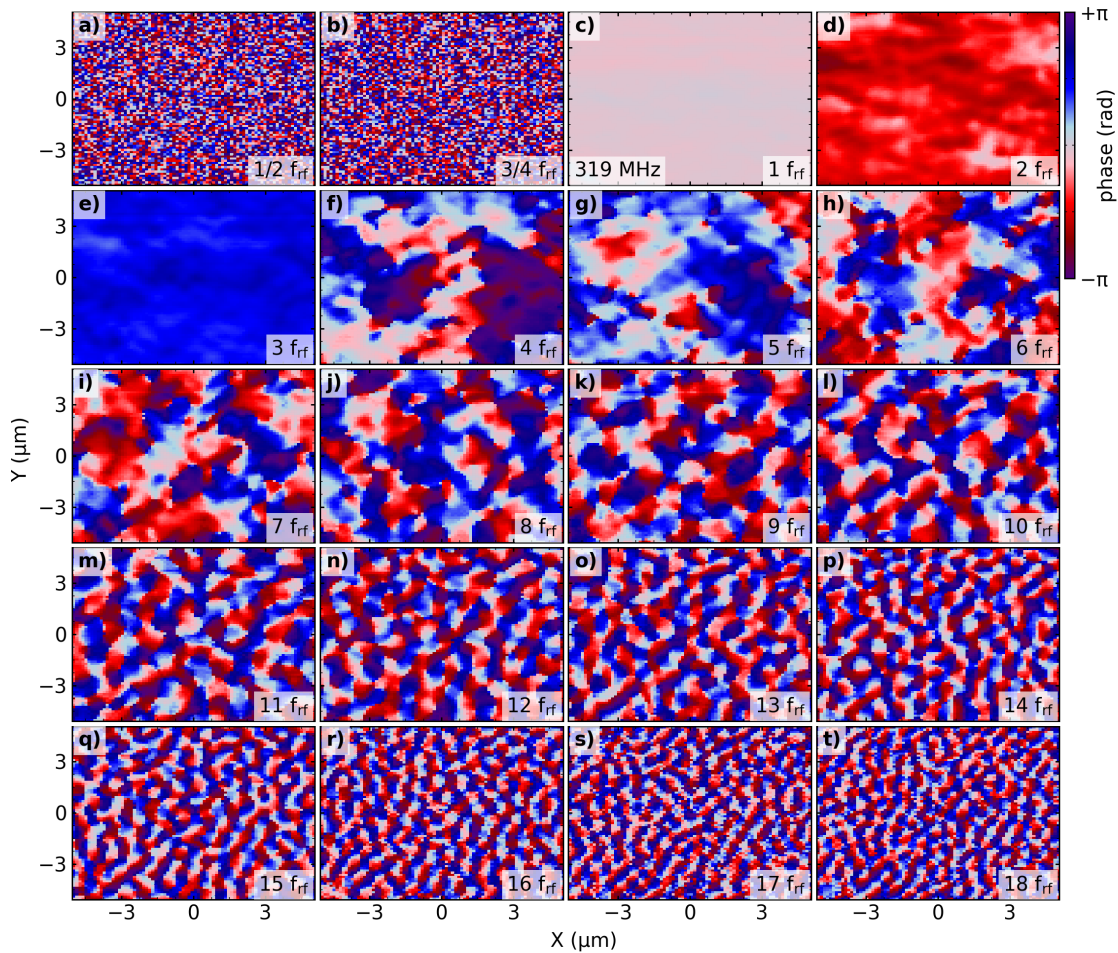
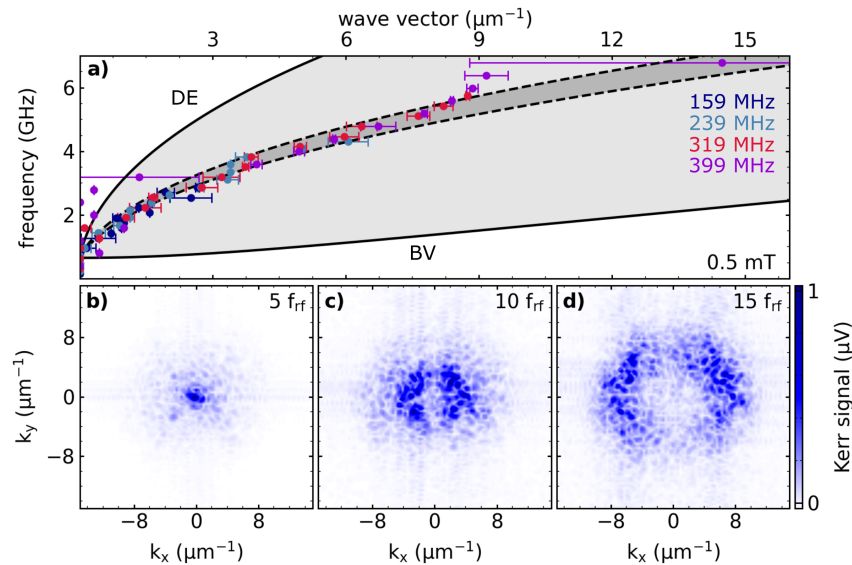


**Figure 8.3 | Spatially-resolved imaging of higher harmonics within an all-magnonic frequency comb.** For a 319 MHz excitation the phase of the SNS-MOKE response is shown in different frequencies channels for a fixed bias field of 0.5 mT. Panel a) and b) depict the case of non-integer harmonics which contain no signal components. The other panels contain the spatially-resolved phase information for interger harmonics, ranging from the fundamental frequency in c) to the 18<sup>th</sup> harmonic in t).

Figure 8.3 shows the obtained spatially-resolved images of the signal's phase in 20 harmonic detection channels. A mostly uniform component is obtained at the fundamental frequency, as shown in c), as expected for an off-resonant excitation. Such a uniform background is also obtained for lower harmonics in d) and e). Surprisingly, a phase-stable fragmentation of this component becomes more and more pronounced in the higher harmonic channels with decreasing pattern size for increasing mode numbers. In addition, the recorded spatially-resolved data for non-integer harmonics such as  $1/2 f_{rf}$  and  $3/4 f_{rf}$  is shown in a) and b). For these particular alias frequencies, no coherent response of the system is obtained at a bias field of 0.5 mT. The existence of stable phase patterns in the higher harmonics is rather surprising, emphasizing the inherent non-linear processes from which the frequency comb emerges.

### 8.3.1. Wave Vectors of the Frequency Comb

Spin-wave patterns in higher-harmonic frequency channels can be analyzed by performing 2D-FFT to access the wave vectors and reconstruct the non-linear spin-wave dispersion of the HHG. To obtain the average IP wavenumber of such symmetric patterns, we determine the maximum values for  $k_x$  and  $k_y$  components in k-space for each quadrant and average them.



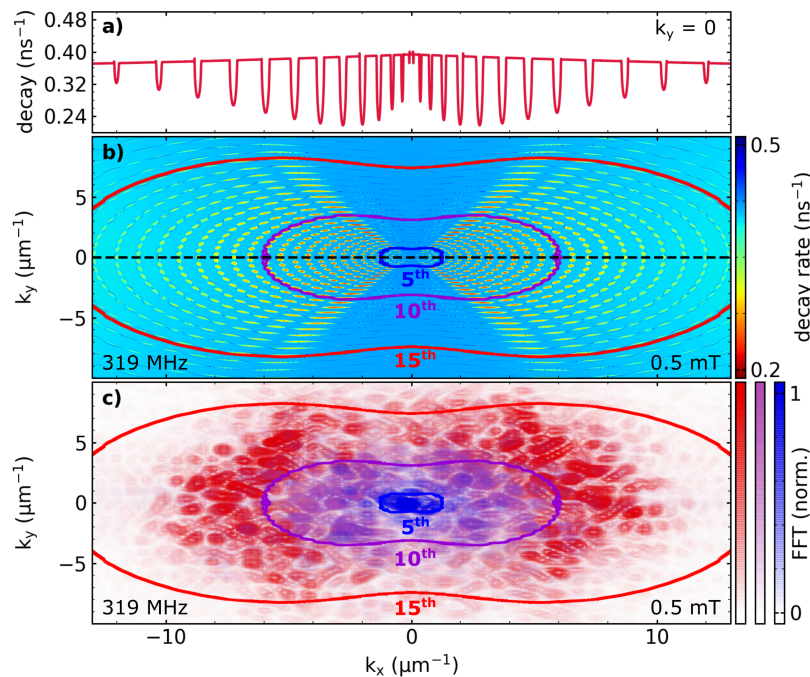
**Figure 8.4 | Extracted in-plane wave-vector distribution of the frequency comb for different fundamental frequencies.** a) From spatially-resolved measurements, such as shown in Fig. 8.3, wave-vector components for 15 higher harmonics are extracted by applying a complex 2D-FFT. The frequency as function of IP wavenumber follows a particular branch located in the center of the spin-wave band. In b) - d) three different 2D-FFT patterns for the 5<sup>th</sup>, 10<sup>th</sup> and 15<sup>th</sup> harmonic of a 319 MHz fundamental are shown, respectively.

Figure 8.4a) shows the frequency of the detected harmonics as a function of obtained IP wavenumber for different fundamental frequencies, indicated by the color code. The calculated spin-wave dispersion for 0.5 mT is depicted by solid lines to identify possible magnon states. Interestingly, only harmonic frequencies within the spin-wave band show a wavenumber that can be clearly distinguished from zero. In contrast, harmonic frequencies below only contain an off-resonant uniform background, as shown in Fig. 8.3c)-e). One has to mention that the determination of the IP wavenumber is not perfectly precise. Besides a larger scanning area in real space, a 2D fitting procedure of the obtained wave-vector pattern in k-space would be required to improve the quality of the wavenumber determination. To further understand this type of analysis, reciprocal space images for three specific cases are presented in Fig. 8.4b)-d). The wave-vector components are arranged in elliptical shapes with a broad linewidth. However, the analysis seems sufficient to reconstruct the basic trend of wave-vector development with harmonic frequency. As one can observe in a), the harmonics of different fundamental frequencies

follow the same dispersion branch, which can be identified as an intermediate branch between DE and BV geometry, which can be qualitatively calculated for an IP field orientation of roughly  $37.5^\circ$ . The momentum necessary to establish the observed patterns in higher-harmonic components might originate from the grain structure of the polycrystalline  $\text{Ni}_{80}\text{Fe}_{20}$  layer, as demonstrated by micromagnetic simulations by Koerner *et al.* [190]. However, the origin of the emerging frequency comb is not solely caused by this spatial variation itself.

### 8.3.2. Lifetime Calculation

To get further understanding of the non-linear behavior of the LLG itself, we utilize the k-space model introduced in section 2.4.2 to calculate the spin-wave lifetime and corresponding frequencies for each point in k-space. In this particular situation, we performed calculations for a 319 MHz fundamental frequency and a bias field of 0.5 mT, as used in the experiments. In contrast to the previously presented calculation, these values are much smaller and correspond to an off-resonant excitation.



**Figure 8.5 | Spin-wave decay rate in k-space for 0.5 mT.** The k-space model allows to calculate the spin-wave decay rate for each wave vector and reveals pockets of strongly decreased decay rate (enhanced spin-wave lifetime). a) A line cut along  $k_y = 0$  shows the pockets which correspond to regions of frequency locking [54]. In b) these pockets expand symmetrically around the uniform mode and appear at all half-integer multiples of the excitation within the spin-wave band. The solid lines depict iso-frequency lines on which the pockets are oriented. In c) the obtained 2D-FFT patterns from Fig. 8.4 are superimposed with the corresponding iso-frequency lines, indicated by the color code.

Compared to the example demonstrated in Fig. 2.6, a large number of pockets with decreased spin-wave decay rates are revealed in k-space, as shown in Fig. 8.5b). Interestingly, the elliptical arrangement of these pockets corresponds to iso-frequency lines of even and odd half-integer harmonics of the driving frequency. The distance between these features in k-space appears much smaller compared to the findings from chapter 7 due to the extremely low excitation frequency and low bias field. Within these pockets, frequency locking occurs, as reported by Bauer *et al.* [54]. Interestingly, a cut at  $k_y = 0$  (Fig. 8.5a)) only provides integer multiples of the excitation. By plotting the calculated iso-frequency curves on top of the k-space spectra from Fig. 8.4b)-d), the obtained wave-vector components are not matching these lines perfectly. Nevertheless, the iso-frequency lines show an upper boundary for the excited spin waves, expanding to larger values with an increasing harmonic number. However, the enhanced spin-wave lifetime might explain the phase stability observed in the SNS-MOKE measurements but does not reveal the generation mechanism of the obtained frequency comb.

### 8.3.3. Origin of the Frequency Comb

From NV-center magnetometry experiments more than 60 harmonics are revealed. As demonstrated in Fig. 8.3 and Fig. 8.4a), the fragmentation of the observed spin-wave pattern increases with harmonic number but detected wave vectors at 2.87 GHz have a wavelength still within the spatial resolution limit of the SNS-MOKE. Therefore, similar harmonic numbers are theoretically accessible by SNS-MOKE measurements for low-frequency excitation, as indicated in Fig. 8.1. At first glance, the generation of a frequency comb with more than 50 harmonics can not be explained by only considering the intrinsic non-linearity of the LLG 2.18. This component only causes a few odd harmonics with strongly decreasing amplitude as a function of harmonic mode number for large driving power levels. Similar behavior can be observed by performing micromagnetic simulations for a perfect  $\text{Ni}_{80}\text{Fe}_{20}$  layer, as demonstrated in reference [190]. In addition, by calculating the spin-wave lifetime with the aid of the analytical model, pockets of decreased decay rates appear for even and odd half-integer multiples of the fundamental frequency. However, none of these magnons is exceeding the threshold condition and becoming critical, which is in agreement with Fig. 8.3b), where no odd-half integer NLSW generation is obtained. Hence, these findings must conclude that an important part of the explanation is still missing.

A plausible explanation might be that the assumption of a perfect  $\text{Ni}_{80}\text{Fe}_{20}$  layer does not hold. From micromagnetic simulations of spatially varying  $M_s$ , Koerner *et al.* found that the obtained spectrum changes from a few harmonics (perfect film) to a frequency comb comparable to the experimental observations. Instead of a uniform distribution of magnetic properties, a spatial variation is the missing link. In addition, for the most straightforward case of such a spatial variation of  $M_s$ , formed by two neighboring regions with slightly different  $M_s$ , a magnonic Mach cone [207] emerges at the boundary.

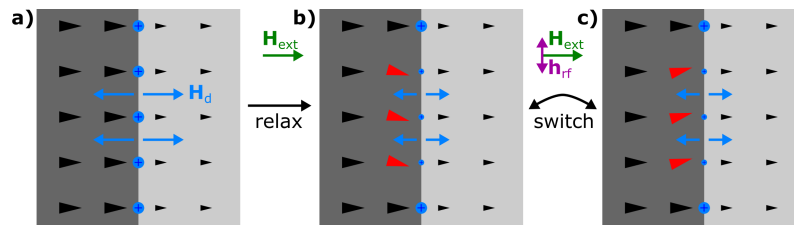


**Figure 8.6 | Model of the switching process under rf-excitation.** a) Simple model of the dynamic behavior at a boundary of two regions with slightly different magnetic properties. Uncompensated surface charges arise at the boundary between regions, causing demagnetization fields  $\mathbf{H}_d$  (blue arrows). b) The free energy is lowered by a tilt of the magnetization in the direction of the boundary, as indicated in red. b)-c) rf-excitation leads to rapid switching between different tilted states and causes spin-wave emission.

The physical mechanism leading to this magnonic Mach cone originates from switching events at the boundaries of neighboring grains. In the case of a  $M_s$  step at the boundary of the two regions (as shown in Fig. 8.6), the magnetization at the boundary tilts to minimize stray fields. This tilted state is energetically degenerated, as indicated in Fig. 8.6b)-c), and by applying an rf-driving field along the boundary, a switching of these states is observed [190]. From this mechanism at velocities larger than the phase velocity of dipolar spin waves, a shock-front emerges due to emitted spin waves, also referred to as spin-Cherenkov effect [207]. In a more realistic model of the sample, a grain structure forms a non-collinear network of coupled non-linear oscillators in which the single shock fronts at each boundary superimpose and form a stable phase pattern. In combination with the increased spin-wave lifetime arising from the non-linearity of the equation of motion, the stabilization of spin-wave HHG might be further favored. This multiplication process easily allows for frequency up-conversion from several MHz up to the 10 GHz regime within the ferromagnetic layer itself.

# Conclusion

---

In this work, we established super-Nyquist sampling magneto-optical Kerr microscopy (SNS-MOKE) as a valuable technique in fundamental magnonics research. The major limitations of conventional TR-MOKE techniques were overcome by exploiting aliasing effects in the frequency domain. Here, the inherent modulation scheme allows for simultaneous detection of the real and imaginary part of the dynamic susceptibility in micron-sized magnetic devices. Besides the arbitrarily high-frequency resolution, SNS-MOKE yields the possibility to detect various frequency components of the magnetic response simultaneously, such as linear and non-linear phenomena or sidebands due to different modulation techniques. Thus, our experimental approach yields the possibility of investigating a large variety of experimental configurations and physical concepts.

In particular, we investigated yttrium iron garnet (YIG) as the most promising material candidate for magnonic applications. We presented a novel approach of locally determining the Gilbert damping parameter while avoiding inhomogeneous linewidth broadening. With this technique, statements on the quality of material systems can be made with remarkable precision. In addition, we exploited the incomparably high-frequency resolution of SNS-MOKE to draw a detailed picture of propagating spin-wave modes in YIG. In this way, we mapped out an avoided crossing in the magnonic band structure and demonstrated the usability of such an intrinsic effect for controlled guiding of magnons. Here, current-carrying wires can easily provide the required additional magnetic fields to allow spin-wave guiding in a dynamic manner.

As a next step, 3D micron-sized YIG sample geometries, fabricated with the aid of novel processes, were investigated in terms of their quality in comparison to extended layer structures. The fabrication process as well as the transfer of YIG devices onto other substrates mostly conserves the excellent magnetic quality. Thus, micron-sized YIG devices might be a suitable alternative for functional magnonic applications compared to extended YIG layers. This technological path is further promoted by the possibility of transferring these devices to arbitrary substrates and implementing them in - to this day - inconceivable experimental configurations. That renders transferred micron-sized YIG devices as a novel building block for future experiments, where local control might be imaginable via the spin-Hall effect (SHE).

One of these nearly impossible experimental geometries is the transfer of a micron-sized YIG structure to a piezoelectric surface acoustic wave (SAW) carrying substrate. Here, SNS-MOKE

yields the possibility of distinguishing between magnetic and non-magnetic contributions to the Kerr signal due to the strain-induced birefringence caused by the traveling SAW. We carried out an intensive study in Ni, one of the typically used material systems for SAW-induced ferromagnetic resonance (FMR) experiments, and compared our findings with the transferred YIG devices. By this procedure, we identified experimental geometries in which magneto-elastic excitations were favored within the material systems and analyzed the wave-vector spectrum. In addition, we investigated how geometrical confinement affects the magneto-elastic coupling.

In the future, transferred YIG devices might be an exciting playground for non-linear phenomena, such as demonstrated for  $\text{Ni}_{80}\text{Fe}_{20}$  microstructures in this thesis. In this model system, we observed previously predicted non-linear spin wave (NLSW) excitations in the low bias field regime for the first time in a spatially-resolved manner. Here, the SNS-MOKE approach enables for simultaneous frequency-resolved detection of coherent linear and non-linear magnetization dynamics with second-to-none precision. A detailed investigation of the threshold behavior and generated wave vectors allows to precisely generate NLSWs. This inherently non-linear process did not offer a coherent response for very small sample geometries. However, we proposed a modification of the excitation geometry by implementing a second frequency source to stabilize the incoherent response. Besides the stabilization of NLSWs, this concept serves as a direct control mechanism that allows to suppress the non-linear response or to set the sign of the obtained non-linearity's phase. The concept applied here might be used as a non-linear magnon amplifier, which either enhances or suppresses propagating NLSWs.

Furthermore, we investigated high-harmonic generation (HHG) in  $\text{Ni}_{80}\text{Fe}_{20}$  structures at very low bias fields. Initial experiments indicated the generation of a six-octave spanning frequency comb. By complementary SNS-MOKE measurements, we emphasized this finding and revealed the complex spin-wave patterns excited at higher harmonics of the excitation frequency due to the spin-Cherenkov effect. This frequency conversion mechanism at fields close to zero offers the possibility of all-magnonic HHG within the magnetic material itself. Thus, electrical signals in the MHz range could be easily up-converted to drive magnetization dynamics at GHz frequencies. Such non-linear effects are even conceivable in transferred YIG structures implemented in tailored excitation geometries.

The roadmap for future experiments comprises a variety of combinations of the introduced concepts. Besides the implementation of YIG microstructures in suitable geometries for NLSW generation, also non-linear detection schemes for SAW-driven experiments are imaginable. In terms of magneto-elastic coupling, additional rf-antennas might be exploited as control mechanism of the elastically excited dynamics. Moreover, both presented non-linear concepts are not solely restricted to  $\text{Ni}_{80}\text{Fe}_{20}$  or YIG but might also apply to other materials as well as heterostructures. In such heterostructures locally applied spin currents generated via the spin-Hall effect could enable controlling of the non-linear processes' efficiency and thus switch the non-linear response.

# Appendix

## A.1. Magnetic Characterization of $\text{Ni}_{80}\text{Fe}_{20}$ Samples

A basic routine of sample characterization in the SNS-MOKE setup contains rf-power dependent measurements, such as shown Fig. 7.3, as well as a frequency-dependent detection of resonance field and linewidth. These measurements were carried out in the extended layer sample and in the sample with different  $\text{Ni}_{80}\text{Fe}_{20}$  elements to ensure that the magnetic properties are in agreement with literature and in order to guarantee that NLSW generation appears under similar conditions in all of these devices.

### A.1.1. Extended Layer Sample

First, we perform frequency-resolved measurements for the extended layer sample at the center of the CPW. Here, the rf-excitation lies in the film plane.

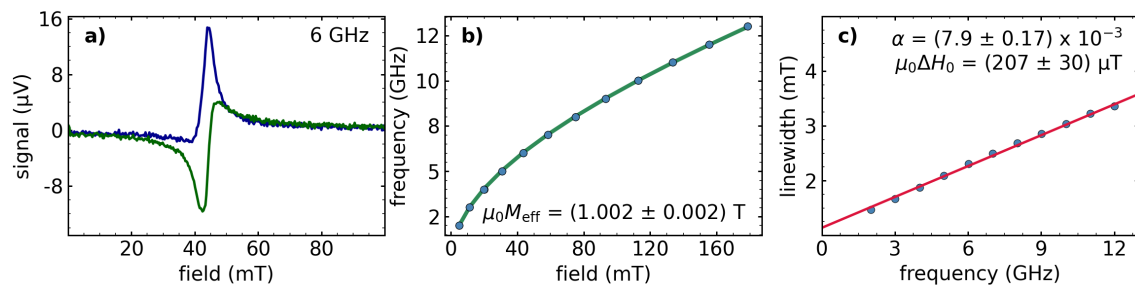


**Figure A.1 | Frequency-resolved measurements to obtain the Kittel fit and determine the Gilbert damping.** a) A field-swept measurement is shown for 6 GHz. Such measurements were performed in a frequency-resolved manner to obtain the Kittel plot in b) and the Gilbert damping in c).

The values for the effective magnetization as well as for the Gilbert damping constant are in good agreement with literature [74].

### A.1.2. Ni<sub>80</sub>Fe<sub>20</sub> Elements

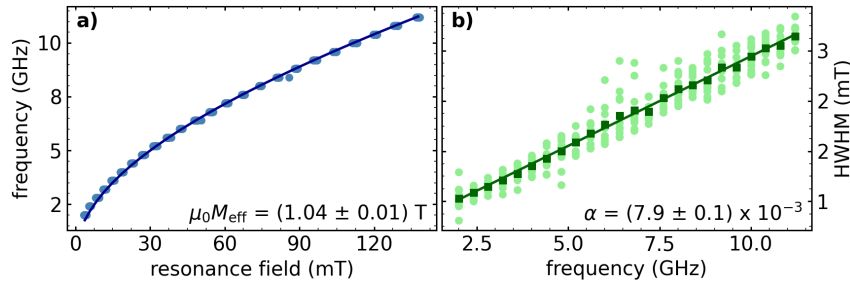


**Figure A.2 | Frequency-resolved measurements in Ni<sub>80</sub>Fe<sub>20</sub>.** For all Ni<sub>80</sub>Fe<sub>20</sub> elements, frequency-resolved measurements were performed in the center of each device. From this procedure the Kittel plot obtained in a) gives an average effective magnetization, with very tiny variations of the obtained data points. The linewidth data shown in b) allows to determine the Gilbert damping, averaged for all devices.

The  $M$  values are in good agreement for all devices shown in Fig. A.2a). However, the linewidth data obtained in b) has a larger variation. One reason might be the different shape of the elements. In particular the smallest element should show a slight enhanced damping. More important for the linewidth fitting is the fact, that in these elements not only the uniform mode is excited, but also DE spin-wave modes appear with non-vanishing amplitude. These modes need to be considered in the fit routine, by using a fit function with a superposition of at least two Lorentzian peaks. This complicates the perfect determination of the linewidth of the main resonance, since the number of fitting parameters doubles. Nevertheless, the obtained damping value is in good agreement with literature and the extended layer sample.

## A.2. Magnetic Characterization of YIG

In order to obtain realistic values for the film thickness  $L$  and the exchange constant  $A_{\text{ex}}$  we analyzed PSSW modes by means of inductive FMR in an extended YIG layer. We used the same sample as shown in chapter 4 and thus also used the same CPW.

Therefore, we first performed frequency-resolved measurements in the point of minimal dispersion by means of SNS-MOKE to determine the effective magnetization and the Gilbert damping constant. These data is shown in Fig. A.3a) and corresponds to the measurements presented in Fig. 4.11. In a second step we performed frequency-resolved measurements in the FMR setup to obtain the resonance positions of the uniform mode and PSSWs.

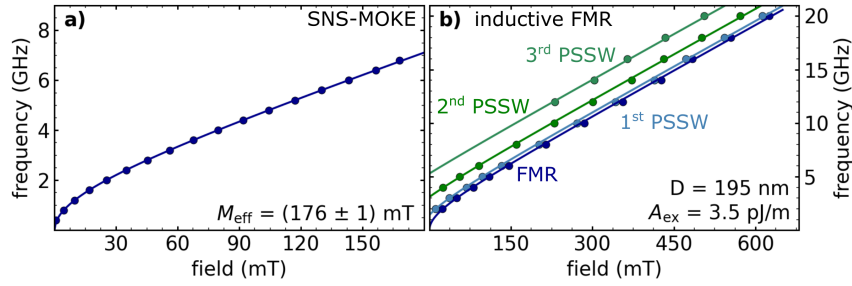


**Figure A.3 | Frequency-resolved SNS-MOKE and inductive FMR measurements in YIG.** a) SNS-MOKE measurements performed in the point of minimal dispersion to obtain the effective magnetization (cf. 4.3). In panel b), frequency-resolved inductive FMR measurements are shown of the FMR mode and three PSSW modes.

The values shown in Fig. A.3b) were fitted by using the preliminary results for  $\mu_0 M_{\text{eff}}$ . The fit routine results in an effective thickness of 195 nm and an exchange constant of  $3.5 \text{ pJ m}^{-1}$ . All obtained values are in good agreement with literature [74] and are close to ones used for the modeling of the avoided crossing in section 4.2.

### A.3. Exchange Coupling in a YIG/Ni<sub>80</sub>Fe<sub>20</sub> Bilayer

Investigating strongly coupled magnon systems in YIG based heterostructures [42, 43, 143] became a hot topic during the last years due its applicability in quantum computing or data storage. On the one hand, the coupling of magnons with cavity photons is studied for a large variety of system. On the other hand magnon-magnon coupling in two layer systems is of interest since it offers to possibility to convert a magnon in a conducting systems into a different magnon in an adjacent insulating system.

The same sample utilized for the magnonic waveguide in section 4.4.1 already consists of a two layer system with 192 nm YIG and 10 nm Ni<sub>80</sub>Fe<sub>20</sub> which made it inevitable to try how such measurements could be performed with a local measurement technique such as SNS-MOKE. Xiong *et al.* [144] reported such experiments with and GGG/YIG/Ni<sub>80</sub>Fe<sub>20</sub> stack placed face-down on a CPW for rf-excitation. In their experiments they used a rather thick YIG layer with  $3 \mu\text{m}$  thickness and mostly utilized the strong IP component of the rf-field on top of the CPW. In contrast to that we performed measurements on a microstructured Ni<sub>80</sub>Fe<sub>20</sub> element (with dimensions of  $10 \mu\text{m} \times 10 \mu\text{m}$ ) within the gap of the CPW on top of the 192 nm YIG layer. The YIG layer thickness used in our experiments increases the spacing between different PSSW modes and therefore allows to detect just one crossing and not a variety of different mode crossing at it would be the case for thicker films [144]. Figure A.4a) shows the detected dispersion branches for Ni<sub>80</sub>Fe<sub>20</sub> and YIG layers. The Ni<sub>80</sub>Fe<sub>20</sub> layer is thin enough to obtain the signal from the underlying YIG layer with the laser. The solid lines depict the calculated dispersion branches for the FMR, 1<sup>st</sup> and 2<sup>nd</sup>-order PSSW of YIG as well as the

FMR mode of  $\text{Ni}_{80}\text{Fe}_{20}$ . A more detailed view of the crossing section of  $\text{Ni}_{80}\text{Fe}_{20}$  FMR and YIG PSSW mode is presented in Fig. A.4b) where a coupling of the two modes becomes clearly visible.

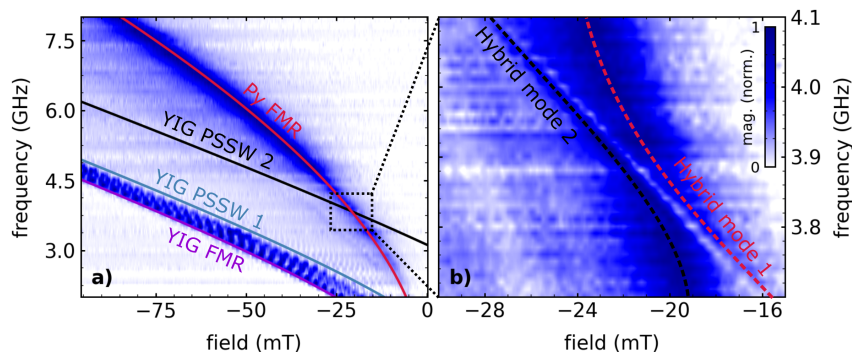


**Figure A.4 | Exchange-coupled  $\text{Ni}_{80}\text{Fe}_{20}$  element on top of YIG layer.** The normalized magnitude measured on top of the 10 nm  $\text{Ni}_{80}\text{Fe}_{20}$  element is shown. a) The YIG and  $\text{Ni}_{80}\text{Fe}_{20}$  FMR modes are clearly visible, next to the YIG FMR also DE modes can be detected through the  $\text{Ni}_{80}\text{Fe}_{20}$  layer. As solid lines the calculated dispersion branches for the FMR modes of YIG and  $\text{Ni}_{80}\text{Fe}_{20}$  as well as the first and second order PSSW mode are depicted. b) A zoom into the crossing area allows to obtain the mode splitting due to the exchange coupling of the YIG's PSSW mode and the  $\text{Ni}_{80}\text{Fe}_{20}$  mode. The dashed lines indicate the hybridized modes as guide for the eye.

The two dotted lines are a guide for the eye and represent the hybridized modes in vicinity of the crossing. The narrow dip passing the  $\text{Ni}_{80}\text{Fe}_{20}$  resonance line suppresses the signal nearly to zero, but compared to other strongly coupled systems the linewidth in the vicinity of the crossing is on the same order as the splittings width which is somehow on the edge of the strong-coupling regime. Note, that for this sample no effort was put in the quality of the YIG/ $\text{Ni}_{80}\text{Fe}_{20}$  interface. By additional cleaning steps before sputtering the  $\text{Ni}_{80}\text{Fe}_{20}$  on top of the YIG the quality of the interface should increase and therefore the transmittance of magnons through the interface. Using a ferromagnetic material with lower damping as  $\text{Ni}_{80}\text{Fe}_{20}$  would give rise to smaller linewidths in the vicinity of the crossing, thus the coupling coefficient would increase. Nevertheless, this experiment expands the possibilities of SNS-MOKE detection of strong coupling phenomena to the next level and will be further exploited in the future.

#### A.4. Spatially-resolved Imaging of SAW-induced Dynamics in Co

In addition to measurements on microstructured elements, as shown in chapter 6, we executed spatially-resolved imaging of SAW-driven FMR in extended cobalt (Co) layers to determine the wave vector behavior as function of field amplitude and field orientation. The patch dimensions are  $500\ \mu\text{m} \times 200\ \mu\text{m}$  and the thickness of the layer is 20 nm. The IDTs had resonance frequencies

of 0.88 GHz, 2.57 GHz, 4.28 GHz and 5.95 GHz. The FMR condition for 4.28 GHz is on the order of 10 mT at  $10^\circ$  field orientation with respect to the SAW propagation.

#### A.4.1. Spatially-resolved Imaging of SAW-driven FMR in a Co Patch

By performing spatially-resolved imaging in the center of the Co patch a clear maximum of intensity is observed in  $10^\circ$  orientation. For larger angular orientation the spin waves align with external field.

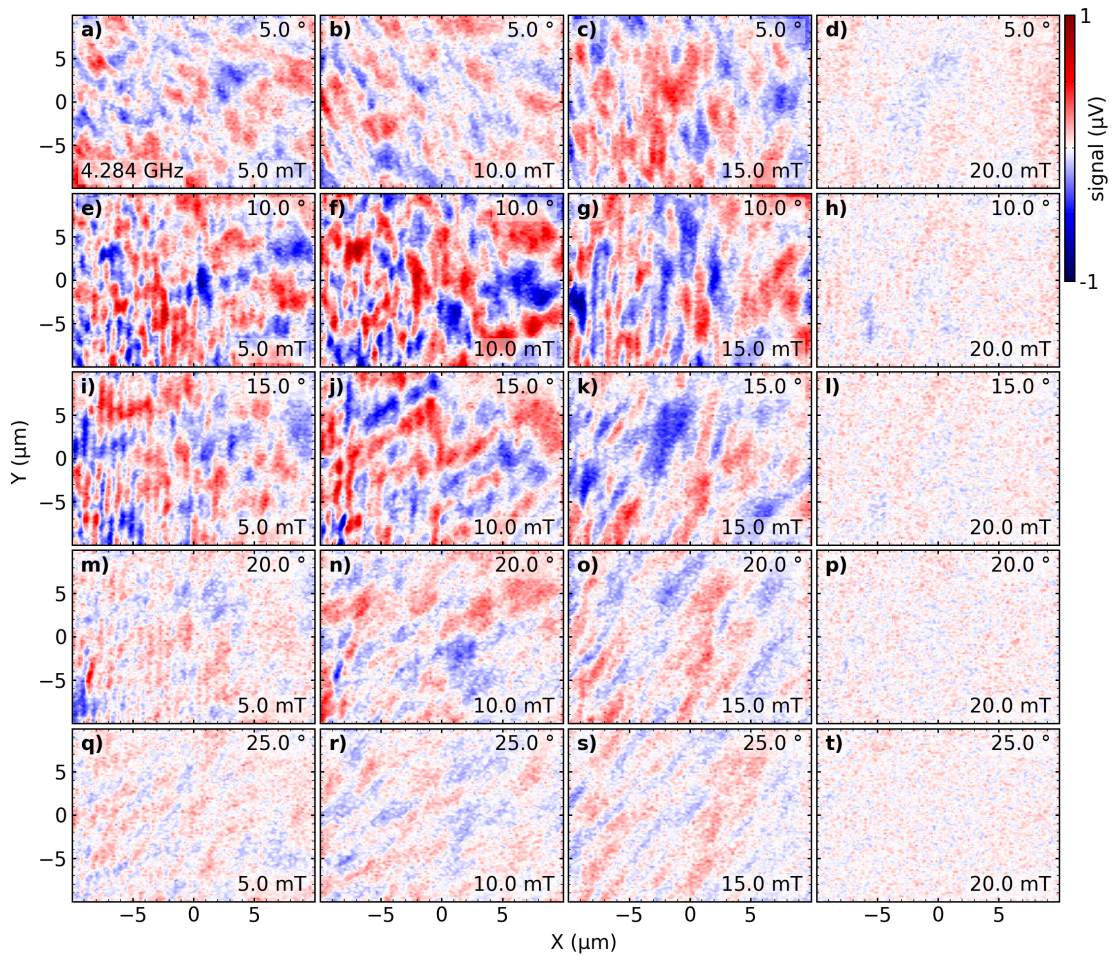


**Figure A.5 | Spatially-resolved imaging at different field amplitudes and orientations in Co.** For different field amplitudes (rows) and angular orientations (columns) the spatially-resolved response in the modulation channel is shown for an extended Co layer. The excitations frequency is 4.2 GHz.

### A.4.2. Wave-vector Analysis of SAW-driven FMR in a Co Patch

By applying a complex 2D-FFT on the obtained images from Fig. 6.9 the wave vectors of the contributing spin waves can be revealed. The complex 2D-FFT further allows distinguishing propagating and standing wave components. While a standing wave must consist of at least two wave vectors with opposing signs, a propagating wave only shows one peak in the  $k$ -space.

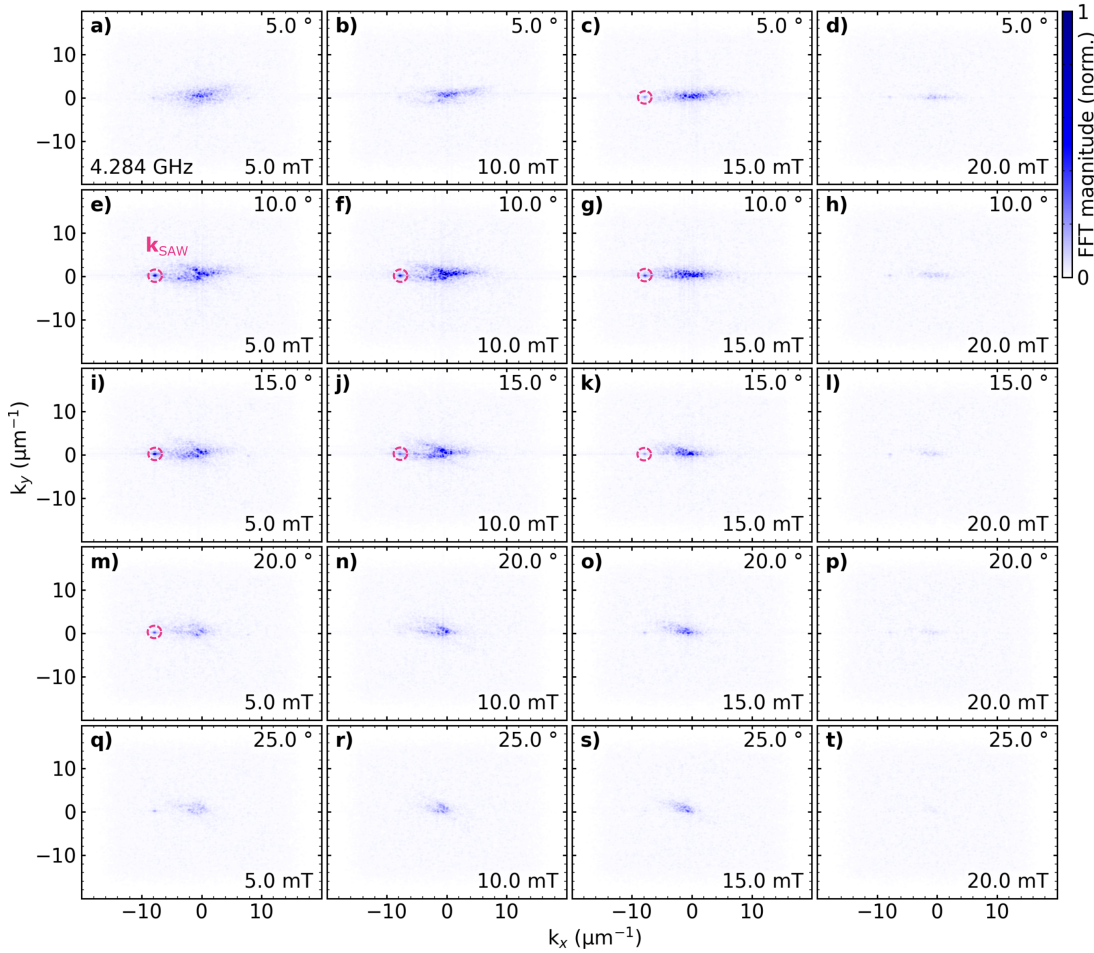


**Figure A.6 | Wave-vector spectra of SAW-driven dynamics for different field amplitudes and orientations.** 2D-FFT of the spatially-resolved measurements from Fig. A.5 are shown. The red circles indicate the wave vector component belonging to the SAW.

In the case of small IP angles between the applied bias field and  $\mathbf{k}_{\text{SAW}}$ , a strong propagating signal contribution can be found at wave vectors belonging to the SAW, as indicated by red circles in Fig. A.6. The long-wavelength component appears to align with the external bias field.

## A.5. Micromagnetic Simulation of NLSW Generation in Ni<sub>80</sub>Fe<sub>20</sub> Elements

The micromagnetic simulations complementing our experimental findings, are performed using the GPU-accelerated software package MUMAX3 [208]. The time- and space-dependent effective magnetic field is defined by the functional derivative of the free energy density  $\mathcal{F}[\vec{m}]$  with respect to the unit vector field of the magnetization  $\vec{m}(\vec{r}, t)$

$$\vec{B}_i^{\text{eff}}(t) = \vec{B}_i^{\text{ext}}(t) + \vec{B}_i^{\text{exch}} + \vec{B}_i^{\text{d}} + \vec{B}_i^{\text{a}}. \quad (\text{A.1})$$

It is composed of the external field  $\vec{B}_i^{\text{ext}}(t)$ , including the static bias field and the oscillating exciting field contribution; the exchange interaction field  $\vec{B}_i^{\text{ex}} = 2A_{\text{ex}}/M_s\Delta\vec{m}_i$ , with the exchange stiffness  $A_{\text{ex}}$  and the saturation magnetization  $M_s$ , the demagnetizing field  $\vec{B}_i^{\text{d}} = M_s\hat{K}_{ij} * \vec{m}_j$ , where we refer to reference [208] for details of the calculation of the demagnetizing kernel  $\hat{K}$  and the uniaxial magnetocrystalline anisotropy field  $\vec{B}_i^{\text{a}} = 2K_u/M_{\text{sat}}m_z\vec{e}_z$ , with  $K_u$  the anisotropy constant. The magnetization dynamics is described by the Landau-Lifshitz-Gilbert (LLG). The effective magnetic field enters the LLG equation,

$$\dot{\vec{m}}_i(t) = -\frac{\gamma}{1+\alpha^2} \left[ \vec{m}_i \times \vec{B}_i^{\text{eff}} + \alpha \vec{m}_i \times (\vec{m}_i \times \vec{B}_i^{\text{eff}}) \right], \quad (\text{A.2})$$

which is solved for every simulation cell  $i$  of the discretized magnetization vector field  $\vec{m}_i$ . The gyromagnetic ratio of an electron is denoted by  $\gamma = 1.76 \times 10^{11} (\text{T}^{-1}\text{s}^{-1})$  and  $\alpha$  is the Gilbert damping parameter.

### A.5.1. Field-swept Spectra of NLSWs Generation

To identify the field regime in which NLSW generation emerges the simulation where carried out over a range of external field values to extract the real and imaginary part of the dynamic response as function of bias field. This allows for direct comparison with the obtained SNS-MOKE data.

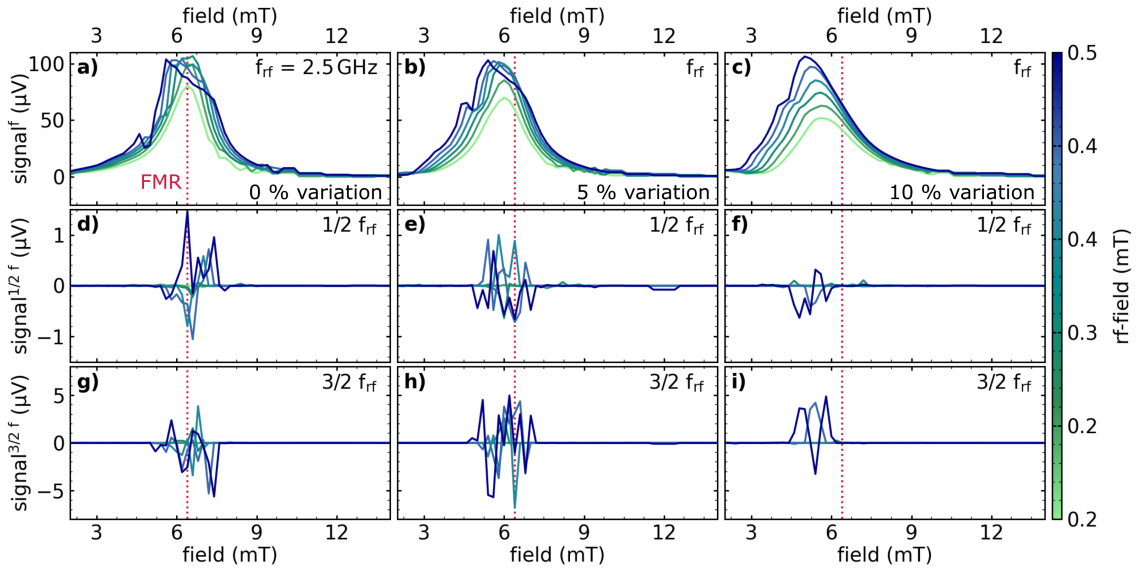


**Figure A.7 | Micromagnetic simulations of the field-resolved spin-wave spectra analyzed at different frequencies with different spatial variations of the saturation magnetization.** Rf-power dependent simulations of the field-resolved spin-wave spectra. a)-c) The imaginary part of the response is analyzed at the driving frequency which results in typical Lorentzian FMR lineshapes for low driving amplitudes. For increasing rf-power levels the phase starts to shift and the mode saturates. From panel a) to c) the spatial variation of  $M_{\text{sat}}$  parameters was increased from 0 % up to 10 % (the size of the grains is 100 nm). For larger variations of  $M_s$  the FMR condition is shifted towards lower fields, as depicted in b) and c) (the dotted red line shows the low power FMR condition for 0 % variation). Panel d)-e) show the imaginary  $1/2 f_{\text{rf}}$  response while g)-i) displays the  $3/2 f_{\text{rf}}$  component. Note that the field range in which NLSW generation appears is broad. The experimentally obtained coherent part of the spectrum is on the order of 1 mT, while the incoherent part accessible by the simulation covers a field range of 3 mT (corresponding to the linewidth of the ferromagnetic resonance) with a symmetric distribution around the FMR.

The simulation were performed for three different amounts of  $M_s$ -variation. In the case of a perfect film (Fig. A.7a)) the imaginary part shown an increase of amplitude as well as saturation for increasing rf-power levels. After passing the threshold, NLSW generation at  $1/2 f_{\text{rf}}$  and  $3/2 f_{\text{rf}}$  arises over a broad field range, as depicted in d) and g). Even in the simulation for the perfect film, these NLSWs do not provide a lineshape easy to interpret. However, the signal components emerge symmetrically around FMR condition and are not limited to a small field range above FMR as in the SNS-MOKE experiments. Thus we believe, that the micromagnetic simulations also visualize the incoherent part of the spectrum, which is not detectable by means of SNS-MOKE. As soon as a spatial variation of magnetic properties is introduced (Fig. A.7b) and c)) the FMR condition shifts towards lower fields and the threshold value for NLSW generation slightly increases. This might give an explanation for the obtained enhanced threshold values in smaller element geometries (cf. Fig. 7.5)), since inhomogeneous internal fields give rise to a spatial variation as well, which enhances as the structure size shrinks.

## A.5.2. Micromagnetic Simulation of spatially-resolved NLSW Generation

The introduced spatial variation of  $M_s$  is now applied to a simulation of the real-space distribution of  $3/2 f_{rf}$  NLSW generation.

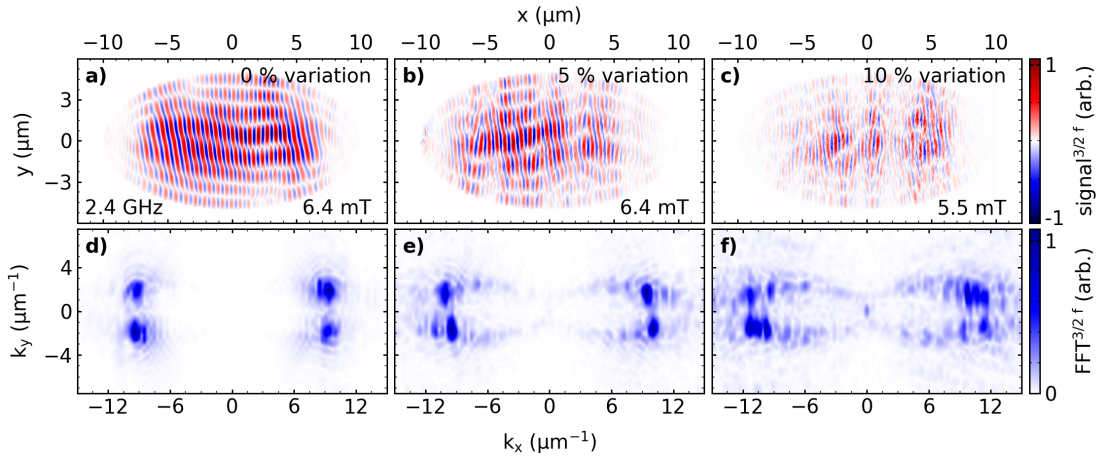


**Figure A.8 | Micromagnetic simulations of spatially-resolved NLSW excitations with different spatial variations of the saturation magnetization.** Real space images at  $3/2 f_{rf}$  obtained from micromagnetic simulations of a  $20 \mu\text{m} \times 10 \mu\text{m}$  ellipse. From panel a) to c) the spatial variation of  $M_s$  parameters was increased from 0 % up to 10 % (the size of the grains is 100 nm). In d) - e) the corresponding 2D-FFTs are shown. By increasing the strength of the variation more magnon-magnon scattering events occur resulting in the population of the magnon modes on the iso-frequency lines. The rf-power level in all images is above the threshold condition.

The change becomes more obvious by performing a 2D-FFT on the real space images obtained in Fig. A.8a)-c). By introducing a spatial variation the four dominant peaks in a) begin to smear out and favor a population of different spin-wave modes. In b) and c) the enhanced signal components follow the iso-frequency lines in the non-linear dispersion. Thus, the micromagnetic simulation are in excellent agreement with spatially-resolved imaging from Fig. 7.9. For the future, it might be useful to obtain the phase of NLSW generation as function of time under continuous rf-excitation to figure out under which conditions these NLSW emerge coherently and become visible in the experiment.



---

# Bibliography

---

- [1] T. N. Theis and H.-S. P. Wong, "The end of moore's law: A new beginning for information technology", *Computing in Science & Engineering*, vol. 19, no. 2, pp. 41–50, 2017. DOI: 10.1109/mcse.2017.29.
- [2] F. Peper, "The end of moore's law: Opportunities for natural computing?", *New Generation Computing*, vol. 35, pp. 253–269, 2017. DOI: 10.1007/s00354-017-0020-4.
- [3] K. Henke, G. T. Kenyon, and B. Migliori, "Machine learning in a post moore's law world: Quantum vs. neuromorphic substrates", in *2020 IEEE Southwest Symposium on Image Analysis and Interpretation*, IEEE, 2020. DOI: 10.1109/ssiai49293.2020.9094596.
- [4] S. A. Wolf *et al.*, "Spintronics: A spin-based electronics vision for the future", *Science*, vol. 294, no. 5546, pp. 1488–1495, 2001. DOI: 10.1126/science.1065389.
- [5] S. D. Sarma, "A giant appears in spintronics", *Nature Materials*, vol. 2, no. 5, pp. 292–294, 2003. DOI: 10.1038/nmat883.
- [6] V. Kruglyak and R. Hicken, "Magnonics: Experiment to prove the concept", *Journal of Magnetism and Magnetic Materials*, vol. 306, no. 2, pp. 191–194, 2006. DOI: 10.1016/j.jmmm.2006.02.242.
- [7] A. Steane, "Quantum computing", *Reports on Progress in Physics*, vol. 61, no. 2, pp. 117–173, 1998. DOI: 10.1088/0034-4885/61/2/002.
- [8] I. Žutić, J. Fabian, and S. D. Sarma, "Spintronics: Fundamentals and applications", *Reviews of Modern Physics*, vol. 76, no. 2, pp. 323–410, 2004. DOI: 10.1103/revmodphys.76.323.
- [9] S. Bader and S. Parkin, "Spintronics", *Annual Review of Condensed Matter Physics*, vol. 1, no. 1, pp. 71–88, 2010. DOI: 10.1146/annurev-conmatphys-070909-104123.
- [10] H.-H. Chen *et al.*, "Phase locking of spin-torque nano-oscillator pairs with magnetic dipolar coupling", *Physical Review B*, vol. 93, no. 22, p. 224410, 2016. DOI: 10.1103/physrevb.93.224410.
- [11] S. Kaka, M. R. Pufall, W. H. Rippard, T. J. Silva, S. E. Russek, and J. A. Katine, "Mutual phase-locking of microwave spin torque nano-oscillators", *Nature*, vol. 437, no. 7057, pp. 389–392, 2005. DOI: 10.1038/nature04035.
- [12] R. Lebrun *et al.*, "Mutual synchronization of spin torque nano-oscillators through a long-range and tunable electrical coupling scheme", *Nature Communications*, vol. 8, no. 15825, 2017. DOI: 10.1038/ncomms15825.

- [13] M. Collet *et al.*, “Generation of coherent spin-wave modes in yttrium iron garnet microdiscs by spin-orbit torque”, *Nature Communications*, vol. 7, no. 10377, 2016. DOI: <https://doi.org/10.1038/ncomms10377>.
- [14] A. Houshang, E. Iacocca, P. Dürrenfeld, S. R. Sani, J. Åkerman, and R. K. Dumas, “Spin-wave-beam driven synchronization of nanocontact spin-torque oscillators”, *Nature Nanotechnology*, vol. 11, no. 3, pp. 280–286, 2015. DOI: 10.1038/nnano.2015.280.
- [15] M. Haidar, A. A. Awad, M. Dvornik, R. Khymyn, A. Houshang, and J. Åkerman, “A single layer spin-orbit torque nano-oscillator”, *Nature Communications*, vol. 10, no. 2362, 2019. DOI: 10.1038/s41467-019-10120-4.
- [16] X. Fong, Y. Kim, R. Venkatesan, S. H. Choday, A. Raghunathan, and K. Roy, “Spin-transfer torque memories: Devices, circuits, and systems”, *Proceedings of the IEEE*, vol. 104, no. 7, pp. 1449–1488, 2016. DOI: 10.1109/jproc.2016.2521712.
- [17] B. Lenk, H. Ulrichs, F. Garbs, and M. Münzenberg, “The building blocks of magnonics”, *Physics Reports*, vol. 507, no. 4-5, pp. 107–136, 2011. DOI: 10.1016/j.physrep.2011.06.003.
- [18] P. Pirro, V. I. Vasyuchka, A. A. Serga, and B. Hillebrands, “Advances in coherent magnonics”, *Nature Reviews Materials*, vol. 6, 1114–1135, 2021. DOI: 10.1038/s41578-021-00332-w.
- [19] A. Barman *et al.*, “The 2021 magnonics roadmap”, *Journal of Physics: Condensed Matter*, vol. 33, no. 41, p. 413 001, 2021. DOI: 10.1088/1361-648x/abec1a.
- [20] S. Neusser and D. Grundler, “Magnonics: Spin waves on the nanoscale”, *Advanced Materials*, vol. 21, no. 28, pp. 2927–2932, 2009. DOI: 10.1002/adma.200900809.
- [21] V. V. Kruglyak, S. O. Demokritov, and D. Grundler, “Magnonics”, *Journal of Physics D: Applied Physics*, vol. 43, no. 26, p. 264 001, 2010. DOI: 10.1088/0022-3727/43/26/260301.
- [22] A. V. Chumak, A. A. Serga, and B. Hillebrands, “Magnon transistor for all-magnon data processing”, *Nature Communications*, vol. 5, no. 4700, 2014. DOI: 10.1038/ncomms5700.
- [23] K. Vogt *et al.*, “Spin waves turning a corner”, *Applied Physics Letters*, vol. 101, no. 4, p. 042 410, 2012. DOI: 10.1063/1.4738887.
- [24] Q. Wang *et al.*, “A magnonic directional coupler for integrated magnonic half-adders”, *Nature Electronics*, vol. 3, no. 12, pp. 765–774, 2020. DOI: 10.1038/s41928-020-00485-6.
- [25] M. Grassi *et al.*, “Slow-wave-based nanomagnonic diode”, *Physical Review Applied*, vol. 14, no. 2, p. 024 047, 2020. DOI: 10.1103/physrevapplied.14.024047.
- [26] T. Jungwirth, X. Marti, P. Wadley, and J. Wunderlich, “Antiferromagnetic spintronics”, *Nature Nanotechnology*, vol. 11, no. 3, pp. 231–241, 2016. DOI: 10.1038/nnano.2016.18.
- [27] V. Baltz, A. Manchon, M. Tsoi, T. Moriyama, T. Ono, and Y. Tserkovnyak, “Antiferromagnetic spintronics”, *Reviews of Modern Physics*, vol. 90, no. 1, p. 015 005, 2018. DOI: 10.1103/revmodphys.90.015005.

- [28] G. Schmidt, C. Hauser, P. Trempler, M. Paleschke, and E. T. Papaioannou, "Ultra thin films of yttrium iron garnet with very low damping: A review", *physica status solidi (b)*, vol. 257, no. 7, p. 1 900 644, 2020. DOI: 10.1002/pssb.201900644.
- [29] A. A. Serga, A. V. Chumak, and B. Hillebrands, "YIG magnonics", *Journal of Physics D: Applied Physics*, vol. 43, no. 26, p. 264 002, 2010. DOI: 10.1088/0022-3727/43/26/264002.
- [30] P. Trempler, R. Dreyer, P. Geyer, C. Hauser, G. Woltersdorf, and G. Schmidt, "Integration and characterization of micron-sized YIG structures with very low gilbert damping on arbitrary substrates", *Applied Physics Letters*, vol. 117, no. 23, p. 232 401, 2020. DOI: 10.1063/5.0026120.
- [31] F. Heyroth *et al.*, "Monocrystalline freestanding three-dimensional yttrium-iron-garnet magnon nanoresonators", *Physical Review Applied*, vol. 12, no. 5, p. 054 031, 2019. DOI: 10.1103/PhysRevApplied.12.054031.
- [32] M. Weiler *et al.*, "Elastically driven ferromagnetic resonance in nickel thin films", *Physical Review Letters*, vol. 106, no. 11, p. 117 601, 2011. DOI: 10.1103/physrevlett.106.117601.
- [33] L. Dreher *et al.*, "Surface acoustic wave driven ferromagnetic resonance in nickel thin films: Theory and experiment", *Physical Review B*, vol. 86, no. 13, p. 134 415, 2012. DOI: 10.1103/physrevb.86.134415.
- [34] M. Küß *et al.*, "Nonreciprocal dzyaloshinskii–moriya magnetoacoustic waves", *Physical Review Letters*, vol. 125, no. 21, p. 217 203, 2020. DOI: 10.1103/physrevlett.125.217203.
- [35] S. Datta, *Surface acoustic wave devices*. Englewood Cliffs, N.J: Prentice-Hall, 1986.
- [36] Y. Li, W. Zhang, V. Tyberkevych, W.-K. Kwok, A. Hoffmann, and V. Novosad, "Hybrid magnonics: Physics, circuits, and applications for coherent information processing", *Journal of Applied Physics*, vol. 128, no. 13, p. 130 902, 2020. DOI: 10.1063/5.0020277.
- [37] Y. Li *et al.*, "Strong coupling between magnons and microwave photons in on-chip ferromagnet-superconductor thin-film devices", *Physical Review Letters*, vol. 123, no. 10, p. 107 701, 2019. DOI: 10.1103/physrevlett.123.107701.
- [38] D. Lachance-Quirion, Y. Tabuchi, A. Gloppe, K. Usami, and Y. Nakamura, "Hybrid quantum systems based on magnonics", *Applied Physics Express*, vol. 12, no. 7, p. 070 101, 2019. DOI: 10.7567/1882-0786/ab248d.
- [39] S. Klingler *et al.*, "Gilbert damping of magnetostatic modes in a yttrium iron garnet sphere", *Applied Physics Letters*, vol. 110, no. 9, p. 092 409, 2017. DOI: 10.1063/1.4977423.
- [40] A. Leo, A. G. Monteduro, S. Rizzato, L. Martina, and G. Maruccio, "Identification and time-resolved study of ferrimagnetic spin-wave modes in a microwave cavity in the strong-coupling regime", *Physical Review B*, vol. 101, no. 1, p. 014 439, 2020. DOI: 10.1103/physrevb.101.014439.

- [41] X. Zhang, C.-L. Zou, L. Jiang, and H. X. Tang, "Strongly coupled magnons and cavity microwave photons", *Physical Review Letters*, vol. 113, no. 15, p. 156 401, 2014. DOI: 10.1103/physrevlett.113.156401.
- [42] H. Qin, S. J. Hämäläinen, and S. van Dijken, "Exchange-torque-induced excitation of perpendicular standing spin waves in nanometer-thick YIG films", *Scientific Reports*, vol. 8, no. 1, p. 5755, 2018. DOI: 10.1038/s41598-018-23933-y.
- [43] S. Klingler *et al.*, "Spin-torque excitation of perpendicular standing spin waves in coupled YIG/Co heterostructures", *Physical Review Letters*, vol. 120, no. 12, p. 127 201, 2018. DOI: 10.1103/physrevlett.120.127201.
- [44] L. Novotny, "Strong coupling, energy splitting, and level crossings: A classical perspective", *American Journal of Physics*, vol. 78, no. 11, pp. 1199–1202, 2010. DOI: 10.1119/1.3471177.
- [45] M. Elyasi, Y. M. Blanter, and G. E. W. Bauer, "Resources of nonlinear cavity magnonics for quantum information", *Physical Review B*, vol. 101, no. 5, p. 054 402, 2020. DOI: 10.1103/physrevb.101.054402.
- [46] T. Brächer and P. Pirro, "An analog magnon adder for all-magnonic neurons", *Journal of Applied Physics*, vol. 124, no. 15, p. 152 119, 2018. DOI: 10.1063/1.5042417.
- [47] R. Verba, M. Carpentieri, G. Finocchio, V. Tiberkevich, and A. Slavin, "Amplification and stabilization of large-amplitude propagating spin waves by parametric pumping", *Applied Physics Letters*, vol. 112, no. 4, p. 042 402, 2018. DOI: 10.1063/1.5019357.
- [48] S. Urazhdin, V. Tiberkevich, and A. Slavin, "Parametric excitation of a magnetic nanocontact by a microwave field", *Physical Review Letters*, vol. 105, no. 23, p. 237 204, 2010. DOI: 10.1103/physrevlett.105.237204.
- [49] C. W. Sandweg *et al.*, "Spin pumping by parametrically excited exchange magnons", *Physical Review Letters*, vol. 106, no. 21, p. 216 601, 2011. DOI: 10.1103/physrevlett.106.216601.
- [50] H. Kurebayashi, O. Dzyapko, V. E. Demidov, D. Fang, A. J. Ferguson, and S. O. Demokritov, "Spin pumping by parametrically excited short-wavelength spin waves", *Applied Physics Letters*, vol. 99, no. 16, p. 162 502, 2011. DOI: 10.1063/1.3652911.
- [51] T. Brächer, P. Pirro, and B. Hillebrands, "Parallel pumping for magnon spintronics: Amplification and manipulation of magnon spin currents on the micron-scale", *Physics Reports*, vol. 699, pp. 1–34, 2017. DOI: 10.1016/j.physrep.2017.07.003.
- [52] V. E. Demidov, M. P. Kostylev, K. Rott, P. Krzysteczko, G. Reiss, and S. O. Demokritov, "Generation of the second harmonic by spin waves propagating in microscopic stripes", *Physical Review B*, vol. 83, no. 5, p. 054 408, 2011. DOI: 10.1103/physrevb.83.054408.
- [53] S. J. Hermsdoerfer *et al.*, "A spin-wave frequency doubler by domain wall oscillation", *Applied Physics Letters*, vol. 94, no. 22, p. 223 510, 2009. DOI: 10.1063/1.3143225.

- [54] H. G. Bauer, P. Majchrak, T. Kachel, C. H. Back, and G. Woltersdorf, "Nonlinear spin-wave excitations at low magnetic bias fields", *Nature Communications*, vol. 6, no. 8274, 2015. DOI: 10.1038/ncomms9274.
- [55] C. Hauser *et al.*, "Yttrium iron garnet thin films with very low damping obtained by recrystallization of amorphous material", *Scientific Reports*, vol. 6, no. 20827, 2016. DOI: 10.1038/srep20827.
- [56] H. Qin, G.-J. Both, S. J. Hämäläinen, L. Yao, and S. van Dijken, "Low-loss YIG-based magnonic crystals with large tunable bandgaps", *Nature Communications*, vol. 9, no. 5445, 2018. DOI: 10.1038/s41467-018-07893-5.
- [57] E. R. J. Edwards, "Study of spin waves in in-plane magnetized thin films by means of Brillouin light scattering and magneto-optical kerr effect", Ph.D. dissertation, Westfälische Wilhelms-Universität Münster, Münster, Germany, 2012.
- [58] M. Farle, T. Silva, and G. Woltersdorf, "Spin dynamics in the time and frequency domain", in *Magnetic Nanostructures*. H. Zabel and M. Farle, Eds., ser. Springer Tracts in Modern Physics. Springer, Heidelberg, Berlin, 2013, vol. 246, ch. 2, pp. 37–83. DOI: 10.1007/978-3-642-32042-2\_2.
- [59] L. Liensberger, L. Flacke, D. Rogerson, M. Althammer, R. Gross, and M. Weiler, "Spin-wave propagation in metallic  $\text{Co}_{25}\text{Fe}_{75}$  films determined by microfocused frequency-resolved magneto-optic kerr effect", *IEEE Magnetics Letters*, vol. 10, pp. 1–5, 2019. DOI: 10.1109/lmag.2019.2918755.
- [60] H. Qin *et al.*, "Nanoscale magnonic Fabry-Pérot resonator for low-loss spin-wave manipulation", *Nature Communications*, vol. 12, no. 2293, 2021. DOI: 10.1038/s41467-021-22520-6.
- [61] P. Grünberg, M. G. Cottam, W. Vach, C. Mayr, and R. E. Camley, "Brillouin scattering of light by spin waves in thin ferromagnetic films (invited)", *Journal of Applied Physics*, vol. 53, no. 3, pp. 2078–2083, 1982. DOI: 10.1063/1.330751.
- [62] S. Demokritov, "Brillouin light scattering studies of confined spin waves: Linear and nonlinear confinement", *Physics Reports*, vol. 348, no. 6, pp. 441–489, 2001. DOI: 10.1016/s0370-1573(00)00116-2.
- [63] S. Demokritov and V. Demidov, "Micro-brillouin light scattering spectroscopy of magnetic nanostructures", *IEEE Transactions on Magnetics*, vol. 44, no. 1, pp. 6–12, 2008. DOI: 10.1109/tmag.2007.910227.
- [64] J. Jorzick *et al.*, "Brillouin light scattering from quantized spin waves in micron-size magnetic wires", *Physical Review B*, vol. 60, no. 22, pp. 15 194–15 200, 1999. DOI: 10.1103/physrevb.60.15194.
- [65] M. Geilen, F. Kohl, A. Nicoloiu, A. Müller, B. Hillebrands, and P. Pirro, "Interference of co-propagating Rayleigh and Sezawa waves observed with micro-focused Brillouin light scattering spectroscopy", *Applied Physics Letters*, vol. 117, no. 21, p. 213 501, 2020. DOI: 10.1063/5.0029308.

- [66] G. D. Fuchs *et al.*, “Excited-state spectroscopy using single spin manipulation in diamond”, *Physical Review Letters*, vol. 101, no. 11, p. 117 601, 2008. DOI: 10.1103/physrevlett.101.117601.
- [67] J. M. Taylor *et al.*, “High-sensitivity diamond magnetometer with nanoscale resolution”, *Nature Physics*, vol. 4, no. 10, pp. 810–816, 2008. DOI: 10.1038/nphys1075.
- [68] C. S. Wolfe *et al.*, “Off-resonant manipulation of spins in diamond via precessing magnetization of a proximal ferromagnet”, *Physical Review B*, vol. 89, no. 18, p. 180 406, 2014. DOI: 10.1103/physrevb.89.180406.
- [69] B. A. McCullian *et al.*, “Broadband multi-magnon relaxometry using a quantum spin sensor for high frequency ferromagnetic dynamics sensing”, *Nature Communications*, vol. 11, no. 5229, 2020. DOI: 10.1038/s41467-020-19121-0.
- [70] J. Förster *et al.*, “Nanoscale x-ray imaging of spin dynamics in yttrium iron garnet”, *Journal of Applied Physics*, vol. 126, no. 17, p. 173 909, 2019. DOI: 10.1063/1.5121013.
- [71] V. Sluka *et al.*, “Emission and propagation of 1d and 2d spin waves with nanoscale wavelengths in anisotropic spin textures”, *Nature Nanotechnology*, vol. 14, no. 4, pp. 328–333, 2019. DOI: 10.1038/s41565-019-0383-4.
- [72] K. Baumgaertl *et al.*, “Nanoimaging of ultrashort magnon emission by ferromagnetic grating couplers at GHz frequencies”, *Nano Letters*, vol. 20, no. 10, pp. 7281–7286, 2020. DOI: 10.1021/acs.nanolett.0c02645.
- [73] R. Dreyer, N. Liebing, E. R. J. Edwards, A. Müller, and G. Woltersdorf, “Spin-wave localization and guiding by magnon band structure engineering in yttrium iron garnet”, *Physical Review Materials*, vol. 5, no. 6, p. 064 411, 2021. DOI: 10.1103/physrevmaterials.5.064411.
- [74] J. M. D. Coey, *Magnetism and Magnetic Materials*. Cambridge University Press, 2001. DOI: 10.1017/cbo9780511845000.
- [75] D. D. Stancil and A. Prabhakar, *Spin Waves: Theory and Applications*. Springer Nature, 2009, 348 pp.
- [76] L. D. Landau and E. M. Lifshitz, “On the theory of the dispersion of magnetic permeability in ferromagnetic bodies”, *Phys. Zeitsch. der Sow*, vol. 8, pp. 153–169, 1935.
- [77] F. Porrati, “Spatially varying magnetic anisotropies in ultrathin films”, Ph.D. dissertation, Martin-Luther-Universität Halle-Wittenberg, Halle (Saale), Germany, 2002.
- [78] L. D. Landau, J. S. Bell, M. J. Kearsley, L. P. Pitaevskii, E. Lifshitz, and J. B. Sykes, *Electrodynamics of continuous media*. Oxford Oxfordshire New York: Pergamon, 1984.
- [79] S. M. Rezende, *Fundamentals of Magnonics*. Springer International Publishing, 2020. DOI: 10.1007/978-3-030-41317-0.
- [80] H. G. Bauer, “Linear and nonlinear magnetization dynamics in thin ferromagnetic films and nanostructures”, Ph.D. dissertation, Universität Regensburg, Regensburg, Germany, 2014.

- [81] G. Woltersdorf, "Spin-pumping and two-magnon scattering in magnetic multilayers", Ph.D. dissertation, Simon Fraser University, Burnaby, BC, Canada, 2004.
- [82] D. Morgan, *Surface Acoustic Wave Filters*. Elsevier Science & Techn., 2010, 448 pp.
- [83] C. Herring and C. Kittel, "The theory of spin waves in ferromagnetic media", *Physical Review*, vol. 88, no. 6, pp. 1435–1435, 1952. DOI: 10.1103/physrev.88.1435.3.
- [84] T. L. Gilbert and J. M. Kelly, "Anomalous rotational damping in ferromagnetic sheets", Report, Armour Research Foundation of Illinois Institute of Technology, Chicago, Illinois, 1955, 1955.
- [85] B. Heinrich, D. Fraitová, and V. Kamberský, "The influence of s-d exchange on relaxation of magnons in metals", *physica status solidi (b)*, vol. 23, no. 2, pp. 501–507, 1967. DOI: 10.1002/pssb.19670230209.
- [86] K. Zakeri *et al.*, "Spin dynamics in ferromagnets: Gilbert damping and two-magnon scattering", *Physical Review B*, vol. 76, no. 10, p. 104 416, 2007. DOI: 10.1103/physrevb.76.104416.
- [87] M. O. Härtinger, "Untersuchung magnetischer materialien mit methoden der ferromagnetischen resonanz", Ph.D. dissertation, Universität Regensburg, Regensburg, Germany, 2017. DOI: 10.5283/EPUB.35434.
- [88] B. Divinskiy, S. Urazhdin, S. O. Demokritov, and V. E. Demidov, "Controlled nonlinear magnetic damping in spin-hall nano-devices", *Nature Communications*, vol. 10, no. 5211, 2019. DOI: 10.1038/s41467-019-13246-7.
- [89] M. Hurben and C. Patton, "Theory of magnetostatic waves for in-plane magnetized isotropic films", *Journal of Magnetism and Magnetic Materials*, vol. 139, no. 3, pp. 263–291, 1995. DOI: 10.1016/0304-8853(95)90006-3.
- [90] D. D. Stancil, *Theory of Magnetostatic Waves*. Springer New York, 1993. DOI: 10.1007/978-1-4613-9338-2.
- [91] R. W. Damon and J. R. Eshbach, "Magnetostatic modes of a ferromagnetic slab", *Journal of Applied Physics*, vol. 31, no. 5, S104–S105, 1960. DOI: 10.1063/1.1984622.
- [92] B. A. Kalinikos and A. N. Slavin, "Theory of dipole-exchange spin wave spectrum for ferromagnetic films with mixed exchange boundary conditions", *Journal of Physics C: Solid State Physics*, vol. 19, no. 35, pp. 7013–7033, 1986. DOI: 10.1088/0022-3719/19/35/014.
- [93] B. A. Kalinikos, "Spectrum and linear excitation of spin waves in ferromagnetic films", *Soviet Physics Journal*, vol. 24, no. 8, pp. 718–731, 1981. DOI: 10.1007/bf00941342.
- [94] P. Kabos, W. D. Wilber, C. E. Patton, and P. Grünberg, "Brillouin light scattering study of magnon branch crossover in thin iron films", *Physical Review B*, vol. 29, no. 11, pp. 6396–6398, 1984. DOI: 10.1103/physrevb.29.6396.

- [95] S. Tacchi *et al.*, “Strongly hybridized dipole-exchange spin waves in thin  $fe-n$  ferromagnetic films”, *Physical Review B*, vol. 100, no. 10, p. 104 406, 2019. DOI: 10.1103/physrevb.100.104406.
- [96] M. G. Cottam, *Linear and Nonlinear Spin Waves in Magnetic Films and Superlattices*. World Scientific Publishing Co Inc, 1994, 476 pp.
- [97] B. A. Kalinikos, M. P. Kostylev, N. V. Kozhus, and A. N. Slavin, “The dipole-exchange spin wave spectrum for anisotropic ferromagnetic films with mixed exchange boundary conditions”, *Journal of Physics: Condensed Matter*, vol. 2, no. 49, pp. 9861–9877, 1990. DOI: 10.1088/0953-8984/2/49/012.
- [98] H. Ulrichs, “Spin-wave instabilities on the nanoscale”, Ph.D. dissertation, Westfälische Wilhelms-Universität Münster, Münster, Germany, 2014.
- [99] V. L. Safonov, M. E. McConney, and M. R. Page, “Parallel pumping of spin waves in a ferromagnet revisited”, *Journal of Magnetism and Magnetic Materials*, vol. 490, p. 165 486, 2019. DOI: 10.1016/j.jmmm.2019.165486.
- [100] A. Venugopal, T. Qu, and R. H. Victora, “Nonlinear parallel-pumped FMR: Three and four magnon processes”, *IEEE Transactions on Microwave Theory and Techniques*, vol. 68, no. 2, pp. 602–610, 2020. DOI: 10.1109/tmtt.2019.2952128.
- [101] V. S. L'vov, *Wave Turbulence Under Parametric Excitation*. Springer Berlin Heidelberg, 1994. DOI: 10.1007/978-3-642-75295-7.
- [102] V. E. Zakharov, V. S. L'vov, and S. S. Starobinets, “Spin-wave turbulence beyond the parametric excitation threshold”, *Soviet Physics Uspekhi*, vol. 17, no. 6, pp. 896–919, 1975. DOI: 10.1070/pu1975v017n06abeh004404.
- [103] P. Krivosik and C. E. Patton, “Hamiltonian formulation of nonlinear spin-wave dynamics: Theory and applications”, *Physical Review B*, vol. 82, no. 18, p. 184 428, 2010. DOI: 10.1103/physrevb.82.184428.
- [104] R. M. White and M. Sparks, “Ferromagnetic relaxation. III. theory of instabilities”, *Physical Review*, vol. 130, no. 2, pp. 632–638, 1963. DOI: 10.1103/physrev.130.632.
- [105] H. Suhl, “Subsidiary absorption peaks in ferromagnetic resonance at high signal levels”, *Physical Review*, vol. 101, no. 4, pp. 1437–1438, 1956. DOI: 10.1103/physrev.101.1437.
- [106] T. Qu *et al.*, “Nonlinear magnon scattering mechanism for microwave pumping in magnetic films”, *IEEE Access*, vol. 8, pp. 216 960–216 968, 2020. DOI: 10.1109/access.2020.3040711.
- [107] L. Körber *et al.*, “Nonlocal stimulation of three-magnon splitting in a magnetic vortex”, *Physical Review Letters*, vol. 125, no. 20, p. 207 203, 2020. DOI: 10.1103/physrevlett.125.207203.
- [108] T. Hula *et al.*, “Nonlinear losses in magnon transport due to four-magnon scattering”, *Applied Physics Letters*, vol. 117, no. 4, p. 042 404, 2020. DOI: 10.1063/5.0015269.

- [109] A. K. Zvezdin, *Modern magneto-optics and magneto-optical materials*. Bristol Philadelphia, Pa: Institute of Physics Pub, 1997.
- [110] Z. Q. Qiu and S. D. Bader, "Surface magneto-optic kerr effect", *Review of Scientific Instruments*, vol. 71, no. 3, pp. 1243–1255, 2000. DOI: 10.1063/1.1150496.
- [111] M. Ribow, "Voltage control of magnetic anisotropy in ultrathin epitaxial magnetic layers", Ph.D. dissertation, Martin Luther University Halle-Wittenberg, Halle (Saale), Germany, 2017.
- [112] Š. Višňovský, V. Pařízek, M. Nývlt, P. Kielar, V. Prosser, and R. Krishnan, "Magneto-optical kerr spectra of nickel", *Journal of Magnetism and Magnetic Materials*, vol. 127, no. 1-2, pp. 135–139, 1993. DOI: 10.1016/0304-8853(93)90206-h.
- [113] Y. Suzuki *et al.*, "Magneto-optical effects of ultrathin ferro-, antiferro- and non-magnetic films", *MRS Proceedings*, vol. 475, 227–237, 1997. DOI: 10.1557/proc-475-227.
- [114] J. Stöhr, "Exploring the microscopic origin of magnetic anisotropies with x-ray magnetic circular dichroism (XMCD) spectroscopy", *Journal of Magnetism and Magnetic Materials*, vol. 200, no. 1-3, pp. 470–497, 1999. DOI: 10.1016/S0304-8853(99)00407-2.
- [115] E. Beaurepaire, J.-C. Merle, A. Daunois, and J.-Y. Bigot, "Ultrafast spin dynamics in ferromagnetic nickel", *Physical Review Letters*, vol. 76, no. 22, pp. 4250–4253, 1996. DOI: 10.1103/physrevlett.76.4250.
- [116] I. Radu *et al.*, "Transient ferromagnetic-like state mediating ultrafast reversal of anti-ferromagnetically coupled spins", *Nature*, vol. 472, no. 7342, pp. 205–208, 2011. DOI: 10.1038/nature09901.
- [117] I Rzdolski *et al.*, "Analysis of the time-resolved magneto-optical kerr effect for ultrafast magnetization dynamics in ferromagnetic thin films", *Journal of Physics: Condensed Matter*, vol. 29, no. 17, p. 174 002, 2017. DOI: 10.1088/1361-648x/aa63c6.
- [118] Y. Hashimoto *et al.*, "Ultrafast time-resolved magneto-optical imaging of all-optical switching in GdFeCo with femtosecond time-resolution and a  $\mu\text{m}$  spatial-resolution", *Review of Scientific Instruments*, vol. 85, no. 6, p. 063 702, 2014. DOI: 10.1063/1.4880015.
- [119] A. R. Khorsand *et al.*, "Element-specific probing of ultrafast spin dynamics in multisublattice magnets with visible light", *Physical Review Letters*, vol. 110, no. 10, p. 107 205, 2013. DOI: 10.1103/physrevlett.110.107205.
- [120] C. von Korff Schmising *et al.*, "Element-specific magnetization dynamics of complex magnetic systems probed by ultrafast magneto-optical spectroscopy", *Applied Sciences*, vol. 10, no. 21, p. 7580, 2020. DOI: 10.3390/app10217580.
- [121] K. Perzlmaier, G. Woltersdorf, and C. H. Back, "Observation of the propagation and interference of spin waves in ferromagnetic thin films", *Physical Review B*, vol. 77, no. 5, p. 054 425, 2008. DOI: 10.1103/physrevb.77.054425.

- [122] C. Dubs, O. Surzhenko, R. Linke, A. Danilewsky, U. Brückner, and J. Dellith, "Sub-micrometer yttrium iron garnet LPE films with low ferromagnetic resonance losses", *Journal of Physics D: Applied Physics*, vol. 50, no. 20, p. 204 005, 2017. DOI: 10.1088/1361-6463/aa6b1c.
- [123] C. Shannon, "Communication in the presence of noise", *Proceedings of the IRE*, vol. 37, no. 1, pp. 10–21, 1949. DOI: 10.1109/jrproc.1949.232969.
- [124] H. Qin, R. Dreyer, G. Woltersdorf, T. Taniyama, and S. van Dijken, "Electric-field control of propagating spin waves by ferroelectric domain-wall motion in a multiferroic heterostructure", *Advanced Materials*, vol. 33, no. 27, p. 2100 646, 2021. DOI: 10.1002/adma.202100646.
- [125] G. Woltersdorf and C. H. Back, "Microwave assisted switching of single domain  $\text{Ni}_{80}\text{Fe}_{20}$  elements", *Physical Review Letters*, vol. 99, no. 22, p. 227 207, 2007. DOI: 10.1103/physrevlett.99.227207.
- [126] T. Sebastian, K. Schultheiss, B. Obry, B. Hillebrands, and H. Schultheiss, "Micro-focused brillouin light scattering: Imaging spin waves at the nanoscale", *Frontiers in Physics*, vol. 3, no. 35, 2015. DOI: 10.3389/fphy.2015.00035.
- [127] A. V. Chumak, V. I. Vasyuchka, A. A. Serga, and B. Hillebrands, "Magnon spintronics", *Nature Physics*, vol. 11, no. 6, pp. 453–461, 2015. DOI: 10.1038/nphys3347.
- [128] A. V. Sadovnikov *et al.*, "Spin wave propagation in a uniformly biased curved magnonic waveguide", *Physical Review B*, vol. 96, no. 6, 060401(R), 2017. DOI: 10.1103/physrevb.96.060401.
- [129] S. Klingler, P. Pirro, T. Brächer, B. Leven, B. Hillebrands, and A. V. Chumak, "Spin-wave logic devices based on isotropic forward volume magnetostatic waves", *Applied Physics Letters*, vol. 106, no. 21, p. 212 406, 2015. DOI: 10.1063/1.4921850.
- [130] G. Woltersdorf, O. Mosendz, B. Heinrich, and C. H. Back, "Magnetization dynamics due to pure spin currents in magnetic double layers", *Physical Review Letters*, vol. 99, no. 24, p. 246 603, 2007. DOI: 10.1103/PhysRevLett.99.246603.
- [131] P. Trempler, "Herstellung und charakterisierung von freistehenden dreidimensionalen yttrium-eisen-granat nanostrukturen", Ph.D. dissertation, Martin-Luther-Universität Halle-Wittenberg, Halle (Saale), Germany, 2021.
- [132] H. G. Bauer, J. Y. Chauleau, G. Woltersdorf, and C. H. Back, "Coupling of spinwave modes in wire structures", *Applied Physics Letters*, vol. 104, no. 10, p. 102 404, 2014. DOI: 10.1063/1.4868250.
- [133] T. Neuman, D. S. Wang, and P. Narang, "Nanomagnonic cavities for strong spin-magnon coupling and magnon-mediated spin-spin interactions", *Physical Review Letters*, vol. 125, no. 24, p. 247 702, 2020. DOI: 10.1103/physrevlett.125.247702.

- [134] M. Wu, B. A. Kalinikos, and C. E. Patton, "Generation of dark and bright spin wave envelope soliton trains through self-modulational instability in magnetic films", *Physical Review Letters*, vol. 93, no. 15, p. 157 207, 2004. DOI: 10.1103/physrevlett.93.157207.
- [135] R. Gallardo *et al.*, "Reconfigurable spin-wave nonreciprocity induced by dipolar interaction in a coupled ferromagnetic bilayer", *Physical Review Applied*, vol. 12, no. 3, p. 034 012, 2019. DOI: 10.1103/physrevapplied.12.034012.
- [136] H. Qin and S. van Dijken, "Nanometer-thick YIG-based magnonic crystals: Bandgap dependence on groove depth, lattice constant, and film thickness", *Applied Physics Letters*, vol. 116, no. 20, p. 202 403, 2020. DOI: 10.1063/5.0009807.
- [137] J. Ding, T. Liu, H. Chang, and M. Wu, "Sputtering growth of low-damping yttrium-iron-garnet thin films", *IEEE Magnetics Letters*, vol. 11, pp. 1–5, 2020. DOI: 10.1109/lmag.2020.2989687.
- [138] C. Dubs *et al.*, "Low damping and microstructural perfection of sub-40nm-thin yttrium iron garnet films grown by liquid phase epitaxy", *Physical Review Materials*, vol. 4, no. 2, p. 024 416, 2020. DOI: 10.1103/physrevmaterials.4.024416.
- [139] M. C. Onbasli *et al.*, "Pulsed laser deposition of epitaxial yttrium iron garnet films with low gilbert damping and bulk-like magnetization", *APL Materials*, vol. 2, no. 10, p. 106 102, 2014. DOI: 10.1063/1.4896936.
- [140] H. Maier-Flaig *et al.*, "Temperature-dependent magnetic damping of yttrium iron garnet spheres", *Physical Review B*, vol. 95, no. 21, p. 214 423, 2017. DOI: 10.1103/physrevb.95.214423.
- [141] B. Yao *et al.*, "Coherent control of magnon radiative damping with local photon states", *Communications Physics*, vol. 2, no. 1, 2019. DOI: 10.1038/s42005-019-0264-z.
- [142] A. V. Chumak, A. A. Serga, and B. Hillebrands, "Magnonic crystals for data processing", *Journal of Physics D: Applied Physics*, vol. 50, no. 24, p. 244 001, 2017. DOI: 10.1088/1361-6463/aa6a65.
- [143] J. Chen *et al.*, "Strong interlayer magnon-magnon coupling in magnetic metal-insulator hybrid nanostructures", *Physical Review Letters*, vol. 120, no. 21, p. 217 202, 2018. DOI: 10.1103/physrevlett.120.217202.
- [144] Y. Xiong *et al.*, "Probing magnon–magnon coupling in exchange coupled  $Y_3Fe_5O_{12}$ /permalloy bilayers with magneto-optical effects", *Scientific Reports*, vol. 10, no. 1, p. 12 548, 2020. DOI: 10.1038/s41598-020-69364-6.
- [145] J. W. Rao *et al.*, "Interferometric control of magnon-induced nearly perfect absorption in cavity magnonics", *Nature Communications*, vol. 12, no. 1933, 2021. DOI: 10.1038/s41467-021-22171-7.
- [146] T. Wolz *et al.*, "Introducing coherent time control to cavity magnon-polariton modes", *Communications Physics*, vol. 3, no. 3, 2020. DOI: 10.1038/s42005-019-0266-x.

- [147] V. V. Danilov, D. L. Lyfar<sup>1</sup>, Y. V. Lyubon'ko, A. Y. Nechiporuk, and S. M. Ryabchenko, "Low-temperature ferromagnetic resonance in epitaxial garnet films on paramagnetic substrates", *Soviet Physics Journal*, vol. 32, no. 4, pp. 276–280, 1989. DOI: 10.1007/bf00897267.
- [148] A. F. van Loo, R. G. E. Morris, and A. D. Karenowska, "Time-resolved measurements of surface spin-wave pulses at millikelvin temperatures", *Physical Review Applied*, vol. 10, no. 4, p. 044 070, 2018. DOI: 10.1103/physrevapplied.10.044070.
- [149] L. Mihalceanu *et al.*, "Temperature-dependent relaxation of dipole-exchange magnons in yttrium iron garnet films", *Physical Review B*, vol. 97, no. 21, p. 214 405, 2018. DOI: 10.1103/physrevb.97.214405.
- [150] Y. Li *et al.*, "Coherent spin pumping in a strongly coupled magnon-magnon hybrid system", *Physical Review Letters*, vol. 124, no. 11, p. 117 202, 2020. DOI: 10.1103/physrevlett.124.117202.
- [151] C. Campbell, "Applications of surface acoustic and shallow bulk acoustic wave devices", *Proceedings of the IEEE*, vol. 77, no. 10, pp. 1453–1484, 1989. DOI: 10.1109/5.40664.
- [152] K. Hashimoto, *Surface Acoustic Wave Devices in Telecommunications: Modelling and Simulation*. Berlin, Heidelberg: Springer, 2000.
- [153] D Sander *et al.*, "The 2017 magnetism roadmap", *Journal of Physics D: Applied Physics*, vol. 50, no. 36, p. 363 001, 2017. DOI: 10.1088/1361-6463/aa81a1.
- [154] K. Uchida, T. An, Y. Kajiwara, M. Toda, and E. Saitoh, "Surface-acoustic-wave-driven spin pumping in Y<sub>3</sub>Fe<sub>5</sub>O<sub>12</sub>/Pt hybrid structure", *Applied Physics Letters*, vol. 99, no. 21, p. 212 501, 2011. DOI: 10.1063/1.3662032.
- [155] L. Thevenard *et al.*, "Surface-acoustic-wave-driven ferromagnetic resonance in (Ga,Mn)(As,P) epilayers", *Physical Review B*, vol. 90, no. 9, p. 094 401, 2014. DOI: 10.1103/physrevb.90.094401.
- [156] D. Labanowski, A. Jung, and S. Salahuddin, "Power absorption in acoustically driven ferromagnetic resonance", *Applied Physics Letters*, vol. 108, no. 2, p. 022 905, 2016. DOI: 10.1063/1.4939914.
- [157] M. Xu *et al.*, "Nonreciprocal surface acoustic wave propagation via magneto-rotation coupling", *Science Advances*, vol. 6, no. 32, eabb1724, 2020. DOI: 10.1126/sciadv.abb1724.
- [158] S. Davis, A. Baruth, and S. Adenwalla, "Magnetization dynamics triggered by surface acoustic waves", *Applied Physics Letters*, vol. 97, no. 23, p. 232 507, 2010. DOI: 10.1063/1.3521289.
- [159] R. G. Kryshstal and A. V. Medved, "Surface acoustic wave in yttrium iron garnet as tunable magnonic crystals for sensors and signal processing applications", *Applied Physics Letters*, vol. 100, no. 19, p. 192 410, 2012. DOI: 10.1063/1.4714507.

- [160] R. G. Kryshnal and A. V. Medved, "Nonlinear spin waves in dynamic magnonic crystals created by surface acoustic waves in yttrium iron garnet films", *Journal of Physics D: Applied Physics*, vol. 50, no. 49, p. 495 004, 2017. DOI: 10.1088/1361-6463/aa93ba.
- [161] D. Fall, M. Duquennoy, M. Ouafouh, N. Smagin, B. Piwakowski, and F. Jenot, "Generation of broadband surface acoustic waves using a dual temporal-spatial chirp method", *The Journal of the Acoustical Society of America*, vol. 142, no. 1, EL108–EL112, 2017. DOI: 10.1121/1.4994676.
- [162] M. Weiß *et al.*, "Multiharmonic frequency-chirped transducers for surface-acoustic-wave optomechanics", *Physical Review Applied*, vol. 9, no. 1, p. 014 004, 2018. DOI: 10.1103/physrevapplied.9.014004.
- [163] D. A. Bas, P. J. Shah, M. E. McConney, and M. R. Page, "Optimization of acoustically-driven ferromagnetic resonance devices", *Journal of Applied Physics*, vol. 126, no. 11, p. 114 501, 2019. DOI: 10.1063/1.5111846.
- [164] T. Yokouchi *et al.*, "Creation of magnetic skyrmions by surface acoustic waves", *Nature Nanotechnology*, vol. 15, no. 5, pp. 361–366, 2020. DOI: 10.1038/s41565-020-0661-1.
- [165] C. Berk, M. Jaris, W. Yang, S. Dhuey, S. Cabrini, and H. Schmidt, "Strongly coupled magnon–phonon dynamics in a single nanomagnet", *Nature Communications*, vol. 10, no. 2652, 2019. DOI: 10.1038/s41467-019-10545-x.
- [166] W. G. Yang, M. Jaris, D. L. Hibbard-Lubow, C. Berk, and H. Schmidt, "Magnetoelastic excitation of single nanomagnets for optical measurement of intrinsic gilbert damping", *Physical Review B*, vol. 97, no. 22, p. 224 410, 2018. DOI: 10.1103/physrevb.97.224410.
- [167] P. Kuszewski *et al.*, "Optical probing of rayleigh wave driven magnetoacoustic resonance", *Physical Review Applied*, vol. 10, no. 3, p. 034 036, 2018. DOI: 10.1103/physrevapplied.10.034036.
- [168] D. A. Bas *et al.*, "Acoustically driven ferromagnetic resonance in diverse ferromagnetic thin films", *IEEE Transactions on Magnetics*, vol. 57, no. 2, pp. 1–5, 2021. DOI: 10.1109/tmag.2020.3019214.
- [169] B. Casals *et al.*, "Generation and imaging of magnetoacoustic waves over millimeter distances", *Physical Review Letters*, vol. 124, no. 13, p. 137 202, 2020. DOI: 10.1103/physrevlett.124.137202.
- [170] P. G. Gowtham, T. Moriyama, D. C. Ralph, and R. A. Buhrman, "Traveling surface spin-wave resonance spectroscopy using surface acoustic waves", *Journal of Applied Physics*, vol. 118, no. 23, p. 233 910, 2015. DOI: 10.1063/1.4938390.
- [171] M. Küß *et al.*, "Symmetry of the magnetoelastic interaction of rayleigh and shear horizontal magnetoacoustic waves in nickel thin films on LiTaO<sub>3</sub>", *Physical Review Applied*, vol. 15, no. 3, p. 034 046, 2021. DOI: 10.1103/physrevapplied.15.034046.

- [172] M. Foerster *et al.*, “Direct imaging of delayed magneto-dynamic modes induced by surface acoustic waves”, *Nature Communications*, vol. 8, no. 407, 2017. DOI: 10.1038/s41467-017-00456-0.
- [173] S. Z. Baba, Y. Nakata, Y. Ito, R. Hisatomi, Y. Nakamura, and K. Usami, “Optical heterodyne imaging of magnetostatic modes in one-dimensional magnonic crystals”, *Physical Review B*, vol. 100, no. 10, p. 104437, 2019. DOI: 10.1103/physrevb.100.104437.
- [174] Y. Nozaki and S. Yanagisawa, “Excitation of ferromagnetic resonance using surface acoustic waves”, *Electrical Engineering in Japan*, vol. 204, no. 3, pp. 3–9, 2018. DOI: 10.1002/eej.23099.
- [175] P. J. Shah, D. A. Bas, I. Lisenkov, A. Matyushov, N. X. Sun, and M. R. Page, “Giant nonreciprocity of surface acoustic waves enabled by the magnetoelastic interaction”, *Science Advances*, vol. 6, no. 49, eabc5648, 2020. DOI: 10.1126/sciadv.abc5648.
- [176] L. Rayleigh, “On waves propagated along the plane surface of an elastic solid”, *Proceedings of the London Mathematical Society*, vol. s1-17, no. 1, pp. 4–11, 1885. DOI: 10.1112/plms/s1-17.1.4.
- [177] C. Deger *et al.*, “Sound velocity of Al<sub>x</sub>Ga<sub>1-x</sub>N thin films obtained by surface acoustic-wave measurements”, *Applied Physics Letters*, vol. 72, no. 19, pp. 2400–2402, 1998. DOI: 10.1063/1.121368.
- [178] G. Veith and M. Kowatsch, “Optical generation of continuous 76-MHz surface acoustic waves on YZ LiNbO<sub>3</sub>”, *Applied Physics Letters*, vol. 40, no. 1, pp. 30–32, 1982. DOI: 10.1063/1.92907.
- [179] P. Kuszewski, “Optical detection of magneto-acoustic dynamics”, Ph.D. dissertation, Sorbonne Université, Paris, France, 2018.
- [180] R. Kryshtal and A. Medved, “Nonreciprocity of spin waves in magnonic crystals created by surface acoustic waves in structures with yttrium iron garnet”, *Journal of Magnetism and Magnetic Materials*, vol. 395, pp. 180–184, 2015. DOI: 10.1016/j.jmmm.2015.07.086.
- [181] E. Schlömann, J. J. Green, and U. Milano, “Recent developments in ferromagnetic resonance at high power levels”, *Journal of Applied Physics*, vol. 31, no. 5, S386–S395, 1960. DOI: 10.1063/1.1984759.
- [182] T. Gerrits, M. Schneider, A. Kos, and T. Silva, “Large-angle magnetization dynamics measured by time-resolved ferromagnetic resonance”, *Physical Review B*, vol. 73, no. 9, 2006. DOI: 10.1103/physrevb.73.094454.
- [183] V. E. Demidov and N. G. Kovshikov, “Stochastic generation accompanying parametric excitation of spin waves in yttrium iron garnet films”, *Technical Physics Letters*, vol. 24, no. 4, pp. 274–276, 1998. DOI: 10.1134/1.1262081.
- [184] H. Ulrichs, V. E. Demidov, S. O. Demokritov, and S. Urazhdin, “Parametric excitation of eigenmodes in microscopic magnetic dots”, *Physical Review B*, vol. 84, no. 9, p. 094401, 2011. DOI: 10.1103/physrevb.84.094401.

- [185] H. Suhl, "The theory of ferromagnetic resonance at high signal powers", *Journal of Physics and Chemistry of Solids*, vol. 1, no. 4, pp. 209–227, 1957. DOI: 10.1016/0022-3697(57)90010-0.
- [186] H. Schultheiss *et al.*, "Direct current control of three magnon scattering processes in spin-valve nanocontacts", *Physical Review Letters*, vol. 103, no. 15, p. 157202, 2009. DOI: 10.1103/physrevlett.103.157202.
- [187] T. Gerrits, P. Krivosik, M. L. Schneider, C. E. Patton, and T. J. Silva, "Direct detection of nonlinear ferromagnetic resonance in thin films by the magneto-optical kerr effect", *Physical Review Letters*, vol. 98, no. 20, 2007. DOI: 10.1103/physrevlett.98.207602.
- [188] I. Barsukov *et al.*, "Giant nonlinear damping in nanoscale ferromagnets", *Science Advances*, vol. 5, no. 10, eaav6943, 2019. DOI: 10.1126/sciadv.aav6943.
- [189] K. Adhikari, S. Sahoo, A. K. Mondal, Y. Otani, and A. Barman, "Large nonlinear ferromagnetic resonance shift and strong magnon-magnon coupling in Ni<sub>80</sub>Fe<sub>20</sub> nanocross array", *Physical Review B*, vol. 101, no. 5, p. 054406, 2020. DOI: 10.1103/physrevb.101.054406.
- [190] C. Koerner, R. Dreyer, M. Wagener, N. Liebing, H. G. Bauer, and G. Woltersdorf, "Frequency multiplication by collective nanoscale spin-wave dynamics", *Science*, vol. 375, no. 6585, pp. 1165–1169, 2022. DOI: 10.1126/science.abm6044.
- [191] T. Makiuchi *et al.*, "Parametron on magnetic dot: Stable and stochastic operation", *Applied Physics Letters*, vol. 118, no. 2, p. 022402, 2021. DOI: 10.1063/5.0038946.
- [192] V. Bolpasi and W. von Klitzing, "Double-pass tapered amplifier diode laser with an output power of 1 W for an injection power of only 200  $\mu$ W", *Review of Scientific Instruments*, vol. 81, no. 11, p. 113108, 2010. DOI: 10.1063/1.3501966.
- [193] S. Blin, G. M. Stéphan, R. Gabet, P. Besnard, and D. Kilper, "Amplification process in a laser injected by a narrow band weak signal", *Europhysics Letters (EPL)*, vol. 52, no. 1, pp. 60–65, 2000. DOI: 10.1209/epl/i2000-00404-8.
- [194] V. E. Demidov *et al.*, "Magnetic nano-oscillator driven by pure spin current", *Nature Materials*, vol. 11, pp. 1028–1031, 2012. DOI: 10.1038/nmat3459.
- [195] V. E. Demidov *et al.*, "Synchronization of spin hall nano-oscillators to external microwave signals", *Nature Communications*, vol. 5, no. 3179, 2014. DOI: 10.1038/ncomms4179.
- [196] K. Wagner *et al.*, "Injection locking of multiple auto-oscillation modes in a tapered nanowire spin hall oscillator", *Scientific Reports*, vol. 8, no. 16040, 2018. DOI: 10.1038/s41598-018-34271-4.
- [197] H. Fulara *et al.*, "Giant voltage-controlled modulation of spin hall nano-oscillator damping", *Nature Communications*, vol. 11, no. 4006, 2020. DOI: 10.1038/s41467-020-17833-x.
- [198] T. Hache *et al.*, "Bipolar spin hall nano-oscillators", *Applied Physics Letters*, vol. 116, no. 19, p. 192405, 2020. DOI: 10.1063/5.0008988.

- [199] M. Romera *et al.*, “Vowel recognition with four coupled spin-torque nano-oscillators”, *Nature*, vol. 563, no. 7730, pp. 230–234, 2018. DOI: 10.1038/s41586-018-0632-y.
- [200] J. Grollier, D. Querlioz, K. Y. Camsari, K. Everschor-Sitte, S. Fukami, and M. D. Stiles, “Neuromorphic spintronics”, *Nature Electronics*, vol. 3, no. 7, pp. 360–370, 2020. DOI: 10.1038/s41928-019-0360-9.
- [201] A. Venugopal, T. Qu, and R. H. Victora, “Manipulation of nonlinear magnon effects using a secondary microwave frequency”, *Applied Physics Letters*, vol. 117, no. 15, p. 152404, 2020. DOI: 10.1063/5.0022227.
- [202] T. Brächer *et al.*, “Phase-to-intensity conversion of magnonic spin currents and application to the design of a majority gate”, *Scientific Reports*, vol. 6, no. 38235, 2016. DOI: 10.1038/srep38235.
- [203] O. Schubert *et al.*, “Sub-cycle control of terahertz high-harmonic generation by dynamical bloch oscillations”, *Nature Photonics*, vol. 8, no. 2, pp. 119–123, 2014. DOI: 10.1038/nphoton.2013.349.
- [204] T. Popmintchev, M.-C. Chen, P. Arpin, M. M. Murnane, and H. C. Kapteyn, “The attosecond nonlinear optics of bright coherent x-ray generation”, *Nature Photonics*, vol. 4, no. 12, pp. 822–832, 2010. DOI: 10.1038/nphoton.2010.256.
- [205] T. van der Sar, F. Casola, R. Walsworth, and A. Yacoby, “Nanometre-scale probing of spin waves using single electron spins”, *Nature Communications*, vol. 6, no. 7886, 2015. DOI: 10.1038/ncomms8886.
- [206] I. Bertelli *et al.*, “Magnetic resonance imaging of spin-wave transport and interference in a magnetic insulator”, *Science Advances*, vol. 6, no. 46, eabd3556, 2020. DOI: 10.1126/sciadv.abd3556.
- [207] M. Yan, A. Kákay, C. Andreas, and R. Hertel, “Spin-cherenkov effect and magnonic mach cones”, *Physical Review B*, vol. 88, no. 22, p. 220412, 2013. DOI: 10.1103/physrevb.88.220412.
- [208] A. Vansteenkiste, J. Leliaert, M. Dvornik, M. Helsen, F. Garcia-Sanchez, and B. V. Waeyenberge, “The design and verification of MuMax3”, *AIP Advances*, vol. 4, no. 10, p. 107133, 2014. DOI: 10.1063/1.4899186.

---

# Curriculum Vitae

---

## Personal information:

Name: Rouven Dreyer  
Date of Birth: 02.07.1987  
Place of Birth: Delmenhorst  
Citizenship: German

## Education:

*since 2017* Member of the *Integrated research and training group (IRTG)* of the CRC/TRR 227 Ultrafast Spin Dynamics

*since 2014* **Ph.D. studies**, Martin Luther University Halle-Wittenberg

- Focus: Magnetization dynamics, non-linear spin waves, surface acoustic waves, optical detection techniques
- Thesis: *Magneto-optical super-Nyquist Sampling of linear and non-linear Spin-Wave Phenomena*
- Supervisor: Prof. Dr. Georg Woltersdorf

*2011 - 2014* **Master of Science in Physics**, Leibniz University Hannover ( $\varnothing 1.1$ )

- Focus: Laser physics, quantum optics, non-linear optics, photonics, meteorology
- Thesis: *Ultrakurz gepulste Laserdioden für Anwendungen in der Photonik*
- Supervisor: Dr. Carsten Reinhardt

*2008 - 2011* **Bachelor of Science in Physics**, Leibniz University Hannover ( $\varnothing 1.6$ )

- Focus: Optics, quantum physics, meteorology
- Thesis: *Aufbau einer Absolutfrequenzstabilisierung für ein Raman-Lasersystem*
- Supervisor: Dr. Carsten Klempt

*2007 - 2008* Civil service, Kinder und Jugendhaus Horizont, Delmenhorst

*1994 - 2007* **Abitur**, Gymnasium an der Willmsstraße, Delmenhorst ( $\varnothing 2.4$ )

Halle (Saale), 18<sup>th</sup> August 2022

---

Rouven Dreyer



---

# List of Publications

---

- F. Heyroth, C. Hauser, P. Trempler, P. Geyer, F. Syrowatka, **R. Dreyer**, S. G. Ebbinghaus, G. Woltersdorf, and G. Schmidt, "Monocrystalline Freestanding Three-Dimensional Yttrium-Iron-Garnet Magnon Nanoresonators", *Phys. Rev. Applied* **12**, 054031 (2019), DOI: 10.1103/PhysRevApplied.12.054031
- P. Trempler, **R. Dreyer**, P. Geyer, C. Hauser, G. Woltersdorf, and G. Schmidt, "Integration and characterization of micron-sized YIG structures with very low Gilbert damping on arbitrary substrates", *Appl. Phys. Lett.* **117**, 232401 (2020), DOI: 10.1063/5.0026120
- H. Qin, R. B. Holländer, L. Flajšman, F. Hermann, **R. Dreyer**, G. Woltersdorf, and S. van Dijken, "Nanoscale magnonic Fabry-Pérot resonator for low-loss spin-wave manipulation", *Nat. Commun.* **12**, 2293 (2021), DOI: 10.1038/s41467-021-22520-6
- H. Qin, **R. Dreyer**, G. Woltersdorf, T. Taniyama, S. van Dijken, "Electric-Field Control of Propagating Spin Waves by Ferroelectric Domain-Wall Motion in a Multiferroic Heterostructure", *Adv. Mater.* **33**, 2100646 (2021), DOI: 10.1002/adma.202100646
- **R. Dreyer**, N. Liebing, E. R. J. Edwards, A. Müller, and G. Woltersdorf, "Spin-wave localization and guiding by magnon band structure engineering in yttrium iron garnet", *Phys. Rev. Materials* **5**, 064411 (2021), DOI: 10.1103/PhysRevMaterials.5.064411
- C. Koerner, **R. Dreyer**, H. G. Bauer, M. Wagener, and G. Woltersdorf, "Frequency multiplication by collective nanoscale spin-wave dynamics", *Science* **375**, 6585, 1165-1169, DOI: 10.1126/science.abm6044
- **R. Dreyer**, A. F. Schäffer, H. G. Bauer, J. Berakdar, and G. Woltersdorf, "Imaging and phase-locking of non-linear spin waves", *Nat. Commun.*, *accepted for publication* (2022)
- A. Pandey, **R. Dreyer**, P. Seyidov, C. Koerner, S. Tirpanci and G. Woltersdorf, "Opto-electric imaging of spin polarization", *Phys. Rev. Lett.*, *under review*
- P. Geyer, **R. Dreyer**, E. Papaioannou, G. Woltersdorf, and G. Schmidt, "3D fabrication of yttrium iron garnet magnon lenses for efficient magnon focusing", *in preparation*
- **R. Dreyer**, P. Trempler, P. Geyer, G. Schmidt, and G. Woltersdorf, "Surface acoustic wave driven magnetization dynamics in transferred YIG microstructures", *in preparation*



---

# Acknowledgments

---

At first, I would like to thank my supervisor Prof. Georg Woltersdorf for his guidance and support over the years of my Ph.D. studies and for the chance to build up the workgroup with him from scratch. This experience was very beneficial to find my own place in between optics and magnetism, together with the possibility to supervise the next generation of promising students in our group. During our discussions about new setups, projects, and publications, I profited from his technical expertise and his amazing knowledge of the world of physics. I am really thankful for the trust he had in my work and the time he gave me to accomplish our projects. He always inspired me in our meetings to search for challenging measurement possibilities for our novel-developed microscopy setup. Moreover, he gave me the opportunity to visit exciting conferences and workshops to present our experimental findings to the scientific community, which resulted in fruitful discussions, collaborations, and friendships.

I would also like to acknowledge Dr. Eric Edwards for helping me in the different development phases of the SNS-MOKE at the beginning of my Ph.D., and for all the exciting discussions ranging from technical problems to world politics.

Moreover, I would like to thank all my collaborators from the different groups for sharing samples, performing simulations, carrying out measurements, and discussing results and manuscripts with me. Here I would like to name Philip Trempler, Philipp Geyer, Sandra Gottwals and Stephanie Lake from Prof. Georg Schmidt's group in Halle; Rasmus Holländer and Huajun Qin from Sebastiaan Van Dijken's group in Aalto; Alexander Schäffer from Jamal Berakdar's group in Halle; James Taylor from the MPI in Halle, Hans Bauer from Bamberg as well as Dr. Mathias Weiler from Munich.

For all the wonderful events, discussions, coffee breaks, and conference visits, I dedicate a big thank you to all the former and current members of my workgroup in Halle (Liane Brandt, Chris Körner, Wolfgang Hoppe, Niklas Liebing, Jens Lange, Atul Pandey, Lukas Geiling, Simon Wisotzki, Markus Muchow, Mirko Ribow, Lea Apel, Alexey Melnikov, Saban Tirpanci, Ingrid Stössel, Palvan Seyidov and the "guitar man" Amine Wahada) as well as to all the other wonderful people from MLU in Halle.

Special thanks go out to all the proof readers of this thesis (Philip Trempler, Aali Schäffer, Philipp Geyer, Julian "Yuri" Bartels, Niklas Liebing, Stephanie Lake, Chris Körner and Wolfgang Hoppe).

Last but not least, I would like to thank all of my friends and the most important persons in my life, my wonderful girlfriend Nicole, my sister Romi and my parents Karin and Claus, for all the endless support during the years of my Ph.D. studies. You always encouraged me to keep on going and follow my way in all phases. Without you, this work would not have been possible.



---

# Eidesstattliche Erklärung

---

Hiermit erkläre ich, Rouven Dreyer, die vorliegende Arbeit **Magneto-optical super-Nyquist Sampling of linear and non-linear Spin-Wave Phenomena** selbständig und ohne fremde Hilfe verfasst zu haben. Es wurden keine anderen als die von mir angegebenen Quellen und Hilfsmittel benutzt. Die den benutzten Werken wörtlich oder inhaltlich entnommenen Stellen sind als solche kenntlich gemacht worden. Ich erkläre, die Angaben wahrheitsgemäßgemacht, keine vergeblichen Promotionsversuche unternommen und keine Dissertation an einer anderen wissenschaftlichen Einrichtung zur Erlangung eines akademischen Grades eingereicht zu haben. Ich bin weder vorbestraft noch sind gegen mich Ermittlungsverfahren anhängig.

Halle (Saale), den 18.08.2022

---

Rouven Dreyer

